ADVANCING THE MAXIMUM ACCELERATING GRADIENT OF NIOBIUM-3 TIN SUPERCONDUCTING RADIOFREQUENCY ACCELERATOR CAVITIES: RF MEASUREMENTS, DYNAMIC TEMPERATURE MAPPING, AND MATERIAL GROWTH

A Dissertation

Presented to the Faculty of the Graduate School

of Cornell University

in Partial Fulfillment of the Requirements for the Degree of

Doctor of Philosophy

by

Ryan Douglas Porter

December 2021

ADVANCING THE MAXIMUM ACCELERATING GRADIENT OF NIOBIUM-3 TIN SUPERCONDUCTING RADIOFREQUENCY ACCELERATOR CAVITIES: RF MEASUREMENTS, DYNAMIC TEMPERATURE MAPPING, AND MATERIAL GROWTH

Ryan Douglas Porter, Ph.D.

Cornell University 2021

Niobium-3 Tin (Nb_3Sn) is the most promising alternative material for Superconducting Radiofrequency (SRF) particle accelerator cavities. Current SRF accelerators use superconducting niobium accelerator cavities, which are nearing their theoretical limits of performance. Nb_3Sn promises increased quality factors, twice the operational temperature (4.2 K instead of 2 K), and almost twice the theoretical accelerating gradient–96 MV/m in a TESLA elliptical style cavity. These advances can reduce the size and complexity of particle accelerators while simultaneously making them more efficient. The capability of operating at 4.2 K enables the creation of small-scale superconducting accelerators that are run off cryocoolers and could be used in research and industrial applications. Current Nb_3Sn cavities achieve quality factors of $2{\cdot}10^{10}$ at 4.2 K. The accelerating gradient, however, is limited far below the theoretical potential of this material, with the best recorded reaching 24 MV/m. In this work we present studies on what is limiting the maximum accelerating gradients in these cavities. We study cavity performance under RF testing, make dynamic measurements of cavity heating during operation, study samples with microscopy, and develop models of Nb_3Sn material growth. In the process we develop new diagnostic tools for SRF development: a dynamic/high speed temperature mapping system that

measures the spatial heat distribution on a cavity at 50 ksps, and high-power test system for measuring the ultimate critical fields (theoretical limit of the accelerating gradient) of new materials. We explore models of cavity losses/heating that limit the accelerating gradient and propose modifications to the material growth process to create Nb_3Sn cavities with higher accelerating gradients and quality factors. We conclude with results from a new cavity coating wherein we have suppressed multi-gap superconductivity that has been seen in these cavities and was a limitation to the quality factor.

BIOGRAPHICAL SKETCH

Ryan was born in Toronto, Ontario, Canada. Ryan lived his early years on a maple syrup and llama farm in rural Ontario and moved to Victoria, BC, Canada during middle school. Ryan began his studies in physics and mathematics at the University of Victoria and earned B.Sc. and M.Sc. in physics. During his M.Sc. Ryan was inspired by accelerator physicists at Canada's national particle accelerator centre, TRIUMF, to pursue accelerator physics. In 2015, he started his graduate studies at Cornell University in the SRF group. He graduated in 2021.

Dedicated to my family, friends, everyone that helped me along the way, and those that this research will hopefully one day help.

ACKNOWLEDGEMENTS

I would like to acknowledge all those who helped with the work presented here, making me into the researcher I have become, and keeping me sane during these past 6 years.

First, I would like to acknowledge my Ph.D. advisor, Prof. Matthias Liepe. This work would not be possible if not for his advice and support. Matthias has allowed me to achieve a degree of success I did not think was possible during my Ph.D. Outside of the research itself Matthias helped me secure numerous conference talks and craft presentations that have won me awards. This has introduced me to almost everyone in the SRF community, many of whom I can now count as friends. I feel I must admit here that some of the jokes I use in talks were created by Matthias himself. He has taught me research, management, and communication skills. During my time in graduate school, I have talked to many other graduate students about their advisors and their experiences are universally worse than my relationship with Matthias. I mean, how many other advisors eat lunch with their graduate students every day (before the pandemic[1]) and periodically watch an episode of the Simpsons with them?

Research, of course, is not done alone; numerous people have contributed to this work. First I would like to acknowledge the CLASSE technical and administrative personal who have helped in almost every aspect of my research (and provided quite a few laughs along the way): Paul Bishop, Holly Conklin, Terri Gruber-Hine, John Kaufman, Greg Kulina, James Sears, Neal Alexander, Gregory Abbot, Randy Miller, Terry Neiss, Katerina Malysheva, Monica Wesley, Joan Curtiss, Jessica Turco, Tim O'Connell, Eric Smith, John Dobbins, Nate Rider, Alexandra Gallyas Sanhueza, Mike Roman, Peter Quigley, and many

[1]Though Matthias still organized a weekly group lunch via Zoom.

more I am neglecting to mention (for which I apologize). Special thanks go to Adam Holic who designed almost everything I needed machined and taught me everything I know about how to make prints that the machine shop will understand. I would like to acknowledge all those that I have supervised and have contributed to this work: Sam Ginnett, Hannah Hu, Songqi Jia, Xu Yan, Matthew Tao, Spencer Halls, Calvin Chen, and Ruth Strauss. I would like to acknowledge my fellow graduate students and scientists in the research group that helped in my research, taught me, and made the workdays enjoyable: Dan Gonella, Daniel Hall, James Maniscalco, Pete Koufalis, Thomas Oseroff, Shura Zeryck, Neil Stilin, Gabriel Gaitan, Liana Shpani, Nicole Verboncoeur, Zeming Sun, Fumio Furatu, and Mingqi Ge. I'd like to acknowledge those who I have collaborated with on this research: Zhaslan Baraissov, Paul Cueva, Michelle Kelley, Danilo Liarte, Nathan Sitaraman[2], Rachel Farber, Sarah Wilson, Tomas Arias, Richard Hennig, David Muller, Jim Sethna, and last but far from least, Sam Posen.

I would like to acknowledge my friends for the support, relaxation, and fun they have provided over the years. Without them I could not have completed my Ph.D. I have roughly divided them into groups–some of which overlap. Fellow groupmates are listed above. My sincere apologies to those I have missed. From my year in the physics department: Michelle, Nathan, Eric, and Eamonn. From the weekly board games nights: James, Beline, Morgan, Alex, Brian, and Caitlyn. From the Ballroom team: Janna, Will, Kemper, Thomas, Eimi, Jeff, Ruby, and the entire rest of the team. My friends from back home who still talk to me constantly and are so excited to see me when I visit: Carleigh, Elise,

[2]Nathan deserves exceptional acknowledgement for the numerous conversations we have had about Nb_3Sn material growth and for answering more questions than I'd like to think about at seemingly any time of the day or night. I'm not sure I can keep track of which ideas about Nb_3Sn growth are his or mine anymore.

Ryan, Meghan, Shelley, John, John, and Heather. I would especially like to acknowledge Carleigh for patiently listening to almost every bad thing that has happened to me in the past 6 years. Her support is one of the reasons I am here today.

Finally, I would like to acknowledge my family. My mother, Jacqueline, my father, Wayne, my brother, Scott, my sister[3], Bernadette, and that sweet silly ball of fluff, the Snuzzlecat (a dog). It goes without saying that they have provided tremendous support over the years and during my Ph.D. Nothing makes me happier than talking to them or going home to see their smiling faces.

[3]-in-law

The work shown here was supported by:

U.S. DOE award DE-SC0008431.

NSF Award 1734189.

Center for Bright Beam (NSF Award 1549132).

This work made use of the Cornell Center for Materials Research Shared Facilities which are supported through the NSF MRSEC program (DMR-1719875).

TABLE OF CONTENTS

LIST OF TABLES

LIST OF FIGURES

CHAPTER 1

INTRODUCTION

Particle accelerators are machines that use electromagnetic fields to accelerate charged particles. These machines create beams of energetic particles for use in a variety of applications. Particle accelerators are a key tool of science where, through direct beam use or the production of x-rays, they are used to probe subatomic particles [A+12], study new materials needed for future technologies, and advance chemical, biological, and medical research [BEW05, Gal14]. 45 Nobel Prizes have been awarded for research that involves particle accelerators (either in the discovery or proving of a theory) [SW14]. Outside of research accelerators find important applications in medicine and industry [HS09, Sab13]. Particle beams are used to treat cancers and generate nuclear isotopes used for diagnostics. Accelerators are used in the production of plastics, food and equipment sterilization, and many other areas. Many other areas of research, medicine, and industry could be enabled by the advancement of particle accelerators [HW15, HS09].

Most major modern accelerators use Radiofrequency (RF) electromagnetic waves to accelerate particles. The RF wave is trapped in a metal resonant structure known as an accelerator cavity. As the RF wave oscillates in the in the accelerator cavity a portion of it is absorbed into the wall as heat through resistive losses. Minimizing these losses is one important objective in RF cavity acceleration.

We introduce standard figures of merit for accelerator cavities here (discussed in greater detail in chapter 2). The accelerating gradient is the maximum energy gain (or loss) of an electron (or other charged particle) when traversing

the accelerator cavity, divided by the charge. We typically express the accelerator gradient in terms of MV/m. An electron traversing (appropriately timed) a 1 m long accelerator that is running at 10 MV/m will gain 10 MeV of energy. To measure the efficiency of an accelerator cavity we use the quality factor, Q, of the cavity.

Accelerator cavities may be built out of copper, but they are limited to small accelerating gradients or pulsed operation. Many applications require continuous beams of high energy particles. Under these circumstances so much RF energy would be absorbed by the cavity walls that the copper would melt (or the accelerator would have to be unfeasibly long). For these applications superconducting materials are used for the accelerator cavities.

Superconductors have a very small resistance in RF fields[1]–roughly one millionth that of copper–allowing the accelerator to operate efficiently with high RF fields/accelerating gradients. Accelerator cavities made from superconductors are called Superconducting Radiofrequency (SRF) accelerator cavities. Niobium has been the standard superconductor for SRF accelerator cavities since the first SRF accelerator was built at SLAC in the 1960's [PSFW64, Pad17].

At currently achievable performance the losses in the walls of accelerator cavities seem trivial. The under construction accelerator, LCLS-II, accelerator is roughly 300 m long (of accelerator cavities) and uses accelerator cavities operating at 16 MV/m with quality factors of $\approx 3 \cdot 10^{10}$ [Ros19]. The total power lost in the accelerator cavities is only 2.7 kW–roughly the power consumption of three homes combined. This seems like nothing for a large accelerator, but the true problem is keeping the accelerator cavities cold. At 2 K is takes $\approx$ 800 W to re-

[1]Superconductors are usually known for having 0 electrical resistance, but this is true only for DC electricity, not AC/RF, as we will see in chapter 2.

move 1 W of deposited heat and a large, complicated cryogenics plant [SKR03]. This increases the power requirements to $\approx$ 2.2 MW. In comparison, copper cavities operating at the same accelerating gradient would consume $\sim$ 1 GW. Niobium cavities are much more efficient than copper cavities, but the cost of refrigeration is quite considerable, making improving the quality factor important.

Niobium accelerator cavities have seen considerable advances and are nearing the theoretical limits of their performance [PVL15]. In lab experiments niobium cavities have reached 50 MV/m–the expected limit[2]–and niobium cavities have reached quality factors of $> 4 \cdot 10^{10}$ at 2 K. In the near future, further advancement of SRF accelerators will require the use of new materials beyond niobium. The most promising material for future SRF accelerators is niobium-3 tin (Nb_3Sn).

Nb_3Sn can potentially operate at nearly twice accelerating gradient compared to niobium–$\approx$ 96 MV/m–and can operate efficiently at 4.2 K (twice that of niobium) [PL14, God06, CS08a]. The accelerating gradient is roughly the energy gain per meter of active accelerator. A higher accelerating gradient allows for shorter and/or higher energy accelerators. The increase in operating temperature significantly reduces the cost to run SRF cavities (to roughly $1/3^{rd}$) and reduces complexity of refrigeration of major accelerators. This increased operating temperature also allows for small SRF cavities to be run off cryocoolers. This can allow for small scale SRF accelerators in research and industry that open new areas therein. For this reason, Nb_3Sn has seen considerable interest.

Recent development has created Nb_3Sn cavities that are capable SRF op-

[2]Accelerating gradient limits depend on both the material and the cavity shape. This is the theoretical limit for a TESLA elliptical cavity [A+00].

eration [PH17, PVL15, PL14, Pos14, Hal17]. These cavities have shown efficient operation at 4.2 K at accelerating gradients that match that requirements of some current, major accelerator facilities [Gal14]–$Q = 2 \cdot 10^{10}$ and 17 MV/m. These cavities are already more efficient than their niobium brethren and attempts to create small scale Nb_3Sn accelerators for industry has already begun [SHL+20, DPG+20, CCPR20]. These cavities, however, are limited to accelerating gradients far below their potential.

Current Nb_3Sn cavities are limited to $\approx$ 17 MV/m [HW15, Hal17] of their theoretical maximum, with the best ever reported performance reaching $\approx$ 24 MV/m [PLS+21]. The cavity is limited to what we refer to as the 'quench field' and is said to 'quench' when this field is reached. Increasing the quench field is important for the development of future particle accelerators such as the International Linear Collider (ILC) [Beh13] or it's upgrades, allowing new machines to be constructed at reasonable prices [AKS05]. The quench field has increased with development (from 14 MV/m in 2015) and information about the current limitations has been gained [HW15, Hal17]. Though previous research has investigated the cause of the limitations, it is not yet understood.

In this work we investigate the cause of accelerating gradient limitations in Nb_3Sn cavities. We collect performance data of cavities (RF testing) to learn as much as we can about the quench mechanism and compare to theoretical models–some models are ruled out and others are proposed. We will detail the creation of novel tools meant to investigate the cavity quench mechanism (among other possible applications): high-speed temperature mapping and a high pulsed power cavity capable of measuring the ultimate accelerating gradient limitations of materials. Preliminary testing of Nb_3Sn using this new high-

speed temperature mapping will reveal never before seen dynamics that alters previous understanding of the quench mechanism. We use microscopy to investigate our material and search for defects–we concentrate on impacts of surface roughness on the quench field. In addition to this, we have worked to understand how our material forms with collaboration of material scientists, microscopists, and condensed matter theorists through the Center for Bright Beams (CBB). Using this we have not only investigated potential causes of accelerating gradient limits in Nb_3Sn cavities, but also how the material forms to create these issues, and, most importantly, look at how to form cavities that do not have these problems. We finally summarize all our insights and comment on possible causes of cavity quench. Using this knowledge, we detail the creation of a new Nb_3Sn cavity that removes material defects and increases performance, though, unfortunately, did not show increased accelerating gradients.

1.1 Organization of the Dissertation

A chapter breakdown of this dissertation is listed below. This dissertation can be roughly divided into 3 main parts. Chapter 2 and 3 present background information required to understand this work. Chapters 4, 5, and 6 detail the development and usage of experimental systems used in this work. Chapters 7, 8, 9, and 10 presents results from investigating the quench field and material growth of Nb_3Sn. This will include experimental results and theoretical models and interpretations. Finally, the conclusion will draw together all the experimental data and comment on the relevance to Nb_3Sn SRF cavity development. The conclusion will suggest how to improve Nb_3Sn cavities using what has been learned and then present preliminary results from a new Nb_3Sn SRF

cavity developed using this knowledge.

- Chapter 2: SRF Background. A brief introduction to SRF accelerator cavities is given, motivating their importance, examining merits of performance, and lightly covering the theory of superconductors in RF fields.
- Chapter 3: Nb_3Sn for SRF Accelerator Cavities. The development of Nb_3Sn is further motivated, and the material is compared to other superconductors. Important material parameters are laid out and the material creation process is detailed.
- Chapter 4: RF Cavity Testing. The process of preparing and testing Nb_3Sn cavities is detailed. The extraction of material parameters from RF cavity data is discussed.
- Chapter 5: High-speed Temperature Mapping. Temperature mapping of SRF cavities is introduced and the development of a first-of-its-kind high speed/dynamic temperature mapping system is detailed. Performance of this new temperature mapping system is explored.
- Chapter 6: A High Field Sample Host Cavity. The development of a new sample testing system for determining the superheating field of superconductors is detailed. The expected performance and fabrication of the system are discussed.
- Chapter 7: RF Measurements of Nb_3Sn Cavities. Results from RF measurements of Nb_3Sn cavities are shown with a focus on understanding the current limits of the accelerating gradient in these cavities. Surface resistance data is also examined to understand material limits and we investigate the apparent existence of 'multi-gap' superconductivity in Nb_3Sn SRF cavities.

- Chapter 8: Dynamic Temperature Mapping of Nb_3Sn Cavities. Preliminary results from high-speed temperature mapping of Nb_3Sn cavities is shown. Nb_3Sn cavities are shown to have dynamic heating including temperature jumps, multipacting type behavior, and migration of cavity quench location. The relevance to accelerating gradient limits is discussed along with several potential theoretical explanations.
- Chapter 9: Surface Roughness. Attention is focused on microscopy of samples which reveals that the Nb_3Sn surface we create is rough. The impact of surface roughness on cavity performance is investigated and several polishing techniques are examined.
- Chapter 10: Nb_3Sn Material Growth. We will explore how Nb_3Sn grows and how feature deleterious to cavity performance form. We investigate how to modify the coating procedures to grow better materials.
- Chapter 11: Conclusion. We will draw together all the experimental data and comment on the relevance to Nb_3Sn SRF cavity development. We will suggest how to improve Nb_3Sn cavities using what has been learned and then present preliminary results from a new Nb_3Sn SRF cavity developed using this knowledge.

CHAPTER 2

SRF BACKGROUND

Here we describe the basics of superconductivity as it applies to SRF accelerators. This provides a light background for those unfamiliar with superconductivity that should be sufficient to understand the material in this dissertation and shows how superconductivity applies to key figures of merit for SRF accelerator cavities. This description is based on *RF Superconductivity for Accelerators* by H. Padamsee *et. al.* [PKH98] and *Introduction to Superconductivity* by M. Tinkham [Tin12]. Those familiar with superconductivity and basic SRF may skip to the next chapter.

2.1 RF Cavities and Charged Particle Acceleration

The simplest particle accelerator to imagine is a charged particle travelling between a negatively and positively charged plate. As the particle traverses the electric field it will gain energy. This type of accelerator is effective and has been utilized throughout history for early accelerators, industrial applications, and as a first-stage accelerator for many modern accelerators [Hel05]. The big limitation of technique is that the potential difference between the two plates eventually becomes limited by the breakdown voltage between the plates; a different method is needed to achieve the high energies needed from modern accelerators.

Instead of using a static electric field a dynamic RF field is used. Bunches of particles can be timed so that they only see an electric field that accelerates them (in the desired direction) and go through the RF field as many times as needed

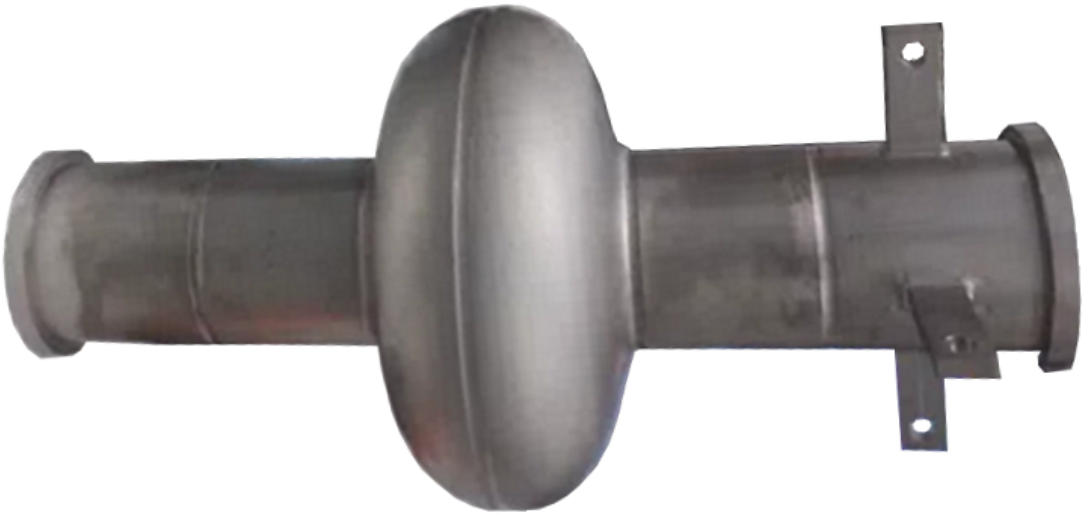

Figure 2.1: An example SRF cavity used in this work. This is a TESLA elliptical cavity shaped for electron (speed of light particle) acceleration [A$^+$00].

to reach the desired energy. This RF field is contained in metallic resonance cavity.

In an accelerator cavity a resonate RF field is established. The cavity is shaped–and a specific resonant mode excited–such that there is an electric field parallel with the particle beam line. Figure 2.1 and 2.2 show an example SRF cavity and a diagram of the electromagnetic fields contained inside. The electric field alternates direction, but the particles are spaced and timed such that the electric field is always aligned to increase their velocity/energy.

In addition to the accelerating gradient a magnetic field is induced at the surface of the cavity (and elsewhere) and an electric current is established in the cavity wall. The electric current results in resistive losses in the cavity wall, draining energy from the cavity and requiring additional input power to maintain the required RF field. In modern accelerators the losses induced in the wall (and the energy required to cool the wall) amount to large operational costs.

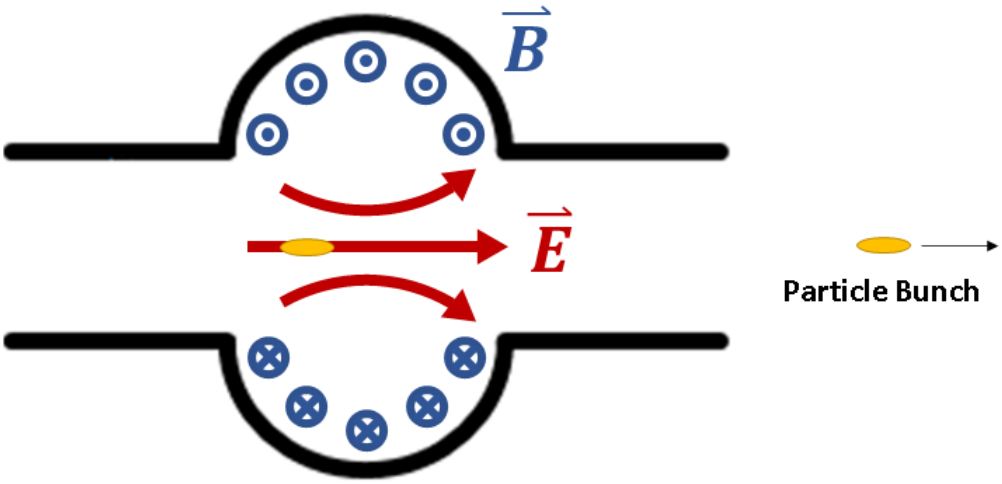

Figure 2.2: A diagram of an SRF cavity. RF fields resonate in the cavity. A mode is excited that has an electric field along the beamline axis. The electric field alternates direction over time and particles will gain or lose energy depending on their timing. The accelerating gradient is defined by the maximum energy change per electron charge of a particle while traversing the cavity, divided by the length of the cavity. Bunches of particles are timed so that they only see an accelerating field when they move through the cavity. In addition to the electric field an azimuthal magnetic field is generated in the cavity. This azimuthal magnetic field induces electric currents at the surface of the cavity wall causing resistive losses in the material.

Reducing these energy costs while obtaining large accelerating gradients is the key goal in the field of SRF accelerators. Using superconductors allows the substantial reduction in losses while increasing in obtainable accelerating gradients (in continuous wave operation), but the superconductors can be improved to decrease energy consumption and increase obtainable accelerating gradients.

2.1.1 Major parameters of SRF cavities

There are three major parameters used when discussing SRF accelerator cavities: accelerating gradient, quality factor, and operating temperature (combined with cryogenic efficiency). The accelerating gradient determines the energy gain of a particle traversing the cavity, while all three parameters determine the energy efficiency of the accelerator. These parameters are different than those used to describe the physics (surface magnetic field, surface resistance, and temperature). In this work we are interested in both the operation of accelerators as well as the underlying physics and will convert between these parameters frequently.

The accelerating gradient, E_{acc}, is defined by the maximum energy change per electron charge, V_{acc}, of a particle while traversing the cavity, divided by the length of the cavity,

$$E_{\mathrm{acc}} = \frac{V_{\mathrm{acc}}}{L} \,, \tag{2.1}$$

This includes the 'transit-time factor' of the particle [Lee11]: the effect of the particle having a finite transit-time through the cavity during which the RF fields are changing. For a relativistic particle (e.g., electrons) traversing a typical elliptical shaped cavity the maximum energy gain occurs when the particle is timed to traverse the middle of the cell when the electric field is at its maximum. For given energy, U, in a cavity electromagnetic simulation software can be used to calculate the accelerating gradient as well at the peak surface magnetic field, B_{pk}. The ratio $[B_{\mathrm{pk}}/E_{\mathrm{acc}}]$ allows for the quick conversion between E_{acc} and B_{pk}.

The quality factor can be determined from the energy in the cavity, U, the

power dissipated on the cavity wall, P_{diss}, and resonance frequency, f_0,

$$Q_0 = \frac{2\pi f_0 U}{P_{\text{diss}}} , \tag{2.2}$$

The energy in the cavity can be calculated by,

$$U = \frac{\mu_0}{2} \int_V |\mathbf{H}|^2 \, dV , \tag{2.3}$$

where μ_0 is the permeability of free space. This is usually calculated using an electromagnetic simulation software. With the surface resistance known we can calculate the power dissipated on the walls,

$$P_{\text{diss}} = \frac{1}{2} \int_S R_s(H) |\mathbf{H}|^2 \, dS , \tag{2.4}$$

The TESLA elliptical [A+00] and Cornell ERL [VL11b, EBC+13] cavities used in this research have been optimized to have flat magnetic field profiles on the cavity walls that sharply fall to zero in the beam tubes (see Fig. 2.3). In addition, we will see that the resistance varies slowly with the magnetic field. This allows us to simplify equation 2.4 by using only a single value of H to determine the surface resistance,

$$P_{\text{diss}} = \frac{1}{2} R_s(H_{\text{pk}}) \int_S |\mathbf{H}|^2 \, dS , \tag{2.5}$$

With other cavity geometries or severe changes in surface resistance a more accurate methods are needed [ML18, Man20]. However, we can avoid such complications in this work.

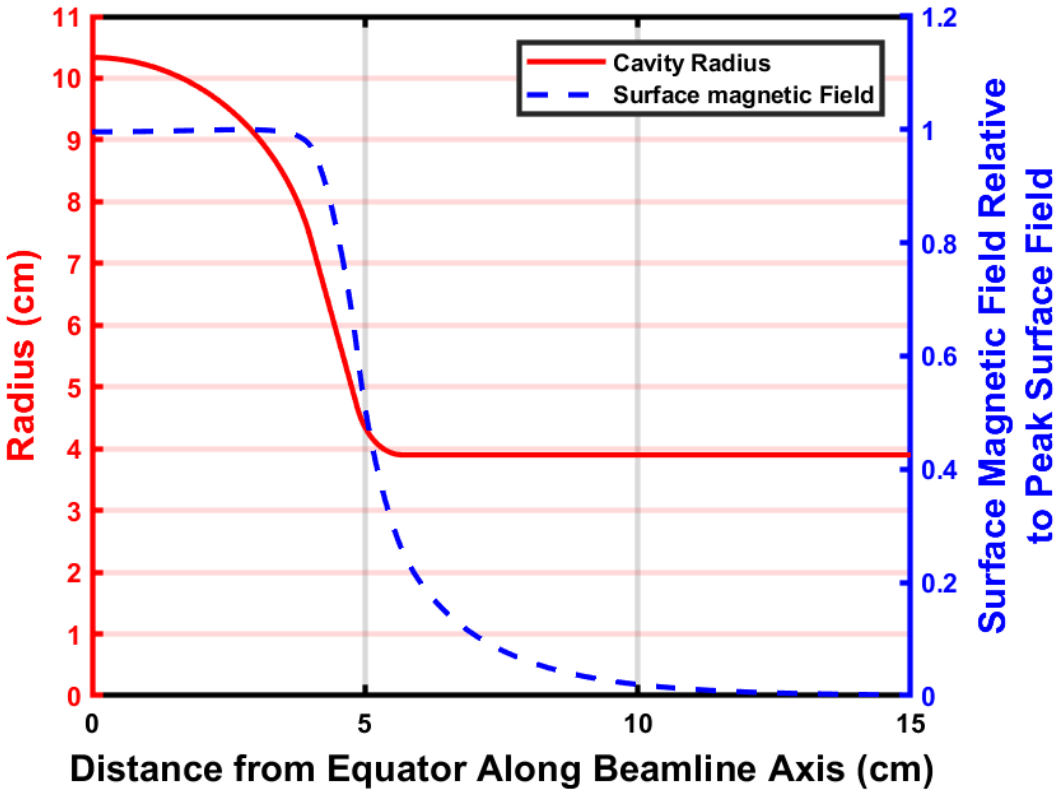

Figure 2.3: The magnetic field distribution on the wall of an LTE cavity. The cavity cross-section is shown start at the equator. The magnetic field distribution was calculated using CLANS.

Combining equations 2.2, 2.3, and 2.5 we get,

$$Q_0 = \frac{2\pi f_0 \mu_0}{R_s} \frac{\int_V |\mathbf{H}|^2 \, dV}{\int_S |\mathbf{H}|^2 \, dS} \,, \tag{2.6}$$

We can simplify this equation by introducing the geometry factor, G, of the cavity,

$$G = 2\pi f_0 \mu_0 \frac{\int_V |\mathbf{H}|^2 \, dV}{\int_S |\mathbf{H}|^2 \, dS} \,, \tag{2.7}$$

The geometry factor can be computed using electromagnetic simulation soft-

ware and is independent of the magnitude of the RF fields (only depending on the distribution of the RF fields). This allows for quick conversion between the quality factor and the surface resistance,

$$Q_0 = \frac{G}{R_s} \,. \tag{2.8}$$

We additionally define the shunt impedance, R/Q. The shunt impedance determines the accelerating gradient for a given power dissipation in a cavity. It is a constant determined purely by the geometry of the cavity and is found through electromagnetic simulation.

Table 2.1 lists computed cavity parameters for the cavities used in this work.

	TESLA (LTE) [HMS92, Edw95]	Cornell ERL [VLF+14]
f [GHz]	1.3	1.3
B_{pk}/E_{acc} [mT/MVm^{-1}]	4.23	4.08
G [Ω]	278	272
E_{pk}/E_{acc}	1.88	1.76
R_a/Q_0 [Ω]	105	116
$E_{pk}/\sqrt{U}$ [MVm^{-1}/$\sqrt{\text{J}}$]	15.1	14.7

Table 2.1: A table of key parameters for the SRF accelerator cavities used in this work. The values in the table are taken from their respective references.

To compute the AC-plug wall power (electric power from the utility company), P_{cryo}, required to keep the accelerator cold we require the Coefficient of Performance, COP, of the cryogenic cooling system. The COP^{-1} measures the efficiency of the refrigeration and tells us how many Watts of AC-plug wall power is required to remove/cool 1 W of dissipated power in the cavity. The higher the operation temperature of an accelerator the more efficient cooling becomes. We arrive at the equation [PKH98],

$$P_{\text{cryo}} = \frac{E_{\text{acc}}^2 L^2}{\frac{R_a}{Q_0} Q_0} \frac{1}{COP} , \tag{2.9}$$

where L is the length of active[1] cavity.

Three plots will commonly be shown in this work to present RF cavity performance data: Q vs E, Q vs T, and R vs 1/T. Example plots are shown in Fig. 2.4. Q vs E plots show the dependence of the quality factor on the accelerating gradient. As discussed below, the quality factor usually changes with the accelerating gradients. The example Q vs E shows a typical trend in SRF cavities called 'Q-slope.' A Q-slope is a decrease in Q with increasing E_{acc}. Figure 2.4a shows the quality factor at both 4.2 K and 1.7 K to show the difference in the quality factors at those temperatures. To better examine the dependence of the quality factor on the temperature Q vs T and R vs 1/T are used. These are shown at a fixed accelerating gradient.

2.2 RF Superconductivity Primer

Niobium and Nb_3Sn belong to the family of "conventional" superconductors that are well described by Bardeen-Cooper-Schrieffer (BCS) theory [BCS57]. In BCS theory, there exists a small attractive potential between opposite spin electrons (usually provided through lattice phonon interactions between the electrons). This causes electron pairs to become correlated and creates an energy gap, 2Δ, that must be overcome to break the pair[2]. However, the Cooper pairs

[1] The portion of the accelerator with active SRF cavities–ignoring beam tubes and other non-accelerating components.

[2] In an ideal BCS superconductor Δ is related to the critical temperature, T_c, and the Boltzmann constant, k_B, by $\Delta(T = 0)/k_B T_c = 1.75$, however, real superconductors vary from this ratio.

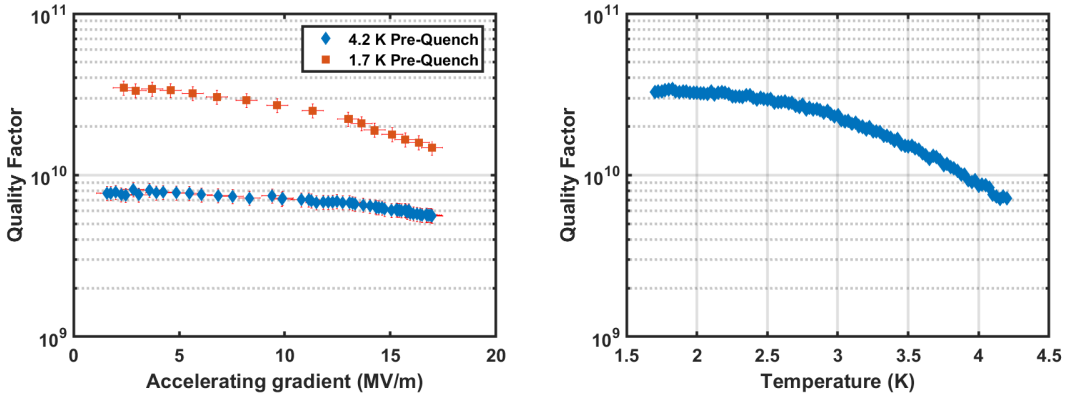

(a) Q vs E.

(b) Q vs T.

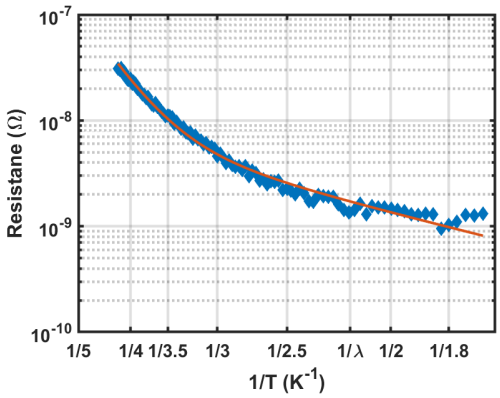

(c) R vs 1/T.

Figure 2.4: RF testing results from the cavity STE1-2–a 2.6 GHz TESLA elliptical style cavity coated with Nb_3Sn [RDPM19]. a) Q vs E at 4.2 K and 1.7 K. b) Q vs T at 3 MV/m. c) R vs 1/T at 3 MV/m. This curve has had a residual resistance (defined in section 2.2) subtracted from it to highlight the temperature dependence. A fit model overlays the data.

obey Boson statistics and at sufficiently low temperatures may form a Bose-Einstein condensate. This creates a scenario where–below a critical current density, j_c–the energy required to break one Cooper pair is related to the energy to break all Cooper pairs in the condensate. The result is a supercurrent of charged Cooper pairs that cannot scatter while flowing through the material and move with zero resistance: superconductivity.

In a low ambient magnetic field, the transition to a superconducting state

establishes supercurrents near the surface of the material that screen magnetic fields from the bulk (with exception of 'pinned magnetic-flux' discussed later). This results in the complete expulsion of magnetic field from the superconductor: the 'Meissner Effect.' External magnetic field can still penetrate the material but decay exponentially such that

$$H(x) = H_0 e^{-x/\lambda} \,, \tag{2.10}$$

where H_0 is the magnetic field at the surface of the superconductor, x is the depth into the superconductor, and λ is decay constant called the 'penetration depth.'

When the surface of a superconductor is exposed to sufficiently high magnetic fields, superconductivity and the Meissner effect begin to break down. There are two types of superconductors: type-I and type-II, and they experience different reactions to increasing magnetic fields. The kinds of superconductors we are concerned with in this work–Nb and Nb_3Sn–are type-II superconductors. In type-I superconductors there is a critical (surface) magnetic field, H_c, at which point superconductivity (locally) breaks down [Tin12]. In type-II superconductors the dynamics are more complicated than in their type-I brethren and multiple critical fields exist. We will focus on the first, H_{c1}; second, H_{c2}; and superheating, H_{SH}, critical fields [Tin12]. Below H_{c1} the material exhibits the Meissner effect. However, between H_{c1} and H_{c2} bulk superconductivity is maintained but it becomes energetically favorable for quanta of magnetic flux to nucleate into the superconductor. These quanta of magnetic flux are referred to as magnetic vortices and superconductor is said to be in the vortex state. In the SRF community it is generally considered impossible to operate an SRF cav-

ity (at any appreciable accelerating gradient) in the vortex state due to heavy resistive losses from the vortices oscillating in the RF fields; however, there exists a surface potential energy barrier to magnetic vortices entering the material. This barrier persists up to H_{SH}. This allows the existence of meta-stable Meissner state up to H_{SH}. H_{SH} is generally considered the ultimate limit for SRF accelerator cavities [PKH98].

In addition to magnetic field limits, the superconducting state only exists up to a critical temperature T_c. This temperature is determined by material properties. In particular, the energy gap depends on the density of states at the Fermi level which is temperature dependent. As T approaches T_c the energy gap approaches zero and superconductivity ceases. In an ideal BCS superconductor [Tin12],

$$\Delta(T \to T_c) \approx 3.06 k_B T_c \sqrt{1 - T/T_c}\,, \tag{2.11}$$

In addition, other aspects of the superconductor change with respect to temperature. Most critically to our current discussion, the critical magnetic fields change with respect to temperature. The exact forms are difficult to work out for all temperatures and is material dependent, but the dependence near T_c is roughly given by,

$$H_{\mathrm{c1,c2,SH}} \sim \left(1 - \left(\frac{T}{T_c}\right)^2\right), \tag{2.12}$$

The critical magnetic fields are roughly illustrated it Fig. 2.5 [Tin12].

While BCS theory shows no electrical resistance to DC currents, the same is

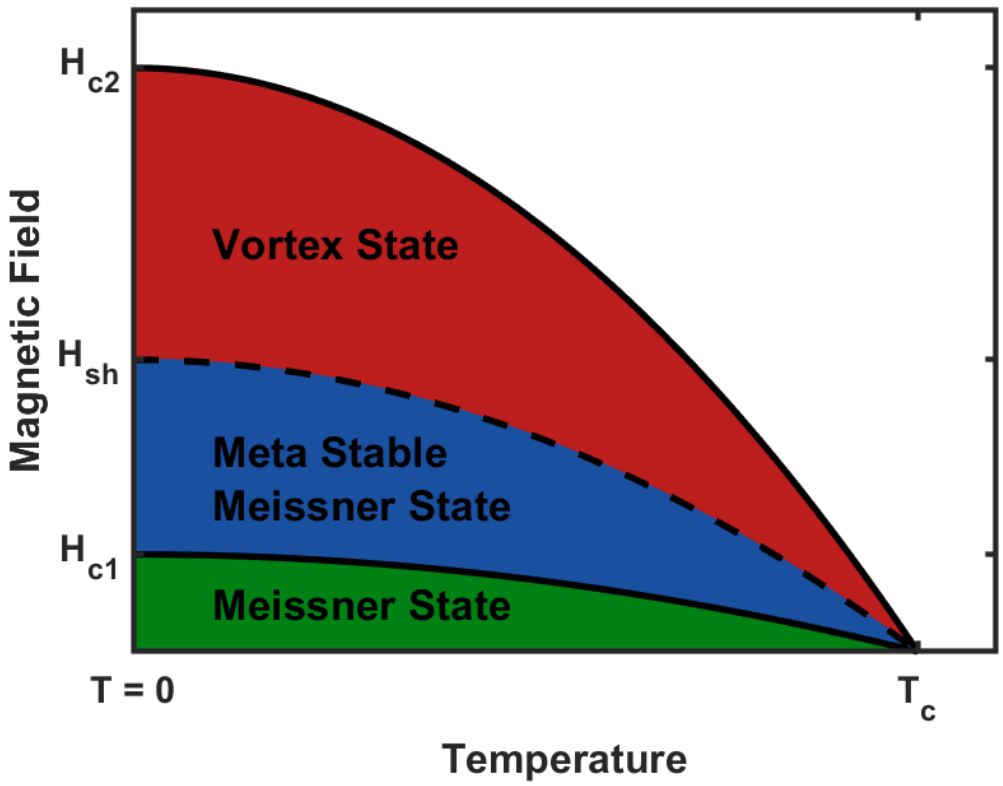

Figure 2.5: Superconducting phase space showing the magnetic field and temperature limits for the Meissner state, meta-stable Meissner state, and the vortex state.

not true in RF fields. In RF fields the Cooper pairs must continually accelerate in alternating directions to screen the magnetic field from the bulk. However, since Cooper pairs have inertia, they cannot instantaneously accelerate, and unpaired electrons will also respond to the changing electromagnetic field. This gives loses near the surface of the superconductor (determined by the penetration depth, λ) which we describe as a surface resistance, R_{BCS}. Fully calculating R_{BCS} is an intensive task, however, at low temperatures ($T < T_c/2$), frequencies ($2\pi f\hbar < \Delta$), and short electron mean free paths ($l < 100\,\mathrm{nm}$) R_{BCS} reduces to a simple functional form [Hei01],

$$R_{\mathrm{BCS}} = A\frac{f^2}{T}\exp\left[-\Delta\frac{T_c}{T}\right] , \tag{2.13}$$

where f is the frequency of the RF field and A is a constant that depends on material parameters. The exponential suppression of the surface resistance at low temperatures is key to the efficient operation of SRF cavities[3].

A short coming of the classical BCS formulation is the lack of magnetic field dependence in R_{BCS}. Recent experimental results in nitrogen doped niobium have shown marked magnetic field dependence in R_{BCS} and a variety of theories have extended BCS theory to look into this [GRS+13a, GRT+17, Gur14b, XRK13, Man20]. Nb_3Sn has not shown magnetic field dependent R_{BCS} so we will treat it as field independent here [Pos14].

In addition to the fundamental BCS resistance there is additional resistance referred to as residual resistance, R_{BCS}. The total surface resistance is then,

$$R_s = R_{\mathrm{BCS}}(T, H) + R_{\mathrm{Residual}}(H) , \tag{2.14}$$

Residual resistance can arise from many sources. These loss mechanisms are usually temperature independent or only weakly temperature dependent compare to R_{BCS}.

One particularly important source of residual resistance is trapped magnetic vortices. When an ideal superconductor enters the Meissner state all magnetic field should be expelled, however, impurities, inclusions, grain boundaries, and

[3]This exponential suppression holds true for 'conventional'/s-wave superconductors. Almost all high temperature superconductors are d-wave superconductors for with R_{BCS} is only polynomially suppressed and RF resistance remains high down to low temperature [Cio14, LD00].

other defects can provide areas where superconductivity is suppressed. These act as local potential minima when the magnetic field is being expelled that can pin magnetic field. Due to the superconducting state, the trapped magnetic field creates magnetic vortices of one magnetic flux quantum each. These magnetic vortices have normal conducting cores and oscillate in the RF fields causing additional losses in the cavity [GC13, LHK+18, CMG+17].

There is a characteristic size for which defects matter: the superconducting coherence length, ξ_0. The superconducting coherence length is the relevant length scale over which the density of superconducting electrons can significantly change and expresses the degree of non-locality of the superconductor. Defects smaller than ξ_0 have little to no effect on the superconducting state.

Another characteristic length we already introduced in equation 2.10 is the penetration depth, λ. In an ideal superconductor free from defects (the 'clean' limit) the penetration depth is given by the London penetration depth [Tin12],

$$\lambda_L = \sqrt{\frac{mc^2}{4\pi n e^2}}\,, \tag{2.15}$$

where m is the mass of the election, e the electron charge, c the speed of light, and n is the density of normal conducting electrons. In the presence of impurities the electron mean free path, l, becomes shorter and the penetration depth has been shown to take the form [Tin12],

$$\lambda(T=0) = \lambda_L \sqrt{1+\frac{\xi_0}{l}}\,, \tag{2.16}$$

which increases as the mean free path becomes shorter. The coherence length

and other superconducting parameters also vary with the mean free path.

2.2.1 Limitations to Achievable Accelerating Gradients

Though H_{SH} determines the theoretical maximum accelerating gradient (for a given cavity geometry) SRF cavities are usually limited below this field. Only recently have niobium cavities managed to reach this theoretical limit [PVL15] and these fields are still unachievable in real accelerators. There have been many documented defects/mechanisms that limit the accelerating gradient. An excellent summary of common defects in SRF cavities is provided in [PKH98].

In general, we outline several categories of limitations. Some defects/mechanisms absorb increasing large amounts of energy as the cavity's accelerating gradient is raised. The cavity remains superconducting, but increasing the accelerating gradient further requires more power than is available in the experiment setup. We refer to this as 'power limited.' In a second limitation all or a large portion of the cavity is driven normal conducting. The large section of normal conducting material almost instantly absorbs all the energy in the cavity. We refer to this as a 'quench.' Within quenches there are multiple phenomenology. In some cases, a large portion of material all turns normal conducting at once at an onset surface magnetic field. We will call this a magnetic quench. A small region can also continually warm up until 'thermal runaway' condition is met in the cavity and uncontrolled heating occurs as the hot spot grows–until all the energy in the cavity is absorbed. We refer to this as a 'thermal quench.'

We will briefly summarize several important quench mechanisms in SRF

cavities:

- Normal conducting inclusion: if a small piece of non-superconducting metal is embedded in the cavity wall it will cause significant heating. In sufficiently high RF fields this can cause a thermal quench. This type of quench has a temperature dependence that can be roughly estimated in terms of the R_n, the resistance of the normal conducting region, a, the radius of the normal conducting region, and k, the thermal conductivity [PKH98]:

$$H_{\text{quench}}(T) \approx \sqrt{\frac{4k(T_c)\,(T_c - T_b)}{aR_n}} \tag{2.17}$$

- Suppressed superconductivity: The surface of the SRF cavity may not have a homogenous gap. Areas of different chemical compositions can have different superconducting gaps [God06]. Thin normal conductors on the surface can become superconducting through the proximity effect [DGH65, Tin12] and reduce the superconductivity in a region. Variations in mean free path, variation in crystal orientation, and grain boundaries can change the superconducting gap. There could also be remnants of other superconductors on the surface (i.e. tin on Nb_3Sn). These areas of depressed superconductivity can have a reduced H_{SH} or caused increased heating.
- Sharp feature: A spike or pit in the surface can create a local region of increased surface magnetic field [PHLM16, PMS08, KGPL99]. This can cause regions to locally exceed H_{SH}. If this occurs over a large enough area this can trigger a thermal quench. In addition, a deep/rough grain boundary

geometry can allow early entry of magnetic vortices into the grain boundary and cause increased losses or cavity quench [CPT+21, Pac20].

- Field emitter: Sharp surface features or normal conducting inclusions also have the potential to emit electrons into the cavity [PKH98]. This comes from local enhancement of electric fields and–if the feature warms up–increased thermionic emission. These electrons are accelerated in the cavity, absorbing energy from the RF fields. Due to the field curvature, these electrons often impact on other parts of the cavity, creating a line of heating parallel to the beamline while emitting electrons. The emission of electrons increases exponentially with the accelerating gradient and the electrons progressively absorb more power. Field emitters often 'power limit' the accelerating gradient as increasing the field requires exponentially more forward power. Some field emitters can be processed: as they emit electrons they heat up and can get hot enough to either melt themselves or explode.

- Multipacting: Multipacting can be understood to be a form of resonant electron emission [SB20, PKH98, Wei84]. An electron ejected from the surface and is accelerated by the RF field. When the electron crashes back into the cavity wall it deposits energy that can eject more electrons. Multipacting is a resonant effect involving this mechanism. In one-point multipacting ejected electrons return to the same point where they were ejected, ejecting more electrons that return to the same. In two-point multipacting ejected electrons from point A hit point B which ejects more electrons that hit point A again. Under the correct circumstances more than one electron will be ejected by each impact and the number of electrons will grow exponentially. The ejected electrons per impact is called the Secondary

Electron Yield (SEY). Due to the acceleration of electrons this process produces radiation. The resonant process will eventually drain the energy in the cavity, reducing the yield of secondary electrons. The cavity can reach a stable equilibrium energy or undergo oscillations in energy.

There is both a material aspect and geometric aspect to this mechanism. Modern elliptical cavities (such as those used here) have been geometrically optimized to minimize multipacting. They typically only see multipacting when there is a contaminant on the surface (possibly even an adsorb layer) that increases the secondary electron yield from an impact. In addition, due to the shape of the cavity, any emitted electrons tend to migrate to the equator and multipacting is only seen near the equator.

Since multipacting usually involves some sort of contaminant that increases the SEY these contaminants can often be burned away/destroyed by the continual electron collisions. When multipacting is encountered, it is common to leave the cavity 'multipacting' for an extended period. Over time the contaminants are burned away, and the accelerating gradient will slowly rise (of course, this is not always successful). The process is called processing[4].

We are particularly interested in the case of multipacting near the cavity equator. In general, multipacting is highly field dependent–being an issue only in a band of E_{acc}. In [SB20] the most problematic accelerating gradient was calculated:

$$E_0 = \frac{35.7Mf}{B_{\text{pk}}/E_{\text{acc}}} \tag{2.18}$$

where f is the frequency of the cavity and M is a magnetic parameter given

[4]We are a very creative group of scientists and engineers.

in the text that is independent of the frequency. The specific value here depends on both the geometry and the location of the multipactor. This equation shows a linear dependence on the frequency of a cavity (provided the cavity is scaled with the frequency). This dependence has also been observed experimentally for equator multipacting [Gen03].

CHAPTER 3

Nb_3SN FOR SRF ACCELERATOR CAVITIES

In this chapter we will introduce Nb_3Sn and discuss background that predates the work in this dissertation [PH17, PVL15, PL14, Pos14, Hal17]. This includes why to pursue Nb_3Sn over other materials, relevant material properties, and fabrication techniques.

3.1 Why Nb_3Sn?

Nb_3Sn has two key advantages over niobium for accelerator applications. The transition temperature of Nb_3Sn is $\approx 18\,\mathrm{K}$ [God06] compared to only $9.2\,\mathrm{K}$ for niobium. In addition to this, theoretical calculations of the superheating field of Nb_3Sn find it to be $\approx 425\,\mathrm{mT}$ [CS08a]–nearly twice as high as the superheating field of niobium, $\approx 220\,\mathrm{mT}$. The improved T_c and H_{SH} gives the material the potential to be material of choice for future accelerators.

The improved T_c offers several advantages. Primarily, an increase in T_c allows the superconductor to be operated at a higher temperature with the same R_{BCS}. With the currently achievable residual resistances for this material Nb_3Sn SRF cavities achieve the same quality factors at $4.2\,\mathrm{K}$ operation as clean niobium does at $2\,\mathrm{K}$. Due to the cooling efficiency of cryogenic systems this offers a huge improvement in energy efficiency. Figure 3.1 roughly demonstrates the efficiency of cryogenic liquid helium plants. The increase in operating temperature roughly decreases the energy consumption by a factor of three.

The increase in energy efficiency can lead to several gains in an accelerator. The overall energy consumptions of the accelerator can be lowered. The accel-

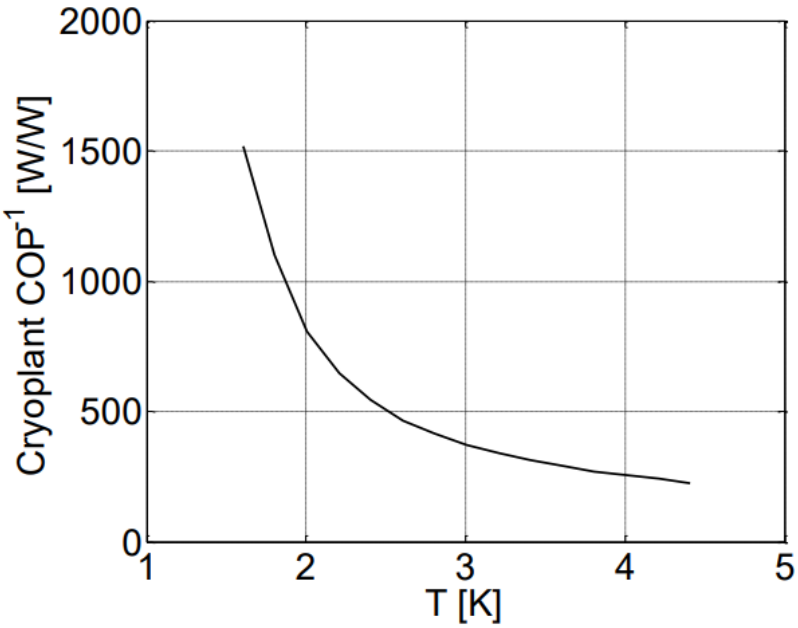

Figure 3.1: The Coefficient of Performance (COP) of a typical large-scale cryoplant for cooling an SRF accelerator. This figure was adapted from [Pos14] using data from [SKR03].

erator could be run at a higher luminosities[1]. The accelerator can also be run at a higher accelerating gradient for the same energy consumption per length either increasing the final beam energy or decreasing the length (and cost) of the accelerator. The improvement in efficiency can be seen as a requirement to operating at higher accelerating gradients. This is demonstrated in Fig. 3.2.

The improvement in operating temperature leads to additional gains. Cooling liquid helium below 4.2 K requires heat exchangers, sub-atmospheric helium, and complicated cryogenic systems. Removing the need to cool below 4.2 K can significantly simplify the construction of cryogenic systems, reduce their cost, and make them easier to operate. The increase to 4.2 K operation also opens to the door to small scale SRF accelerators cooled by cry-

[1]Meaning more particles could be put through the accelerator per unit of time by increasing the duty factor, decreasing the bunch distance, or more adding particles per bunch.

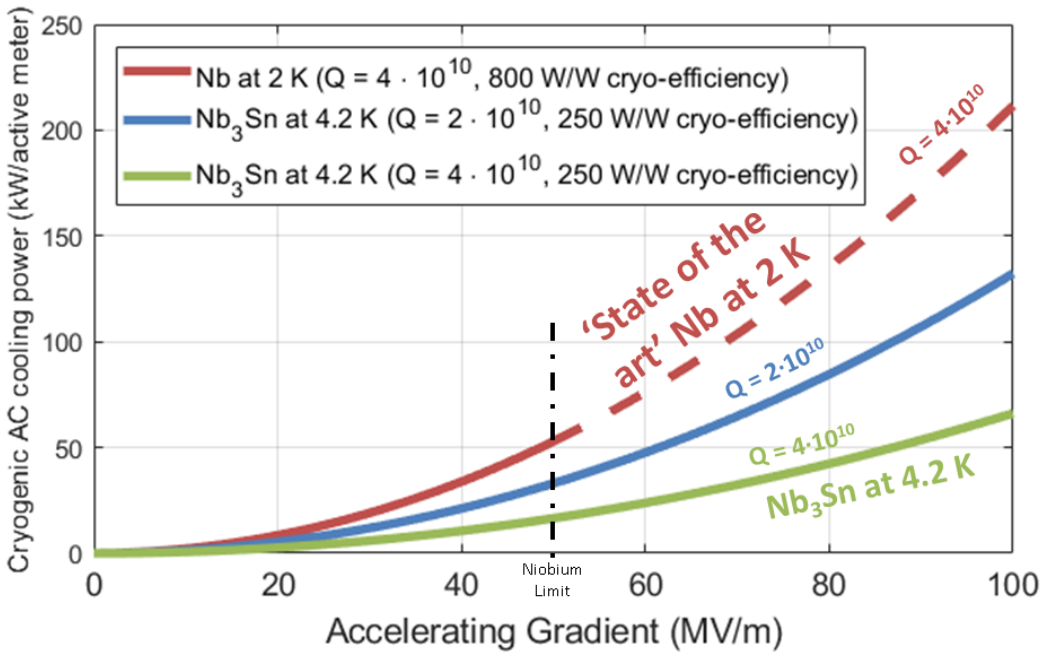

Figure 3.2: Wall power required to run an accelerator per meter of active accelerator. This compares niobium with Nb_3Sn in TESLA elliptical cavities. This does not include energy transferred to the beam. Nb_3Sn with a Q of $2 \cdot 10^{10}$ at 4.2 K is current achievable. Nb_3Sn with a Q of $4 \cdot 10^{10}$ at 4.2 K is potentially achievable. Niobium with a Q of $4 \cdot 10^{10}$ at 2 K is achieved in the best cavities. The line for niobium becomes dashed at 50 MV/m as this is its field limit. This assumes that Q has no field dependence–Q may decrease significantly beyond currently achievable accelerating gradients.

ocoolers [SHL+20, DPG+20, CCPR20]. Unlike cryoplants that are used for accelerators, cryocoolers can be made small scale, and easy to operate (without highly trained technicians). These could be made simple to operate and be utilized in a number of industrial and scientific applications including compact x-ray sources, water-treatment, polymer cross-linking roads, and more [HW15, HS09]. Several early proof of principle systems have already been developed and further development is in progress [SHL+20, DPG+20, CCPR20].

The increased superheating field allows for larger accelerating gradients (E_{acc}). Nb_3Sn has the potential to reach $\approx$ 96 MV/m in a TESLA style ellipti-

cal cavity. Combined with other technologies such as travelling wave structures we could see accelerating gradients in excess of 120 MV/m [AKS05].

3.1.1 Alternative Materials

Justifying the pursuit of Nb_3Sn over other alternative materials deserves some attention. Niobium became the dominant material for SRF cavities because it has the highest T_c of all elemental superconductors. Using an elemental material drastically simplifies the physics involved and makes creating a high-quality homogenous material easier. Due to the finite BCS resistance in RF fields, SRF cavities are more sensitive to material impurities. When moving into compound superconductors we should justify the pursuit of Nb_3Sn.

Unfortunately, most of the high temperature superconductors are not usable for SRF applications. Though the T_c of these materials is much higher, almost all these materials are d-wave superconductors. The d-wave superconductors have been seen to not have exponential suppression of the BCS resistance and have large residual resistances [Cio14, LD00]. The result is that these materials would be much less efficient, even when taking into account improvement in cooling efficiency. The notable exception to this is the iron-based superconductors which show s-wave superconductivity [BS17]. The iron-based superconductors are a promising area of pursuit; however, these materials need considerable development to determine their RF performance and to be applied to the complex geometries of SRF cavities.

The highest T_c of the conventional superconductors is MgB_2 and this material has seen considerable interest as a SRF cavity material [TWX+16, Ere09,

Tsu02]. This material may have a larger superheating field than Nb_3Sn, however, the critical fields in this material have significant anisotropy [LPT+17, KB03]. This makes estimating the superheating field difficult and estimates vary from below niobium to greater than Nb_3Sn depending on the crystal orientation and the individual estimate [LPT+17]. In addition, utilizing the higher of two superheating fields present in the material would require fabrication of a cavity with only one crystal orientation on the curved surface, posing fabrication difficulties.

The niobium A15 compounds–the class of material the Nb_3Sn belongs to–are other promising candidates. Nb_3Al, Nb_3Ga, Nb_3Ge, and Nb_3Si all have similar T_c's [DH75, DJD+81, MZRB79, KTO05, DR84]. Of these materials only Nb_3Sn is stable for 3:1 stoichiometry at room temperatures [VF16, Ste15]. Non-niobium A15's of interest include V_3Ga, V_3Si, and Mo_3Re. These materials have slightly lower T_cs than Nb_3Sn, but could be promising materials to pursue.

In summary, Nb_3Sn is one of the best candidates for SRF operation. Furthermore, this material has seen significantly more development than other promising materials. Some other potential materials have significant technical problems to overcome while Nb_3Sn has already shown successful SRF operation.

3.2 Material Parameters

Nb_3Sn is an A15 structure alloy of niobium and tin (see Fig. 3.3). The material has seen significant development from the superconducting magnet community and much literature exists on the properties of Nb_3Sn under DC magnetic fields. An excellent review of the properties of Nb_3Sn is presented in [God06]. Here we

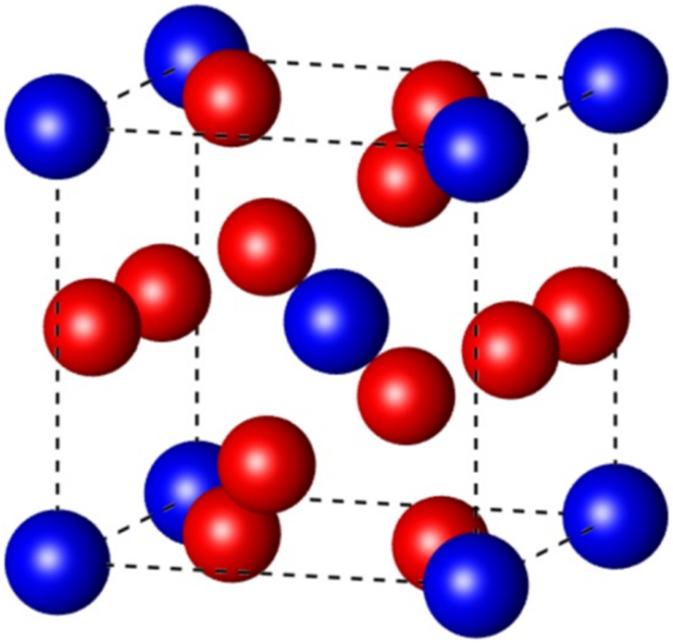

Figure 3.3: The A15 structure of Nb_3Sn. The large blue spheres are tin, and the small red spheres are niobium. This figure was adapted from [Hal17].

will summarize parameters of particular interest to the work presented in this dissertation.

Table 3.1 shows superconducting parameters of niobium and Nb_3Sn. We want to bring extra attention to λ and ξ, the penetration depth and coherence length. The penetration depth determines how thick our Nb_3Sn layer must be to effectively screen the magnetic field from the substrate. Assuming a lossy substrate, the Nb_3Sn layer should be at least 1 µm to render the contribution of the substrate to the surface resistance insignificant. The coherence length of Nb_3Sn is much shorter than that of niobium. This makes Nb_3Sn more sensitive to small defects than niobium is. This brings Nb_3Sn into the regime where grain boundaries could impact the superconducting state [LF81].

Figure 3.4 shows the temperature dependent thermal conductivity of niobium and Nb_3Sn. The thermal conductivity of Nb_3Sn is roughly 3 orders of

	Nb [MM65, LPT+17, NM75]	Nb_3Sn [God06, CS08a]
T_c [K]	9.2	18
Δ/k_BT_c	1.8	2.2
$\mu_0 H_{SH}$ [mT]	219	425
$\lambda(T=0)$ [nm]	50	111
$\xi(T=0)$ [nm]	22	4.2

Table 3.1: A table of superconducting parameters of niobium and Nb_3Sn. These parameters will depend on mean free path of the material and vary mildly depending on preparation. We show these for rough comparison between the materials.

magnitude lower than that of niobium. For this reason Nb_3Sn should be kept relatively thin, at most $\sim 10\,\mu m$ to avoid severe thermal instability[2] [DHL17]. Since SRF cavities must have a wall thickness on the order 1 mm to withstand vacuum conditions, Nb_3Sn must necessarily be deposited on a substrate material.

The phase diagram of the binary Nb-Sn system is shown in Fig. 3.5[3]. We note several key takeaways. The A15 structure persists from roughly 18 to 25 at. % Sn content. Ideal Nb_3Sn is 25 at. % Sn. We refer to lower content $Nb_{4-x}Sn_x$ (in A15 structure) as Sn-depleted Nb_3Sn. In Sn-depleted Nb_3Sn Nb atoms have replaced some of the Sn atoms in the lattice. Second, we note that the phase diagram significantly simplifies above 930 C reducing to only three materials: Nb, Nb_3Sn, and Sn. Fabricating Nb_3Sn above this temperature can make it easier to avoid other Nb-Sn compounds.

Unfortunately, Sn-depleted Nb_3Sn can have severely reduced superconducting performance. Figure 3.6 shows the dependence of T_c and H_{c2} with respect to Sn at. %, while Fig. 3.7 shows the dependence of the superconducting gap.

[2] In addition, the material is quite brittle and thicker layers are more prone to cracking.

[3] Additional measurements have been conducted by [Oka90, Oka03, TSGS02, LDGL09] examining the boundaries of the Nb_3Sn region. Recent theoretical calculations have also examined this [SCP+21]. This will discussed in more detail in chapter 10.

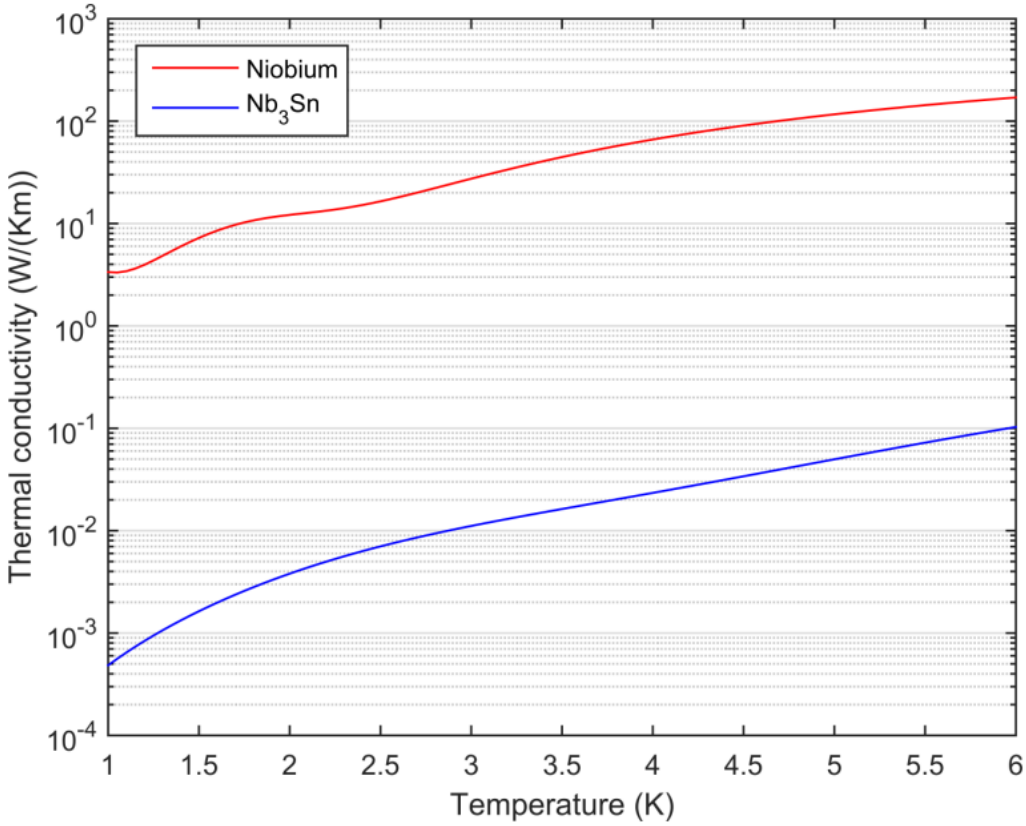

Figure 3.4: Temperature dependent thermal conductivity of niobium and Nb_3Sn. This plot originally appeared in [Hal17] using data from [KB96] and [CC64].

There is some discrepancy between the measured Sn-content in the two figures caused by experimental errors. The reduction in superconducting parameters shows the importance of creating Nb_3Sn with good (close to 25 at. %) stoichiometry.

3.3 Fabrication Technique

Niobium accelerator cavities are typically produced by taking large sheets of niobium and pressing them into 3D shapes (followed by electron beam weld-

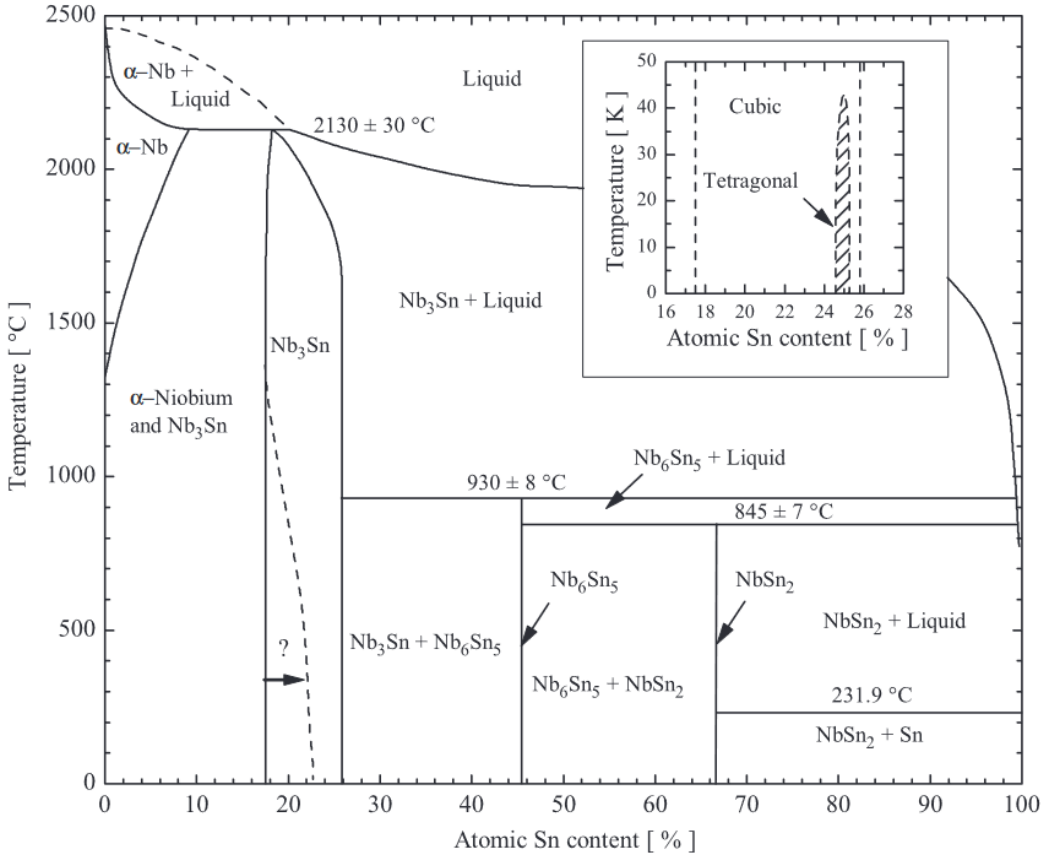

Figure 3.5: The phase diagram of the binary Nb-Sn systems. The A15 structure is favorable from 18 to 25 at. %. The inset shows a low-temperature phase diagram depicting a change in crystal structure. This image was adapted from [God06] which in turn was adapted from [CC64].

ing). Unfortunately, Nb_3Sn is too brittle for a similar manufacturing technique and would crack during forming [Hil80]. Instead, Nb_3Sn must be formed in the final cavity shape. In addition, fabrication techniques used for superconducting magnets and wires are unsuitable for SRF cavities. In the DC regime the resistance of defects and impurities is not nearly as deleterious as in RF applications. In fact, defects are desirable as pinning sites to trap magnetic vortices that would cause loses if allowed to move with the DC supercurrent. Thus far the only technique that has made Nb_3Sn of sufficient quality for SRF applications is the vapor diffusion process.

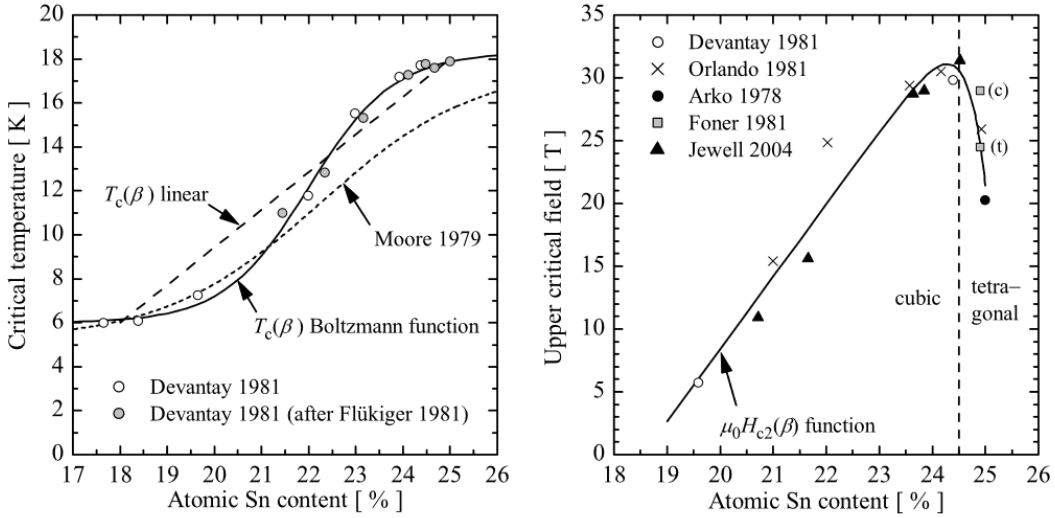

Figure 3.6: Left: the critical temperature of Nb_3Sn versus the tin content (at. % Sn). Right: H_{c2} of Nb_3Sn versus the tin content (at. % Sn). Note the large reduction in T_c and H_{c2} as the tin content falls. This image was adapted from [God06].

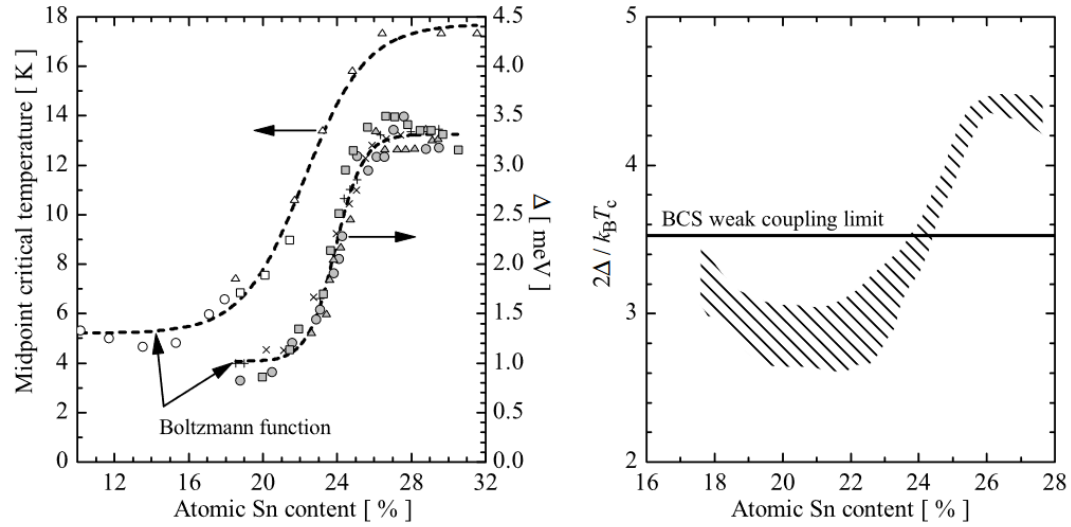

Figure 3.7: Left: the critical temperature and superconducting gap of Nb_3Sn versus the tin content (at. % Sn). Right: The superconducting gap of Nb_3Sn versus the tin content (at. % Sn). The transition from weak coupling to strong coupling BCS is denoted. This image was adapted from [God06] which was adapted from [MZRB79].

The vapor diffusion process of creating Nb_3Sn was originally developed by Saur and Wurm [SW62]. The technique was applied to SRF cavities with some success during the 20th century [HMP+75, Hil80, MM78, HGM+84, BKM+97, MKM96, AMC86, ABHT83, Sti78]. In the vapor diffusion process a fully formed Nb cavity is placed in an ultra-high vacuum furnace where $SnCl_2$ and Sn is vaporized, allowed to absorb into the surface and form a $\sim$ 1 µm layer of Nb_3Sn on the niobium substrate.

This method offers several advantages during development. Using a niobium substrate allows us to use existing fabrication techniques to create the substrate cavity. Using niobium ensures ample supply of niobium during the deposition process and minimizes the number of compounds that need to be used during the deposition process–reducing the chance of contamination. Some substrate materials, particularly copper, may be desirable for cost and performance reasons but are highly mobile and deleterious to RF superconducting performance if in the superconductor.

By end of 20th century development of Nb_3Sn for SRF had stalled. Cavities were plagued by severe Q-slope starting at H_{c1} which many believed was fundamental [MKM96]. In 2009 a new Nb_3Sn program was started at Cornell University that created cavities without a Q-slope [PLX11, PL11, PL13]. This reignited interest in Nb_3Sn for SRF cavities and new programs were started at other labs [EKR+15, PMRT15].

Additional fabrication techniques including Chemical Vapor Deposition, Sn-electroplating with thermal conversion, and Nb_3Sn sputtering are being pursued [G+21, Val21, S+21c, KHS21, S+21a, G+19, RSI+16, BBR+16, Kri12, Mit10, DRR+09, RDS+09, DKR+06, CRZ+06, Ham75, Hak88, HHO74]. These techniques

may offer advantages in the future but have yet to create Nb_3Sn that can achieve similar performance to Nb_3Sn produced through vapor diffusion. In this work we will focus on the vapor diffusion process employed at Cornell University.

We will now detail the furnace setup and standard coating [HLM16] process utilized at Cornell University at this time. Additional details of the setup can be found in [Pos14, Hal17, PMRT15, PVL15, PVL15, HLM16]. For an excellent review of coating setups at other labs and a historical review of the development of Nb_3Sn for SRF see [Hal17].

A diagram of the Nb_3Sn coating chamber and a picture of the high temperature vacuum furnace are shown Fig. 3.8. The furnace consists of two vacuum spaces the 'hotpot' and the vacuum insulation. The coating chamber is inserted into the furnace hotpot where the lower section of it can be heated (the upper section above the heat shields is a thermal transition and is not heated). The coating chamber is separate vacuum zone that is connected to the main furnace 'hotpot' by an external vacuum line. While the furnace is being pumped down or degassed this connection is open. During high temperature processes the connection is closed to prevent tin from contaminating the main furnace. The furnace is equipped with both a turbo molecular pump and a cryopump. A scroll pump is used to back the turbo molecular pump. The system has a supply of ultrahigh purity N2 for letting up to atmosphere.

The coating chamber is comprised of steel at the top where the temperatures are low. The lower section is a welded niobium tube. These are connected by a copper transition piece brazed to each section. The heatshields are comprised of niobium. On the bottom of the furnace are tungsten feet on which the cavity can sit (the cavity would solder to the chamber floor during coating if the feet

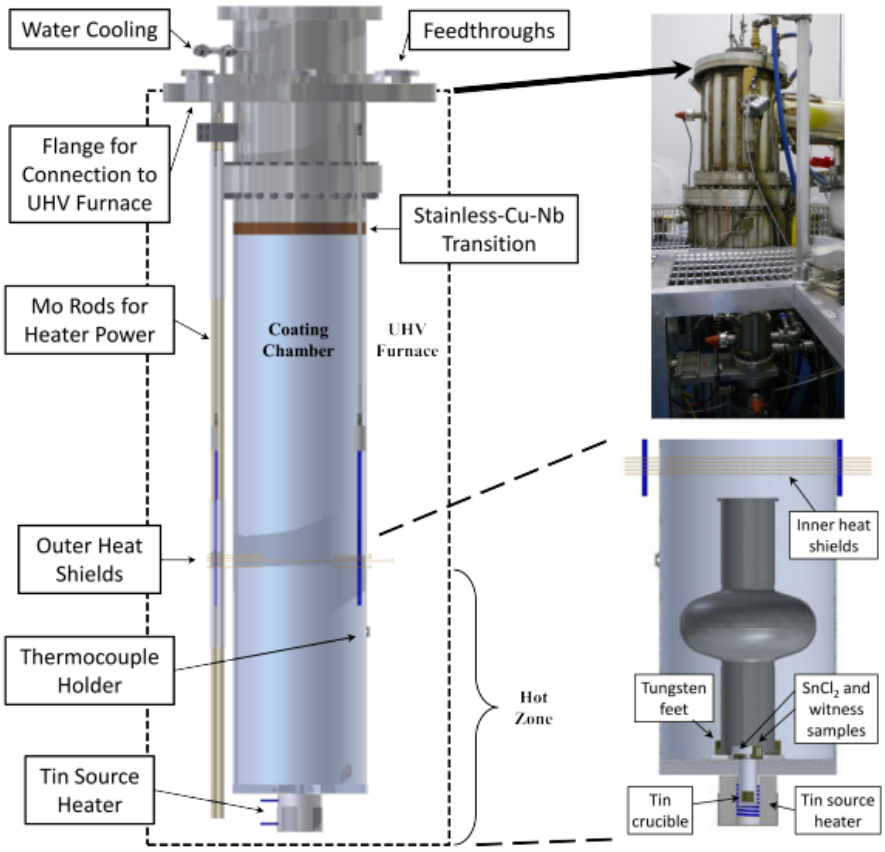

Figure 3.8: A diagram of the Nb_3Sn coating chamber. The coating chamber is inserted into a high-temperature vacuum furnace. Note that the cavity sits on tungsten feet just above the Sn source. The Sn source sits in a secondary hot zone, while the $SnCl_2$ boat sits just about the secondary hot zone. This figure was adapted from [Hal17].

were absent). Tungsten has a very low vapor pressure at all temperatures used in this process, so tungsten contamination is unlikely. This setup minimizes contamination of the Nb_3Sn.

At the bottom of the coating camber is a small secondary hot zone in which sits a crucible of high purity tin. This area has a separate heater on the outside of the coating chamber, allowing it to be increased to a higher temperature than the rest of the furnace. This allows us to increase the vapor pressure of tin during the coating process while keeping the cavity temperature lower. This allows us

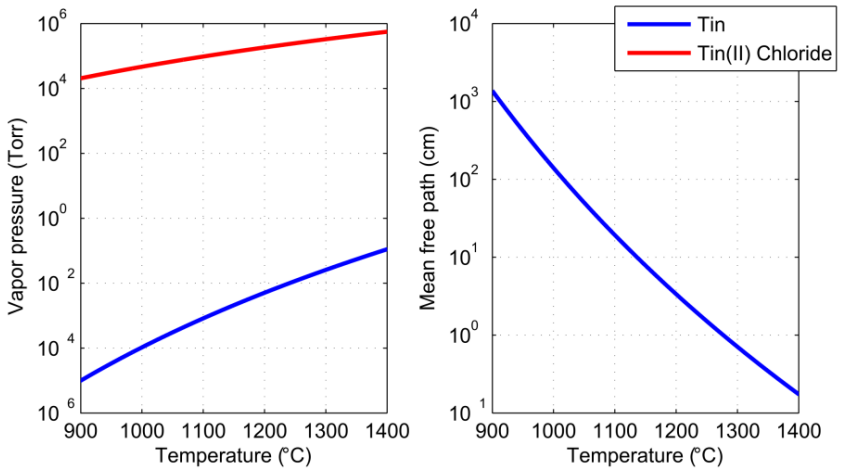

Figure 3.9: Left: the vapor pressure of tin and $SnCl_2$ versus temperature. Right: the mean free path of tin at the saturated vapor pressure versus temperature. This figure was adapted from [Hal17] using data from [Pei83, MO87].

to control both evaporation rate of tin from the source and reaction rate of tin on cavity (temperature dependent) separately. The vapor pressure of tin is shown in Fig. 3.9.

Just above the secondary hot zone sits a small container of $SnCl_2$. $SnCl_2$ has a much high vapor pressure than tin and is used as a low temperature ($\approx 500\,C$) nucleation agent. Early work by Siemens found the use of a nucleation agent reduced the likelihood of forming regions that were essentially uncoated [MM78]. Siemens similarly found that growing a thick oxide on the substrate or increasing the tin flux through heating the tin source also reduced the likelihood of forming these regions [MM78].

Before loading, cavities are ultrasonically cleaned in deionized water, internally high pressure rinsed with deionized water, and externally cleaned using methanol and lint free rags. Samples are ultrasonically cleaned in methanol and rinsed just before loading. The furnace is located inside a cleanroom. This

minimizes external sources of contamination.

The cavity is loaded into the furnace with at least 2 g of tin in the crucible and 220 ± 5 mg of $SnCl_2$. All $SnCl_2$ is used during the process. Approximately 1.5 to 1.7 g of tin is used during the process–determined by measuring the tin crucible before and after the coating. The furnace is then sealed and slowly pumped down over two days. Before turning on the furnace the pressure reaches $\approx 10^{-7}$ Torr.

After the pump down the heating process is turned on. The furnace temperature is raised 180 C to degas cavity and furnace. This temperature is held for 48 hours. After the degas phase, the valve connecting the coating chamber to the hotpot is closed. The coating process can then start.

Figure 3.10 shows the temperature profile of the 'standard' coating process. The temperature is raised to 500 C and held for 5 hrs. This allows for the $SnCl_2$ to vaporize and nucleate tin sites on the cavity wall. After the nucleation step, the secondary heater is turned on and the temperature of the tin source is allowed to rise above that of the coating chamber/cavity. Once the temperature gradient between the tin source the cavity reaches 270 C the furnace temperature is ramped up to the coating temperature of 1150 C. The temperature ramp up to coating takes a significant amount of time: $\approx$ 3 hours. The tin source is held at 1400 C once this temperature is reached. This state is held for 1.5 hours after which the secondary heated is turned off. The cavity temperature is held for an additional hour to allow the cavity to anneal and absorb any excess tin on the cavity surface.

After the temperature drops below 30 C the pumping line to the hotpot is

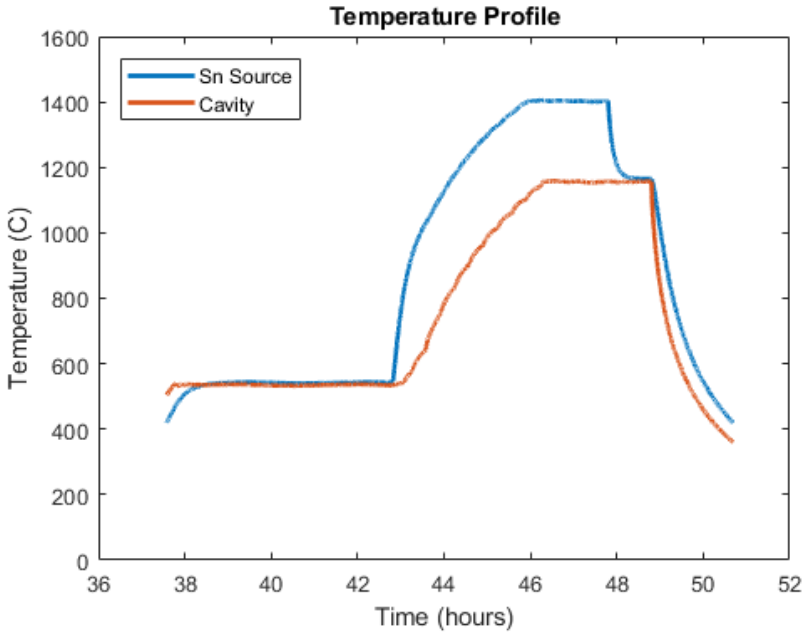

Figure 3.10: Temperature profile from the coating of a Nb_3Sn cavity. Both the temperature of the cavity and the Sn source are shown.

opened and the entire furnace is let up with ultra-high purity N2. Once at atmospheric pressure the samples can be removed from the furnace.

This coating process creates a Nb_3Sn film on the cavity that is 2 to 3 µm thick with grains sizes ~ 1 µm. Figure 3.11 show an off angle SEM image of the surface of an Nb_3Sn sample and Fig. 3.12 shows TEM cross-section.

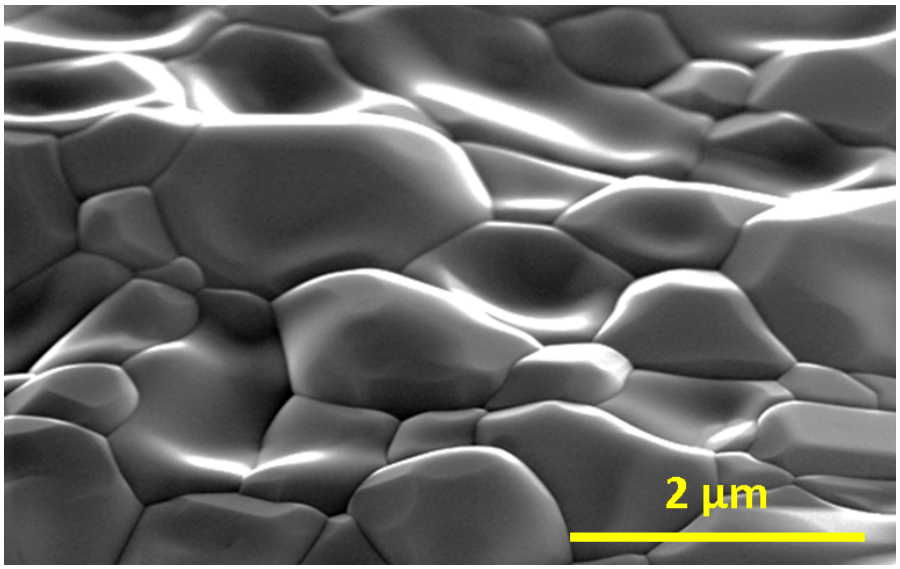

Figure 3.11: Scanning Electron Microscope (SEM) image of the Nb_3Sn surface. This figure was adapted from [Pos14].

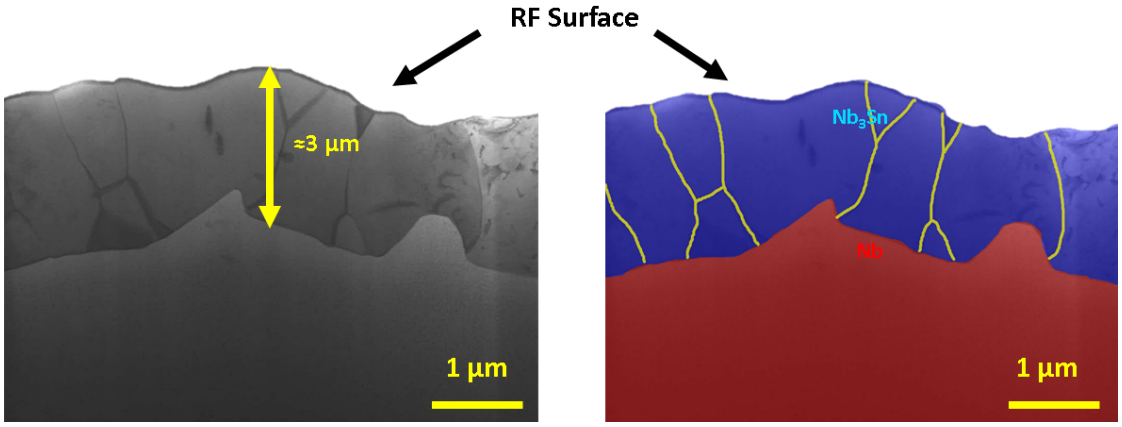

Figure 3.12: A Transmission Electron Microscope (TEM) image of cross section of the Nb_3Sn layer. The right image is color-coded to highlight materials and grain boundaries. This figure was adapted from [Hal17].

CHAPTER 4

RF CAVITY TESTING

We now move into experimental systems used in this work. We start with RF testing of SRF cavities. We will discuss the cavity preparation, experimental setups, testing procedures, extraction of quality factors and accelerating gradients, determination of superconducting parameters, and trapped magnetic flux measurements. Two additional important RF testing topics are temperature mapping and high-pulsed power testing. We have developed new testing systems involving these that will be covered in detail in chapters 5 and 6. We leave discussion of these topics to those chapters. Those uninterested in the minutiae of RF testing may wish to skip to section 4.6 which discusses the extraction of superconducting parameters from RF measurements. For the particularly interested reader, RF testing procedures are discussed in great detail in [PKH98].

Accelerator cavities are run in horizontal cryostats in real accelerators; however, the assembling of horizontal cryostats requires a great deal of work that is not required if beam is not being accelerated. Fortunately, we can conduct all necessary RF testing of a cavity without inserting a beam and can use a greatly simplified vertical test cryostat. We refer to this form of testing as vertical testing (versus horizontal testing).

Our vertical test system consists of test "inserts" on which the cavity and any instrumentation can be mounted, and a vertical cryostat set into the floor. Figure 4.1 shows a schematic of a vertical test cryostat with insert inside and an insert being lowered into a cryostat. The insert has a 'top plate' that bolts onto the top of the cryostat. We refer to the area above this top plate as the warm side and below as the cold side. The test stand has an antenna/coupler to supply RF power

to the cavity, a pumping line to keep the cavity under vacuum pressure (connected to an ion pump on the warm side), and warm to cold cable feedthroughs for instrumentation. The cryostat consists of two nested vacuum walled Dewars. The inner Dewar (where the insert/cavity sits) can be pumped down and filled with Liquid Helium (LHe)[1]. The outer Dewar can be filled with Liquid Nitrogen (LN2) and acts as a thermal shield for the inner Dewar. The cryostat is filled with liquid helium to cool to the cavity 4.2 K–the boiling point of liquid helium at 1 atm. To cool below 4.2 K the cryostat is slowly pumped down below atmospheric pressure, cooling the LHe through evaporative cooling. This combination gives us a system that can relatively easily test SRF cavities down to ≈ 1.6 K.

4.1 Cavity Preparation

SRF cavities must be carefully prepared for testing. SRF materials are sensitive to material imperfections and dust on the surface[2]. Cavities must be carefully etched and cleaned to minimize potential problems. Here we discuss the typical procedure for preparing SRF cavities.

It should be noted that niobium SRF cavities must be constructed from high purity niobium to minimize contaminants that impact performance. We note that poor purity niobium has relatively poor thermal conductivity. The Residual-Resistance Ratio (RRR) is a good measure of the purity of the material. Cavity cells of niobium cavities are typically made with niobium for which the RRR varies from 200 to 300–the highest purities that can be readily purchased.

[1]The cryostat used for the testing detailed in this dissertation can hold 500 L of LHe!

[2]Dust particles on the surface are exposed to strong electric fields and may become field emitters.

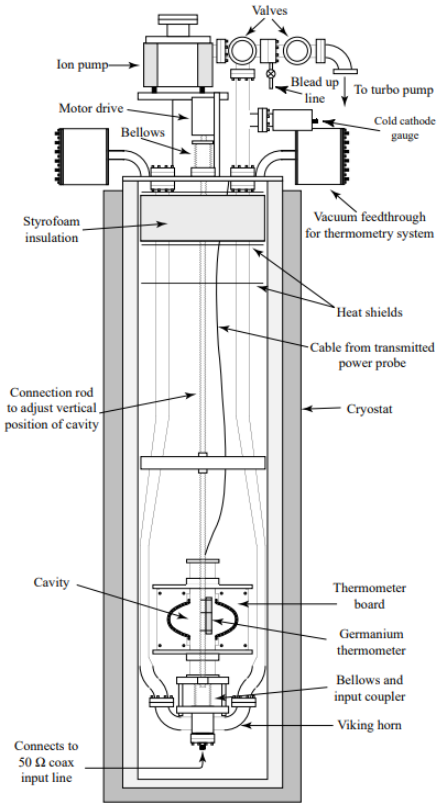

(a)

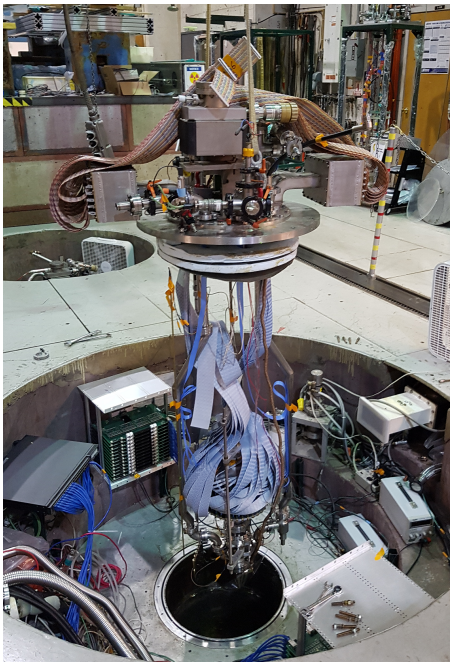

(b)

Figure 4.1: a) Diagram of a test insert in a vertical test cryostat. This was modified from [Kno97]. b) A fully dressed cavity on a test insert being lowered into a vertical test cryostat. The cavity is not visible due to instrumentation on it. The cavity is inside the blue ribbon cables near the bottom.

Cavity beam tubes and other components can be made from lower purity 'reactor grade' niobium. Niobium cavities are formed from niobium sheet metal that is pressed into shape (in the case of beam tubes, pulled). The cavities used here are made using 3 mm plate. The separate pieces are then welded together. To prevent gas contamination, the cavities are welded under vacuum using electron beam welding.

After construction the cavities receive chemical etching and polishing. This removes embedded material and creates a smooth surface. Several processes exist for this. In this work we primarily utilize Buffered Chemical Polish (BCP)

and Electropolishing (EP). We will discuss these in more detail below. New cavities in the Nb_3Sn program receive 100 µm of BCP and re-used Nb_3Sn cavities receive 20 µm of BCP to remove the old Nb_3Sn coating and reset the surface. The chemical treatments are followed by a 30 min ultrasonic cleaning in deionized water and Liquinox®Detergent, followed by a 30 min ultrasonic cleaning in deionized water, followed by a high-pressure rinsing with deionized water. This removes any residual acids or salts left behind by the chemical treatments. After drying, the cavities are ready for the next step.

After chemical treatments, cavities are usually degassed in an ultrahigh vacuum furnace to remove contaminant gases. In particular, the process of electropolishing creates hydrogen which is absorbed into the niobium surface. The high levels of dissolved hydrogen form hydrides on the surface of niobium cavities which have been shown to cause "Q disease" and decrease cavity performance [PKH98]. This process consists of baking the cavity at 800 C for several hours optionally followed by exposure to air and an additional bake at 120 C for 48 hours. The 120 C has been associated with the dissolution of the oxide into the cavity wall, forming an oxygen interstitial layer 10 – 20 nm into the cavity surface and the suppression of 'nano-hydride' growth on the cavity surface [Saf01, CMS+10, BGM+19, RECS13, Rom09]. Since Nb_3Sn cavities are baked at 1120 C during the coating process these step is typically skipped.

Other treatments may be applied to the cavity. In particular, the Nb_3Sn coating detailed in the previous chapter. On some cavities, before Nb_3Sn coating we grow a thick oxide on the surface using electrolytic anodization (we provide more details in the next section). We call these cavities anodized. The addition of this thick oxide layer modifies the Nb_3Sn growth process and prevents the

formation of large, thin Nb_3Sn grains and improve the quality factor. The use of anodization in Nb_3Sn cavities was originally studied in [HMP+75] and the use of it to prevent large, thin Nb_3Sn grains was studied in [Hal17]. We will discuss the impacts of anodization in chapter 10. Unless otherwise stated, the cavity used in this work were not anodized prior to coating.

Once the SRF cavity has been prepared it must be assembled onto the vertical test stand. This must be done inside a cleanroom with the utmost of care to prevent dust contamination. We assemble our inserts in a Class 10 (ISO 4) cleanroom that is used only by the SRF research group at Cornell University. One end of the cavity is capped with a niobium plate with a small pickup antenna in it for measuring the energy in the cavity. A vacuum seal is made with indium wire and steel clamps. The cavity (with plate) is then high pressure rinsed with deionized water [PKH98, KL95]. After drying, the cavity is carefully placed on the insert[3], using an indium wire and steel clamps to make a vacuum seal. The cavity is then slowly pumped down to vacuum and checked for leaks. The final pressure is $\sim 1 \times 10^{-8}$ Torr. The test insert can then be removed from the cleanroom and fitted with instrumentation (section 4.3).

[3]Care must be taken to ensure the vertical test stand is also clean. All vacuum components of the insert were carefully cleaned before the insert was assembled using solvents and deionized water. Any components that were ever exposed to greases or oils are not used in the vacuum system. After testing the test stands must be brought back into the cleanroom and the cavity removed. Before being brought in, all the components of the test stands are either wrapped in particle free plastic or wiped with isopropyl alcohol and lint free rags. Once inside, the components near the cavity are cleaned again using particle-free methanol and a lint free rag. The cavity and indium wire can them be removed.

4.2 Chemical Treatments

Here we lightly detail chemical processes used in this work including specifications of our setup. Those uninterested in the specifics of the chemical processes may skip to the next section with impunity. Any details believed important by the author will be noted at appropriate times.

Niobium is a stable material that few chemicals readily dissolve. Almost all chemical etching and polishing techniques of niobium rely on the formation of niobium oxide and its removal by Hydrofluoric (HF) acid. There are several common techniques used in the field of SRF. In addition, anodization can be useful for Nb_3Sn growth and a step of an etching/polishing process.

4.2.1 Buffered Chemical Polish

Buffered Chemical Polish (BCP) treatments utilize a mixture of HF, HNO_3, and H_3PO_4 that the cavity is either filled with or submerged in [KWS70, Zha14]. The chemical process involves H_3PO_4 reacting with niobium to form Nb_2O_5 which then reacts with the HF to form soluble NbF_5. The phosphoric acid serves as a buffer to stabilize the reaction rate. Changing the concentration of phosphoric acid or the temperature changes the etch rate. We use the standard 1:1:2 ratio of HF (49%), HNO_3 (65%), and H_3PO_4 (85%).

BCP is has advantages in terms of etch rate and a relatively simple setup but creates rougher surfaces than electropolishing does. BCP can be more easily applied to complex geometries than electropolishing and can be used to etch the outside of SRF cavities. In addition, it etches much faster than electropolishing

(roughly 10 times the etch rate. It has, however, been shown that BCP leaves a rougher surface than electropolishing and has a crystal orientation-dependent etch rates [TRK+06, BBZ+07]. This creates sharp edges and cliffs at niobium grain boundaries.

4.2.2 Electropolishing

Electropolishing (EP) is an electrochemical polishing technique used on a variety of materials [Jac35, HF19, Zha14]. In this technique the material to be polished is the anode. The material to be polished and a cathode are submerged an appropriate electrolyte. A power supply is connected, driving electrons from the anode surface and dissolving the electrode into the electrolyte. For niobium electropolishing a 1:9 volume ratio of HF (48%) to H_2SO_4(96%) solution is used and an aluminum cathode [Zha14, Sai03, DSMS71]. The electrolytic process creates niobium oxide which subsequently reacts with fluoride ions to form soluble H_2NbF_5.

As noted above, EP creates a smoother surface than BCP, but has a slower etch rate and requires a geometrically appropriate cathode. Hydrogen is generated at the cathode that is absorbed into the niobium cavity. This often requires a 800 C to mitigate the deleterious effects of hydrogen [PKH98].

4.2.3 Anodization

Anodization is an electrolytic process to grow a thick oxide on a material [Gra75, Hal17]. In this technique an oxide is grown on the anode. The anode and an-

other cathode are placed in an appropriate electrolyte and voltage is applied, driving the growth of an oxide on the anode.

We use the same process listed in [Hal17]. The used electrolytic is 10% NaOH aqueous. Since we are concerned with creating Nb_3Sn a tin wire is used as the cathode to minimize risk of any contamination from the cathode material. The end of the wire is wrapped in a small loop and hung near the equator of the cavity which is filled with the electrolyte. The cavity wall is roughly 4 to 8 cm from the anode. The cavity is anodized to a 30 V potential between the anode and cathode. The voltage is raised in roughly 5 V steps, waiting for the current to drop to 0 A. In addition, the current is limited to a maximum of approximately 10 mA/cm^2 [4]. After the process is complete the cavity interior is colored light blue. We estimate the oxide film to be roughly 70 nm based on the relationship of 2.2 nm/V found in [JCC+91].

For samples the anodization process is similar, but the sample is hung in the middle of the tin wire loop and is $\approx$ 6 cm from the wire. The samples gain the same blue appearance as the cavity.

Parameters of the anodization process may impact the final oxide structure and the surface chemistry. This may cause changes in how $SnCl_2$ reacts with the oxide during the nucleation step of Nb_3Sn growth. Figure 4.2 shows a Pourbaix diagram of the Nb-H_2O system. Above zero voltage (and relatively neutral solutions) we should only form Nb_2O_5, but there are many locations where, for example, OH^- groups may sit and change the reactivity of the material with $SnCl_2$ [S+21b]. We will further discuss the anodized oxide and the effects on

[4] The use of this current limitation has been shown to grow a uniform oxide film [ONSA04]. Current densities below 3 mA/cm^2 may result in different oxide structures and changed index of refraction [JCC+91, CP87].

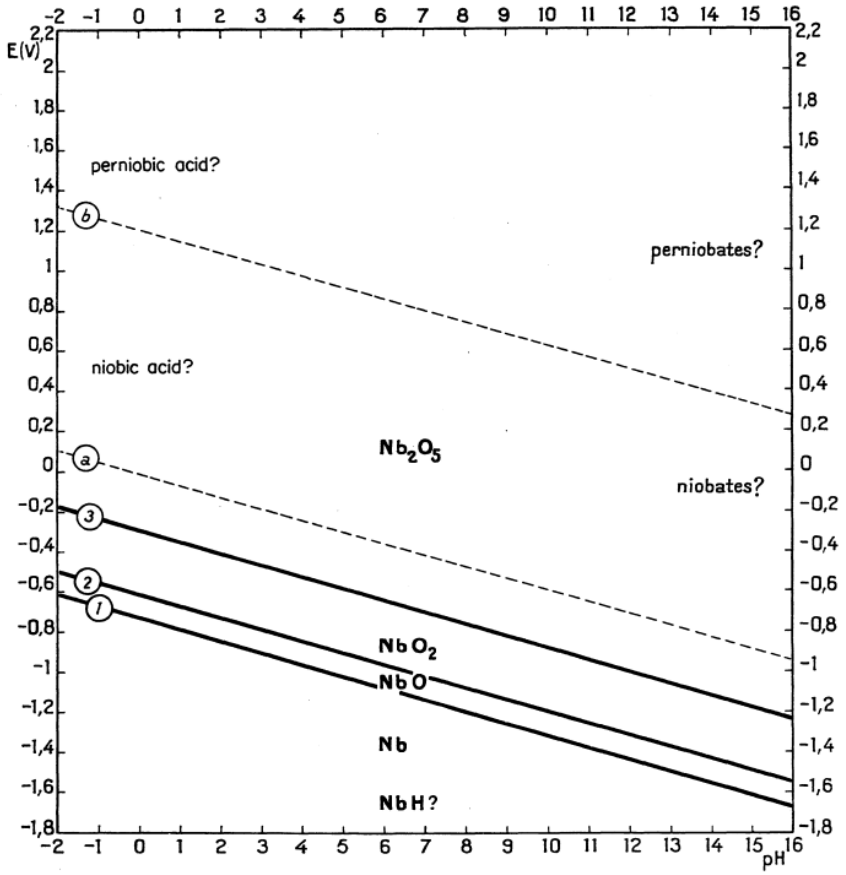

Figure 4.2: A Pourbaix diagram of the Nb-H_2O system. Note that above zero voltage Nb_2O_5 is formed. However, highly acidic or alkali solutions may allow the dissolving of various compounds into the solution. This figure was modified from [Pou74].

$SnCl_2$ nucleation in chapter 10.

4.2.4 HF Rinsing and Oxipolishing

Since Hydrofluoric acid (HF) removes niobium oxide, an HF rinse creates an easy way to remove a small amount of material. This process will remove the native oxide on the material. If the surface is exposed to oxygen again the oxide will regrow, and the oxide can be stripped again. The native oxide layer

is $\approx$ 5 nm and growing the native oxide consumes 2 nm of the underlying niobium [GH80, AAC+99].

Much more material can be removed if the sample is first anodized to grow a thicker oxide layer. This technique is referred to as oxipolishing (or oxypolishing) [Die78, Hil80]. Using the anodization technique listed above we estimate removal of $\approx$ 33 nm of niobium or Nb_3Sn per application [Hal17].

4.3 Instrumentation

Here we highlight several key pieces of equipment that are needed to test the cavity. RF connections and antennas are handled by the insert and RF cables run out of the pit. Here we will primarily talk about temperature sensors, magnetic field sensors, and equipment for slow cooling the cavity.

Temperature measurements are necessary to know the operating temperature of the cavity. For this we use three Lakeshore Cryotronics Cernox®brand thermometers (CX-1050 CX-SD package). These are calibrated to ±4 mK at 4.2 K and below. The three sensors sit on the external surface as shown in Fig. 4.4 on both irises and on the equator. The sensors are pressed into the cavity wall using PTFE tape to improve thermal contact–though they are most accurate for reading the liquid helium bath temperature.

We use magnetic field sensors to measure the ambient magnetic field, the trapped magnetic field, and the transition temperature through seeing magnetic field expulsion when entering the Meissner state [M+15]. The magnetic field sensors are Mag-01H Type F Fluxgate Magnetometers made by Barting-

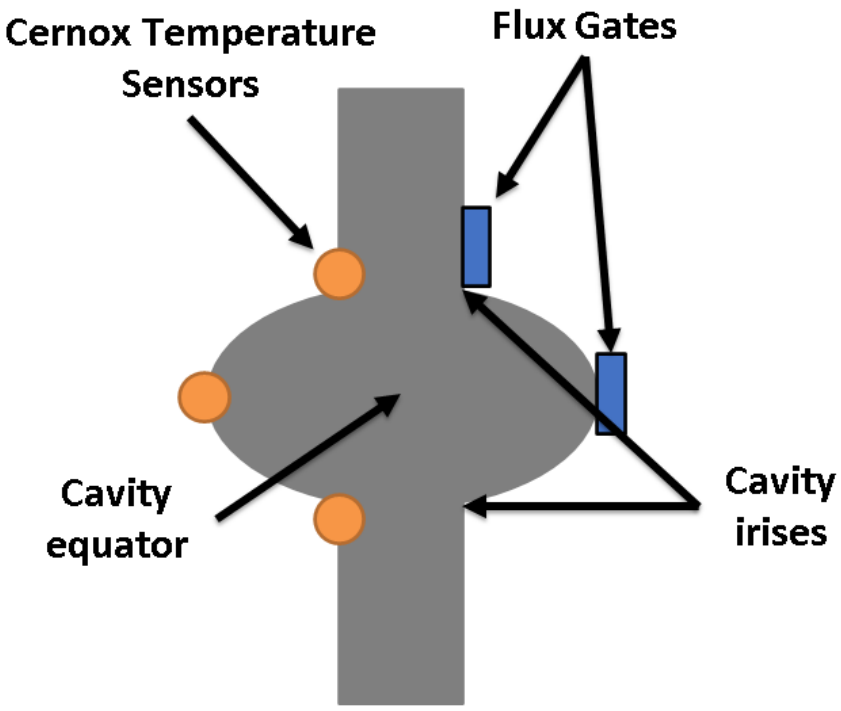

Figure 4.3: A diagram of an SRF cavity with instrumentation. Three important locations are labelled: the upper iris, equator, and lower iris. The irises are where the cavity cell meets the beam tubes. The equator is the middle line of the cavity. Cernox temperature sensors are placed at both irises and on the equator. Flux gate magnetometers are placed vertically on the upper iris and the equator.

ton Instruments. These sensors measure magnetic flux along a single axis and are sensitive to the 1 nT level. The magnetic field in the cryostat is assumed to be primarily vertical because the earth's magnetic field is mostly vertical at our latitude and a place vertical magnetic shield around the sides of the cryostat. There are two magnetic fields sensors on the cavity as indicated in Fig. 4.4.

Standard cooling of niobium cavities involves adding liquid helium as quickly as possible (without boiled off gas over pressurizing the system) to the cryostat–this form of cooling results in poor SRF performance of Nb_3Sn cavities. Our Nb_3Sn cavities are Nb_3Sn on niobium. This bi-metal interface creates a thermal couple [Pos14, Hal17]. During 'fast' cooldowns a large temperature

gradient is established across the cavity. This temperature gradient generates a thermoelectric current which in turn generates a magnetic field. This magnetic field is in part trapped when the cavity goes through the superconducting transition. This creates a large residual resistance[5].

To mitigate this a 'slow cool' procedure is followed. Just above T_c the flow of helium is throttled, and a 'slow cool stinger' is used. Helium is added through the slow cool stinger where is must flow across resistive elements that act as heaters (see Fig. 4.4). This allows the temperature of the helium to be increased and slows the cooling rate. The heating can be adjusted by using a potentiometer and the cooling rate of the cavity can be carefully controlled. By slowing the cooldown rate the cavity is given more time to equilibrate and the temperature gradient from the bottom to the top is decreased. Using this technique the thermal gradient from the bottom to the top iris can be reduced to as low as 20 mK–roughly the level of uncertainty on the thermometers–and residual resistance from cooldowns can be made negligible [Hal17, Pos14].

4.4 RF Systems

The RF/microwave system used during the test has several key roles: providing power to charge the SRF cavity, keeping the forward power matched to the cavity resonance frequency, measuring the cavity resonance frequency, measuring the forward power to the cavity, measure the reverse power coming from the cavity, and measuring the transmitted power. Figure 4.5 shows the overall layout of the RF system. We will briefly discuss how this system functions.

[5]The effects of thermal gradients on Nb_3Sn cavity performance was studied in [Hal17].

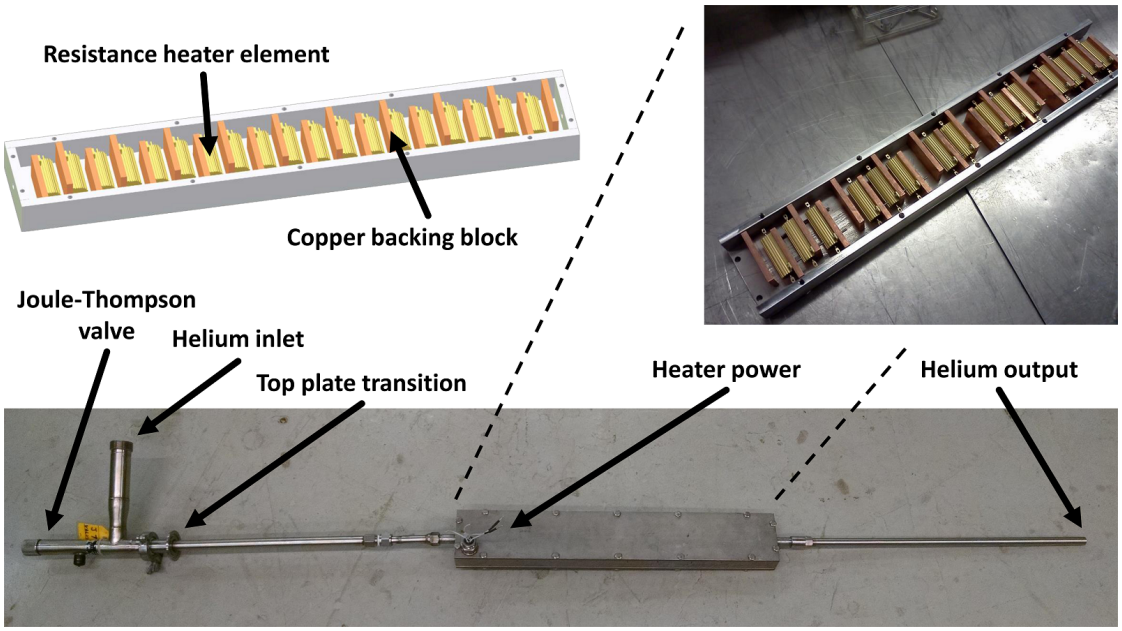

Figure 4.4: The slow cool stinger developed in [Pos14]. In the top right the front plate is removed to make internals visible. The LHe must flow over the resitors/heaters where it is warmed up. The heat added is controlled by a potentiometer. The flow rate can be slowed by adjusted a JT-valve. Figure was adapted from [Hal17].

A variable frequency RF signal generator (voltage-controlled oscillator) creates the initial signal. The signal is amplified and sent to the RF cavity. Along the way the power is sampled by directional couplers and: a. used to measure the frequency (not shown), b. sent to the Phased-Locked Loop (discussed below), c. measure the forward power, P_f. Power is reflected, P_{ref}, from the cavity and emitted, P_e, out of the cavity if it is charged. The amplitudes of the reflected and emitted waves and add get a reverse power, P_r, from the cavity. The reverse power is separated from the forward power signal using a circulator[6]. Part of the reverse power is sampled using an RF power meter while the rest is put into a $50\,\Omega$ load.

[6]Circulators have three ports: 1, 2, and 3. Signals coming in port 1 come out port 2, signals coming in port 2 come out port 3, and signals coming in port 3 come out port 1. This allows signals to be separated based on the direction of propagation.

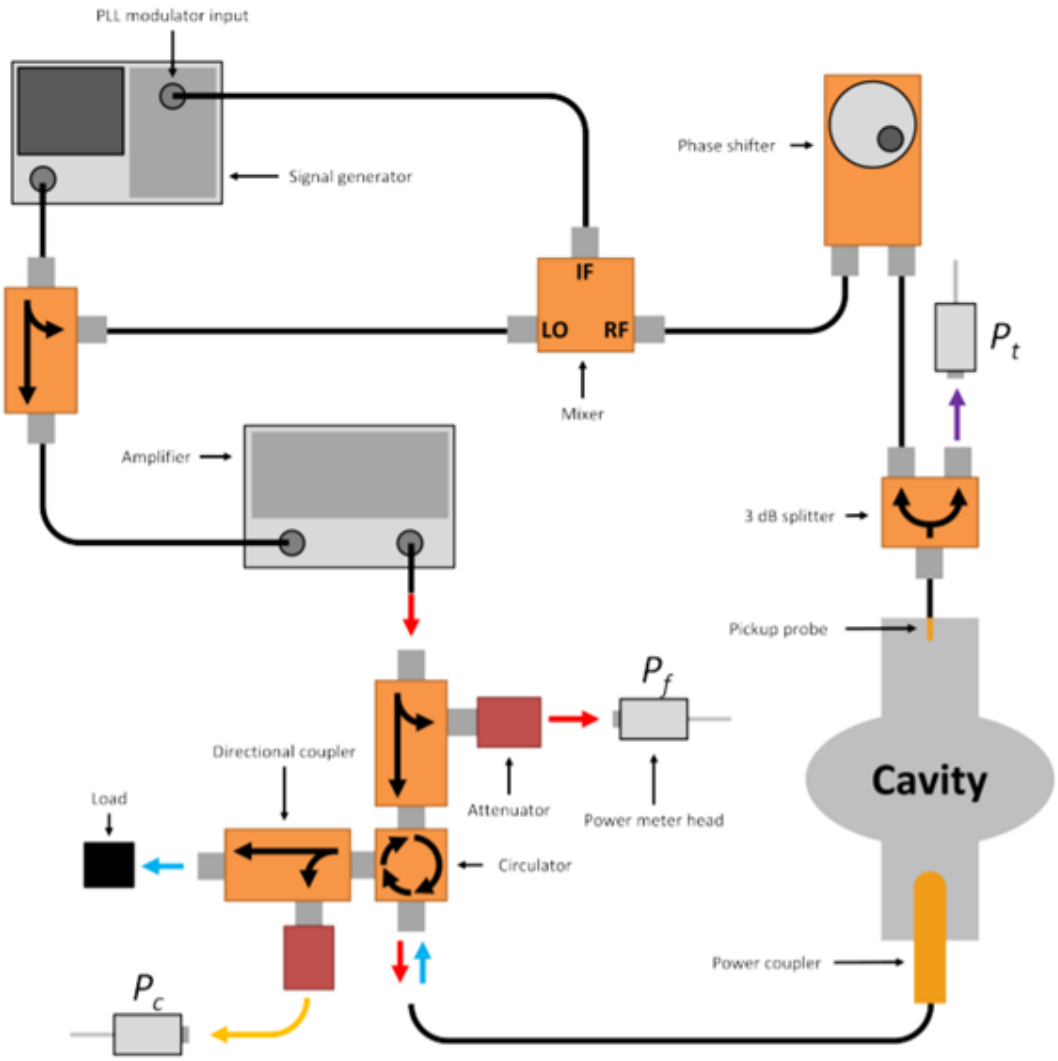

Figure 4.5: A diagram of the RF equipment setup for testing cavities. This includes RF generation, RF measurement, and the phase-locked loop. Not shown are the DC blocks and isolators in the system. Also missing is the frequency counter for measuring the frequency. This figure was adapted from [Hal17].

If the cavity is excited some of the energy is picked up by a small 'transmitted power probe' located on the top plate of the cavity. Some of this transmitted power, P_t, is sampled and used as a measure of energy stored in the cavity, U, while the rest is fed into the phase-locked loop.

The Phase-Locked Loop (PLL) serves the important task of keeping the

signal generator's output frequency matched to the cavity's resonance frequency [Kro03]. The full bandwidth, Δf, of an SRF cavity is small due to the high loaded quality factors. The loaded quality factor, Q_L, includes all loss mechanisms of the energy stored in the cavity, including power emitted from the coupler. We find,

$$\Delta f = \frac{f_0}{Q_L} \sim \frac{10^9\,\text{Hz}}{10^{10}} = 0.1\,\text{Hz}\,, \tag{4.1}$$

where f_0 is the cavities resonance frequency. This bandwidth is smaller than the changes in the cavity resonance caused by vibrations in the cryostat, meaning a fixed frequency output cannot stay on the cavity resonance. The PLL utilizes an RF mixer to create a DC output signal that depends on the difference between the phase of the forward and transmitted power signals. This signal is fed into the signal generator to modulate the output frequency. We spare the details of the PLL, but it relies on the quick phase change of a resonator as the driving frequency passes through the resonance. The phase adjuster allows the relative phase shift from differing cable lengths between the forward and transmitted power to be removed. It must be carefully adjusted to get the cavity perfectly on resonance (maximum P_t signal). The PPL will keep the phase-difference between the two signals the same even as the resonance frequency changes–keeping the driving signal on resonance.

Before meaningful measurements of forward and reverse powers can be made, we must measure the attenuation of the signals. We are interested in the forward and reverse power directly at the cavity, but our power meters are far away and only measure a sample of the power. Using a Network Analyzer (NA) we can determine the attenuation of cables and other components. This

allows us to calibrate/correct our measurements.

4.5 Measurements

We will now discuss measurements done on the RF cavities during testing.

4.5.1 Quality Factor and Accelerating Gradients

The quality factor and accelerating gradient is measured using decay curves. This technique is detailed in [PKH98] and we give key details here. The cavity is charged with a fixed forward power until the energy in the cavity reaches a steady state, then the forward power is turned off and the decay of the energy in the cavity is measured. The decay of energy in the cavity, U, is given by,

$$U(t) = U_0 e^{-\frac{2\pi f_0}{Q_L} t}\,, \tag{4.2}$$

where U_0 is the energy in the cavity at t = 0 (the start of the decay), and Q_L is called the loaded quality factor. We can use either P_e or P_t to measure the decay curve and we choose P_e. By taking the slope of the logarithm of the decay curve we can determine Q_L.

We want to know the 'intrinsic' quality factor, Q_0, of the cavity. That is, the quality factor determined only by the losses on the cavity wall, P_{wall}. In this system, however, energy from the cavity is both absorbed by the cavity wall and leaks out through the power coupler/antenna. The total energy lost from

the cavity is,

$$P_{\text{tot}} = P_{\text{wall}} + P_e + P_t \,, \tag{4.3}$$

where P_e is the power the leaves through the power coupler and P_t the power that leaves through the transmitted power probe. We have designed our transmitted power probe such that this loss is negligible compared to the other two and it will be ignored. The loaded quality factor is given by,

$$\frac{1}{Q_L} = \frac{1}{Q_0} + \frac{1}{Q_e} \,, \tag{4.4}$$

where Q_e is called the external quality factor and is given by,

$$Q_e = \frac{2\pi f_0 U}{P_e} \,, \tag{4.5}$$

In our effort to determine Q_0 we introduce, β, the coupling constant. β is given by,

$$\beta = \frac{Q_0}{Q_e} \,, \tag{4.6}$$

We use two methods to measure β which we will refer to as β_r and β_e. β_r is determined from forward and reverse powers while the cavity is fully charged [PKH98],

$$\beta_r = \frac{1 \pm \sqrt{\frac{P_r}{P_f}}}{1 \mp \sqrt{\frac{P_r}{P_f}}} \,, \tag{4.7}$$

where the top sign is used if $P_f < P_e$ and the bottom sign if $P_f > P_e$. β_e is determined from the forward and emitted powers [PKH98],

$$\beta_e = \frac{1}{2\sqrt{\frac{P_f}{P_e} - 1}} , \tag{4.8}$$

In both of these cases we want to know what P_e is while the cavity is fully charged. To measure P_e we use the reverse power immediately after the forward power is turned off. When the forward power is turned off the reflected power becomes zero. Due to the finite turn-off time of the forward power, and the time between digital samples on the power meters, this will always be an estimate, however, with modern RF equipment the change in P_e should be negligible. By measuring β in two different ways we can spot issues in the system by looking at their difference. We use an average of β_r and β_e for the final value.

We can then calculate the intrinsic quality factor of the cavity,

$$Q_0 = Q_L(1 + \beta) , \tag{4.9}$$

To calculate the accelerating we will first calculate the dissipated power on the cavity walls,

$$P_{\text{wall}} = \frac{4\beta}{(1 + \beta)^2} P_f , \tag{4.10}$$

and the energy in the cavity,

$$U_0 = \frac{Q_0 P_{\text{wall}}}{2\pi f_0} , \tag{4.11}$$

With the energy known we can use the cavity parameters, $[E_{\text{pk}}/\sqrt{U}]$ and $[E_{\text{pk}}/E_{\text{acc}}]$ listed in table 2.1. This value of E_{acc} (and Q_0) is specifically for the fully charged cavity.

There is one aspect we have passed over. The above calculations assume that Q_L is independent of the energy in the cavity–independent of the magnetic field, H. We know that this is not true since Q_0 can vary with H. However, if Q_0 varies slowly then Q_0 is roughly constantly for the first few points immediately after the power is turned off. Conducting these measurements then becomes a balance of using more points/time to reduce noise in the measurement, but not so many that the non-constancy of Q_0 becomes an issue. Fortunately, in this work Q_0 varies relatively slowly with field and this is not a significant source of error.

Once one good measurement Q_0 is made then Q_e can be determined. Q_e is independent of H and can be used to determine Q_0 and β all field levels[7]. Similarly, using one measurement we can calibrate the P_t port which has the relationship,

$$P_t = \alpha U \ , \tag{4.12}$$

where α is the calibration constant to be determined. Using these values, we can calculate Q_0 and E_{acc} for the entire measured decay curve. We refer to this as continuous Q vs E (as opposed to only using the single point when the cavity is fully charge) and it is detailed in [Hal17].

[7] We use adjustable couplers/antennas that can be move in and out of the cavity, changing Q_e. Q_e must be determined again after the coupler is moved.

4.5.2 Frequency Versus Temperature

One parameter we are interested in extracting is the penetration depth, λ, of cavity. This cannot be measured directly, however, the penetration is a function of temperature, and we can measure the change in penetration depth versus temperature from which useful superconducting parameters can be extraction.

When the penetration depth of the cavity wall changes, the effective size of the cavity changes. This causes the frequency of the cavity to change. Since the change is small it can be calculated perturbatively using Slater's Theorem [Cio04, Hal70a, Sla50],

$$\Delta f \approx -\frac{\mu_0 \pi f_0^2}{G} \Delta\lambda \,, \tag{4.13}$$

where G is the geometry factor familiar to us from chapter 2. Thus we can determine the change in penetration depth by measure the frequency vs temperature, f vs T.

Measuring f vs T is relatively easy. A Network Analyzer (NA) is attached across the cavity and the transmission from the forward power port to the transmitted power port is measured (and cables leading to the pit). The NA sweeps over frequencies. There will only be transmission when the output of the NA is close to the cavity resonance. The cavity is warmed up to T_c while the NA tracks the frequency, and both the temperature and resonance frequency are recorded.

Changes in pressure in the cryostat can also change the shape of the cavity and the resonance frequency (similarly, so can changes in temperature but thermal expansion is negligible at cryogenic temperatures). We only use the portion

of the f vs T above 4.2 K where the pressure change is small. The portion of the measurement below 4.2 K sees large changes in pressure since evaporative cooling is used. If needed, we use a small section of the low temperature curve (where λ barely changes but the pressure changes greatly) to create a pressure-frequency (df/dp) calibration and use this to correct the high temperature data.

4.5.3 Trapped Magnetic Flux

Measuring the trapped magnetic flux in the cavity is important for determining its contribution to the residual resistance. Our system for measuring the trapped magnetic field is similar to [M$^+$15]. When the cavity goes through the superconducting transition some magnetic field will be expelled (including the possibility of no expulsion). The value on the magnetic field sensors will change from B_{NC} before transition to B_{SC} after the transition. The trapped magnetic field, B_{trap}, can be calculated as [M$^+$15],

$$B_{\mathrm{trap}} = B_{\mathrm{NC}} + \frac{(B_{\mathrm{SC}} - B_{\mathrm{NC}})}{\alpha_{\mathrm{PD}}} , \tag{4.14}$$

where α_{PD} is a factor determining how much of the change is seen by the fluxgate based on its geometric position[8].

The value of α_{PD} has been calculated using CST Studio. A Helmholtz coil is simulated, and the magnetic field distribution found. A cavity is then placed in the Helmholtz coil. The cavity is modeled as a (near[9]) perfect diamagnet. A

[8]Note that all magnetic field values used in the above equation should be the magnitude/absolute value. If the direction of the magnetic field flips when going through the transition, then there are additional problems involved and this equation is not appropriate.

[9]$\mu_r = 0.0000001$.

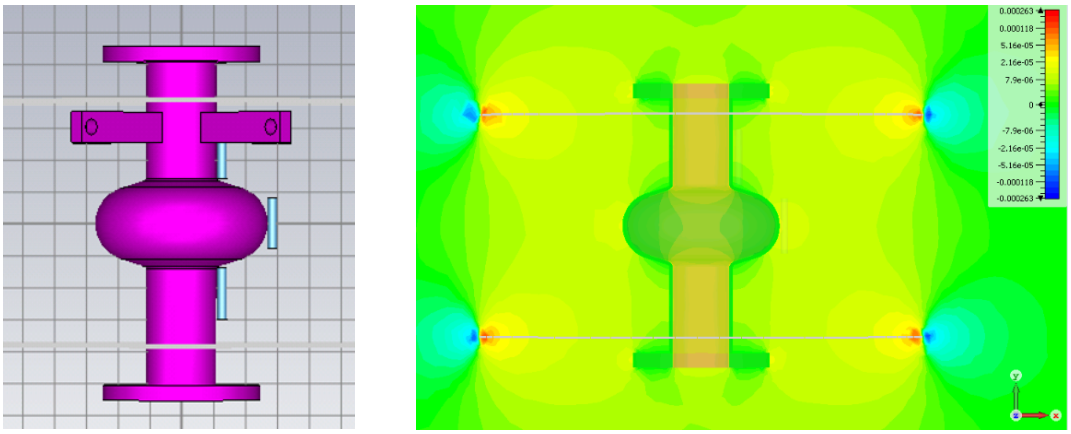

(a) (b)

Figure 4.6: a) Geometry of a 2.6 GHz cavity used in a CST Studio simulation of magnetic flux expulsion. Note the small blue cylinders on the left side: these are simulated Fluxgate Magnetometers. The magnetic field is integrated over a small active region within these to determine the trapped flux measurement. b) The simulated field strength along the y-axis. The Helmholtz coil is generating a magnetic field and the cavity is a near perfect diamagnet. The plot appears darker in the cavity beam tubes due to the fuchsia cavity also being displayed.

perfect diamagnet will expel all magnetic fields, much like a superconductor. The magnetic field is integrated of over the active area of a magnetic field sensors at location the sensors would sit on the cavity and the measured field is estimated (see Fig. 4.6). Table 4.1 lists the simulated value of α_{PD} for the 1.3 GHz and 2.6 GHz TESLA elliptical cavities used in this work and the magnetic field sensor locations.

	Top Iris	Equator	Bottom Iris
1.3 GHz (LTE)	0.58	-0.68	0.58
2.6 GHz (STE)	0.44	-0.41	0.48

Table 4.1: A table of simulated α_{PD} values for the 1.3 GHz and 2.6 GHz TESLA elliptical used in the Cornell University SRF Nb_3Sn program. The sign change between the irises and the equator reflects that when magnetic field is expelled the reading will go down at the irises but up at the equator. These cavities have tabs used during loading into the Nb_3Sn growth furnace. These create an asymmetry between the two iris measurements.

The values in table 4.1 were tested for the 2.6 GHz cavity geometry during an

RF test. This was done by cooling a cavity through transition in a near 0 (≈ 2 mG) magnetic field then applying a 106 mG external field using a Helmholtz coil. The field strength of the Helmholtz coil was confirmed when the cavity was normal conducting. This provides a measurement of a perfectly expelling cavity. The calculated and real values were different by 0.5 %, 2.7 %, and 1.4 % for the top iris, equator, and bottom iris respectively. This test was done with very careful placement of the magnetic field sensors in order to replicate the model. The simulated values have not been confirmed for 1.3 GHz cavities at the time of writing.

One subtlety is the trapping of magnetic field in the vacuum enclosed by the beam tube of the cavity (not in the material). If the cavity cools from the bottom up, it is likely that all magnetic flux enclosed by the beam tube will remain there. The magnetic flux enclosed by the beam tube does not contribute to the residual resistance[10]. The calculated values assume that magnetic flux remains in the beam tube and that no other magnetic flux is added to it during magnetic field expulsion (this is modeled using a section perfectly magnetized material inside the beam tube). However, depending on how the cavity cools this might not be true. If the bottom flange or the cavity bell cools from the outside towards the inside, then most of the magnetic flux expelled from the superconductor could be pushed into the beam tube vacuum. Cooling dynamics could result in drastically different external magnetic fields and incorrect trapped magnetic flux measurements.

[10]This is not exactly true, but the contribution will be very small [Man20].

4.6 BCS Fitting of Cavity Data

We will now discuss our standard technique for BCS fitting of cavity data. This is important for extracting superconducting parameters of the material. Much of the underlying analysis code was developed by Nicholas Valles and is detailed in [Val13]. The same procedure is roughly followed with two major exceptions: we determine T_c using magnetic flux expulsion measurements and continuous Q vs E measurements are used to get fixed accelerating gradients during for Q vs T fitting. We will detail key parts of the analysis process.

We want to fit out cavity data to a model of superconductivity. We need a more involved calculation of the BCS resistance, and the penetration depth then is discussed in chapter 2. More generally the surface resistance can be written in terms of the temperature, frequency, transition temperature, energy gap, coherence length, London penetration depth, mean free path, and magnetic field as,

$$R = R_{\mathrm{BCS}}(T, f, T_c, \Delta, \xi, \lambda_{\mathrm{Lon}}, l, H) + R_0(H) \,, \tag{4.15}$$

Similarly,

$$\Delta f \sim \Delta\lambda = \lambda(T, f, T_c, \Delta, \xi, \lambda_{\mathrm{Lon}}, l, H) - \lambda_0 \,, \tag{4.16}$$

where λ_0 is a fitting constant. We will fit R vs T and f vs T data to a calculated model to determine superconducting parameters and R_0.

To calculate R_{BCS} and λ we use a code developed by J. Halbritter called

SRIMP [Hal70b]. This code has been adapted into MATLAB. This code calculates the $H = 0$ case of BCS. In chapter 1 we discussed the difficulty of extending BCS surface resistance to non-zero magnetic fields, but also noted that this does not appear to be required for current Nb_3Sn. We will ignore all field dependence in BCS and use this field independent calculation. Since the residual resistance is magnetic field dependent, we will conduct our BCS fits at fixed accelerating gradients and do an independent fit for every accelerating gradient of interest.

We have a total of 7 undetermined variables in equations 4.15 and 4.16. This is too many to reliably fit and we must acquire some of them from other places. We get T_c from magnetic flux expulsion measurements. For ξ and λ_{Lon} we use values from literature that are listed in table 3.1 (for Nb_3Sn). This leaves 4 unknown variables to fit for.

We use R vs T and f vs T data to fit two unknown variables each: Δ and R_0; and l and λ_0 respectively. We then use MATLAB's fminsearch function [fmi] to minimize the error functions for both the surface resistance[11],

$$\text{RSS}_{\text{R}}(\Delta, R_0) = \sum_T \left[\log\left(R_{\text{data}}\right) - \log\left(R_{\text{BCS}}(T, \Delta) + R_0\right)\right]^2 \ , \tag{4.17}$$

and the penetration depth,

$$\text{RSS}_{\lambda}(l, \lambda) = \sum_T \left[\log\left(\Delta\lambda_{\text{data}} + \lambda_0\right) - \log\left(\lambda_{\text{BCS}}(T, f(T), l)\right)\right]^2 \ . \tag{4.18}$$

When writing out the error functions we have dropped dependence on the vari-

[11] A logarithm is used in the resistance fit to increase sensitivity to the low temperature resistance. The logarithm is used in the penetration depth fit to match historic fitting algorithms used by the Cornell SRF group. It does not serve a purpose known to the author.

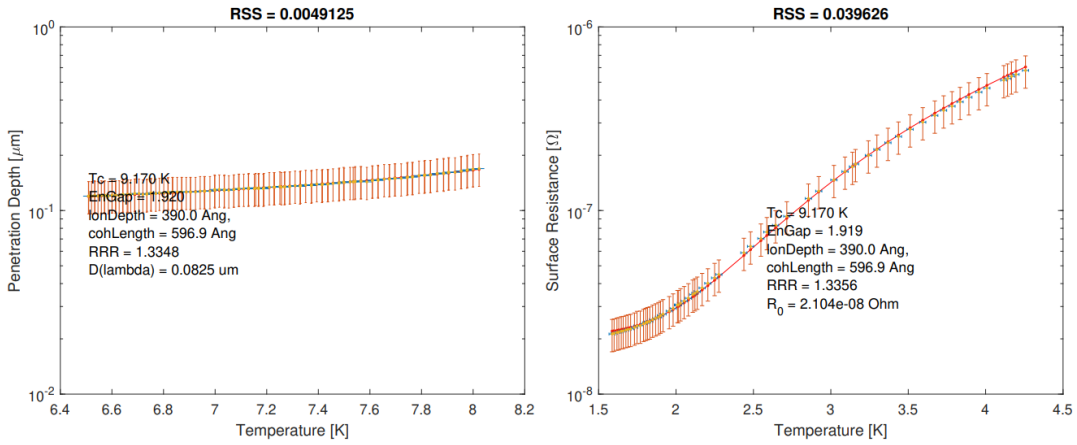

Figure 4.7: An example of SRIMP fitting curve on a niobium RF data. The points are measured data and the lines are theoretical. The λ vs T is being fit on the left and R vs T on the right. This figure was adapted from [Man20].

ables fit using the other error function. This is to make them easier to read. They still depend on the variables fit in the other equation.

We conduct the fits iteratively. We start with reasonable guesses for the unknown parameters. We first fit the R vs T data and extract the parameters. We then use this new parameter set to fit the f vs T data. We continue in this fashion until RSS functions are below a certain threshold. Figure 4.7 shows an example final fit from a niobium cavity. This process is then repeated for all accelerating gradients we are interested in.

CHAPTER 5

HIGH-SPEED TEMPERATURE MAPPING

We have developed a new temperature mapping system to aid in understanding the quench mechanism of Nb_3Sn and other cavities. In short, we have created new data acquisition electronics to allow the acquisition of temperature maps at up to 50 ksps, allowing for never before achieved measurements of dynamic heating. In this chapter, we discuss the development of this equipment. We start with an introduction to temperature mapping of SRF cavities, motivate the creation of a new system, detail the new system, and characterize the systems performance. In chapter 8 we will show preliminary results from Nb_3Sn cavities taken during the commissioning of this equipment that have scientifically interesting implications.

This new system was developed in conjunction with many others. The former graduate student N. Banerjee made large contributions to this system–particularly in overhauling the firmware used on the data acquisition electronics and characterizing electronic noise–and we acknowledge him here. Development of this system is also detailed in N. Banerjee's Ph.D. dissertation [Ban20].

5.1 Temperature Mapping

Temperature mapping (T-mapping) is a useful tool in understanding Superconducting Radiofrequency (SRF) cavity performance and limitations [PKH98]. This diagnostic technique involves placing numerous thermometers (often 100's) on the outside of an SRF cavity and measuring the heating of the outer cavity wall during operation. Figure 5.1 shows a partially disassembled T-map

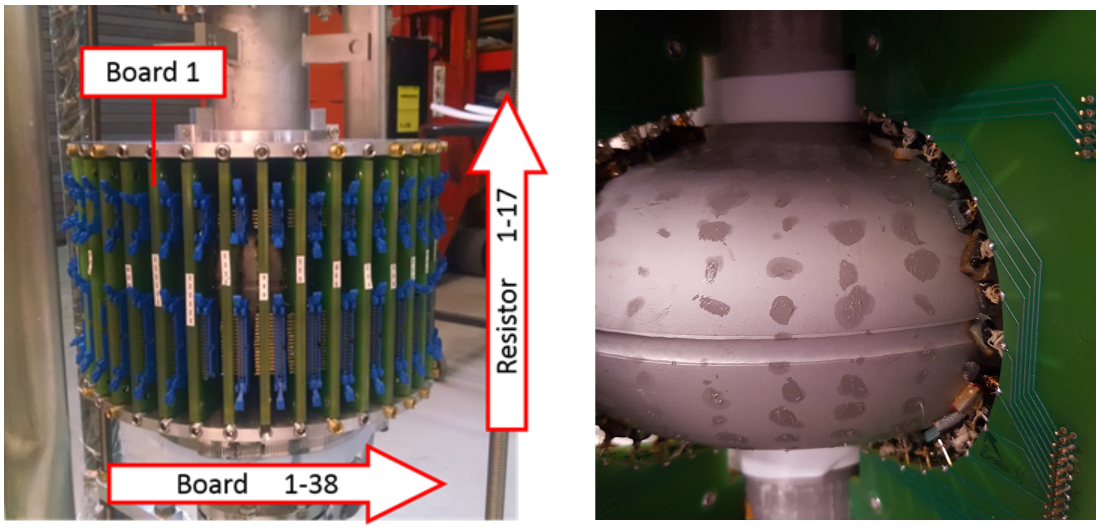

(a) (b)

Figure 5.1: Pictures of the Cornell 1.3 GHz single-cell T-map. a) The 1.3 GHz temperature map attached to a single cell cavity. Twisted pair ribbon cables have not yet been connected. b) Partially removed T-map boards showing location of sensors on cavity.

on a Nb_3Sn cavity. Areas of increased temperature can reveal the location of cavity quench or areas of increased resistance that lowers the cavities quality factor. These locations can then be investigated to determine what is responsible through optical inspection or microscopy of cavity cutouts. In addition, temperature maps can reveal important information about the quench source or even identify the problem without subsequent measurements: the heating distribution can indicate the quench culprit. The heating signature of many problems in SRF cavities are well known and documented [Kno97, PKH98]. The understanding that temperature maps provide helps overcome limitations in SRF cavities.

Temperature maps are usually displayed as a heat map of the cavity. Figure 5.2 show two example maps: a temperature map and a quench map. The maps are read like maps of the world. The top and the bottom are the irises of the cav-

ity, and the equator runs horizontally across the middle. Each square on the plot represents a single temperature sensor. White squares represent malfunctioning sensors. Historically, temperature maps usually show the increase in temperature of a sensor while the cavity is in a steady state (in terms of field), while 'quench maps' show the integrated temperature while the cavity is quenched many times in succession.

Temperature mapping of SRF cavities can be traced back to the 1980's when Cornell University developed a temperature map for a 1.5 GHz cylindrical pillbox cavity [KMR87]. Subsequently, Cornell and other institutions developed temperature maps for elliptical cavities and other geometries [Kno97, PGH+12, S+95, CBC+07]. Temperature mapping has become a key tool in SRF and new systems continue to be developed [CHPS09, KAK+18].

5.1.1 The Cornell SRF Group Temperature Mapping System

Cornell University's current temperature mapping system was largely developed during the 1990's. Jens Knobloch's Ph.D. dissertation details the creation of a 1.5 GHz cavity T-map at Cornell and includes details on the thermometer design [Kno97]. Subsequently, the 1.3 GHz T-map we use here was created [PGH+12]. This 1.3 GHz T-map differs only in the shape so that it fits the TESLA elliptical cavity geometry, and the removal of thermometers on the cavity beam tube. The remainder of the system has not been changed–with the exception of the new data acquisition electronics that we are detailing in this chapter.

The temperature map consists of 38 printed circuit boards fitted vertically

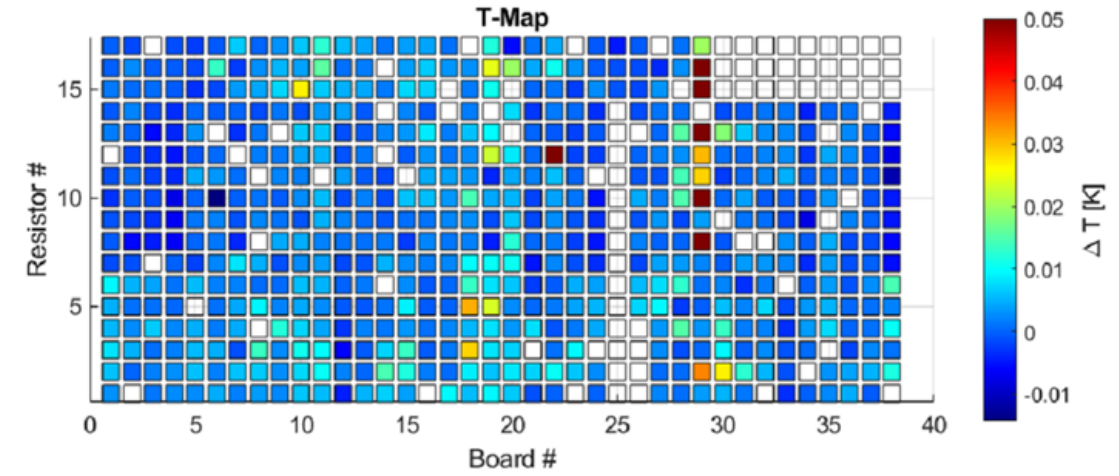

(a) A temperature map of a Nb_3Sn cavity with field emitter. The field emitter is indicated by the vertical line of heating seen in the upper right. White squares indicate non-functional thermometers.

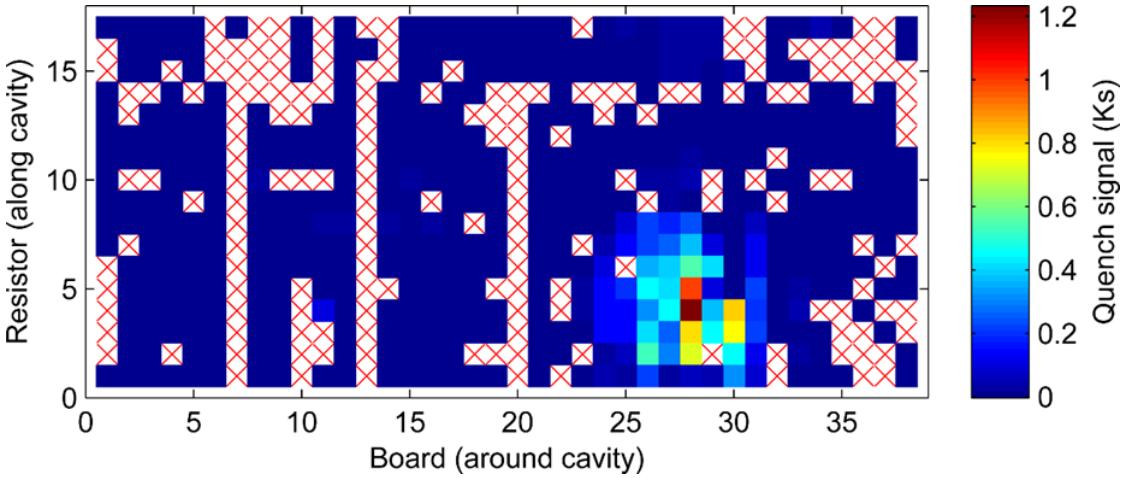

(b) A quench map of a Nb_3Sn cavity taken with the old temperature mapping system [H+17a, Hal17]. The hot spot in the lower right indicates a localized thermal quench. Quench maps are acquired by allowing the cavity to quench many times and slowly measuring each sensor so that several quenches are measured on each channel. Places that are on average hotter are likely the quench site. The plot is displayed as integrated temperature. White squares with red x's indicate non-functional thermometers. This figure was adapted from [Hal17].

Figure 5.2: Example temperature maps. These maps are read like a map of the world. The horizontal middle line is the equator of the cavity, and the top and bottom are the irises of the cavity.

around the cavity (see Fig. 5.1a). Each board holds 17 thermometers. The board is shaped so that the thermometers are pressed flat against the cavity and spaced from iris to iris (see Fig. 5.1b). In addition, 3 boards have a bath a thermometer mounted on the side of the board that does not touch the cavity wall. These serve to measures the helium bath temperature. A small amount of thermal grease (Apiezon N-type) is applied to the thermometers and the boards are pressed against the cavity. Each thermometer is mounted on a springed pogo stick so that the contact against the cavity wall is maintained and a relatively fixed and equal force is applied on all thermometers. Each thermometer is connected to the printed circuit board by manganin wires.

The thermometers on the T-map are made in house. Off the shelf cryogenic thermometers are prohibitively expensive for creating a T-map. We create thermometers using Allen-Bradley carbon resistors, as do most T-mapping systems [Kno97]. The resistance of Allen-Bradley carbon resistors depends strongly on temperature when used at cryogenic temperatures. Typical Allen-Bradley resistors used in our T-map have a temperature dependence of $5 - 10\,\Omega/\mathrm{mK}$ at 2 K. Allen-Bradley carbon make excellent and relatively affordable cryogenic thermometers.

We modify the resistors to create our thermometers. These sensors come in a barrel casing. Part of the casing is filed off on the side that faces the cavity wall. This improves the sensitivity of the sensor to the cavity wall temperature. Additionally, the sensor is surrounded in a G10 housing and Stycast to provide physical support and to shield the sensor from the helium bath. A diagram of one sensor is shown in Fig. 5.3.

To measure the temperature, we must measure the voltage drop/resistance

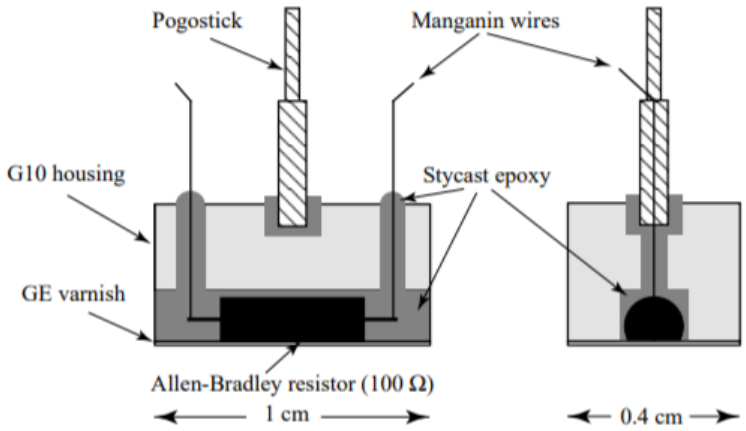

Figure 5.3: Diagram of a T-map thermometer. This figure was adapted from [Kno97].

of these sensors and then convert this to temperature. To this a calibration curve must be made using a well calibrated cryogenic sensor. For calibration we use the same Lakeshore Cryotronics Cernox®brand thermometers we use for standard RF cavity testing. We will discuss calibration in more detail in section 5.3.

The thermometers are read by Data Acquisition (DAQ) electronics located outside of the cryostat. The T-map is connected to the DAQ by twisted pair ribbon cables that transition from the cold cryostat to the outside temperature. Figure 5.4 shows an SRF cavity with T-map and ribbon cables before being lowered into the cryostat. In the most basic description, the DAQ electronics consist of a constant current source and an analogue to digital converter (ADC) to read the voltage across the thermometer (and cables). In the data acquisition electronics a $\sim$ 1 MΩ and high-stability voltage supply (at 5 V) are used to create a

simple constant current source. The voltage drop across the cavity is amplified and read by an ADC with a 25 ksps sample rate.

Due to the cost of high-quality amplifiers and ADCs in the late 1990's–when the DAQ system was made–there are only two ADCs in the entire DAQ system. These ADCs are multiplexed to all the sensors in the T-map to read them out (each ADC is responsible for roughly half the T-map). This means that though the individual ADC used is fast, it takes several minutes to read out the entire temperature map and the sensors are not read in parallel.

5.1.2 Motivation for Dynamic Measurements

As discussed above, current temperature mapping systems take several minutes to read out the temperature of the entire array. This makes the systems effectively capable of only taking long exposure pictures and they cannot resolve dynamic effects. However, many SRF cavity processes are dynamic: charging a cavity takes ~ 1 s and cavity quench takes place on time-scale of $0.1 - 10$ ms. Other cavity processes–such as multipacting and field emission–may have dynamic components that have never been measured.

Of particular interest to us in this work is the demonstration of dynamic heating in Nb_3Sn cavities in [H$^+$17a, Hal17]. In this work, D. L. Hall *et. al.* used the Cornell SRF T-map to measure a single sensor at a time at a 25 ksps sampling rate. When this was done at the apparent quench site of the cavity interesting dynamic heating was seen. Sudden, fast temperature jumps were observed at the quench site. These jumps occurred close to the cavities quench field but without the cavity quenching. Figure 5.5 shows the temperature of the

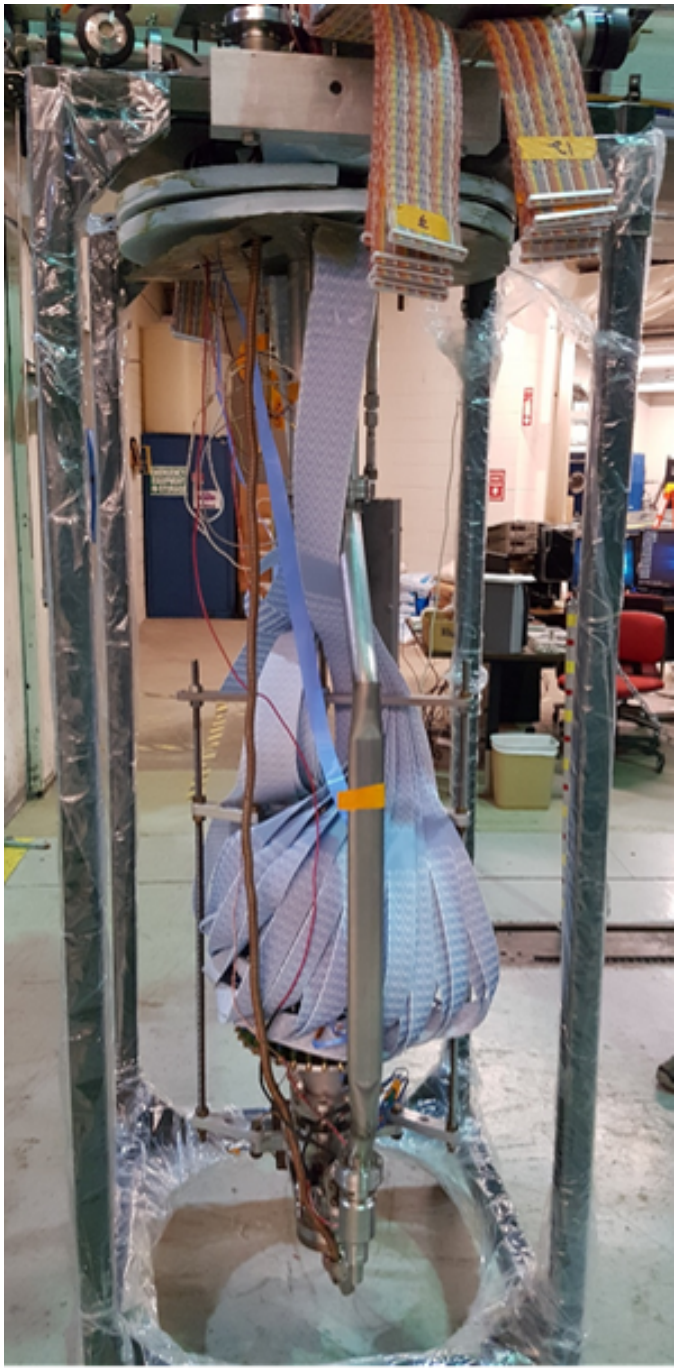

Figure 5.4: A SRF cavity on a test insert with temperature map attached. The cavity itself is obscured by the T-map and associated ribbon cables.

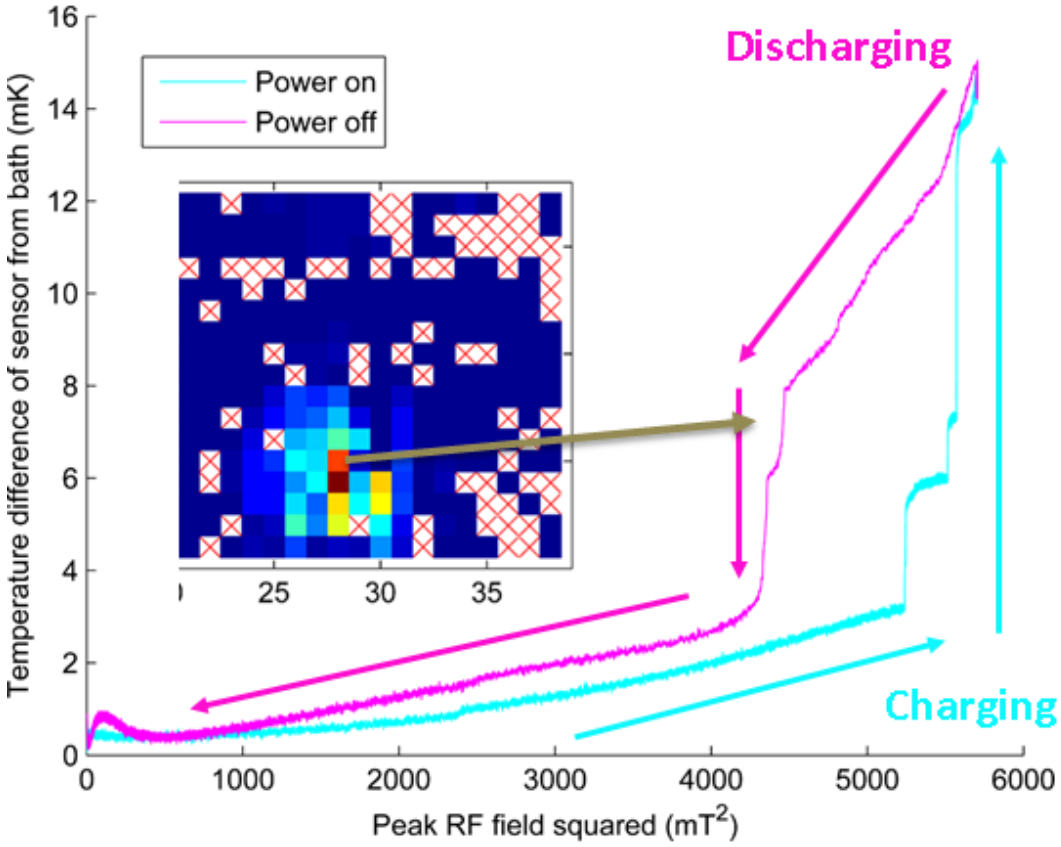

Figure 5.5: The temperature versus the B_{pk}^2 at the cavity quench site as the field is raised and lowered. The temperature suddenly jumps up as the cavity charges. During the discharge cycle the same dynamics are seen but with a hysteresis. The inset is from 5.2b and highlights the location of the measurement. This figure was adapted from [Hal17].

thermometer on/near the quench site as the field rises and falls. It is speculated that these dynamic events are related to Nb_3Sn cavity quench.

Measuring dynamic processes may provide key insights into the cause of quench in Nb_3Sn (and other materials) cavities or other performance problems in SRF cavities. Though we can measure a single sensor at 25 ksps at a time with the old DAQ system, it is a slow process and most of the cavity cannot be measured. Any evolution during cavity quench could not be captured. To truly observe dynamic processes in SRF cavities we needed a new data acquisition

system.

5.2 The New Data Acquisition System

We have developed[1] new DAQ electronics that have a dedicated ADC for each thermometer and can read the entire temperature map at 50 ksps. This allows for the measurement of dynamic effects and is sufficiently fast to measure the evolution of quench in SRF cavities. In addition, the new systems achieves very low noise in its measurement, as low as 15 µK depending on the mode of operation. The old system could–at best–achieve 1 mK resolution in a temperature map. Reading out helium bath temperature and cavity wall temperature simultaneously also allows for the correction of any helium bath temperature drifts during the measurement. We will discuss more specifics of the hardware.

There are 23 DAQ boards (can be scaled up or down) in two crates. Each DAQ board can measure 32 channels/thermometers. This gives 732 channels connected to 649 thermometers. Due to the pre-existing wiring, 83 channels are not connected to thermometers.

Each crate contains one leader board and 10/11 follower boards. A backplane in each crate provides power and the thermometer bias voltage to the boards and contains several interconnects (principally trigger and ADC clock synchronization). The leader board is responsible for sending a trigger signal to each board in the crate. The leader board can be triggered through ethernet, or

[1]The new data acquisition electronics were designed by the CLASSE electronics shops to meet pre-determined specifications. Firmware/on board software was developed by the CLASSE electronics shop, N. Banerjee, and R. D. Porter [Ban20]. PC-side data acquisition and control software was developed by R. D. Porter, N. Banerjee, M. Tao, and S. Halls [TPL19, HPL18].

through an external BNC connection. In addition, the leader board in Crate 1 sends a trigger signal to the leader board in Crate 2, ensuring both crates trigger simultaneously.

Each DAQ board contains a Mars ZX2 SoC module (combined FPGA and Programmable System/CPU module), 4 Analog Acquisition (daughter) Boards, ethernet connection, and additional ports for control and diagnostics. A picture of a DAQ board is shown in Fig. 5.6. The Mars ZX2 SoC module runs embedded Linux and is responsible for accepting outside commands, configuring the system, running data acquisition, and writing data to external storage. Each analog acquisition boards collects data from 8 channels/thermometers and contains an Programable Gain Instrumentation Amplifier (PGIA), a fixed Differential Amplifier (DA) (gain = - 5), and an ADC (24-bit, 144 kHz). Voltage signals from thermometers enters the PGIA where (configurable) gain and voltage offsets are applied, it then goes through the fixed amplifier and is then digitized in the ADC.

The software and firmware architecture for the data acquisition system has three layers. The first layer consists of programable logic in the FPGA. This layer is responsible for controlling the ADCs to acquire data at the requested rate and store it into a fast Block RAM buffer. This buffer is small and can only hold 2048 points from each channel. It must be emptied quickly to prevent data from being overwritten. The second layer of firmware runs on the Programmable System and is responsible for moving data from the buffer to DDR3 RAM in the Mars ZX2 SoC module. Currently, the maximum data acquisition rate is set at 50 ksps and gives the programmable system sufficient time to transfer the data. The maximum acquisition time is limited by the DDR3 RAM storage to ≈ 60 s when

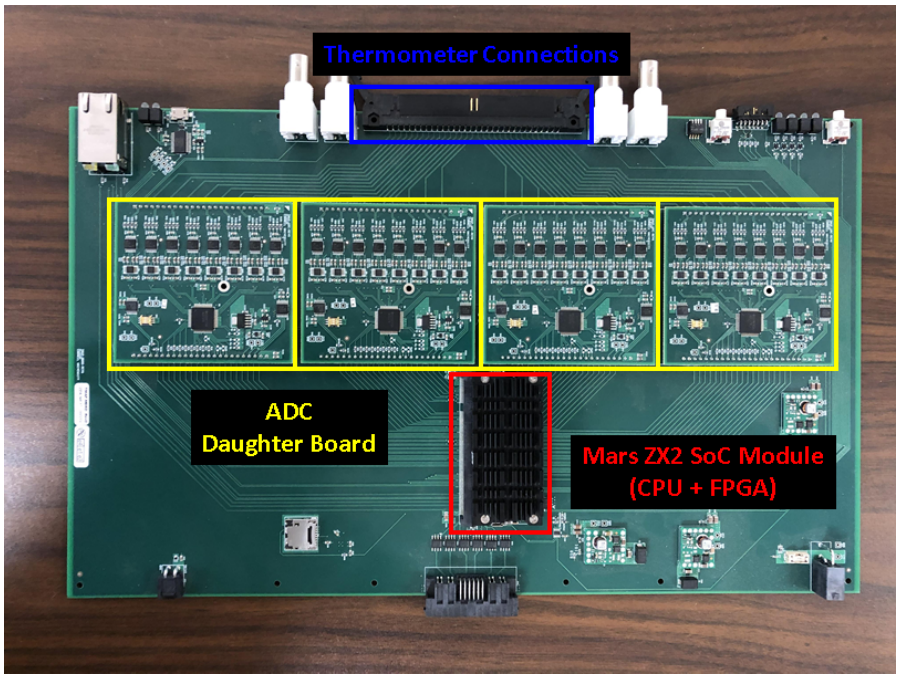

Figure 5.6: A picture of one of the new data acquisition boards. The connection to the thermometers, the ADC daughter board modules, and the MARS 2X2 SoC Module are highlighted.

running at 50 ksps. After data acquisition is complete the data is transferred to a network drive location via ethernet. The final level is client software written in MATLAB and running on a PC. This system transfers user commands to the DAQ boards.

An additional configuration step is run to synchronize the clocks of each individual ADC. Each ADC has an internal clock that determines when it will take its first measurement. Offsets between these clocks cause the measurements to start at slightly different times. To correct for this the leader board in crate one sends out a timing signal to all ADCs. The acquisition time windows are aligned using a special aperture trigger. This aligns the ADC clock to sample at the same time. After this is done the maximum offset between triggers is 20 ns, which is determined by the distance the signals have to travel. The offset is much less

than the minimum sample time of 20 µs [Ban20].

The overall setup of the temperature mapping system is shown in Fig. 5.7. Two crates of data acquisition boards sit on the warm side of the system. The DAQ boards are connected to the T-map by twisted pair ribbon cables. Cernox sensors, fluxgate magnetometers, and all standard equipment for RF testing is also connected. The T-map DAQ boards are connected to the trigger output of the RF power meters allowing simultaneous triggering and recording of RF data and temperature data.

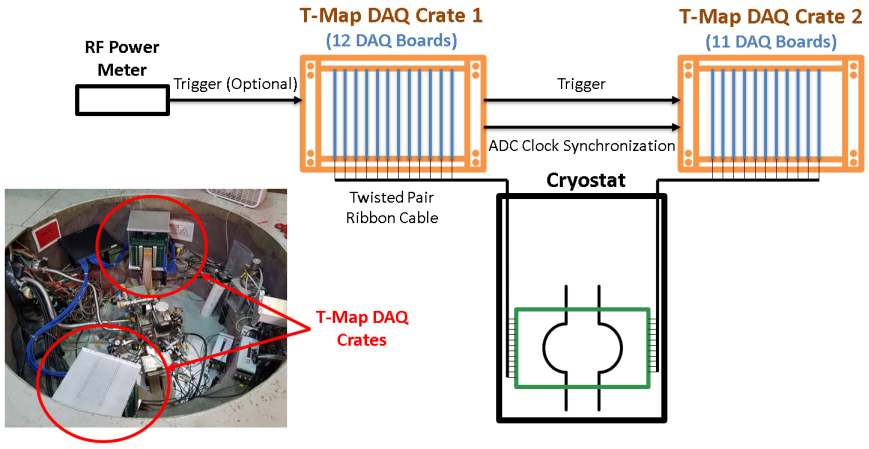

Figure 5.7: Diagram of experimental setup showing connection between T-map, DAQ, and power meters.

5.3 Data Acquisition Process

Here we detail the data acquisition process we are using for the T-map. It consists of three main parts: calibration, RF-off measurement, and RF-on measurements. In addition, we discuss some of the typical data post processing. This information is needed both to understand the T-map results, and to understand noise analysis in the next section. In addition to T-map measurements, we mea-

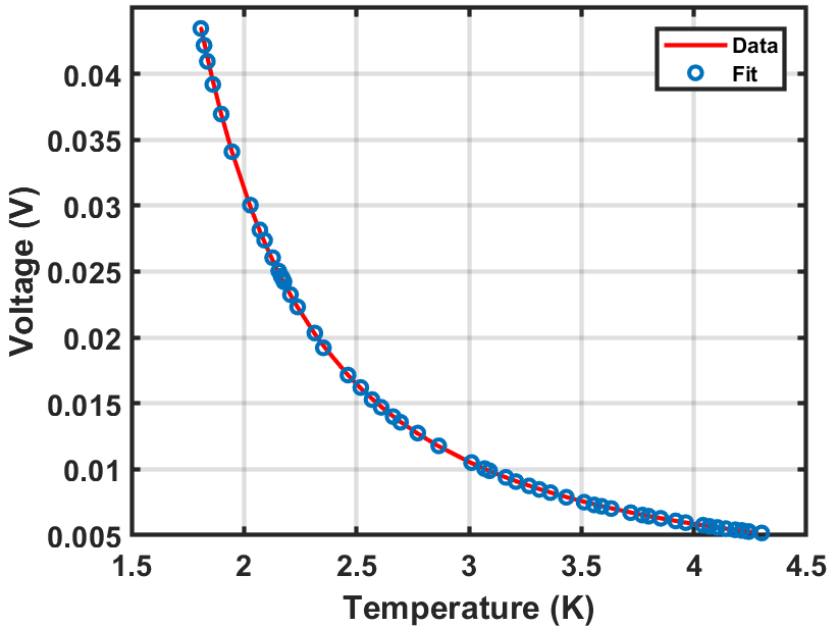

Figure 5.8: Example calibration data for the temperature map. Fit model shown in red.

sure the quality factor vs field and temperature for the cavity during RF testing.

To convert voltage to temperature a calibration curve must be made for each thermometer. The calibration is created by measuring both the T-map (25,000 points each in 1 s) and a calibrated Cernox sensor (at the cavity equator) from 4.2 K (in liquid helium) down to just below the lowest measurement temperature without applying RF to the cavity (at the time of measurement). If the cooldown rate is slow enough there should not be a significant temperature gradient from the top of the T-map to the bottom. These measurements are taken roughly every 0.05 K during the cooldown. The resulting curve is fit to a modified regression model of a semi-metal: $V(T) = V_0 - V_\infty e^{\frac{g}{T}}$ [Ban20, Rv15, SH68]. An example calibration curve and fit is shown in Fig. 5.8. The resistance of these thermometers changes significantly when thermal cycled to room temperature, and they must be calibrated every time the T-map is used.

At desired measurement temperatures two 20 s T-map measurements are taken with the RF power off (RF-off). This serves two purposes. The difference of the two RF-off temperature maps is used to find broken channels: the difference should have a mean close to zero, and some statistical noise (when analyzing time data) on each channel. Channels that lie outside of normal bounds are determined to be faulty. In addition, the RF-off measurements reveal the offset between a T-map sensor and a bath sensor, so the offset can be corrected.

RF-on T-maps are taken with the forward power to the cavity (P_f) on. These can be one of two forms: static or dynamic. For static T-maps the cavity is charged, allowed to reach equilibrium, and a short T-map is taken. This is the equivalent of older T-maps, but our new system can achieve much better temperature resolution (down to 15 µK at 1.8 K). For the dynamic T-maps shown here, the T-map is configured for a long measurement (e.g. 20 s at 25 ksps or 50 ksps) and is configured to measuring when they receive a trigger input signal from the RF power meter (the RF power meters are configured to trigger off a rise in measure forward power). When the power is turned on the power meters and T-map trigger simultaneously and both the RF power and temperature is recorded.

The final temperature map data is calculated as a difference in temperature, ΔT, between the T-map temperature and the bath thermometer. An additional correction is applied that uses the RF-off measurement to correct for the difference between an individual thermometer and the bath thermometers. This helps remove any offsets from the calibration. The final equation is,

$$\Delta T\left(i,j,t\right) = T_{ON}\left(i,j,t\right) - T_{BATH,ON} - \overline{\left(T_{OFF}\left(i,j\right) - T_{BATH,OFF}\right)}\,, \tag{5.1}$$

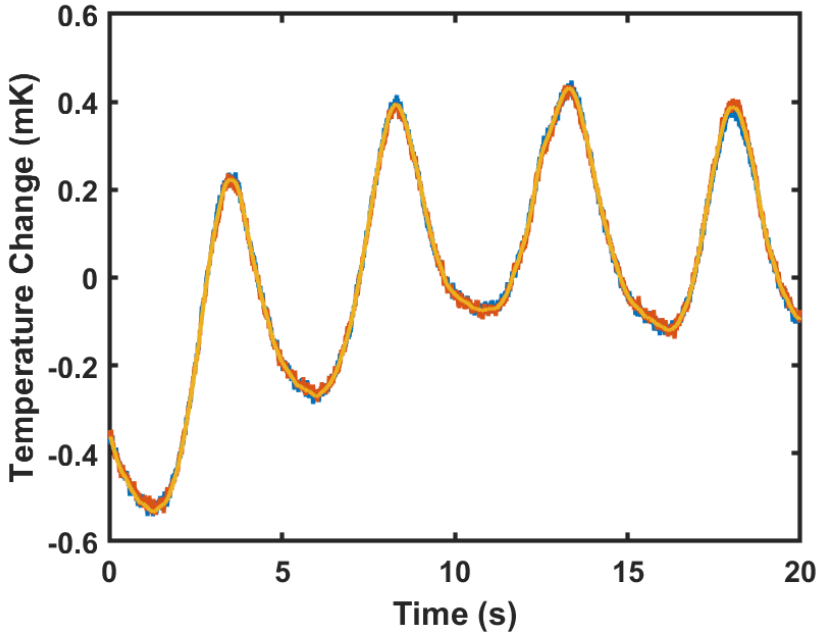

Figure 5.9: Temperature of 3 bath sensors during an T-map acquisition at 1.8 K. Some smoothing has been applied and the mean values were subtracted. Note the 300 µK oscillations caused by the cryogenics system.

Collecting the dynamic temperature on every channel allows us to correct for changes in the bath temperature during the measuring. The importance of this is well demonstrated in Fig. 5.9. There is a control loop in our cryostat that is used at sub atmospheric pressures to keep the temperature constant. A valve in opening and closing to adjust the temperature and pressure, but it cannot do so perfectly. We see a 300 µK oscillation in the temperature in Fig. 5.9 that is caused by this. Without correcting for the bath drift our measurement uncertainty would be much higher.

5.4 Noise and Uncertainty Analysis

An important figure of merit of a temperature mapping system is the measurement uncertainty. If we want to measure low heat phenomena (low field surface resistance, etc.) we need low uncertainties, and some dynamic effects may result in only small changes. There are three main uncertainties in the system that we will consider: measurement noise, calibration uncertainties, and sensor sensitivity to cavity wall temperature. Overall, the noise is low compared to our previous system.

After correction for bath temperature oscillations there are two main sources of noise [Ban20]: 60 Hz noise from outside sources, and noise from the PGIA amplifier and offset. 60 Hz is fairly small in the system and can easily be filtered in the frequency domain if needed. A breakdown of noise from the electronic components is shown in Fig. 5.10. Noise from the PGIA is the most significant source. Since these electronics are on the warm side, the operation temperature makes no difference in the overall noise. The PGIA noise depends on frequency and increases as the sample rate does. In current configuration of the T-map the standard deviation of the noise is $\approx$ 30 µK at 1 ksps, increasing to $\approx$ 150 µK at 50 ksps.

The calibration curve provides another source of error. We have computed standard deviation estimates of our fit values and temperature readings [Ban20]. An example for one thermometer is shown in Fig. 5.11 and is fairly representative of all thermometers. The standard deviation varies with temperature and is $\approx$ 15 µK at 2 K.

The above computation ignores the uncertainty in the Cernox cryogenic

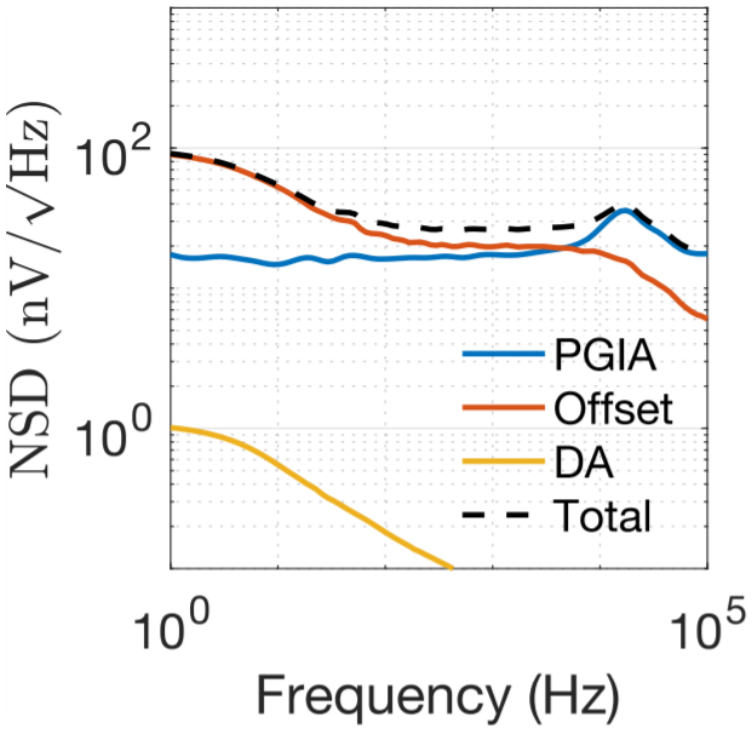

Figure 5.10: Modeled noise contributions of electronic components of the T-map DAQ electronics [Ban20]. The noise is dominated by contributions from the amplifiers. Noise from other components, such as the ADC, are negligible. This figure was originally published in [Ban20].

thermometers used for calibration. The uncertainty on these thermometers is ±4 mK, higher than the uncertainties in many of our measurements. The absolute temperature we record from our thermometers is no more accurate than this uncertainty. We gain an advantage by subtracting two temperature measurements. This will cancel out a large fraction of the uncertainty here that come from these sensors (i.e., precise but not accurate). There will still be an additional small uncertainty that will depend on the difference between temperature readings, but this is difficult to determine without having more accurate cryogenic thermometers. This source of error is likely small compared to 'sensor sensitivity' discussed below.

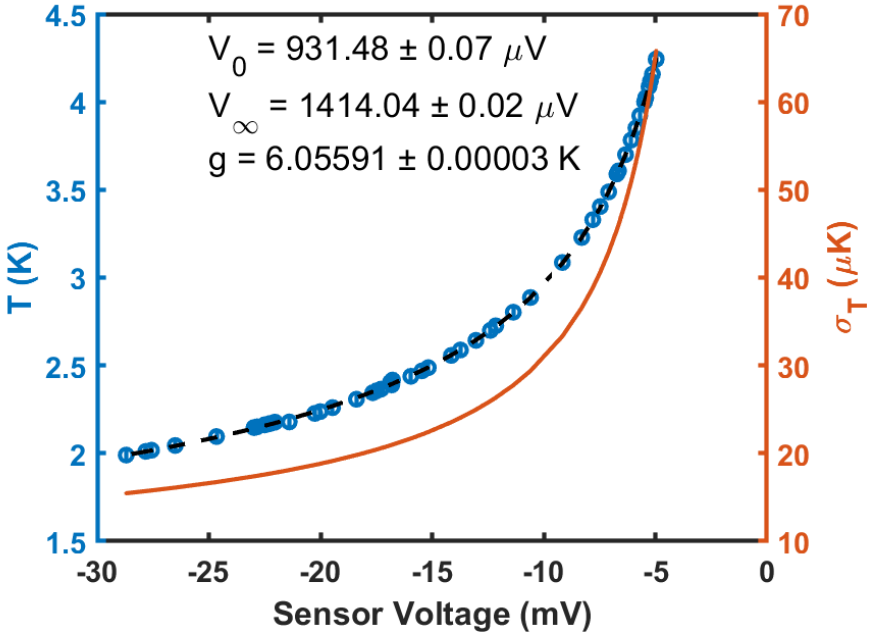

Figure 5.11: Calibration curve and uncertainty of calibration of a T-map thermometer. Originally published in [Ban20].

We can further investigate our uncertainties by taking many measurements of the same thing. Here we take two RF-off measurements (1,000,000 samples per channel at 50 ksps) at nominally the same temperature, subtract them from each other (using equ. 5.1), and analyze the mean and standard deviation of each channel. Figure 5.12 shows the standard deviation and mean values for a pair of RF-off measurements taken at 1.9 K. Ideally, the resulting value would be zero. This gives us an idea of the statistical (mean of standard deviation) and systematic (standard deviation of mean) noise in the system, 154 µK and 14 µK respectively at 1.9 K.

These two measures of uncertainty demonstrate a great improvement in our temperature mapping system. Our old system, when averaging over several measurements could only achieve an uncertainty of $\approx$ 1 mK. With the lower noise electronics and bath oscillation correction we can get the uncertainty

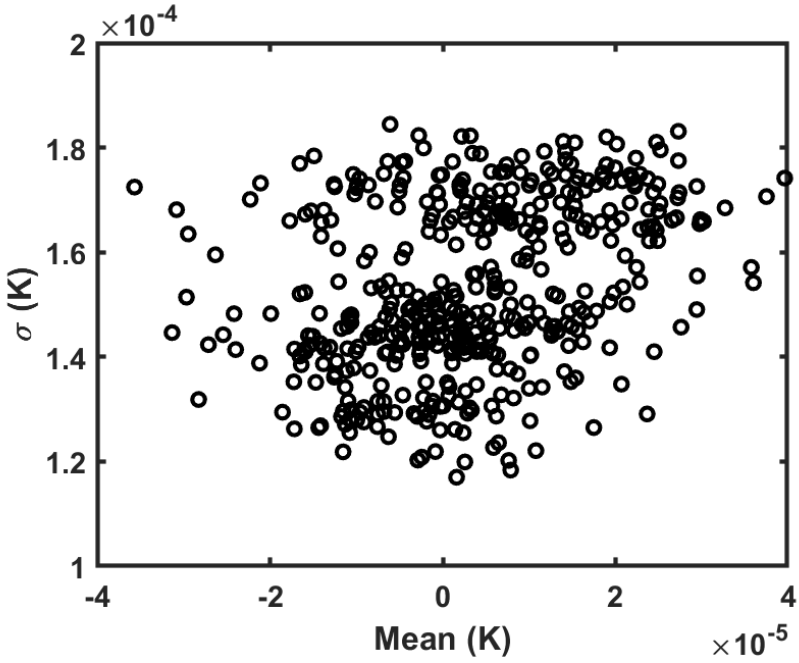

Figure 5.12: A scatter plot of the mean and standard deviation of each thermometers in the T-map at 1.9 K. This is showing the bath temperature corrected difference between two RF-off T-maps, each 1,000,000 points taken at 50 ksps. The mean standard deviation and standard deviation of the mean provide an estimate of the statistical and systematic noise in the system.

down to $\approx 15\,\mu$K after averaging.

There is one more source of uncertainty to consider: sensor sensitivity to cavity wall temperature. When measuring the cavity wall temperature, the thermometer is both being warmed by the cavity wall and cooled by the liquid helium bath. The final temperature of the sensor is somewhere between the wall temperature and the helium bath temperature. We refer to the fraction of the thermometer temperature rise to the real wall temperature rise as the sensitivity. A previous estimate from Cornell found that the sensitivity of one of our sensors is 0.35 ± 0.13 [MK85]. This suggests an additional 37% uncertainty in temperature measurements (ΔT). In addition, many aspects may affect this estimate: quantity and consistency of thermal paste used, Kapitza resistance of cav-

ity wall, and operating temperature could conceivably change the value. This uncertainty is primarily important when comparing temperature rises between thermometers or theoretical models; the low noise still allows us to measure very small changes in temperature on a single sensor.

The cavities measured in this dissertation have a large indent at the equator weld seam that creates poor thermal contact at the equator. This reduces the sensitivity of the sensors at the weld seam. In all the results we show here our equator has zero heating on the scale displayed. In some cases, this is likely because of the poor contact made by equator sensors.

Overall the system is very sensitive to small changes in temperature, managing a statistical uncertainty of $\approx 15\,\mu K$ after averaging in the right conditions. Accurate measurements of the temperature difference are dominated by the sensor sensitivity and should be studied in more detail. Still, the system is a significant improvement, and the high sensitivity will allow it to see small changes that have previously been unmeasurable in addition to the fantastic capability to measure dynamic heating.

5.5 Commissioning Measurements

Now we will present several examples of dynamic temperature map measurements made with this system. These tests were done on Nb_3Sn cavities. Here we demonstrate the capabilities on the T-mapping system while discussing results relevant to the physics of Nb_3Sn in chapter 8. The forward, reflected, and transmitted power were recorded, and the external quality factor were also determined from quality factor measurements.

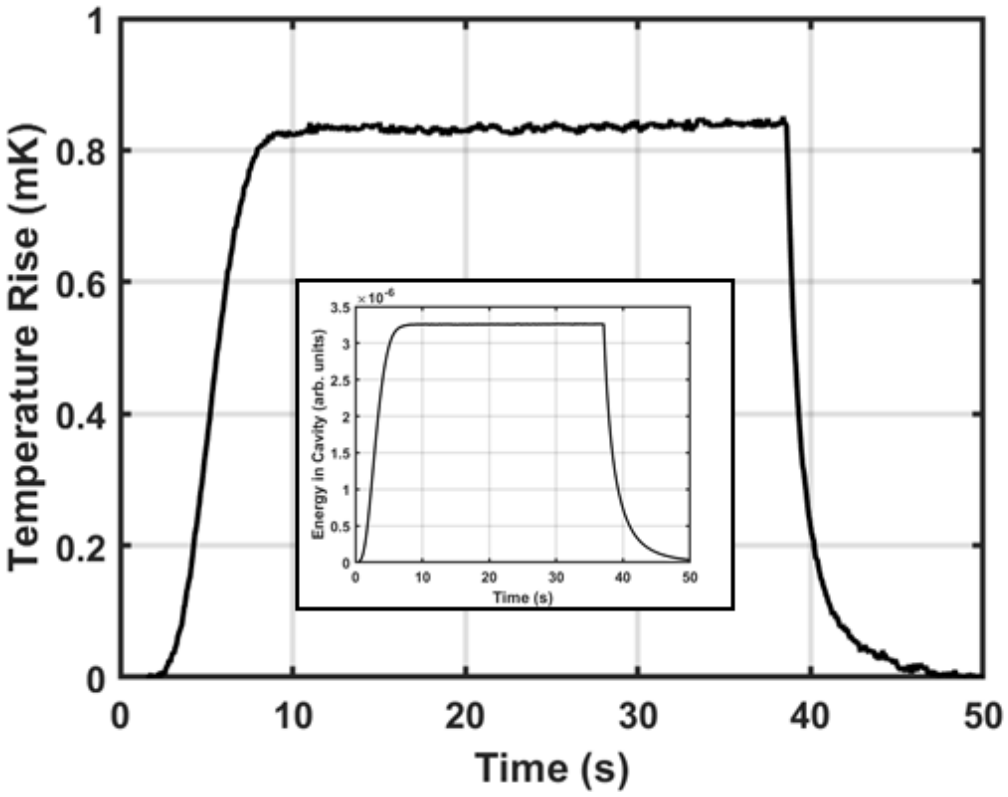

Figure 5.13: Average temperature of all functioning sensors on T-map during a charge-discharge cycle of the cavity. Some smoothing was applied. Inner plot displays the transmitted power with is proportional to the energy in the cavity. Measurement were done at 1.8 K.

5.5.1 Cavity Charge and Discharge

Figure 5.13 shows the average temperature of the entire T-map while the cavity is charged and discharged at 1.8 K. The temperature follows the transmitted power/energy curve of the cavity except for a slow rise in temperature during operation.

To test the accuracy of the T-map we can try to compute the quality factor from the heating data. This can be computed up to a constant that depends on material parameters which depend on the various aspects of the system (sensor

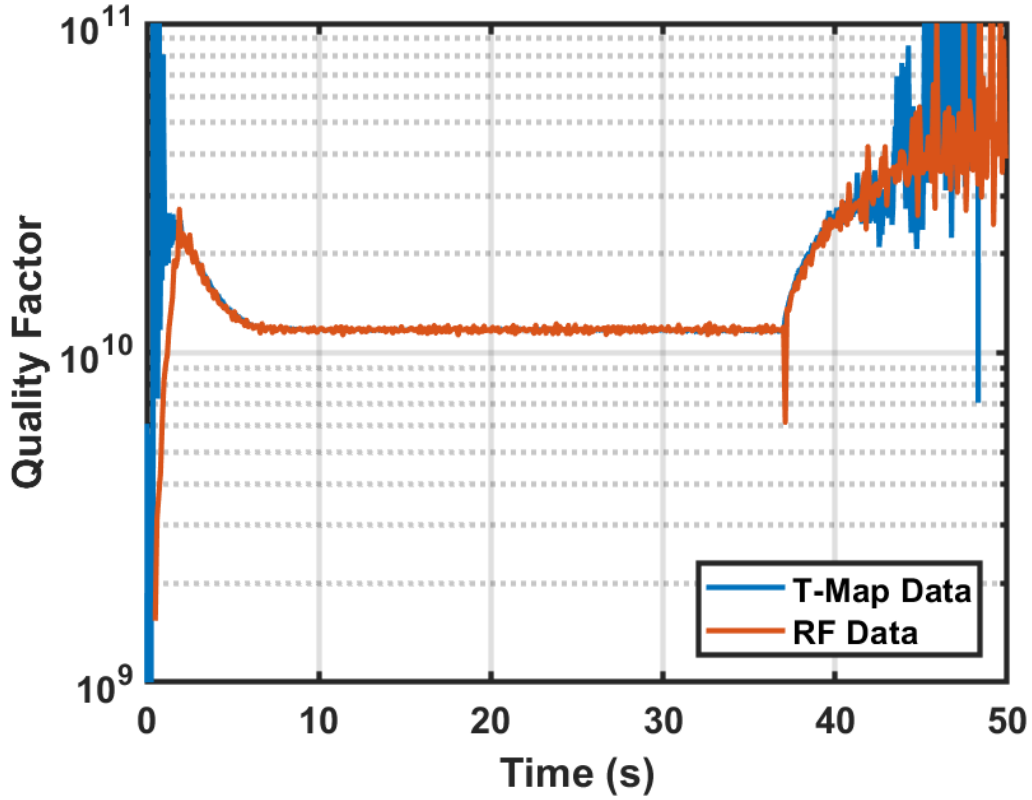

Figure 5.14: The quality factor vs time during the RF power charge-discharge cycle. The quality factor is calculated from recorded RF power data, and again from the wall temperature and transmitted power from the cavity.

sensitivity, Kapitza resistance, and other thermal properties of the cavity). Similarly, we can calculate the quality factor from the RF data. Figure 5.14 shows the quality factor versus time as the cavity is changed and discharged using both the T-map data and the RF data. The quality factor computed from T-map data has been scaled to match the RF data at a single point. This shows very good agreement between the two measurements–they both have the same trend. This gives us confidence that we are measuring the heating/losses of the cavity.

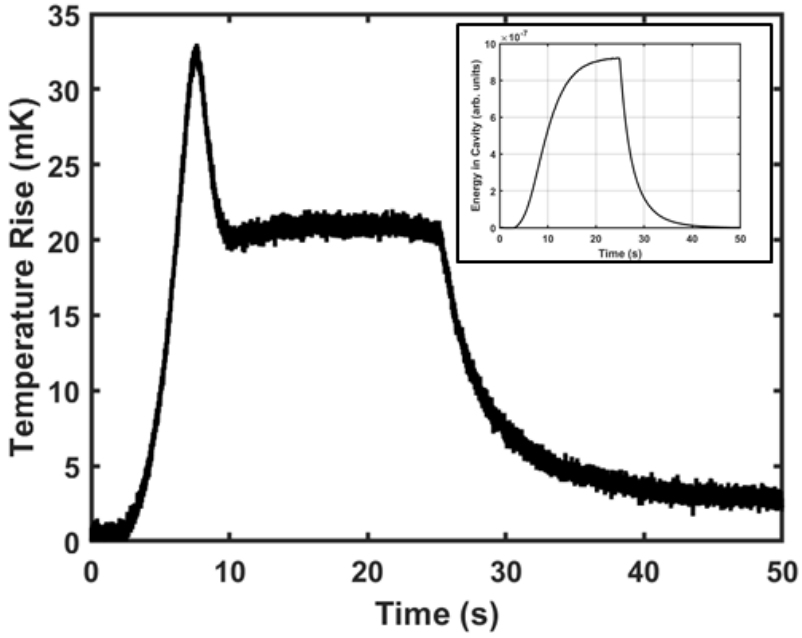

Figure 5.15: The temperature of a T-map thermometer during a charge-discharge cycle of the cavity. Some smoothing applied. The inset displays the transmitted power with is proportional to the energy in the cavity. Measurement done at 4.2 K. Notice that the temperature rises and then suddenly drops.

5.5.2 Temperature Slips

At 4.2 K (or anywhere above the superfluid transition temperature) we see interesting dynamics in the charge-discharge cycles. Figure 5.15 shows the temperature on one thermometer. The temperature rises and then suddenly falls. This appears on every thermometer on the T-map (when above the superfluid transition temperature), but do not occur at the same time, surface field, or local temperature: there is some amount of randomness. We refer to these as temperature slips.

The temperature slips are likely a transition from convection cooling to nucleate film boiling at the liquid helium-Nb_3Sn interface [Lan07]. Figure 5.16a shows a diagram of different steady-state heat flow regimes in non-superfluid

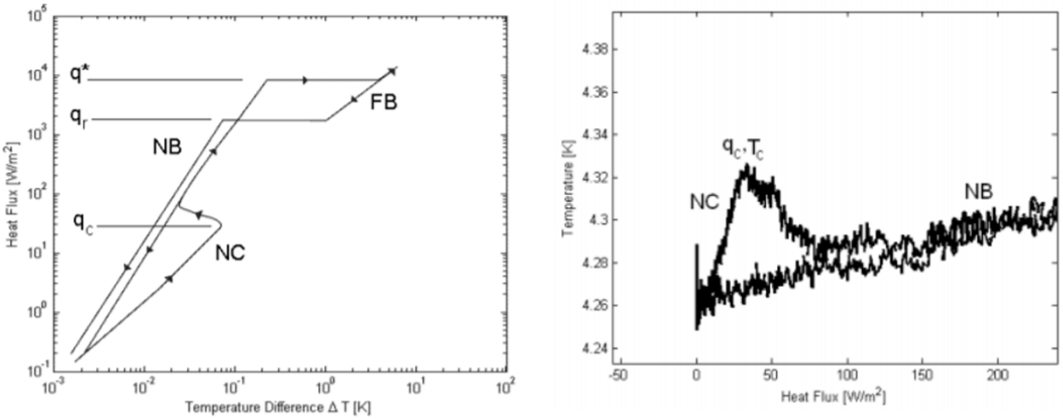

(a) (b)

Figure 5.16: a) Schematic of regions of different steady-state heat flow behaviors versus the heat flow plot. The x-axis shows the elevated temperature of the wall compared to the helium bath. b) The temperature of a heated wire in liquid helium demonstrating the transition from normal convection (NC) to nucleate film boiling (NB) regime. This figure was adapted from [Lan07].

LHe. The low heat flux mode is convection cooling. At slightly higher heat fluxes the system can transition to nucleate film boiling. This substantially improves the interface conductance, cooling the cavity wall more efficiently and resulting in a temperature drop. Much of the conduction cooling area is metastable, explaining the somewhat random timing of the temperature drop. An experiments where metal wires were heated in liquid helium baths show almost identical temperature curves (see Fig. 5.16b) [Lan07].

CHAPTER 6

A HIGH FIELD SAMPLE HOST CAVITY

In chapter 3 we posited that the superheating field of Nb_3Sn is 425 mT based on the calculation in [CS08a]. However, we offered no experimental evidence to support this value. We see that Cornell Nb_3Sn cavities are limited far below this value at $\approx$ 80 mT in Continuous Wave[1] (CW) operation. This begs the simple question: is the theoretical calculation correct? We can explore this using High Pulsed Power (HPP) testing.

We can reach higher quench fields in Nb_3Sn cavities if we use HPP testing. During ordinary CW RF testing the forward power is $\sim$ 1 W and the cavity can take several seconds to fully charge. High pulsed power utilizes forward power $\sim$ 1 MW in short pulses ($\ll$ 1 s). This power is often supplied by klystron [Vel87]–roughly thought of as a giant tube amplifier. The high forward power allows the cavity to be charged very quickly: in μs to ms.

The quick charge time allows cavities to 'outrun' thermal defects/quenches and reach higher fields. If a cavity is quench is caused by a thermal defect–in which a spot is heating up over time and then causing the cavity to quench–there is a time scale for the evolution of this quench. By raising the fields very quickly we can reach higher accelerating gradients before the cavity has a chance to quench off of the defect [Val13, HP97]. If the cavity reaches the superheating H_{SH} then the cavity will instantly quench regardless of the charge time, allowing us to probe the superheating field.

[1] Meaning that the cavities are operated for an extended period of time with a fixed accelerating gradient. This is in opposition to pulsed operation where forward power pulses may be $\sim$ 1 ms.

One limitation of this technique is the minimum time to raise the field in the SRF cavity. As we try to reach higher accelerating gradients the charge time of the cavity will become longer. In addition, as the fields get higher the thermal defect will warm up faster and the time scale of the thermal quench decreases. We will see that high pulsed power testing of Nb_3Sn cavities with our system can attain higher fields, but becomes limited by the charge time of the cavity before H_{SH} can be reached.

To reach higher fields we have designed a cavity that is optimized to quickly charge to large surface magnetic fields on a small sample. This cavity will serve to probe the superheating field of Nb_3Sn and other future SRF materials. This allows H_{SH} to be determined without extensive development to mitigate every possible defect. We call this cavity the Cornell High Pulsed Power Sample Host Cavity (CHPPSHC)–or CHIP cavity for short[2].

In this chapter we will discuss the development of the CHPPSHC. Though we have motivated the creation of this cavity in the context of Nb_3Sn, this new test system will be a useful tool for testing the ultimate field of all future SRF materials. We will start by reviewing high pulsed power measurements of Nb_3Sn cavities to motivate the creation of CHPPSHC and to understand the limitations that must be overcome. We will then discuss the design of the cavity, review key simulations, and discuss expected performance. Finally, we will discuss fabrication and assembly. At the time of writing commissioning and Nb_3Sn tests have not been conducted–these are expected within the next year.

[2]The author also explored the acronym Pulsed Operation Transversally Antisymmetric Thousands of Oersted cavity (POTATO) to create the full name POTATO CHIP, but this was popularly rejected by their research group.

6.1 High Pulsed Power Testing of Nb_3Sn Cavities

HPP testing of Nb_3Sn cavities has been reported in [PVL15, PLX11, MGH+16, HP97, Cam85]. We will concentrate on the results from [PVL15] (these results are also discussed in [Pos14]). This source is most relevant to current Nb_3Sn cavities at Cornell University having tested recent Nb_3Sn cavities using the same equipment.

Figure 6.1 shows HPP testing of Nb_3Sn cavities from [Pos14, PVL15]. The results are plotted as the quench field versus T^2. This is because the temperature dependence of H_{SH} is given approximately[3] by equ. 2.12: $H_{SH}(T = 0)(1-(T/T_c)^2)$. At 4.2 K they find the quench field to be roughly 110 mT $\approx$ 26 MV/m–lower than the theoretical H_{SH}, but higher than what is seen in CW operation. The increase in quench field in HPP testing shows that we have not reached H_{SH} in CW testing and suggests that quench is being triggered by a thermal defect (this is also supported by temperature mapping, as we will see in chapter 8).

Using the expected temperature dependence of the superheating field we can make a better attempt to measure the quench field. By measuring the quench field close to T_c we can charge the cavity faster and the activation of some defects may be suppressed. This allows us to push closer to the ultimate field. We can then use equ. 2.12 to estimate H_{SH} at 0 K. This technique finds that $H_{SH}(T = 0)$ would be $\approx$ 250 mT if the trend near T_c continued.

We can see the importance of the charging time in Fig. 6.2. This shows the quench field that was found versus the time it takes the cavity to quench. Each point is taken with a different forward power. The higher the forward power the

[3] This equation is expected to be within roughly 10% of the real value [CS08b].

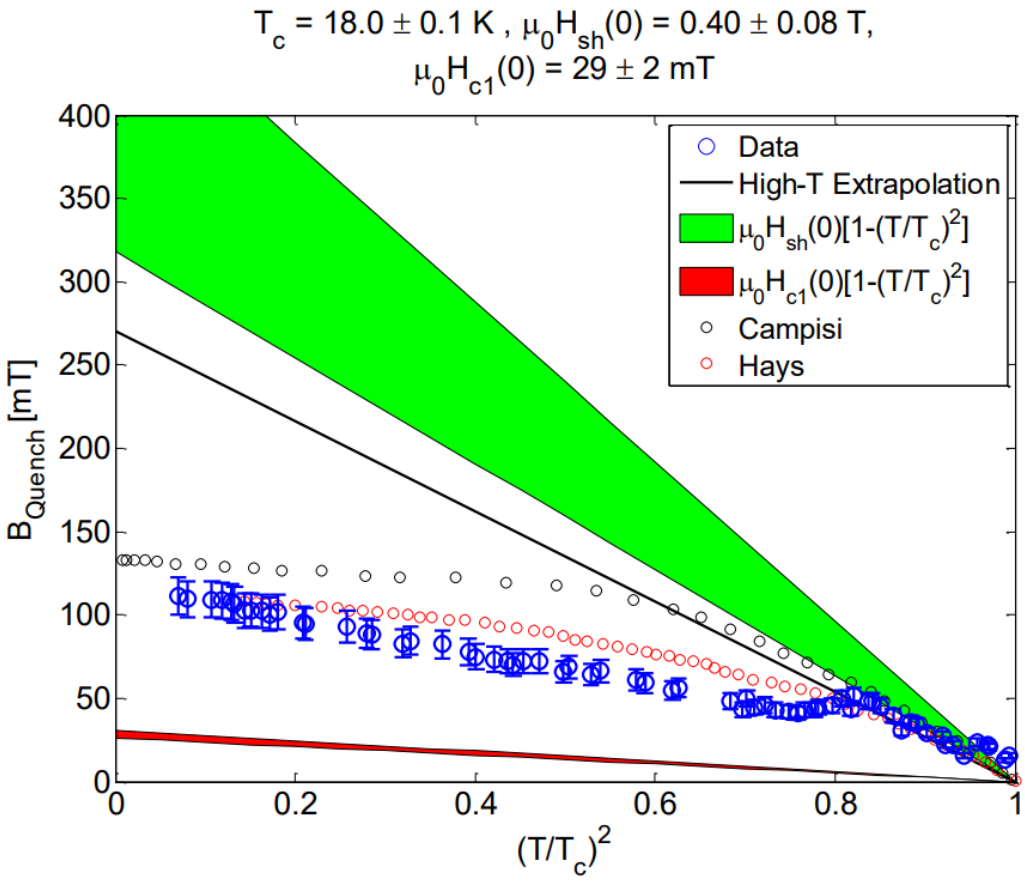

Figure 6.1: HPP testing of an Nb_3Sn cavities. Data is overlayed from [HP97] and [Cam85]. The colored bars show estimate ranges for various critical field. The black bar is a fit to equ. 2.12 using only data close to T_c. This figure was adapted from [Pos14].

higher the measured quench field becomes. The point with the highest quench field was taken utilizing 1 MW of forward point–the maximum power for this system. It is likely that this trend will continue if we could increase the field on the sample faster.

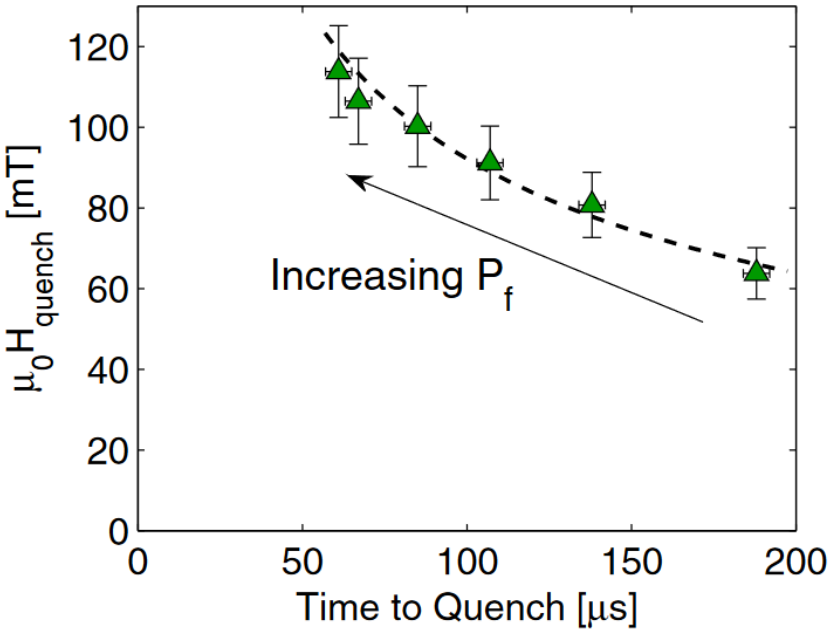

Figure 6.2: The quench field versus the time to quench in HPP testing of an Nb_3Sn cavity. Each point is taken with a different forward power, but a fixed bath temperature (4.2 K). The higher the forward power the higher the measured quench field becomes. This figure was adapted from [Pos14].

6.2 CHPPSHC Introduction

The previous section shows that one of the limitations to determining H_{SH} is how quickly the surface magnetic fields can be raised on the material. One way to raise the surface magnetic field faster is to increase the forward power delivered to the system. Our klystron has a maximum output power of 1 MW which has already been utilized. Purchasing a new klystron would prohibitively expensive. The other option is to increase the ratio of $[B_{pk}/\sqrt{U}]$. That is, increase the peak surface magnetic field for the same amount of energy in the cavity. Increasing the $[B_{pk}/\sqrt{U}]$ ratio is the preferable option.

CHPPSHC is a cavity optimized to have a large $[B_{pk}/\sqrt{U}]$ ratio on a rela-

tively small sample. The sample can be changed out to test different superconducting materials or preparations. The system is designed to work on the 1.3 GHz klystron system that we possess. The simple sample geometry (relative to a cavity) also allows for the testing of materials that cannot yet be applied to a complicated geometry.

6.3 Designs and Simulation

The full designs of the CHPPSHC are shown in Fig. 6.3. There are several components to this schematic, and we will break this down into parts. For easy reference table 6.1 lists key parameters of the CHPPSHC that will be discussed in the text. We will first start with a simplified model of the cavity bell shape and explain how the cavity attains high surface magnetic fields on the sample.

	Design Parameters
f_0	1.3103 GHz
Q	$8 \cdot 10^5$
$B_{pk}/\sqrt{U}$	510 mT/ $\sqrt{\text{J}}$
β	1 - 20
Sample Height	4.6 cm
Sample Width	9.2 cm
Sample Thickness	3 mm

Table 6.1: A table of key parameters for the CHPPSHC.

Figure 6.4 shows the cavity bell section of the cavity. The curved portion at the bottom is the sample. In the full model there is an air gap around the sample. Two components of this design contribute to the high surface magnetic fields.

The overall shape of the cavity was optimized to increase the surface mag-

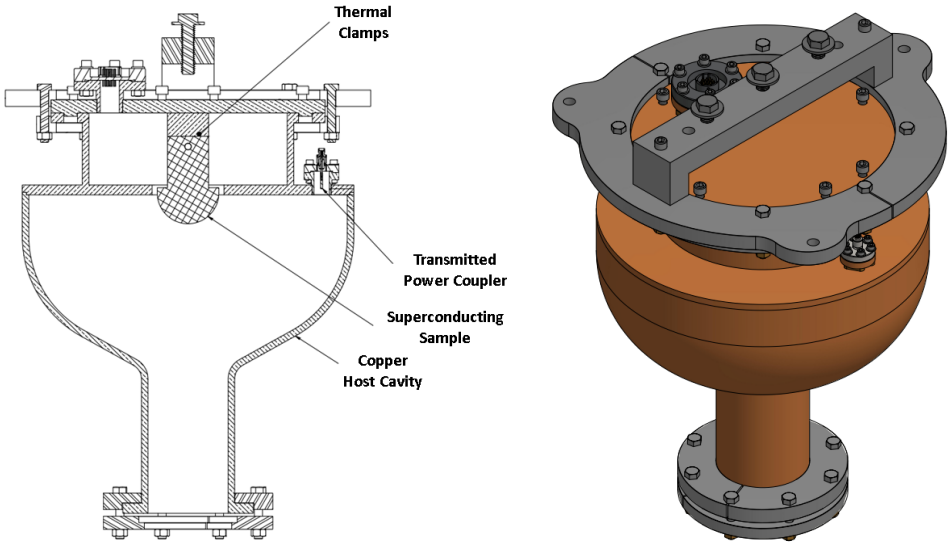

(a) (b)

Figure 6.3: Schematics of the final CHPPSHC design. a) Cross-section. b) External view.

netic field at the center of the bottom plate. This optimization was conducted at Cornell University by Y. Xie *et. al.* using a genetic optimization algorithm [XHL09]. This cavity is driven in its first dipole mode which is shown in Fig. 6.5. CST Studio Suite 3D E&M was used to simulate the field in the cavity and found that the peak surface magnetic field, B_{PK}, is $48.9\,\mathrm{mT}/\sqrt{\mathrm{J}}$. Comparatively, a TESLA elliptical cavity has a B_{PK} of $34.9\,\mathrm{mT}/\sqrt{\mathrm{J}}$ and a cylindrical pillbox cavity has $34.2\,\mathrm{mT}/\sqrt{\mathrm{J}}$. This choice of geometry gives a 40% increase in the surface magnetic fields.

We use a ellipsoidal sample to further increase the peak surface magnetic field. An ellipsoidal shape results in an enhanced surface magnetic field on the tip [SP08, Kub14]. Figure 6.6 shows the surface magnetic field on the cavity and sample. Considering both the B_{PK} and manufacturing techniques we chose dimensions of the ellipsoidal sample to have a thickness of 3 mm, a height of

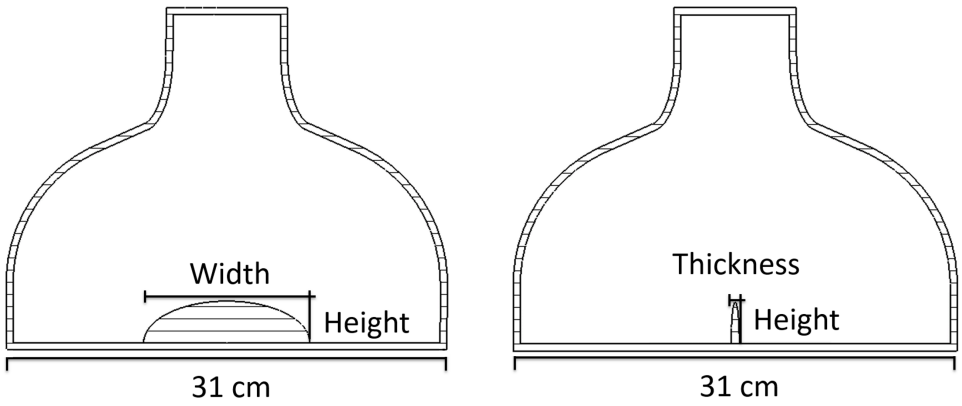

(a) x-z plane cross section.

(b) y-z plane cross section.

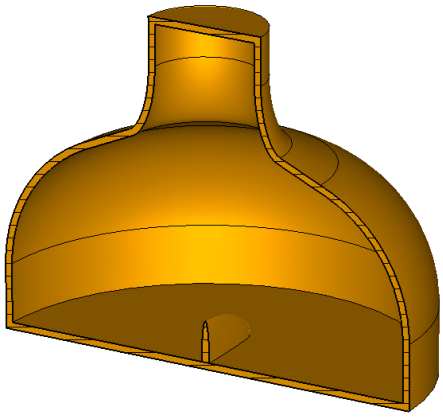

(c) Cross section.

Figure 6.4: CHPPSHC bell design. In this diagram the cavity is flipped vertically from that shown in Fig. 6.3. The 'beam tube' is at the top of the cavity and is not filled in in the true system.

4.6 cm, and a width of 9.2 cm. This sample shape (combined with the bell geometry) gives an expected B_{PK} of 510 mT/ $\sqrt{\mathrm{J}}$.

We require the cavity to go above the T_c of niobium, preventing using superconducting niobium for the cavity. Instead, we use copper for the main cavity geometry. Copper can be used in HPP and still reach high field strengths.

Using copper requires that the superconducting sample be thermally separated from the RF cavity walls. To accomplish this, we have added a small gap between the superconductor and the RF cavity wall. Below the sample we have

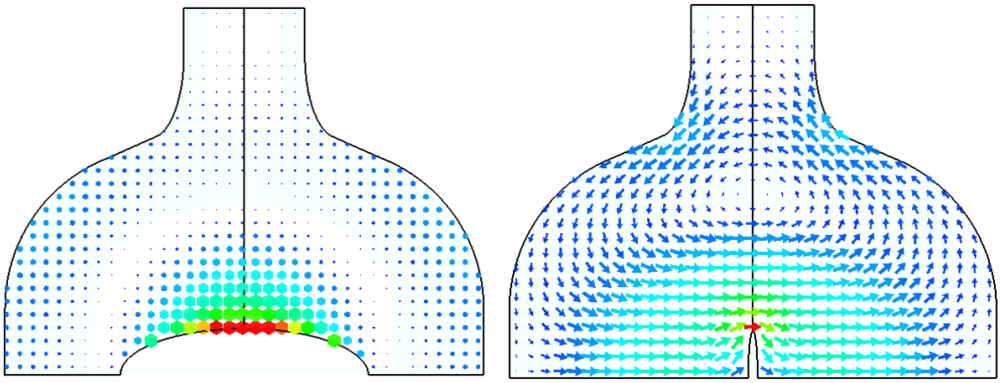

(a) The magnetic field pattern in x-z plane.

(b) The magnetic field pattern in y-z plane.

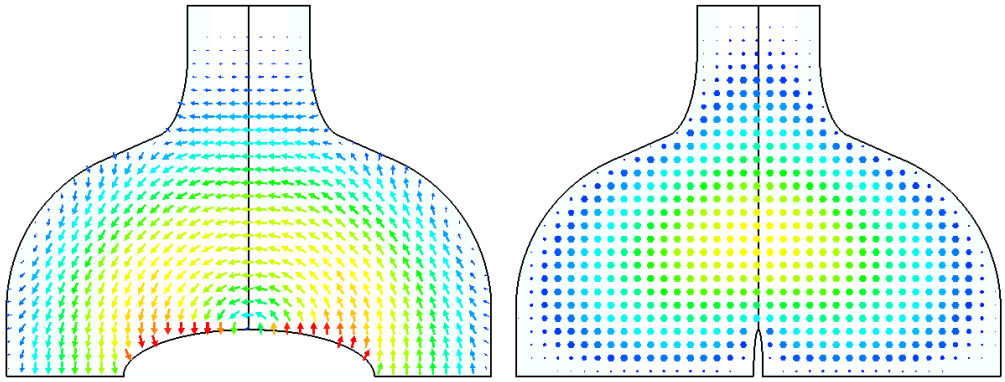

(c) The electric field pattern in the x-z plane.

(d) The electric field pattern in the y-z plane.

Figure 6.5: Electric and magnetic field patterns in the cavity for the operating mode.

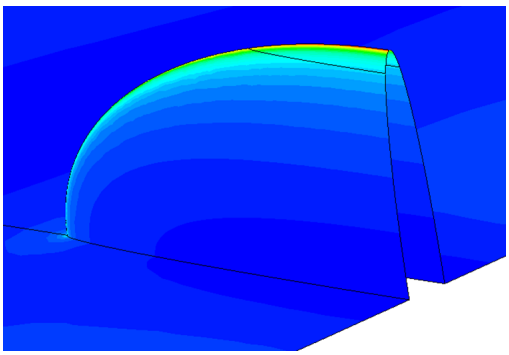

(a) Surface magnetic field magnitude. The scale has been adjusted so that field pattern off the sample is visible.

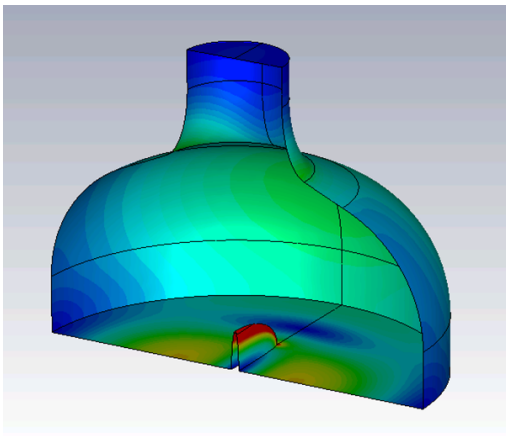

(b) Surface magnetic field magnitude on sample.

Figure 6.6: Surface magnetic fields on the sample and cavity bell.

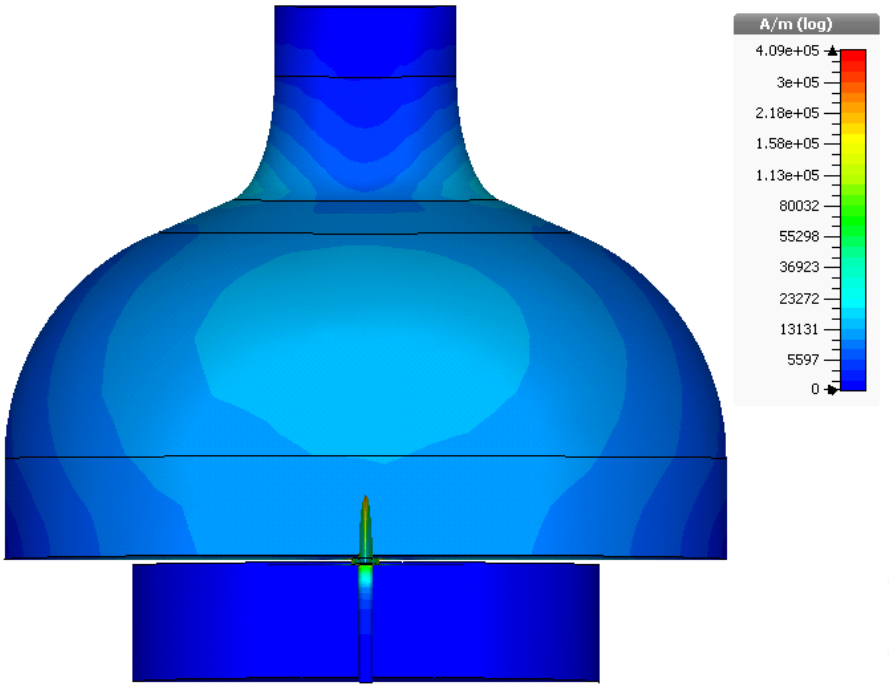

Figure 6.7: The surface magnetic field in the upper and lower cavities. A y-z cross-section is shown.

added a small cavity (visible at the top of Fig. 6.3a), creating an upper and lower cavity. The sample has a long flat portion that bolts to the far side of this chamber. This connection serves as mechanical support and a thermal anchor to the helium bath to provide cooling. The second cavity has low RF fields as shown in Fig. 6.7. This setup provides thermal gap for the sample.

The sample is small enough that we cannot detect any change in the RF data when the sample quenches. Instead, two Cernox brand cryogenic thermometers are pressed against the base of the sample. One thermometer is used to monitor the overall sample temperature during cooldown and just before RF power is applied. The second sensor is read out at a high rate and used to detect the sample quench[4]. Indium is used to increase the thermal contact. Seeing a large

[4]This uses separate electronics that can sample at a high rate but only for a short period of time.

spike in temperature on the second sensors will allow us to detect the sample quench.

For sample testing the entire system is cooled to 4.2 K. To determine the quench field at a given temperature the forward power is pulsed on, and the thermometer monitored. If no quench is detected, then the forward power is slowly increased until the thermal signature of quench is detected. The field level in the cavity and on the sample is determined using transmitted power and normal RF testing techniques (the transmitted power is calibrated using lower power CW testing). To test below 4.2 K the temperature of the bath is lowered. To test above 4.2 K a small heater at the base of the sample is used to increase the temperature of the sample. This allows the system to test H_{SH} over a wide temperature range (up to T_c).

6.3.1 Sample Geometry and Surface Magnetic Fields

Electromagnetic simulations were conducted on the cavity to optimize the sample geometry and investigate the impacts of misshapen geometry. Figure 6.8 shows plots of how B_{PK} depends on the sample geometry. The final sample geometry was determined using these simulations and machining considerations. The sample thickness was chosen to be 3 mm to allow manufacturing from readily available niobium sheet metal of the same thickness. A height of 4.6 cm was chosen as this maximized the peak magnetic field and a width of 9.2 cm was chosen because there was heavily diminishing returns on peak magnetic field when using wider samples and so that the radii were matched in the height and width dimension–making machining easier. Our final sample geometry was

relatively easy to manufacture and attains a high B_{PK}.

Additional simulations were conducted to measure the extent that machining tolerances may change the peak fields. Estimating all ways that the sample could be misshapen is not possible. Several simple changes were done: 1 mm displacement in x, y, and z axes; and flattening the last 1 mm of the sample tip. These changes resulted in less than a 1% change in B_{PK}. The simulation with the flattened obtained only a 0.2% reduction in the B_{PK} but the B_{PK} location moved to two new locations on the sample. This suggests that B_{PK} on the sample is quite robust, but sharp gashes or other features may still be problematic.

6.3.2 Cavity Antenna and Coupling

To couple to the dipole mode in the cavity a new antenna needed to be designs and made. A simple loop antenna was designed to be affixed to existing equipment. A diagram of the coupler in the CHPPSC is shown in Fig. 6.9. The coupling factor, β, was calculated for several positions and a length was chosen that would allow for a wide variety of βs to be obtained during testing: from $\beta = 1$ to $\beta = 20$. The β range was chosen based on calculations discussed in section 6.4.

6.3.3 Cavity Tuning

Having the cavity resonance frequency close to that of the klystron's output frequency is important. The klystron has a limited output bandwidth to work with. The frequency of maximum output was measured to be 1.3103 GHz. The

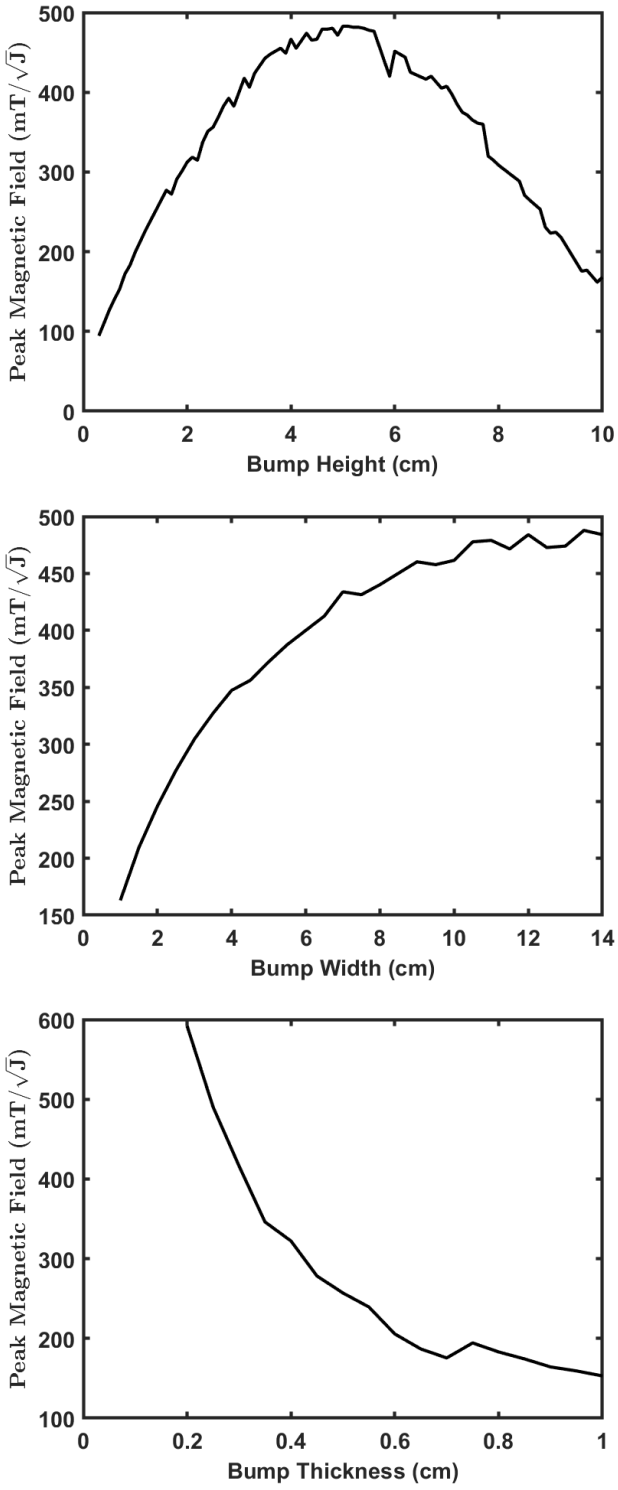

Figure 6.8: Peak surface magnetic field on sample for 1 J in the cavity. The simulated geometry is shown in Fig. 6.4. In each plot the unlisted dimensions are Height = 3 cm, Width = 6 cm, and Thickness = 0.3 cm. There is some noise in simulated data due to the way the geometry is meshed for the simulation.

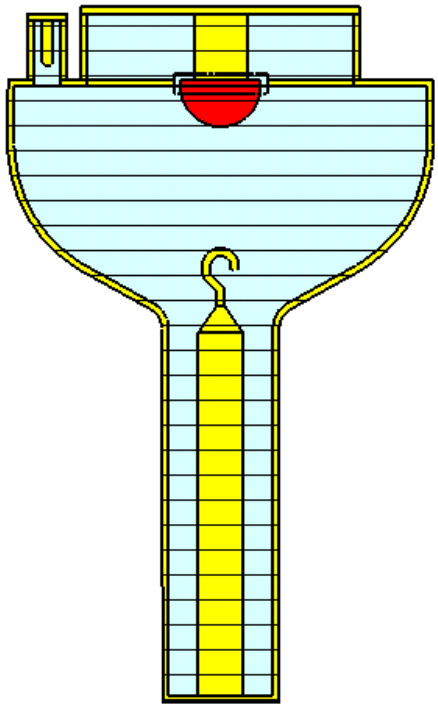

Figure 6.9: A schematic of the hook coupler used for the CHPPSHC in the CHPPSHC. Note the orientation of the loop with respect to the sample plane.

bandwidth of the CHPPSHC is $\approx$ 2 kHz while the bandwidth of the klystron is $\approx$ 5 MHz. We need the cavity's resonant frequency to be within 5 MHz of of the klystrons center frequency. To accomplish this the cavity geometry was carefully tuned to obtain the same frequency. This includes account for thermal contraction of copper when cooling the cavity [SDR92]. If the final resonant frequency is not well aligned, we will have to tune the cavity: this will include stretching the cavity to change the resonance frequency.

6.3.4 Mechanical Simulation

Mechanical simulations of the cavity were conducted to ensure the cavity is structurally sound and measure distortion of the cavity geometry when the

cavity is pumped down to vacuum. The final designs were found to be able to withstand vacuum. The thickness of the top plate was increased to ensure structural stability (0.375″). With final geometry, the sample was found to only shift by 190 µm into the cavity. This shift caused a decrease in B_{PK} by 0.2%.

6.3.5 Thermal Calculations

Since we are detecting the quench of the sample using the thermometry, we need a good understanding of the thermal dynamics of the sample. There are some simple calculations of the system that can be done to understand it.

From the electromagnetic simulations we can find the power dissipated on the sample. When B_{PK} is 425 mT at 4.2 K the power dissipated on the sample when superconducting is 0.13 W and in the normal conducting state it is 1781 W. Over 20 µs at 425 mT only 2.55 µJ would deposited in the superconducting sample (in reality the field would ramp up over this period, giving significantly less heating). Similarly, 1 µs in the normal conducting state would deposit 1.78 mJ, three orders of magnitude higher. The amount of power deposited in 1 µs at this field would raise the average temperature of the sample by 30 mK (at 4.2 K). The change in heating when the sample quenches is sufficiently large to detect and differentiate from the normal conducting state.

The heating calculated above are averages while we will have a transient heat pulse that passes our sensors. We want to calculate the transient behavior and find the temperature versus time at our thermometer. To simplify the problem, we will approximate the entire sample as a bar that is being heated at one end and use the 1D heat equation. The bar is 3 mm thick by 4 cm wide and 9 cm

from the sample tip to the helium bath. This simplified problem can be solved using Green's functions. The time evolution of the temperature distribution is given by [Set21]:

$$T(x,t) = \int T(y,0)\frac{1}{\sqrt{4\pi D t}}\exp\left(-\frac{(x-y)^2}{4Dt}\right)\mathrm{d}y\,, \tag{6.1}$$

where,

$$D = \frac{k}{c\rho}\,, \tag{6.2}$$

where k is the thermal conductivity, c is the heat capacity, and ρ is the density (we approximate k and c by their values at the temperature of the helium bath).

The value $\sqrt{2Dt}$ gives us a rough estimate of the diffusion distance of the heat distribution in a time t. For 1 µs–the length of our normal conducting pulse–this gives us $\approx$ 5.8 mm. This is rough $1/10^{\text{th}}$ of the distance to the thermometer. Since this length scale is relatively small, we can estimate the initial temperature distribution as a delta function. To account for boundary conditions at the sample and at the helium bath we can use an infinite set of delta functions with alternating signs (similar to using image charges). Our initial temperature distribution is then,

$$T(x,0) = \frac{2U_\mathrm{d}}{c}\left[\ldots - \delta(x-2x_\mathrm{tip}) + \delta(x-x_\mathrm{tip}) - \delta(x+x_\mathrm{tip}) + \delta(x+2x_\mathrm{tip}) - \ldots\right]\,, \tag{6.3}$$

where U_d is the energy deposited in the sample during the pulse, δ is the delta function, $x = 0$ is the helium bath location, and x_tip is the distance to the tip of

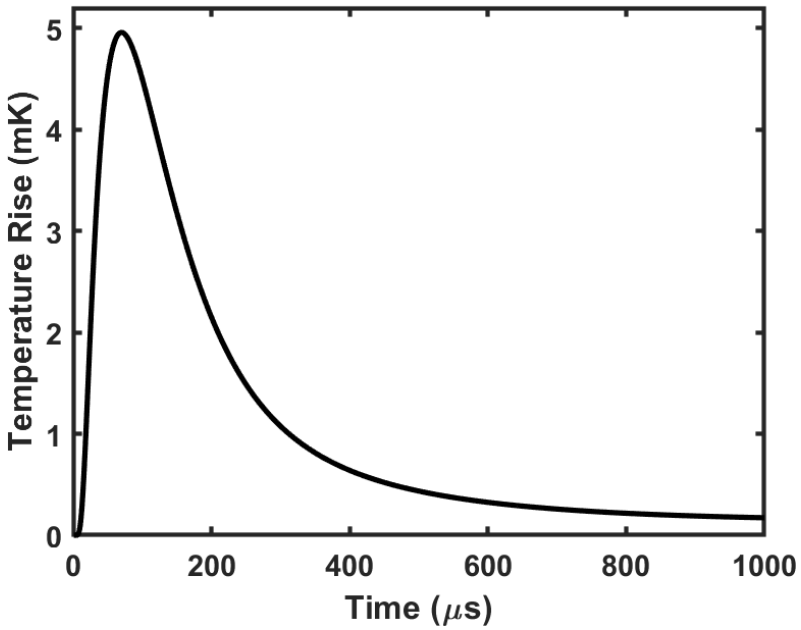

Figure 6.10: The estimated temperature at the thermometers if the sample is normal conducting for 1 µs at a B_{PK} of 425 mT and 4.2 K. The peak temperature is 5 mK and occurs 70 µs after the pulse.

the sample.

Combining equ. 6.1 and 6.3 we get the temperature over time at the thermometer,

$$T(x,t) = \frac{2U_{\mathrm{d}}}{c}\frac{1}{\sqrt{4\pi Dt}}\left[... + \exp\left(-\frac{(x-x_{\mathrm{tip}})^2}{4Dt}\right) - \exp\left(-\frac{(x+x_{\mathrm{tip}})^2}{4Dt}\right) + ...\right], \qquad (6.4)$$

where we have neglected two additional terms in the infinite series when writing the equation. This equation is easily computed for first several terms (the most important). The result is shown in Fig. 6.10. The temperature peaks at 5 mK, 70 µs after the pulse. This is a measurable temperature rise[5].

[5]In the previous chapter we demonstrated temperature measurements with sensitivities below 1 mK.

This calculation is not a perfect estimate of our system and is meant primarily to demonstrate the functioning of the system. In reality only part of the sample will quench, which will reduce the temperature rise. In addition, the RF field will continue to rise after passing the quench field. These make it hard to determine the quench field from a single measurement. Instead (for each temperature) we will need to do sets of measurements with different pulse lengths and magnitudes of forward power and fit the data to extract a quench field.

6.4 Expected Performance

We now look at some characteristics of performance of the system. We are interested in what peak fields that cavity can reach and how quickly it can be charged. We will look at several parameters. These are calculated assuming that we can get the full forward power of 1 MW to the cavity.

Figure 6.11 shows the B_{PK} that would be reached in CW operation (if possible). The maximum field occurs at $\beta = 1$ and is almost 4.5 T. Of course, this cavity is made for pulse mode operation. The high B_{PK} value demonstrated the optimization of magnetic field on sample and is not a field that will be reached during testing.

A more significant parameter is the charge time to a given field, B_{PK}. Figure 6.12 shows the optimized charge time for a desired field. The cavity will continue to charge past this field level, but this is the time it takes to reach the given field. We have optimized these with respect to the coupling constant, β. At 425 mT the optimized charge time is $\approx 1\,\mu$s for $\beta \approx 200$. However, the large values of β are not reachable using the current coupler design (though this could

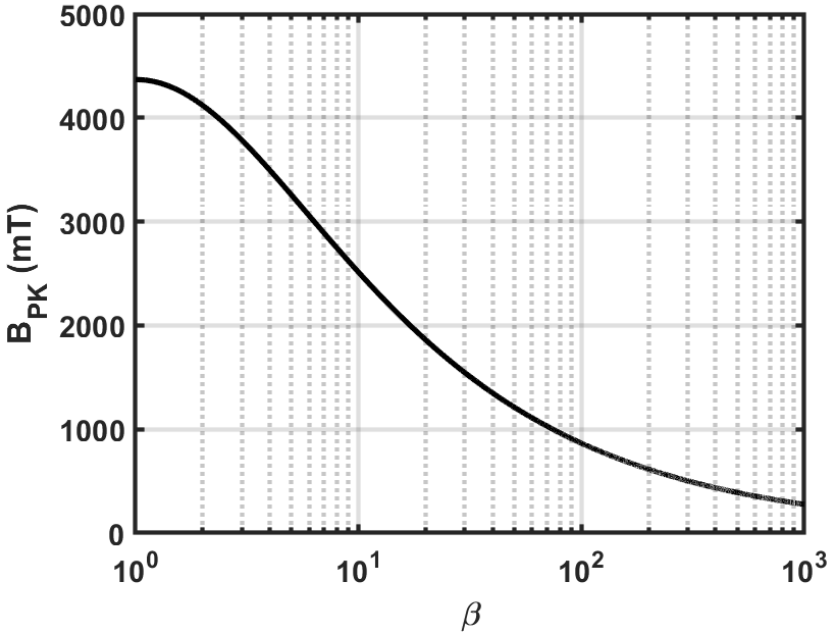

Figure 6.11: The maximum theoretically achievable B_{PK} (CW operation) with 1 MW of forward power versus the coupling constant, β.

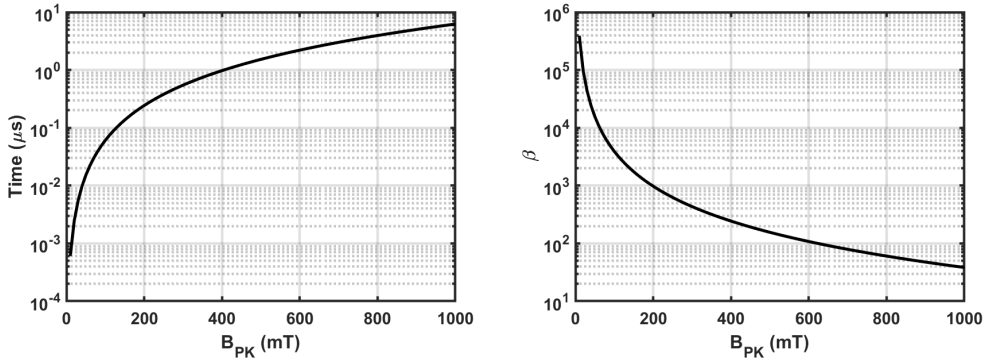

(a) (b)

Figure 6.12: Optimized a) charging times and b) β for the desired B_{PK} for 1 MW of forward power.

be changed if desired). Charge times this quick would likely make it difficult to determine the exact quench field using our thermal method.

For a final measure of performance we can look at how quickly the cavity can reach a B_{PK} of 425 mT using the designed β range of the antenna: 1 to 20.

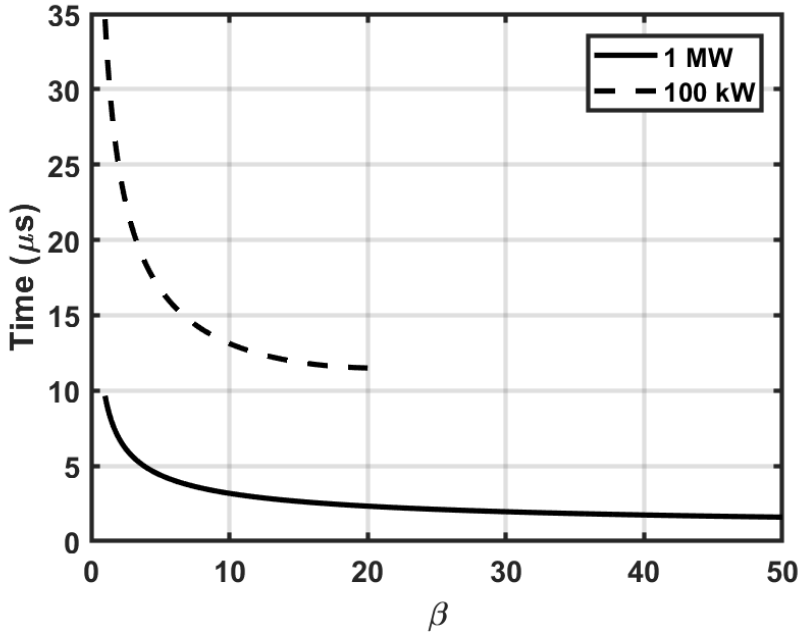

Figure 6.13: The time to reach a B_{PK} of 425 mT for various values of β. The charge time is shown for both 1 MW and 1 kW of forward power. Above $\beta = 20$ the charge time starts increasing for the 100 kW scenario and is not shown. The cavity antenna is designed to vary from $\beta = 1$ to $\beta = 20$.

Figure 6.13 shows the charge time to 425 mT. The charge time to 425 mT is 2.3 µs at $\beta = 20$. If we only manage to get 100 kW of forward power we could still reach 425 mT in only 11.5 µs. This charge time is much faster than can be accomplished in single-cell cavities and should allow higher vales of B_{PK} to be reached before a thermal quench occurs.

6.5 Fabrication and Assembly

Fabrication of the CHPPSHC began in the spring of 2020. As of writing this all parts have been constructed. We show here some interesting aspects of the fabrication process.

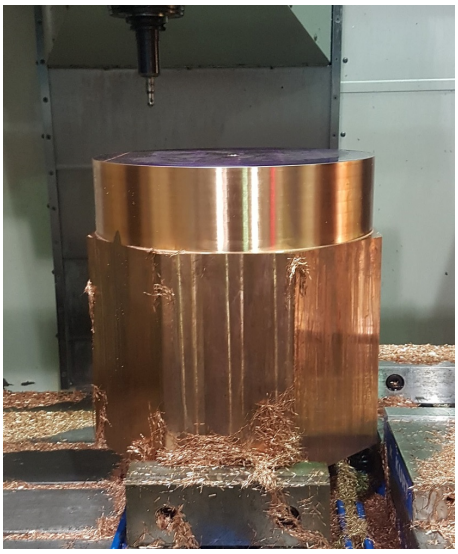

(a) Main cavity bell copper block.

(b) Main cavity bell partially milled.

(c) Complete copper bell being indexed to confirm the shape.

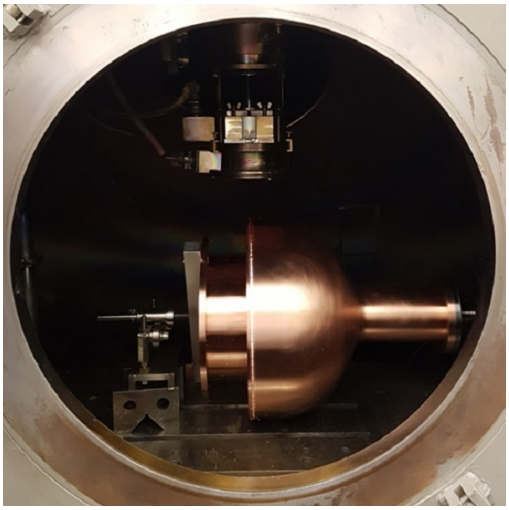

(d) The main copper body after electron beam welding.

Figure 6.14: CHPPSHC bell being fabricated at various stages.

The main body of the cavity were machined from two large blocks of copper. This allowed for thick cavity walls that can withstand atmospheric pressure when the cavity is at vacuum. Figure 6.14 shows the evolution of the main copper body of the cavity. The two main components of the body were then electron beam welded together.

Four niobium samples were made for the CHPPSHC. These sample were machined on a CNC mill (by a very talented machinist). A lot of care was needed to minimize deflection of the sample during the machining process. One sample has already been coated in Nb_3Sn for future testing.

The CHPPSHC is a useful new tool in exploring the ultimate fields of new materials, including Nb_3Sn. The cavity has been built and the final assembly and commissioning tests are planned. Initial commissioning will be done on niobium samples for which H_{SH} is relatively well known[6] [VL11a, Val13, PVL15]. This will allow us to confirm that the system is functional. Hopefully the CHPPSHC will determine the superheating fields of Nb_3Sn in the near future.

[6]The superheating field of niobium has been found to change based on pretreatments [VL11a, Val13].

CHAPTER 7

RF MEASUREMENTS OF NB_3SN CAVITIES

We now start looking at experimental data pertinent to the quench of Nb_3Sn cavities. Here we examine results from RF testing of Nb_3Sn cavities. Since many quench mechanisms have a temperature or frequency dependence, we look at the dependence of the quench field on these variables. This allows us to rule out various quench mechanisms. We examine the impact various cavity baking treatments (800 C, and 75 C; and 160 C N_2 infusion). We then look at the surface resistance of our cavities to gain insight into material properties and discover evidence of multi-gap superconductivity in our cavities. We will discuss temperature mapping of Nb_3Sn in chapter 8.

7.1 Standard Performance of Cornell Nb_3Sn Cavities

We will begin with a summary of the standard CW RF performance of 1.3 GHz Nb_3Sn cavities at Cornell University. Current state-of-the art Nb_3Sn cavities at Cornell University achieve a quality factor of $2 \cdot 10^{10}$ at 4.2 K and low fields, and a maximum accelerating gradient of 15 – 18 MV/m. No radiation is detected during cavity testing (which could suggest the emission of electrons in the cavity). The quality factor slowly decreases–roughly linearly–to $1 \cdot 10^{10}$ (at 4.2 K near the quench field). The behavior at 2 K is similar except for a higher quality factor because of decreasing BCS-resistance. Figure 7.1 shows several Q vs E_{acc} curves taken at 4.2 K using 1.3 GHz cavities and a comparison of Q at 4.2 K and 2 K.

Applying a simple BCS fit to R vs $1/T$ data (as detailed in section 4.6) finds that the BCS-surface resistance (field-independent) is $\approx$ 8 nΩ at 4.2 K and that

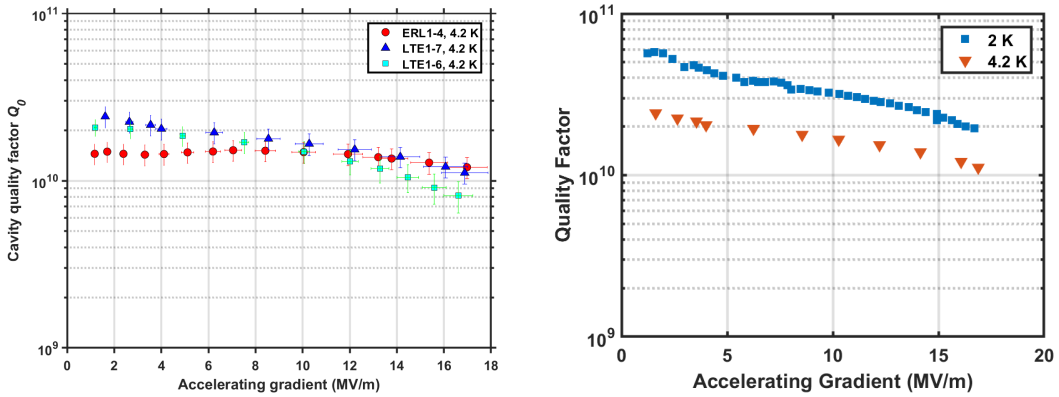

(a) (b)

Figure 7.1: a) Q vs E at 4.2 K of several 1.3 GHz Nb_3Sn elliptical cavities made at Cornell University. b) Q vs E at 4.2 K and 2 K of a 1.3 GHz Nb_3Sn TESLA elliptical cavity.

	Experimental Result
T_c [K]	18
Δ/k_BT_c	2.15
l [nm]	3.0
R_0 [nΩ]	8

Table 7.1: Typical results of parameters found during Nb_3Sn cavity testing.

the residual resistance is $\approx 8\,n\Omega$ at 10 MV/m. Additional parameters are listed in table 7.1. In particular, we note the very short mean free path of 3 nm. The residual resistance found here was investigated D. L. Hall in [Hal17, HLLS17]. He finds that this residual resistance is primarily caused by ambient magnetic field that is trapped during cooldown. Experiment and theory suggest that the residual resistance caused by trapped magnetic flux will have a linear field dependence [Hal17, HLLS17, L+17] in explaining the slope we see in Q vs E plots. We will see in section 7.6 that BCS fitting in Nb_3Sn cavities requires somewhat more complicated methods.

As discussed in chapter 6, higher quench field are achieved in high pulsed power testing of Nb_3Sn cavities. This suggests that our Nb_3Sn cavities are being

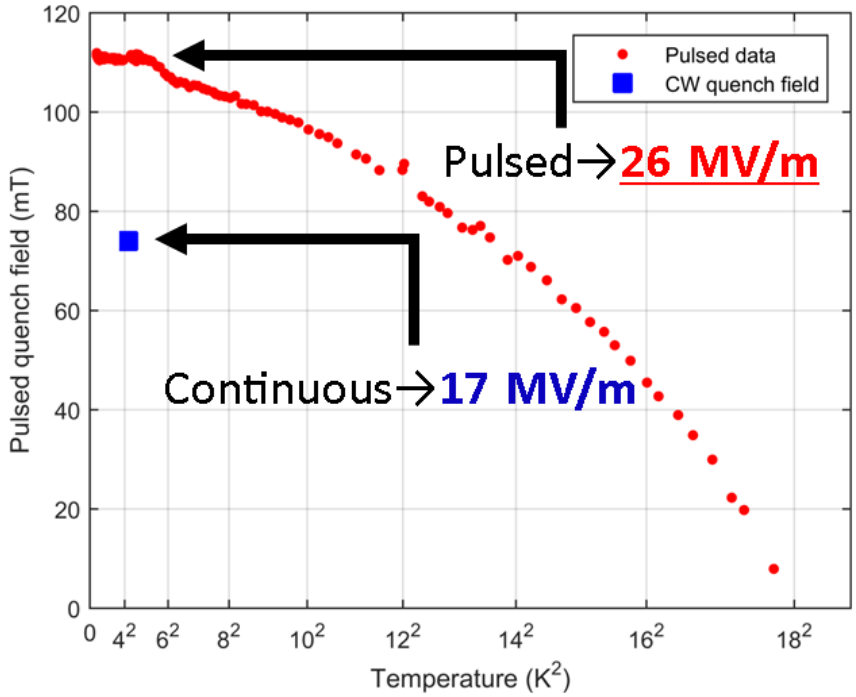

Figure 7.2: High power pulse testing of a Cornell Nb_3Sn cavity. Figure adapted from [Hal17].

limited by a thermal defect. Figure 7.2 shows the results of pulsed power testing as quench field versus temperature. We additionally note that the quench field increases slightly more than is expected (based on equ. 2.12) from 6 K to 5 K.

7.2 Reproducibility of the Quench Field

The quench field of Nb_3Sn cavities at Cornell University is remarkably reproducible. Figure 7.3 shows a histogram of all 1.3 GHz Nb_3Sn cavities tested in the past 5 years. With few exceptions, they all quench between $14 - 18$ MV/m (at 4.2 K), with a mean of ≈ 16 MV/m. This shows that the quench mechanism is mostly consistent across our cavities despite modifications to the growth process.

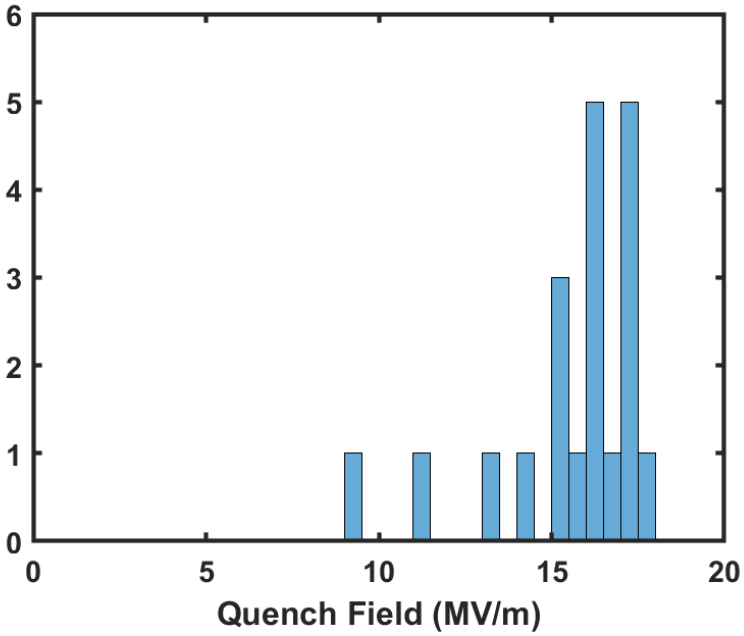

Figure 7.3: A histogram of all 1.3 GHz Nb_3Sn cavities tested in the past 5 years. The bin width is 0.5 MV/m.

7.3 Temperature Dependence of the Quench Field

During regular cavity testing we do not observe any significant difference in the quench field with respect to temperature (for $T \leq 4.2$ K). To confirm this we have carefully measured the quench field at 4.2 K and $\sim$ 2 K[1] in several of our cavities. During regular cavity testing we increase the power and accelerating gradient in relatively large steps ($\sim$ 0.5 MV/m near the quench field) which could obscure temperature dependence. For these measurements we very carefully approach the quench field so that we can make a Q vs E measurement within 0.05 MV/m of the actual quench field[2].

For the measurement of these accelerating gradients, we use a specific cali-

[1]The actual measurement temperature varies from 1.7 K to 2.1 K depending on the cavity test.

[2]One could also turn on the power, increase it until the cavity quenches, and record the last P_t before quench, instead of making relatively slow Q and E measurements.

bration to reduce statistical noise between the measurements. Our E_{acc} measurements are accurate to roughly 10%, but this error is dominated by systematic errors primarily arising from calibrations. By using the same calibrations (without physically disturbing the equipment) we can compare the quench field between temperatures with less uncertainty. In this case we use the same $\sqrt{P_t}$ to E_{acc} (see sec. 4.6) calibration for all the points.

We find that the field does not change with respect to temperature (or after cavity quench) within our uncertainties. Figure 7.4a shows the results of this for STE1-2, a 2.6 GHz cavity. In all our measurements we find that the quench field at 4.2 K and 1.7 K are within 1%. This has been confirmed on 5 cavities (1 2.6 GHz cavity and 4 1.3 GHz cavities).

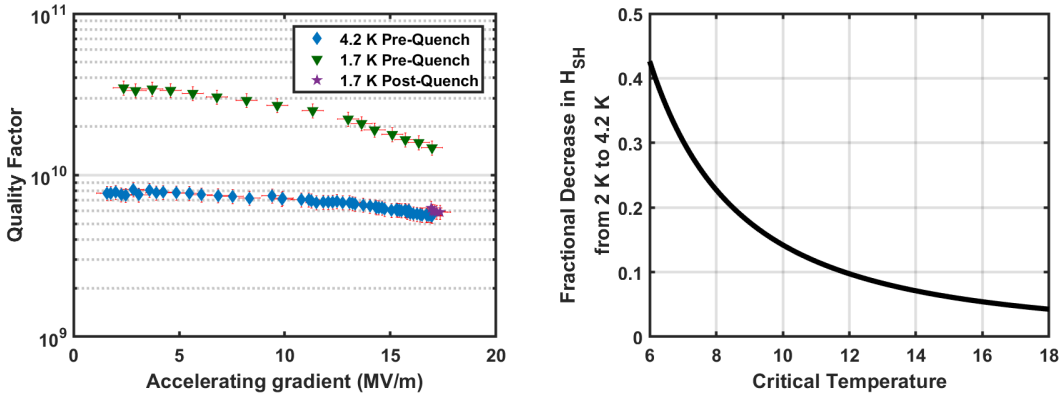

(a) (b)

Figure 7.4: a) Q vs E to quench of STE1-2 at 4.2 K before quench, 1.7 K before quench, and 1.7 K after quench (only points near the quench field are shown). The 1.7 K data was taken after re-cooling the cavity following quench at 4.2 K. All three quench fields are within $\approx$ 1%. b) The expected fractional decrease in H_{SH} when going 2 K to 4.2 K based on equ. 2.12.

Several different quench mechanisms have temperature dependence that could be detected, and we will briefly discuss the superheating field of tin depleted regions. Tin depleted regions have a significant reduction is superheating–as low as $B_{\text{SH}} \approx 70$ mT [God06]. Tin depletion and its impact on

Nb_3Sn is discussed in section 3.2. A potential quench mechanism could be from a large tin depleted region reaching its superheating field. This would, however, have a large temperature dependence that we do not see here. Figure 7.4b shows the hypothetical reduction in the superheating field between 4.2 K and 2 K based on equ. 2.12. Even for perfectly stoichiometric material we would expect a 5% change in quench field if we were reaching the superheating field. This does not rule out the possibility that tin depleted regions play a role in cavity quench, only that the mechanism would need to be more complicated than that described here.

7.4 Frequency Dependence of the Quench Field

To measure the dependence of the quench field (and other measures of performance[3]), two new 'high-frequency' Nb_3Sn cavities were made: a 2.6 GHz cavity and a 3.9 GHz cavity. These two cavities are $1/2$ and $1/3^{rd}$ scales of the 1.3 GHz TESLA elliptical cavities we use (except for the vacuum flanges). These cavities were prepared as detailed in chapter 4 with the exception of receiving 100 µm of electropolishing. The cavities followed the same Nb_3Sn standard coating procedure, however, the cavities were physically closer to the tin and $SnCl_2$ source due to their smaller size. These cavities are shown in Fig. 7.5.

The two high frequency cavities achieved roughly the same quench fields. Figure 7.6 shows Q vs E curves at 4.2 K up to quench. The 2.6 GHz and 3.9 GHz cavities achieves quench fields of 18 ± 1.8 MV/m and 17 ± 1.7 MV/m, consistent with typical 1.3 GHz results. Having only two data points at higher frequencies

[3]Quality factor and magnetic flux trapping measurements were reported in [PLM19], but will not be discussed here.

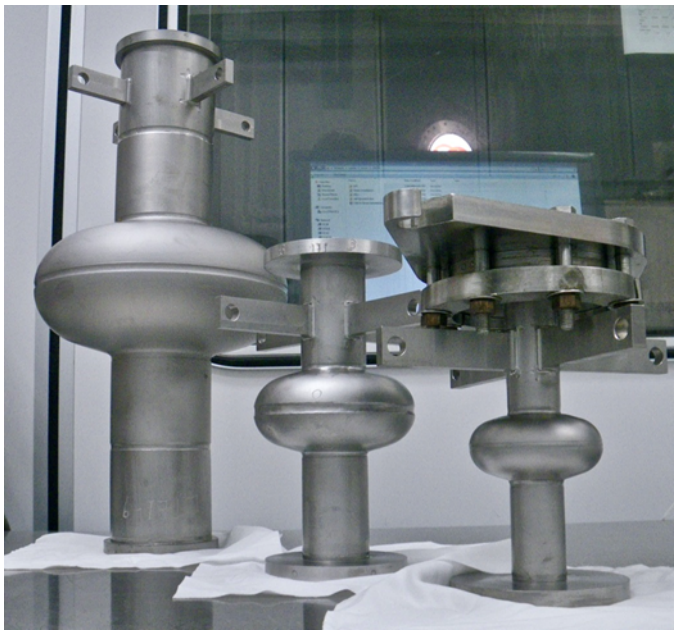

Figure 7.5: Left to right: a 1.3 GHz, a 2.6 GHz, and a 3.9 GHz Nb_3Sn cavity. The 3.9 GHz cavity has a top plate and clamps attached that are used during testing.

we cannot completely rule out a frequency dependence but we can conclude that the quench mechanism is not strongly frequency dependent. For instance if $E_{\text{quench}}(f) \sim f^{-\frac{1}{2}}$ then $E_{\text{quench}}(3.9\,\text{GHz}) \approx 9.2\,\text{MV/m}$ and we would have been able to measure this change.

7.5 Post-Coating Furnace Treatments

Various furnace/baking treatments of niobium have resulted in large improvements in performance. 800 C vacuum bakes are a standard treatment to remove hydrogen from niobium cavities. Recently, doping the cavity with nitrogen has been shown to cause improvements in performance, in particularly, the appearance of the so called 'anti-Q slope' (wherein the quality factor increases with increasing accelerating gradient) [GRS+13b, Gon16, MGL17]. In this treatment

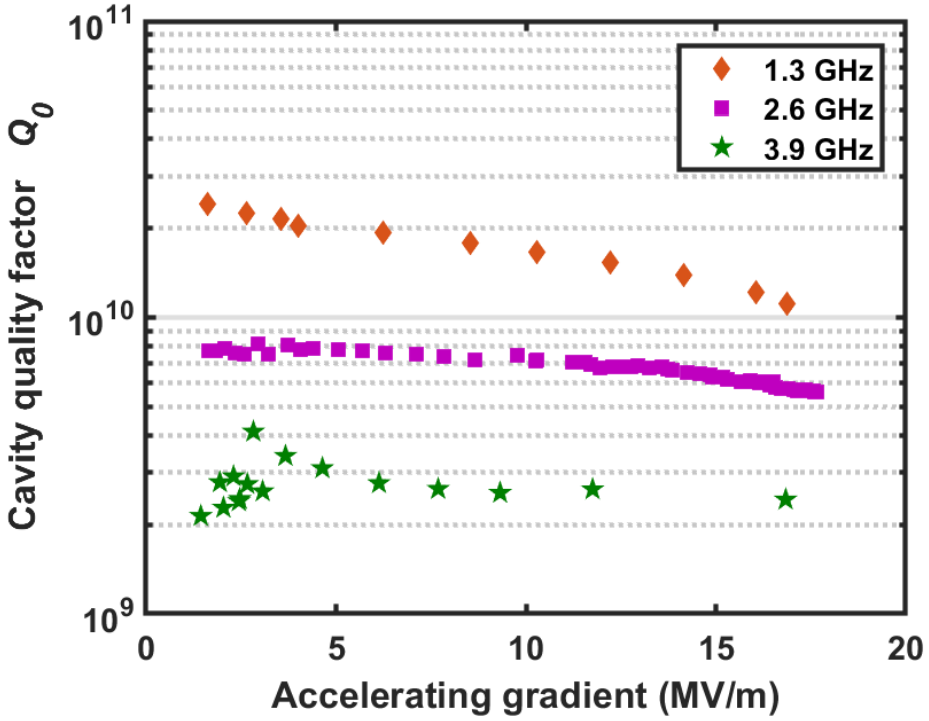

Figure 7.6: Q vs E curve at 4.2 K of 1.3 GHz, 2.6 GHz, and 3.9 GHz Nb_3Sn cavities.

a cavity is exposed to low pressures of nitrogen at 800 C and nitrogen absorbs into the surface. Niobium nitrides are formed on the surface during the process that must be chemically etched away. Development in this area has continued and has led to the discovery of low temperature (120 – 160 C) nitrogen doping termed 'nitrogen infusion,' which produces increased quality factors and accelerating gradients in niobium cavities without the need for post-bake chemical treatments [GRT+17, Man20]. Finally, it was reported in the last year that a 75 C bake of a niobium cavity achieved increased accelerating gradients [GRB+18]. We would be remiss to not try these treatments on our Nb_3Sn cavities.

Here we detail the baking and testing procedures used. Baseline tests were done of the Nb_3Sn cavity, LTE-10, with a standard coating. After testing the cavity was surrounded by box of insulating material (while still on vertical test

insert) and was heated to ≈ 75 C for 48 hours. The temperature was monitored using several thermal couples inside the insulated box and the heaters were controlled by a PID loop. The temperature varied from 70 C to 80 C during the process. Fans were used on the indium seals near the cavity to keep their temperature low and prevent the seals from overheating. After the process the cavity was tested again. Following this the cavity was removed from the test insert, the vacuum seal flanges were soaked in nitric acid to dissolve any residue indium, and the cavity was baked at 800 C for 3 hours in Ultra High Vacuum (UHV). During the bake the cavity was kept in a niobium foil box to prevent contamination from the furnace and to prevent contaminating the furnace with tin. An additional Nb_3Sn cavity, ERL1-4, received a N_2-infusion process as follows: 800 C for 3 hours in UHV + 160 C for 3 hours in UHV + 160 C for 48 hours in 3 mTorr N_2. This treatment has been successfully used at Cornell University for niobium cavities [Man20].

The results of these treatments are shown in Fig. 7.7. For all treatments there was no statistically significant change in the quench field. There was no statistically significant change in the quality factor of the 75 C baked cavity, however, there were statistically significant decreases in the quality factors of the 800 C baked and nitrogen infused cavities at higher fields, and the appearance of Q-slope type behavior after the 800 C bake.

Though the mechanism of these treatments is not fully understood, it is known that dissolved hydrogen and other gases, and the mean free path play a role [MGL17, Man20, Gon16, Rom09, CKML03]. During 1120 C baking during the growth process many of these impurities may have already been degassed. In addition, hydrogen and other interstitial impurities prefer niobium to Nb_3Sn[4]

[4]Unpublished calculations by N. Sitaraman and A. Fonseca.

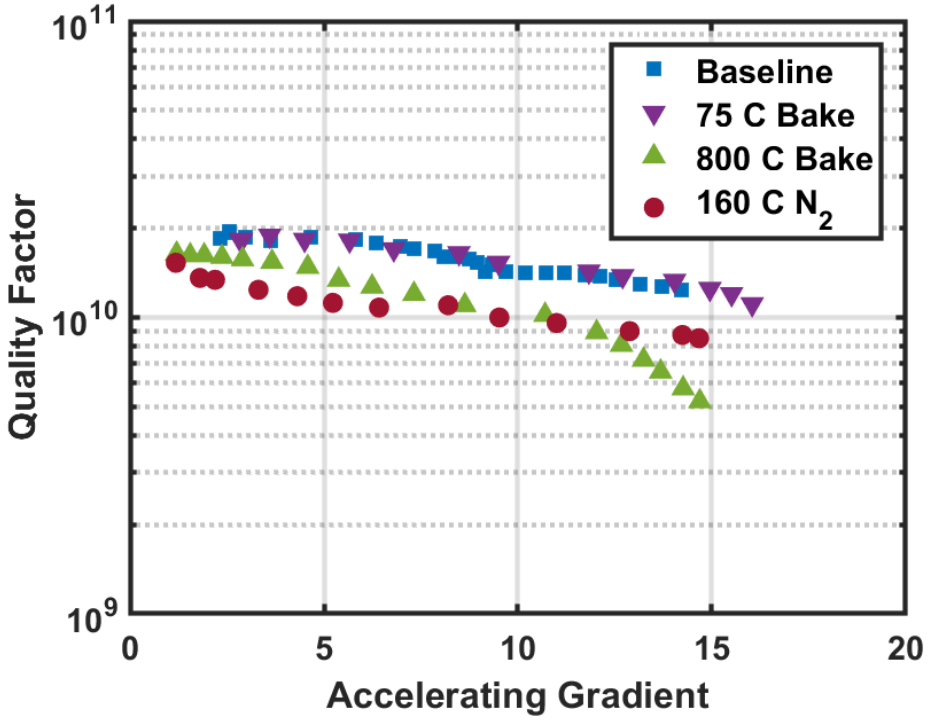

Figure 7.7: Q vs E curves at 4.2 K showing the effect of various furnace treatments on Nb_3Sn cavities: 75 C in situ for 48 hours, 800 C UHV for 3 hours, and 160 C N_2-infusion (800 C for 3 hours in UHV + 160 C for 3 hours in UHV + 160 C for 48 hours in 3 mTorr N_2.). The 160 C N_2-infusion was done on a different cavity than used for the other three, however, its baseline performance was similar and was omitted for simplicity. 10% error bars on data points have been omitted.

and may migrate to the niobium substrate, making 800 C degassing unnecessary. Regarding the mean free path, it has been shown that the formation of anti-site defects (wherein a niobium and a tin atom have swapped position in the lattice) is extremely common at these temperatures [SCP+21]. The anti-site defects create a short mean free path that is not changed by baking. Finally, some of these treatments may make changes to the first several nanometers of material and have material effects that are not relevant in Nb_3Sn. It may be the case that these processes have no similar effect in Nb_3Sn cavities.

Decreases in quality factor may be caused by tin depletion in grain bound-

aries from additional baking. The increased temperature may allow tin in grain boundaries to migrate further into the material and form low tin content Nb_3Sn. It is energetically favorable to form tin depleted Nb_3Sn over stoichiometry Nb_3Sn in a niobium rich environment [SCP+21]. Tin diffusion is slow through Nb_3Sn but fast through grain boundaries, causing grain boundaries to become depleted faster. Tin rich and tin poor grain boundaries have been shown to cause Q-slope behavior in Nb_3Sn cavities [CPT+21]. To successfully (if they have any beneficial effect in Nb_3Sn) 800 C bake or nitrogen infuse Nb_3Sn cavities will likely require the process to be done during the coating treatment for which we are modifying our Nb_3Sn growth furnace to accommodate.

7.6 Evidence of Multi-Gap Superconductivity

Figure 7.8a and 7.8b show the quality factor vs temperature and resistance vs temperature of a Nb_3Sn cavity (in this case, a 2.6 GHz cavity). The R vs 1/T plot exhibits an unexpected behavior: the low temperature resistance should be residual dominated ($R_{BCS}(T = 2\,K) \approx 10\,p\Omega$) and be flat, but instead has a mild slope. Figure 7.8b shows a BCS fit applied to the data (as described in sec. 4.6). At low temperatures we don't get agreement with the data: the experimental data has more of a temperature dependence than we expect. Clearly this cavity has more complicated dynamics than our single-gap BCS model accounts for.

Figure 7.8c shows an extracted temperature dependent surface resistance[5]. This plot appears as two straight line regions with a transition between them.

[5]This was extracted using a tin-depleted model that is discussed below. This curve simply amounts to subtracting a constant residual resistance, R_0, from the data in Fig. 7.8b. Changing the value of R_0 changes the slopes seen in Fig. 7.8c but the same 'two slope' structure remains.

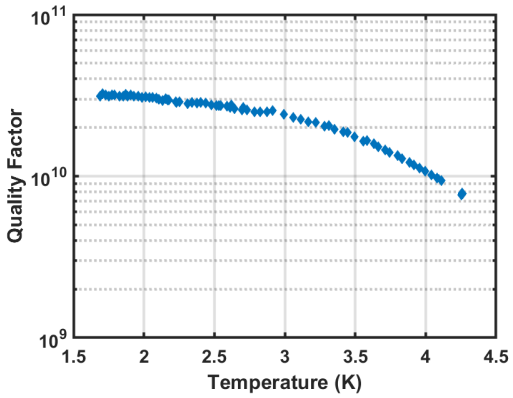

(a) The Q vs T curve of a 2.6 GHz Nb_3Sn cavity at 3 MV/m.

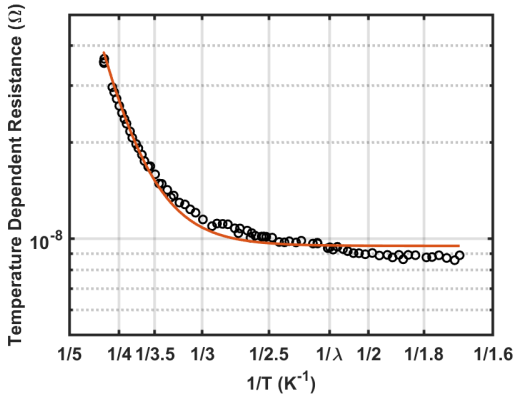

(b) R vs 1/T curve of a 2.6 GHz with a single-gap BCS curve fit.

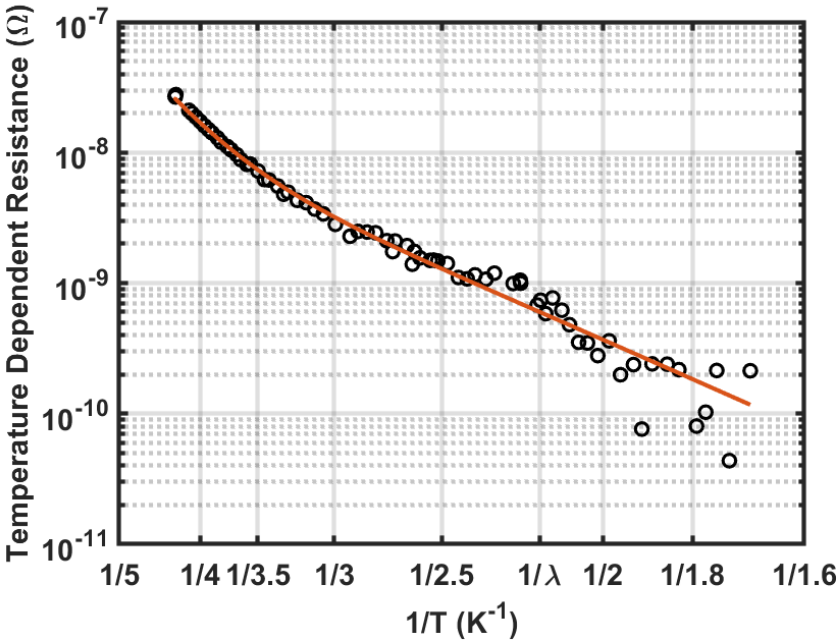

(c) The temperature dependent component of the resistance vs 1/T.

Figure 7.8: Performance plots of a 2.6 GHz Nb_3Sn cavity.

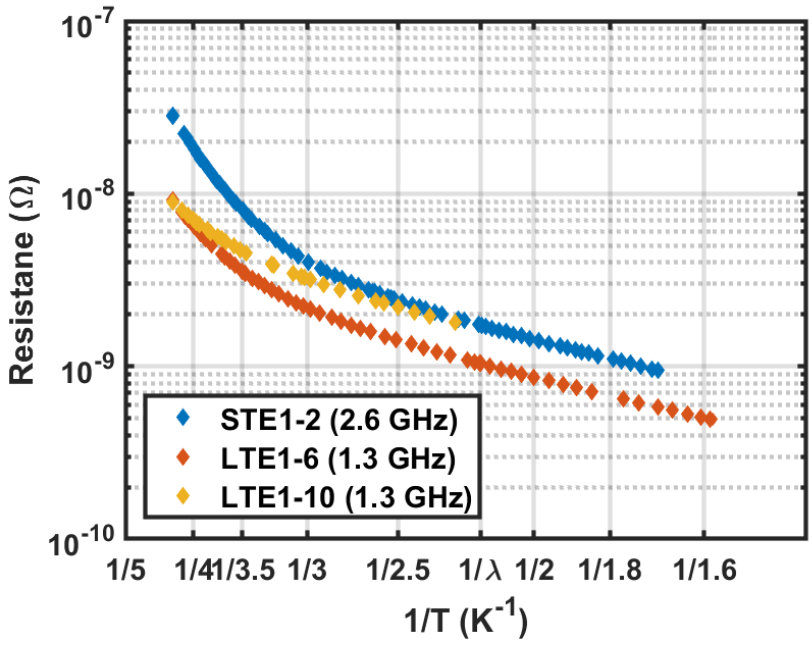

Figure 7.9: The temperature dependent resistance of several Nb_3Sn cavities. Notice that all of them present the same 'two-gap'/'two-slope' behavior.

This is what the sum of two exponentials looks like on a logarithmic plot. Recalling that $R_{\mathrm{BCS}}(T) \sim exp(-\Delta/k_bT)$, this suggests that the data could be represented by the sum of two or more R_{BCS} functions with different Δs and T_cs. Hence we will refer to this phenomenon as 'double-gap' or 'multi-gap' superconductivity.

In general, all Nb_3Sn cavities coated at Cornell show this behavior. Figure 7.9 shows the temperature dependent resistance for several cavities. We can see that they show the same 'multi-gap' type behavior.

Understanding the cause of this could help us improve our Nb_3Sn cavities. We noted that standard BCS fitting finds that for a typical Nb_3Sn cavity the BCS-surface resistance (field-independent) is $\approx$ 8 nΩ at 4.2 K and the residual resistance is $\approx$ 8 nΩ at 10 MV/m. Reanalyzing cavity data with a tin-depleted model (discussed below) we find that the breakdown is $\approx$ 5 nΩ stoichiometric Nb_3Sn BCS, $\approx$ 4 nΩ tin-depleted Nb_3Sn BCS, and $\approx$ 7 nΩ residual resistance. This

suggested that under ideal conditions we could reduce our surface resistance to a mere 5 nΩ at 4.2 K and achieve quality factors of $5.5 \cdot 10^{10}$–a significant improvement. In addition to this, the mechanism causing the multi-gap behavior may also be involved in the quench mechanism.

7.6.1 Models

We investigate three models to explain what we see in the data: a tin depleted region, fundamental 2-gap superconductivity, and the presence of a normal conducting layer on the surface of the cavity[6]. We provide details here.

7.6.2 Tin-Depleted Regions

We know that tin-depleted regions can be formed in Nb_3Sn and that severely tin-depleted regions have (relatively) poor superconducting behavior (see Fig. 3.6 and 3.7). There is also experimental evidence of tin-depletion in Nb_3Sn cavities [BPG+15, Hal17, Pos14]. Figure 7.10a shows Energy-Dispersive X-ray Spectroscopy (EDS) maps of Nb_3Sn cross-sections. These studies find tin-depleted grains on the surface of the cavity. No grains with more than 3 at. % tin-depletion were found on the surface, however, this technique is statistically limited as only a near infinitesimal proportion of a cavities surface area can be examined (roughly, 100 grains out of 10^{10}). Additional evidence has been provided by point contact tunneling spectroscopy of Nb_3Sn samples from Cornell University [PGH+20, BPG+15, PLP14]. This technique probes the superconduct-

[6]These models were investigated in conjunction with S. Ginnett and also reported in [GPL20].

ing gap, Δ, at the surface of a material (less than the penetration depth of the magnetic field). Figure 7.10b shows results from a recent Nb_3Sn cavity witness (a sample coated with the cavity). This technique finds a spread in the superconducting gap that could be caused by tin-depletion. This provides a potential explanation for the observed 'multi-gap' superconductivity: regions of tin depleted Nb_3Sn with a reduced gap.

To examine this we will use a simple model where there are only two Nb_3Sn phases. Most of the cavity will be stoichiometric Nb_3Sn with a small portion, p, being a tin-depleted phase. The model for our surface resistance is,

$$R_s = (1-p)\cdot R_{\mathrm{BCS},\Delta 1}(T) + p\cdot R_{\mathrm{BCS},\Delta 2}(T) + R_{\mathrm{Residual}}(H)\ , \tag{7.1}$$

where $R_{\mathrm{BCS},\Delta 1}$ and $R_{\mathrm{BCS},\Delta 2}$ are the BCS resistance of the stoichiometric and tin-depleted regions. There is no obvious double-gap signature in the f vs T data, so we conduct our double-gap fitting using the R vs T data and use the results from single gap fitting for the mean free path. Finally, since we cannot independently measure T_c and Δ we use the dependence reported in [God06].

We choose an at. % tin for the second material then fit the residual resistance and the material ratio using MATLAB's fminsearch algorithm. Figure 7.11 shows fits of the same cavity data for several different tin depletion levels. At 23 at. % and above the fits are visibly bad at low temperatures. Assuming 22.3 at. % tin, the cavity shown in Fig. 7.11 has a residual resistance of 8.6 nΩ, a second gap BCS resistance contribution of 7.5 nΩ and stoichiometric Nb_3Sn BCS contribution of 18 nΩ at 4.2 K. Similar analyses on 1.3 GHz cavities find stoichiometric Nb_3Sn BCS contribution of $\approx$ 5 nΩ at 4.2 K.

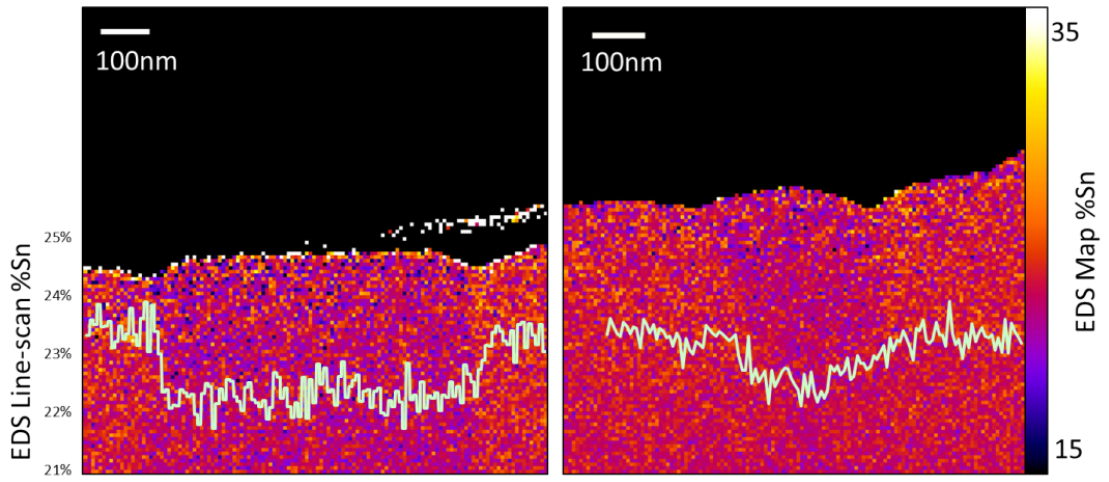

(a) Energy-Dispersive X-ray Spectroscopy (EDS) maps of Nb_3Sn cross-sections showing the tin content (normalized over total tin and niobium content). Overlayed is a EDS line-scan across the region showing the tin content along the line. We can see a tin depleted Nb_3Sn grain in each image. The black region is the cavity vacuum. This image courtesy of P. Cueva and D. A. Muller, Cornell University and Center for Bright Beams (CBB).

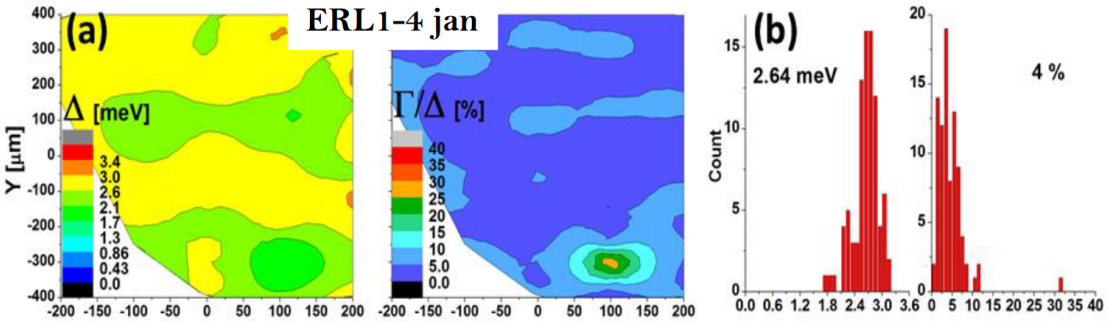

(b) Point contact tunneling spectroscopy of Nb_3Sn samples from the Cornell University SRF group. Left: Surface map of Δ, the gap, and Γ, the pair breaking parameter (discussed in the next section). Right: A histogram of observed Δ and Γ from the surface scans. This figure was adapted from [PGH$^+$20].

Figure 7.10: Evidence of tin-depletion in Nb_3Sn sample produced by the Cornell University SRF group.

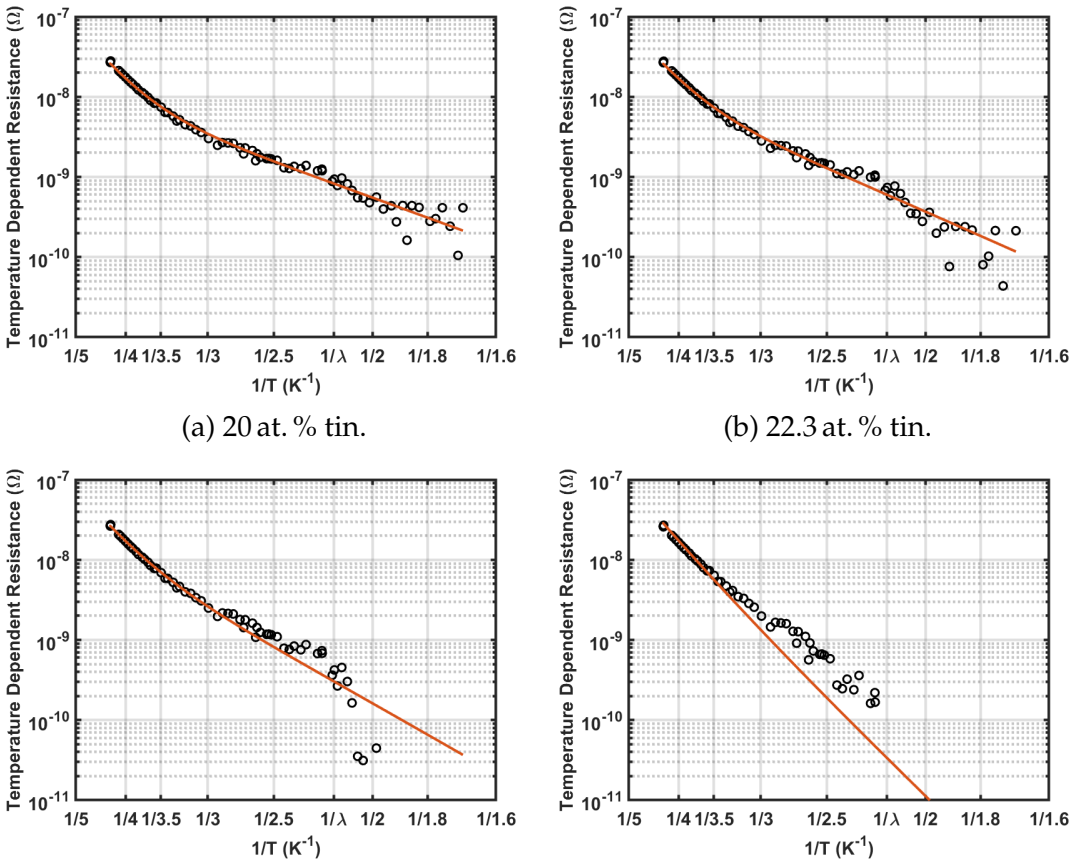

(a) 20 at. % tin.

(b) 22.3 at. % tin.

(c) 23 at. % tin.

(d) 24 at. % tin.

Figure 7.11: Fit double gap BCS curves with various assumed tin percentages for the tin depleted regions. 20 at. % tin and 22.3 at. % tin fit the data well while 23 at. % tin and 24 at. % tin do not.

In general we get good agreement when the tin percentage is less than $\approx$ 23 at. %. This is summarized in Fig. 7.12. This shows the Residual Sum of Squares (RSS) from the fit and the fit parameters vs the tin-percentage. RSS is similarly low for all values below 23 at. %. Below this level both the material ratio and the residual resistance flatten out. These parameters are roughly given by $R_{\text{residual}} = 8.5\,\text{n}\Omega$ and $p < 1 \cdot 10^{-3}$ for this particular cavity.

The small material ratio, p, suggests we are dealing with a small amount of low tin content material. This can make this very hard to spot using microscopy.

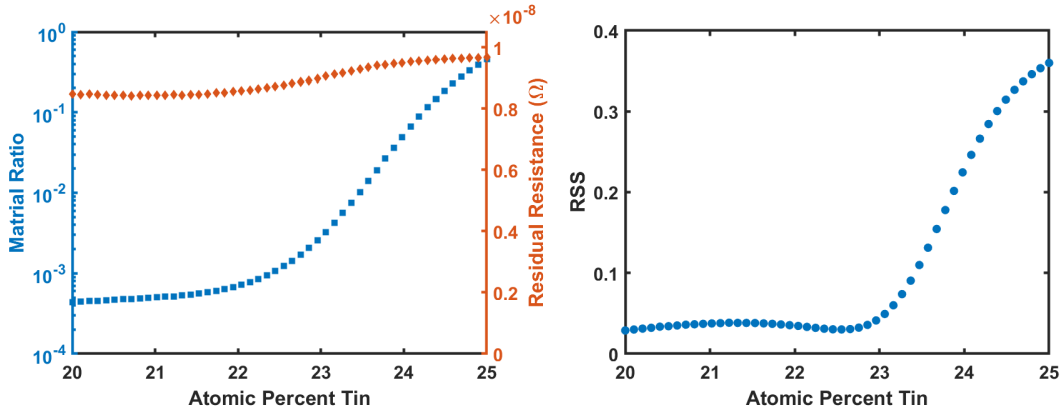

(a) Fit material ratio and residual resistance versus at. % tin.

(b) Residual Sum of Squares from the fit versus at. % tin.

Figure 7.12: Fit parameters and goodness of fit versus assumed tin percentage for a 2.6 GHz cavity.

If we assume that the low tin content material is isolated in single grains, then we would need to look at thousands of grains before we would expect to find one. Preparing the material cross-sections needed to do this measurement is extremely time consuming making their use limited.

One short coming of this model is that there is likely not just two phases of Nb_3Sn, there is likely a continuum following a roughly Gaussian distribution. The two sets of BCS parameters we extract are really an amalgam of multiple tin-depleted regions. If the distribution of the tin-depletion were known, it might be possible to calculate this effective gap. However, we do not need to know exactly what the gaps are, only that this model can fit the cavity data–suggesting that tin depleted regions are playing an active role in our Nb_3Sn cavities.

7.6.3 Fundamental Two-Gap Superconductivity

A question one may ask is whether Nb_3Sn fundamentally has two gaps (as, say, MgB_2 does [MRYJbA11]). Evidence of two gap superconductivity has been claimed in [GGB+04], while evidence against it has been claimed in [JZS+14]. As we have seen, the appearance of a second gap can also be caused by tin-depleted regions rather than a fundamental phenomenon. Though it is not commonly accepted that Nb_3Sn has a second gap we can use our current machinery to try such a fitting. In [GGB+04] a gap of $0.4\,k_bT_c$ is claimed. Figure 7.13 shows a fit with this second gap. There is reasonable agreement (recalling 10% uncertainty in Q values). However, the ratio, p, is $1.3 \cdot 10^{-4}$. We expect p 0.5 for a double gapped material (a fraction of the possible crystal orientations). In MgB_2 this ratio has been found to be 0.6 [MRYJbA11]. We find this explanation unlikely due to the small contribution the second gap makes.

7.6.4 A Thin Normal Conducting Layer

Here we look at a model of a thin ($< \xi$) normal conducting layer on the surface of our Nb_3Sn. This layer could be a layer NbO or other oxide on the surface. In addition, a significantly poorer superconductor on the surface could be expected to have similar behavior (though we have not yet modeled this), such as unabsorbed tin, or a thin heavily tin-depleted layer of Nb_3Sn (potentially created by over-annealing a cavity [BPG+15]). In all these cases the surface layer can experience losses, however, for a sufficiently thin material the layer will become superconducting (through the proximity effect) with a gap worse than that of the bulk material. In addition to this, the layer can reduce the gap of the un-

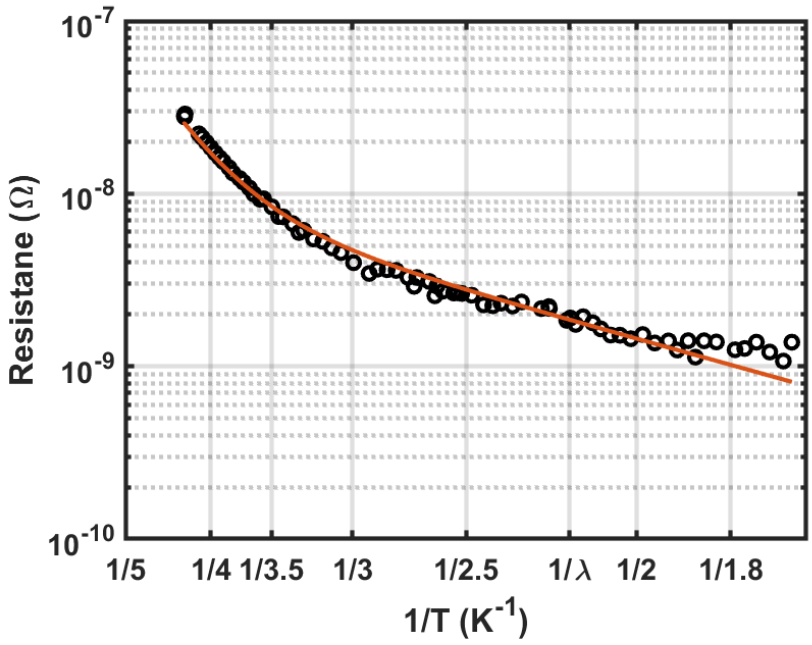

Figure 7.13: Fit fundamental two-gap superconductivity model to R vs T from a 2.6 GHz Nb_3Sn cavity. A residual resistance has been subtracted from the data to highlight the temperature dependence.

derlying in a region close to the surface. The normal conducting layer can drive increased losses and could look like a second material with a different gap.

To investigate this we implement a model by by A. Gurevich and T. Kubo [GK17]. The model we implement assumes a normal conducting layer of thickness, d, and conductivity, σ_n[7]. The model is only valid when $d < \xi$. As noted above, this layer both becomes superconducting through the proximity effect and suppresses the superconductivity of the underlying superconductor near the surface. They utilize a Dynes modified BCS [DNG78] resistance model for the bulk and introduce the Dynes parameter, Γ, which accounts for smearing of the density of states caused by impurities and other aspects of the bulk material (the Dynes parameter is related to the number of quasiparticle states

[7]They additionally investigate the case of suppressed superconductivity near the surface that gradually increases moving into the bulk.

below the superconducting gap). In our cavities $\Gamma \approx 0.03\Delta$ (see Fig. 7.10b). They formulate the Usadel equations for the system and solve them using a quasiclassical green's function approach [BWB+99]. They arrive at an overall resistance formula with components solved for separately,

$$R_{\text{Total}}(T) = R_{\text{bulk}}(T) + \delta R(T) \,, \tag{7.2}$$

where R_{bulk} is the contribution from the bulk to the surface resistance and δR is the contribution of the normal conducting layer. This is the degree to which we will describe their approach here.

We have implemented their formulae and translated parameters into experimentally relevant parameters. The relevant parameters are $d\sigma_n$ (only the combination of the normal layer thickness and conductivity is relevant in this model), the contact resistance between the superconducting and normal conducting layer, R_B, and the induced coherence length in the normal conductor, ξ_n. For details on how to convert the parameters used in [GK17] to experimental parameters please see [GPL20]. In addition, we add an additional residual resistance[8] term to their formulation in order to fit our data.

The experimental data was fit by assuming a fixed value $d\sigma_n$ and fitting for R_B, ξ_n, and R_0. Results of fitting are summarized in Fig. 7.14. We were able to find good fits to the experiments for a wide range of parameters. In particular, every value $d\sigma_n < 1 \cdot 10^{-3}$ achieves a good fit to the experimental data. We

[8]It should be noted that the addition of a Dynes parameter to the superconductivity introduces a temperature independent component to the surface resistance [GK17],

$$R_i = \frac{2\pi^2 \mu_0^2 f^3 \sigma_s \Gamma^2}{\Delta^2 + \Gamma^2} \,, \tag{7.3}$$

where σ_s is the conductivity of the superconductor when in the normal conducting state.

can further restrict the range of reasonable values by noting that ξ_n should be at least several atomic spacings (> 1 Å) for it to have any meaning. This restricts $d\sigma_n$ to between $1 \cdot 10^{-5}$ S and $1 \cdot 10^{-3}$ S. Assuming a 1 nm normal layer this puts the normal conducting material conductivity, σ_n, between $1 \cdot 10^4$ S/m and $1 \cdot 10^6$ S/m– reasonable values for a conductor. Overall, we can make physically reasonable fits to the data.

Figure 7.14c shows the difference between a hypothetical cavity with and without the normal layer modelled here. Similar to the tin-depleted model we see a decrease in the fundamental BCS resistance of Nb_3Sn.

7.7 Summary

We have gathered a great deal of experimental data that can inform us of the nature of our quench mechanism. We have seen that the quench field is reproducible (14-18 MV/m), temperature independent (below 4.2 K), and frequency independent (or 'weakly' dependent). Reaching the superheating field of a large tin depleted region would show a strong temperature dependence. We expect multipacting to have a strong frequency dependence (see section 2.2.1) which we do not see. Our current results appear to rule out these quench mechanisms. In the next chapter we will explore temperature mapping results that will implicate other mechanisms–particularly the thermal instability of Nb_3Sn layer as important candidates.

We have also seen evidence of a second gap in the material. We cannot definitively say what causes the second gap, but our models suggest the depression of the superconducting gap either through tin-depleted regions or thin sur-

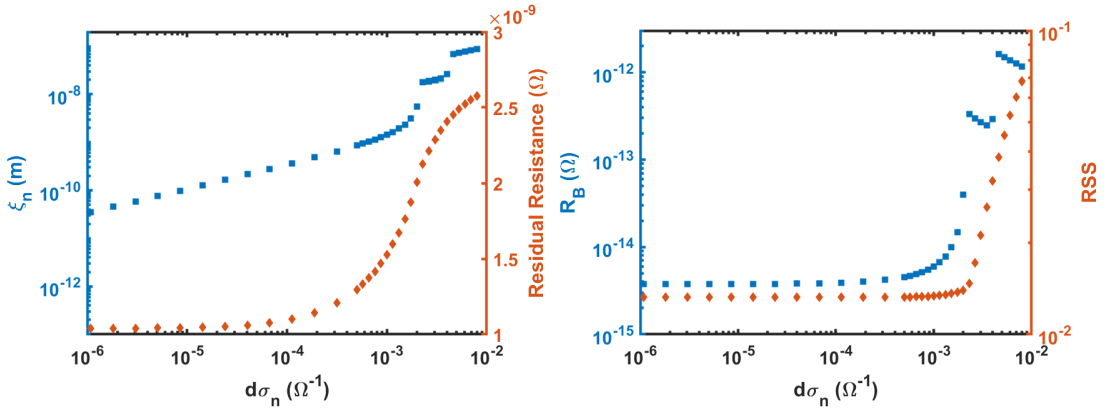

(a) (b)

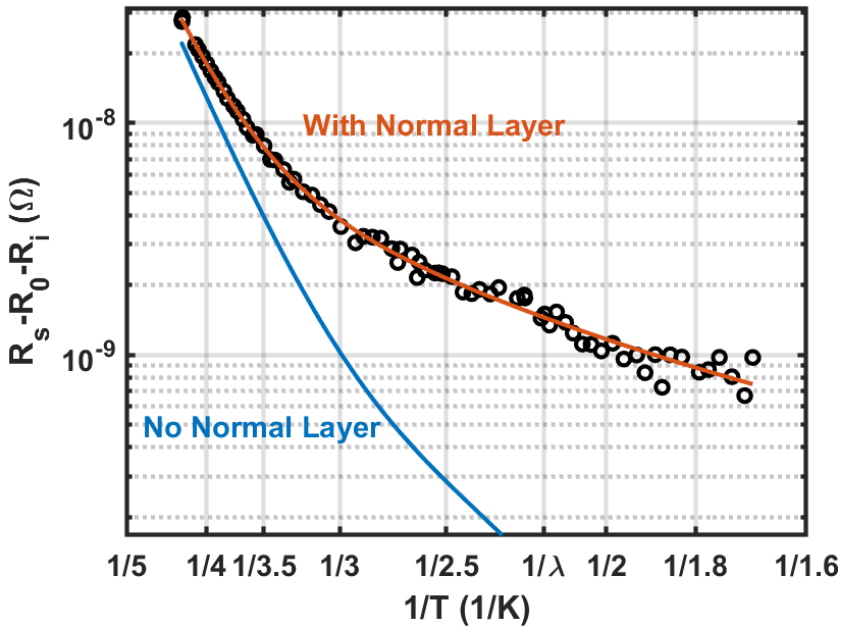

(c)

Figure 7.14: Fitting results of a normal conducting surface layer model on a 2.6 GHz Nb_3Sn cavity. a) Fitted induced coherence length, ξ_n, and residual resistance, R_0, versus choice of $d\sigma_n$. b) Fitted contact resistance, R_B, and Residual Sum of Squares (RSS) after fitting versus choice of $d\sigma_n$. c) R vs T data with normal conducting layer model fit overlayed. The displayed data is the total surface resistance with (fit) residual resistance, R_0, and Dynes parameter induced residual resistance, R_i subtracted. Additionally plotted is the same model but without any normal conducting layer showing the large potential decrease in surface resistance.

face layers of depressed superconductivity caused by normal conductors or low T_c superconductors (including tin-depletion) is responsible. Both tin-depleted grains and thin layers of tin depletion at the surface have been seen in Nb_3Sn samples and seem a likely candidates [BPG+15, Hal17, Pos14]. We will revisit this in our conclusion with additional evidence that suggests tin-depleted regions/thin layers are responsible.

CHAPTER 8

DYNAMIC TEMPERATURE MAPPING OF NB_3SN CAVITIES

In chapter 5 we introduced temperature mapping and gave an overview of the design and capabilities of a new high-speed temperature mapping system. The commissioning of this equipment was done using Nb_3Sn cavities and we can learn a lot about the Nb_3Sn quench mechanism by looking at these data sets, which we do here. We will start by talking about the distribution of heating on our cavities, then examine temperature jumps and the cavity quench dynamics. We will conclude by examining thermal models of the cavity wall and looking at theoretical models of cavity temperature jumps. In particular, the thermal modeling will implicate thermal instability of the Nb_3Sn layer as a major driver of cavity quench. These models inspire ways to potentially improve the quench field in Nb_3Sn cavities.

We remind the reader that this data should be considered preliminary. During commissioning of the T-map electronics errors were found and failures occurred creating only partial data sets. More detailed studies will be conducted on Nb_3Sn cavities in the future.

A total of 4 Cornell Nb_3Sn cavities have received testing with the new temperature mapping systems. Their identification codes are (in chronological order of testing): LTE1-9, LTE1-10, ERL1-4, and LTE1-6. Temperature mapping during tests of LTE1-9 and LTE1-10[1] were effected by errors that compromised most of the T-map data, but have since been resolved (firmware errors and insufficient cooling of the electronics). LTE1-6 was, unfortunately, the victim of a

[1]These cavities were receiving RF as part of other experiments and the temperature map was attached to test functioning.

field emitter that caused a premature cavity quench and is awaiting retesting. ERL1-4 is a standard coating (see section 3.3) Nb_3Sn cavity. This is the cavity for which we have the most complete data set. Here we will concentrate on results from the cavity ERL1-4.

ERL1-4 received two days of T-map testing. For both days one DAQ board had failed (this board is being replaced). On day 1 some of the ADCs were saturated at low temperatures (on the highest resistance sensors). The preamplifiers in the T-mapping electronics were turned down slightly to prevent this from happening again. Low temperature tests from day 1 show more 'bad sensors' in T-maps (white squares with no data). On day 2 an additional DAQ board failed creating another white rectangle in the temperature maps (the on-board software simply froze, and the board was easily fixed after the test). We address these so inconsistencies between operational sensors on temperature maps is understood.

8.1 Static Temperature Maps

Though we are excited about dynamic measurements we will start by showing some static temperature maps. This temperature mapping system is more sensitive than those used in the past and could see small temperature rises that were previously unobservable.

Two static T-maps are shown in Fig. 8.1: one at 4.2 K and one at 1.8 K, both before the cavity quenched for the first time. Interestingly, both cavities show significant variation in distribution of heating. At 4.2 K there is more heating on the upper half of the cavity than on the lower half. This could suggest a

higher BCS resistance on the top of the cavity. We note that the cavity/T-map is oriented identically to how it is in the furnace: the top half of the cavity is further from the tin source, but portions have 'line of sight' to the tin source. Additional heating on the upper half cell has been seen before [Pos14]. At 1.8 K the temperature distribution is more randomized with most channels showing no heating with the detection limit (15 µK). We could potentially be seeing the distribution of residual resistance (and 'multi-gap' material) in this cavity (for stoichiometric Nb_3Sn the BCS resistance is ~ pΩ at 1.8 K).

Sensor sensitivity adds some complexity to interpreting these results. We discussed 'sensor sensitivity' in chapter 5. We quoted a previously found value the sensor sensitivity is 0.35 ± 0.13 [MK85]–meaning the sensors on average read only 35% of the wall temperature rise (above the helium bath temperature). This value was found for thermometers used on niobium surfaces. Changes in thermal interface resistance (between the thermal grease and the cavity wall and Kapitza resistance between superfluid helium and the cavity wall) could change the sensitivity. In addition, small changes in the application the temperature map sensors to the cavity (amount of thermal paste, pressure, etc.) could also cause changes. It is unlikely that this value is much worse than what was previously seen and we are likely seeing a true distribution of heating.

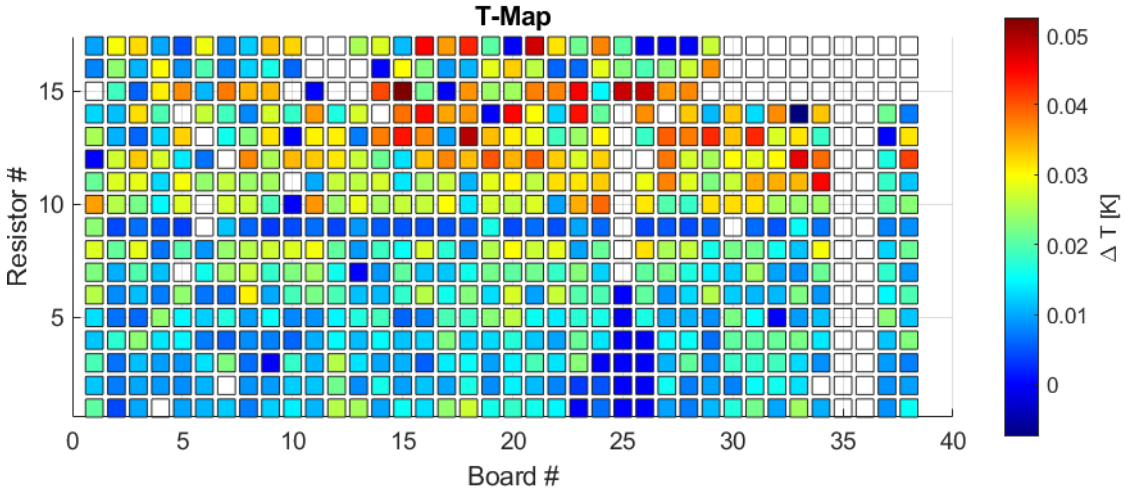

(a) T-map at 4.2 K and 13 MV/m before quench of ERL1-4 (day two).

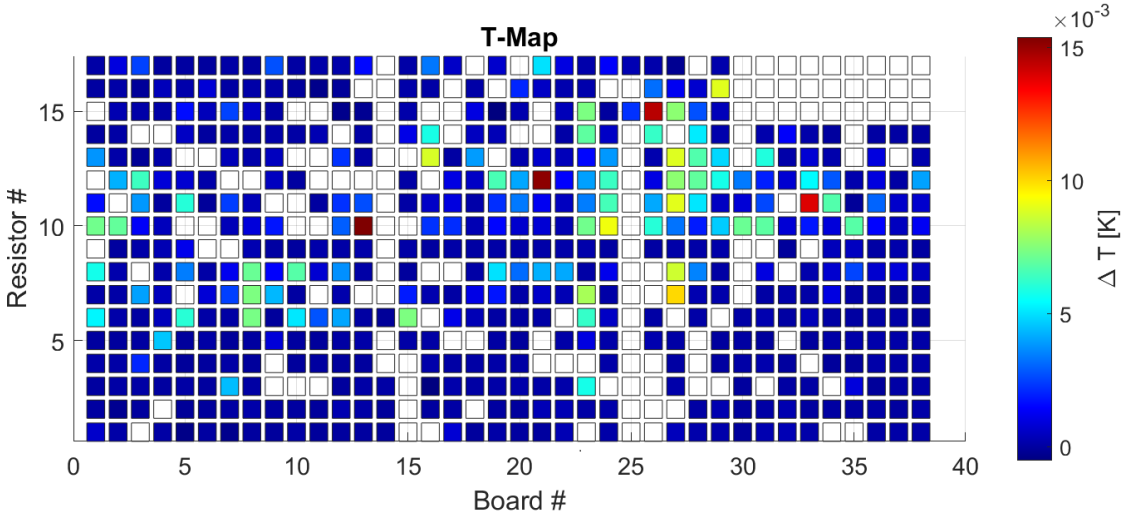

(b) T-map at 1.8 K and 17 MV/m before quench of ERL1-4 (day one).

Figure 8.1: Static (cavity fully charged) temperature maps of ERL1-4. Note that poor thermometer contact is made along the equator of the cavity, reducing the measured temperature.

8.2 Temperature Jumps

In chapter 5 we briefly discussed experiments by D. L. Hall *et al.*[2] wherein dynamic heating was measured at the quench site of a Nb_3Sn cavity. These experiments revealed sudden jumps in temperature that were apparently quantized. These we dubbed 'temperature jumps.' These jumps only occurred within $\approx 0.5\,\mathrm{MV/m}$ of the cavity quench field. The mechanism involved and its relation to the quench mechanism has been the object of much speculations [PHL+19, Hal17, HCL+17]. We can conduct a similar experiment with our system on all thermometers at once.

ERL1-4 was cooled to 1.8 K (day one) and the cavity was charged and discharged over a 50 s window while recording the T-map at 25 ksps. The T-map is triggered when the power to the cavity is turned on. We repeated this process many times, gradually raising the forward power—and thus the maximum field in the cavity—until the cavity quenched. The last iteration before quench was conducted at $\approx 0.09\,\mathrm{MV/m} \pm 0.01\,\mathrm{MV/m}$ below the quench field.

Figure 8.2 shows the temperature rise and fall over time of several thermometers where temperature jumps were observed. Figure 8.3a shows the temperature rise versus B^2. As the cavity is charged a nearly linear (vs the field strength squared) rise in temperature is seen first which is expected for Ohmic heating (some curvature is seen due to the field dependent residual resistance). At high fields the temperature suddenly jumps. There are multiple sizes of jumps seen on single sensors–the larger jumps appear to be roughly

[2]The author would like to note that he was a participant in these experiments when he was a young graduate student and had significantly less grey hair. His task was to manually turn on the power after the temperature recording was started. This task was eventually replaced by an automation script. The author would still like to think that he is more valuable than four lines of scripting.

integer multiples of the smallest jumps seen on the sensor. As the cavity discharged, we see the opposite: the temperature jumps down but there is a hysteresis. The jump down appears to be more spread out, but this may be an aspect of the discharge curve being much steeper than the charging curve at this fields level combined with the lower sampling rate of the RF power meters (compared to the temperature map). This behavior is similar to what was described by D. L. Hall *et al.*.

The large jump seen in Fig. 8.3a is likely the sum of multiple small jumps that happen at the same time. We can see this by looking at the discharge cycle in more detail. Figure 8.3c shows a charge-discharge cycle of the same sensor, but this time the forward power is ramped up and ramped down (instead of simple turned on and off). This gives us a better resolution during the discharge cycle. We can see that the jump down is clearly made from multiple jumps down–suggesting that the jump up is also comprised of multiple simultaneous jumps.

Fig. 8.3a also shows that the jumps are occurring at a specific magnetic field. When the fields are ramped (in only one way) it is not clear if the jumps occur at a specific magnetic field or at a specific time. The jumps could have occurred a fixed time after another magnetic field threshold was reached–for instance, a slowly evolving thermal runaway. By slowing ramping the field we can differentiate the magnetic field magnitude from the time, demonstrating a distinct onset field.

These temperature jumps were observed at many locations on the cavity. Figure 8.4 marks all thermometers that saw temperature jumps at 1.8 K. There at 56 channels in all (and some may be obscured by bad channels)–11% of all working channels. These jumps are of different heights and some channels con-

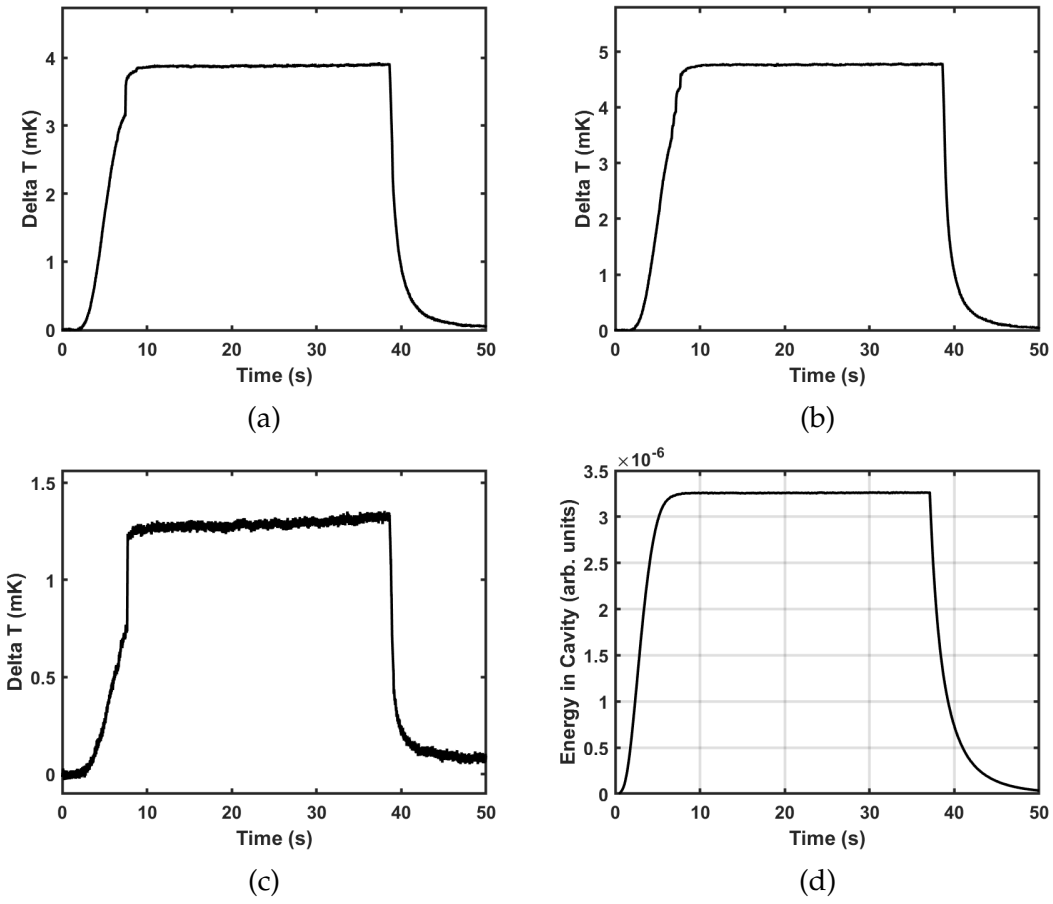

Figure 8.2: a, b, c) The temperature change on several thermometers during the charge discharge cycle. RF power is turned on at 0 s and the cavity takes ≈ 9 s to charge. The power is turned off at ≈ 40 s and the cavity discharges. a) A ≈ 0.5 mK temperature jump is observed at ≈ 7 s. Two smaller ≈ 0.1 mK jumps are also present but may be difficult to see at this scale. b and c show thermometers that are adjacent to each other. d) The energy in the cavity during the charge-discharge cycle.

tain multiple jumps. A histogram of all the surface magnetic fields at which jumps occur is shown in Fig. 8.5. Jumps were also observed when testing LTE1-9 and LTE1-10.

Not all temperature jumps are independent: some jumps occur at near-identical timing on adjacent sensors (see Fig. 8.6). Thermal spread from a single heat source could be warming multiple temperature sensors. We conducted

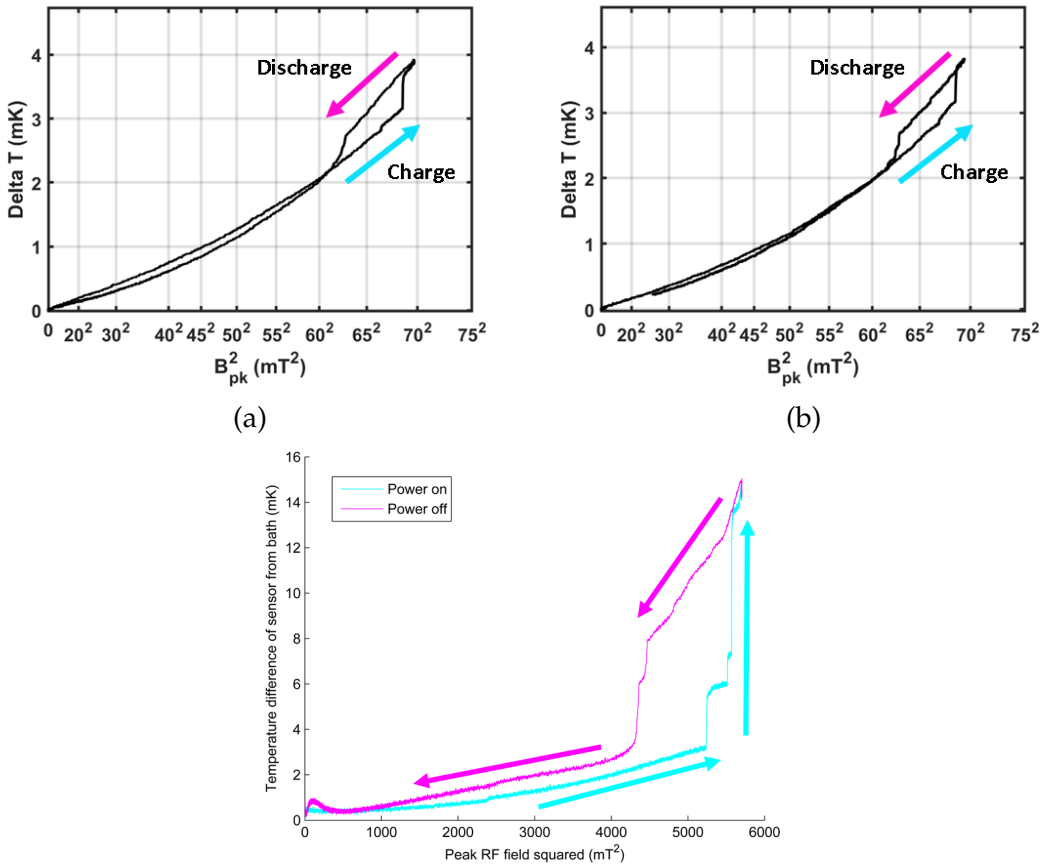

Figure 8.3: Temperature versus B^2 as the cavity is charged and discharged. a) The same charge cycle as shown in Fig. 8.2a. b) The same thermometer as a) but the forward power was ramped up and down to slow the charge and discharge speed. The jumps appear to occur at the same fields, but the downward jumps are more pronounced. It can be seen that there are 4 distinct jumps during the discharge cycle. c) Previous measurements by by D. L. Hall *et al.*.

thermal simulations of the thermal spread from point defects in our system (detailed in section 8.4). We find that at the spacing of our thermometers ($\approx$ 1 cm) the temperature rise drops to $\approx$ 5% and should still be measurable by our system on adjacent sensors (for the larger jumps we see). This shows that some adjacent sensors are likely measuring a temperature jump from the same source.

The distribution of jumps contains additional peculiarities. In many in-

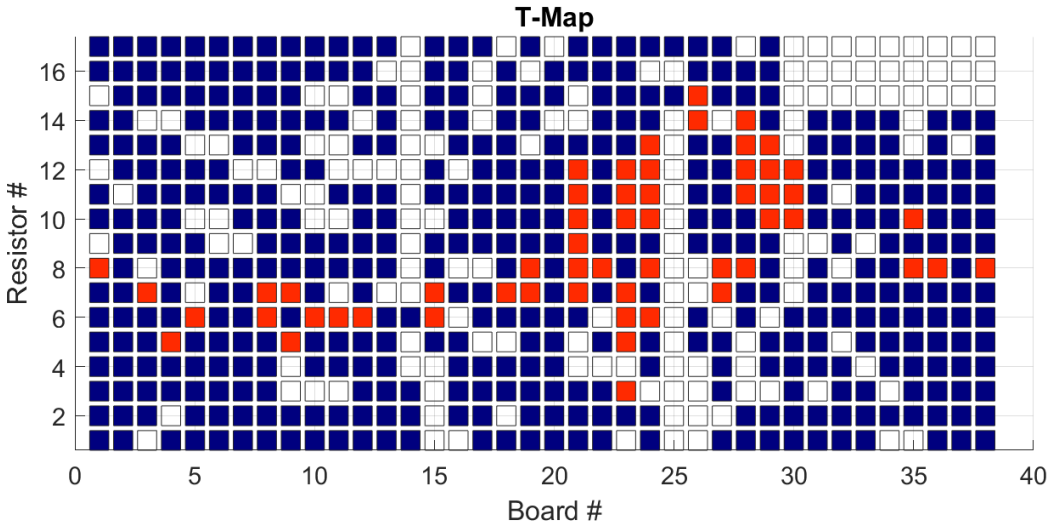

Figure 8.4: All channels where at least one temperature jump was observed are marked in red (ERL1-4).

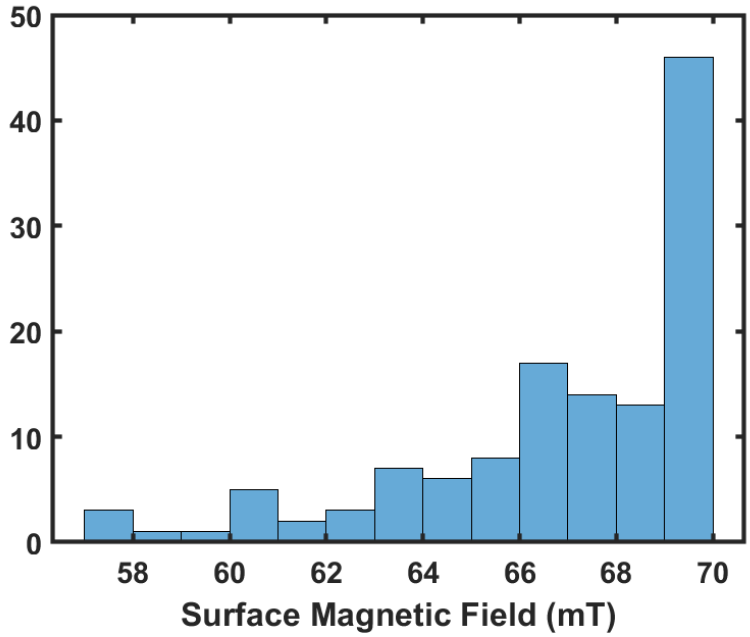

Figure 8.5: A histogram of the magnetic fields at which temperature jumps occur in ERL1-4. This magnetic field value does not account for any local surface magnetic field enhancement that may occur at the jump's location. Notice that the number of jumps grows as the field increases.

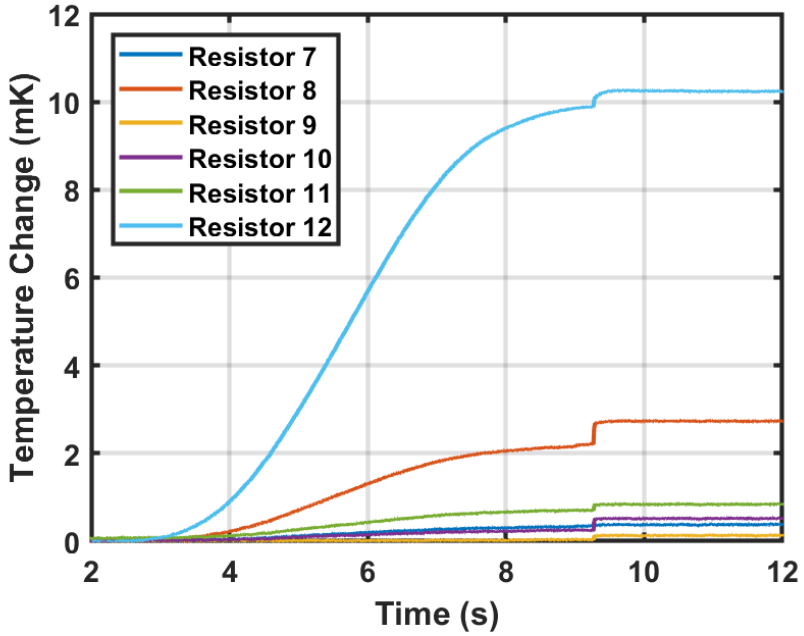

Figure 8.6: Temperature versus time of thermometers on board 21. Notice the jumps that occur at the same time. The jumps on board 21 were only seen when the cavity quenched–not at the lower field measurements. This may be an artefact of the multipacting quench, but more investigation is needed.

stances sensors adjacent to those that show jumps do not show any jumps. Some of these channels show no heating (see below), but others do. It is curious that we do not see jumps on these channels. In addition, there are some locations with a considerable vertical spread of temperature jumps. One such location is along column 21 where all the sensors have a jump at the same time (some channels have additional jumps). This is all in contrast to the measurements by D. L. Hall *et al.* where no jumps were seen on sensors adjacent to the quench site (we note that our thermal modelling–discussed below–of temperature spread from a jump defect suggests D. L. Hall did not have the temperature resolution to see the signal of a jump on adjacent sensors). These distributions are not explained by previous proposals. The vertical spread of heating seen is reminiscent of field emission in which electrons impinge on a vertical line (parallel

to the beamline axis). The distribution of jumps warrants more investigation in future studies, and we remind the reader that these studies are preliminary.

Some thermometers in the temperature map show very little heating (before quench and at 1.8 K). This may be a result of a distribution of residual resistance on the surface or that some sensors have particularly low sensitivity at low temperatures. Low sensitivity sensors may not be able to read temperature jumps once below the superfluid helium transition temperature. At 4.2 K, where the helium thermal interface conductance is lower, thermometers read increased heating and additional channels appear to show temperature jumps. In addition, after the cavity is quenched, the residual resistance increases and many thermometers that had previously not read any heating then do. We suspect that our sensors are working and we merely seeing the distribution of residual resistance, however, more measurements and analysis are needed to draw a firm conclusion.

8.2.1 Cavity Quench

Using the new system, we can record the temperature map as the cavity goes through quench and make videos of the thermal evolution. The author regrets that the .gif format is not fully supported by paper and directs the interested reader to [Por20, P$^+$21]–a presentation wherein these videos are reported. Figure 8.7 shows a frame from a T-map video of cavities LTE1-9 and ERL1-4 going through their first quench (after cooldown). Both quenches take place over $\approx$ 50 ms and at 17 MV/m.

The quench is not localized and is spread preferentially along the equator.

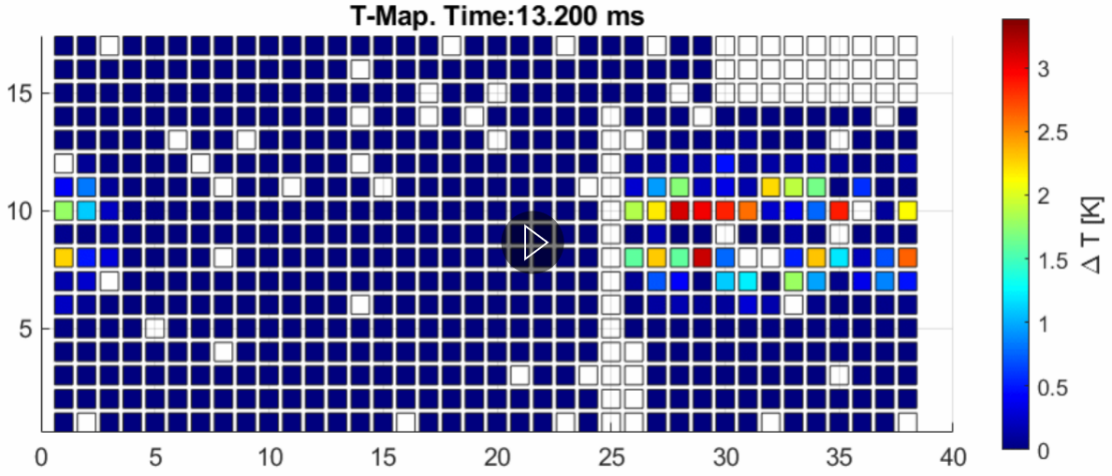

(a) LTE1-9 quench at 1.9 K.

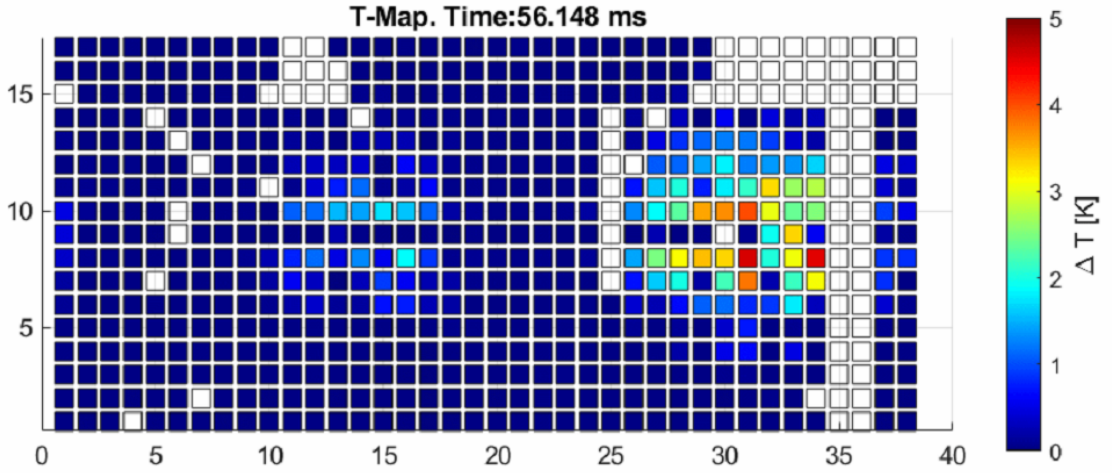

(b) ERL1-4 quench at 4.2 K.

Figure 8.7: A frame from a quench T-map video of both LTE1-9 and ERL1-4. These show what appears to be multi-pacting quench behavoir. The video play button was left in plot b) to further tempt the reader to watch the videos presented in this talk [Por20].

The quench did not originate in one spot and spread but turned on across the entire region. Observation of the timing of temperature spikes across sensors and quenches (with the same signature) shows a degree of randomness: there is timing change between sensors and timing change on the same sensor between different quenches (see Fig. 8.8). In one quench of ERL1-4 the heating signature was instead concentrated on the equator between columns 5 and 20. The

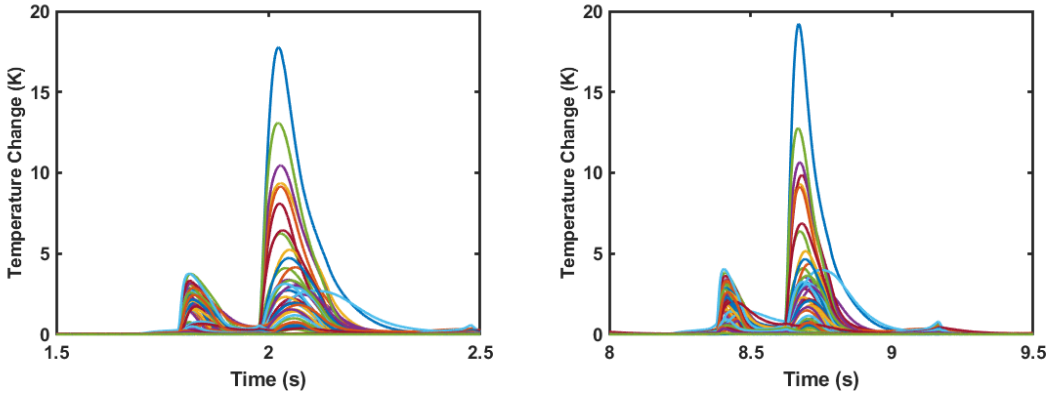

(a) (b)

Figure 8.8: Heating on equator sensors of two different multipacting quenches. The 3 hottest sensors maintain a consistent temperature profile, but below this there is a degree randomness in the timing and heating of different thermometers. A smaller spike in heating is seen just before the main multipacting quench. This is a multipacting quench that occurred on another part of the cavity's equator.

concentration of heating at the equator, the non-locality of the quench, and the randomness we believe suggests a multipacting type of mechanism is at play[3].

This behavior was not expected based on previous (static) temperature mapping. Previous quench maps of Nb_3Sn cavities have shown highly localized quench sites. Here we see the opposite.

Multipacting is often associated with the production of radiation which we did not detect here. However, this radiation be directed and may have missed our single sensor. In addition to this, the entire multipacting type quench takes place over only $\approx 50\,\text{ms}$ and we see no indication of multipacting before this. Since we only record the radiation once per second we could completely miss the radiation signature in a data recording.

[3]However, we will point out, no one has ever (until–maybe–now) taken a dynamic temperature map of a multipacting induced quench.

8.2.2 Quench Site Evolution

After the first cavity quench we continued to record the temperature as the cavity went through additional quenches. Figure 8.9 shows a T-map taken over the next 32 cavity quenches of ERL1-4 showing the average temperature. We can see that there are now two quench regions: along the equator, and at a localized spot in the bottom left.

Time resolved thermometry reveals that the quenches move back and forth between the two sites. Quenches at the equator show some randomness in location and relative heating. The second site, however, has highly reproducible dynamics: the same location and relative intensities. After the first 33 quenches the quench site settled on the second, localized site (see Fig. 8.10). The next 100 quenches were recorded and all of them occurred at the second site. A likely explanation is that we processed the multipacting site and hit a defect at with a slightly higher field limitation.

This also reveals why the multipacting quench was not previously observed. The previous temperature mapping system measures a quench map over 100's of quenches. Since only a handful of the first few quenches are multipacting we could only see the second site in these measurements.

8.3 Dynamic Heating at the Second Quench Site

Curiously, while D. L. Hall *et al.* observed temperature jumps at the (localized) quench site, we do not. Before the first quench at this location we cannot detect any temperature rise ($< 10\,\mu K$). Figure 8.11 shows the temperature at the second

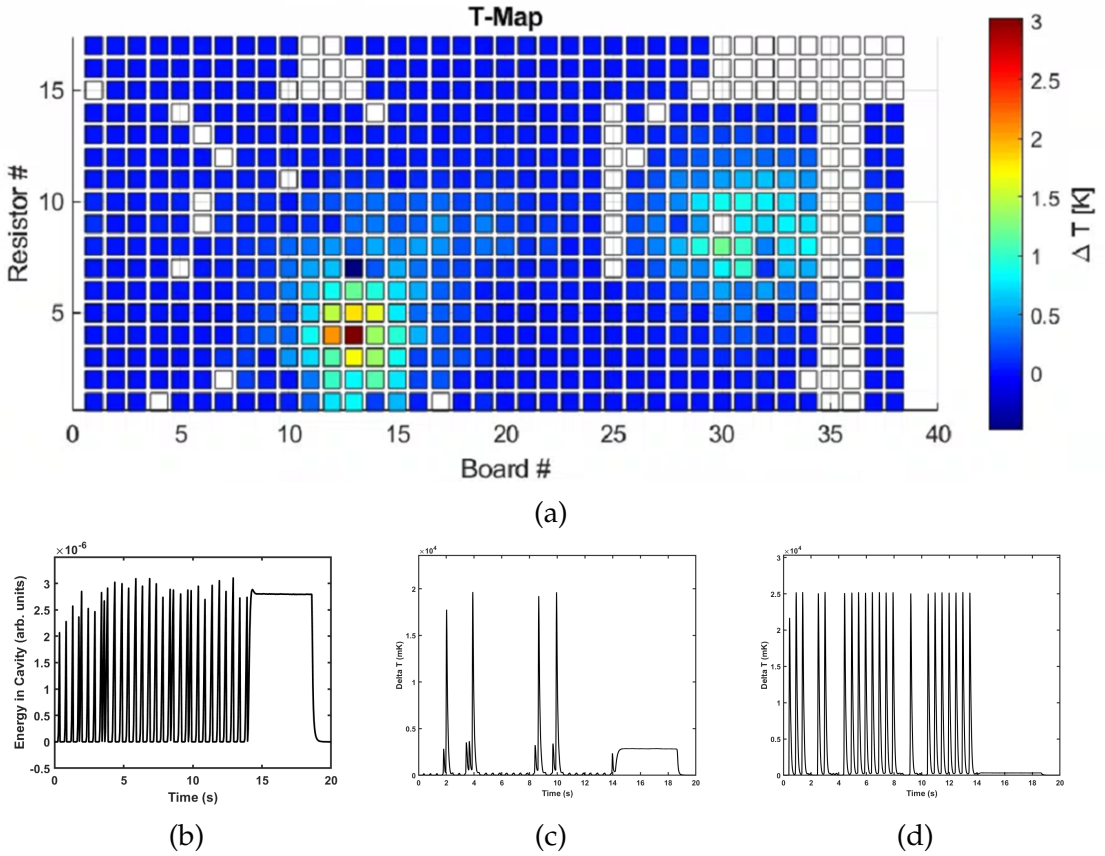

Figure 8.9: a) A temperature map (at 4.2 K) showing the average temperature while the cavity is quenched 32 times. These are the 2nd through 33rd quenches of this cavity. Two different hot spots emerge, indicating two quench locations. b) Shows the transmitted power (proportional to the energy in the cavity) over time during the measurement. The measurement lacks the time resolution to gauge whether the peak heights are changing. Two temperature vs time plots at c) the equator quench region and d) the second localized quench sites. Large temperature spikes indicate quench at or near the thermometer. Medium height temperature spikes indicate a quench that is still somewhat near (still on the equator). We can see that quench is moving between the equator and the hot spot in the lower left.

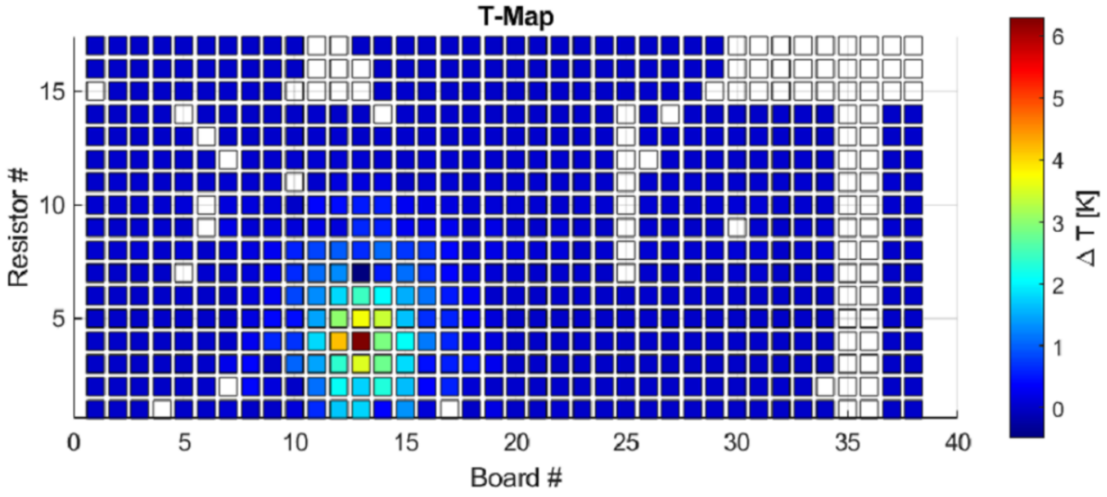

Figure 8.10: A temperature map (at 4.2 K) showing the average temperature while the cavity is quenched many times. This temperature map was taken after the cavity had previous quenched 33 times. We see only a single localized quench site.

quench site during the first quench at this location at 1.8 K. The first quench to occur here shows a rise in temperature to 40 µK followed by the cavity quench (the temperature spikes sharply). No dynamics appear. After the first quench at this site there is considerable heating when the cavity is charged but no jumps are observed (other than quench–if the cavity is quenched).

This may not indicate that jumps are unrelated to quench. One possible explanation is that the first jump to occur here was large enough to cause the cavity to quench. Thermal simulations (discussed below) suggest that large jumps are made up of multiple small, nearby jumps (or heating is spread over a large area). The quench field is determined not by the large jumps we see but the size of the small jumps. If the first jump here is slightly larger than the others it would instantly cause the cavity to quench. We are then likely at a state where other regions are very close to causing quench.

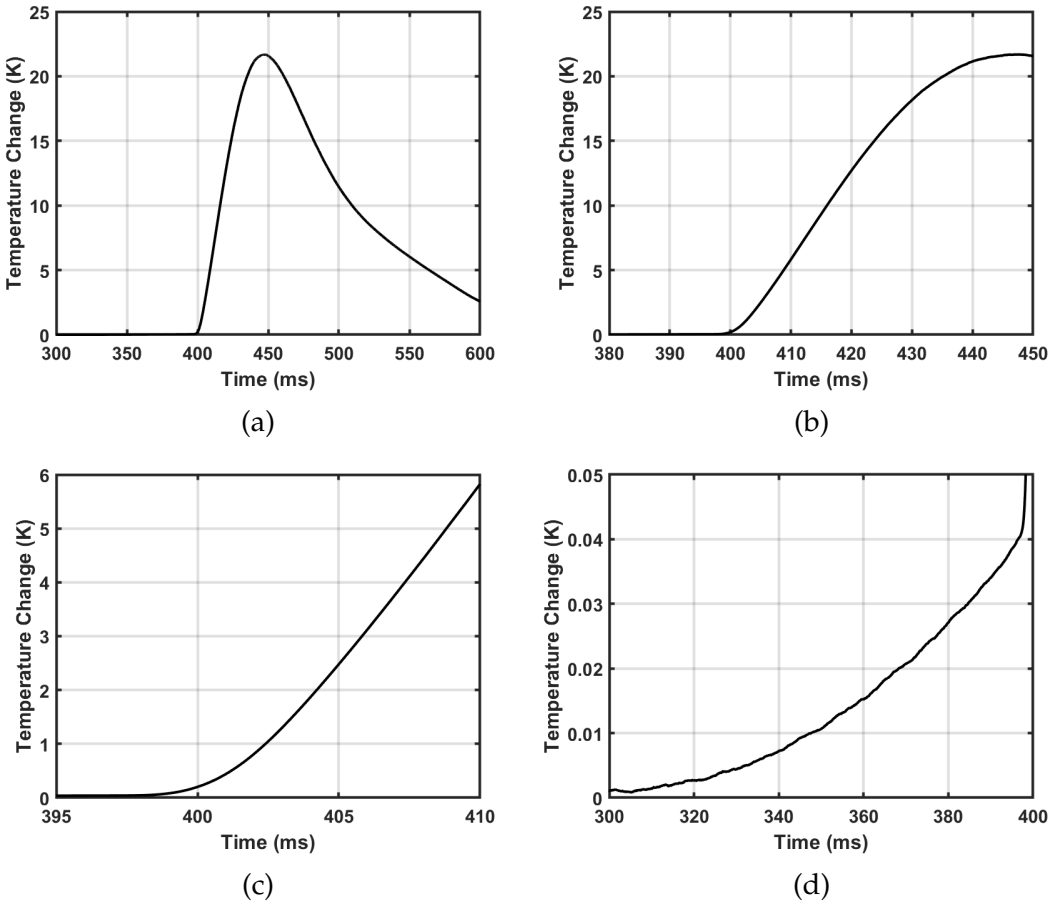

Figure 8.11: Heating at the second quench site during the first quench at this location at different zoom levels.

8.4 Thermal Modeling of Defects

Heat from the RF surface layer or a defect must travel through several layers of material before reaching a temperature sensor which obscures the signal. The issue is schematically shown in Fig. 8.12. Our cavity wall is made up of 3 µm of Nb_3Sn, 3 mm of niobium, and an additional 3 µm of Nb_3Sn. In order to understand what we are measuring we have conducted thermal modeling and calculations of heat transport in our cavities.

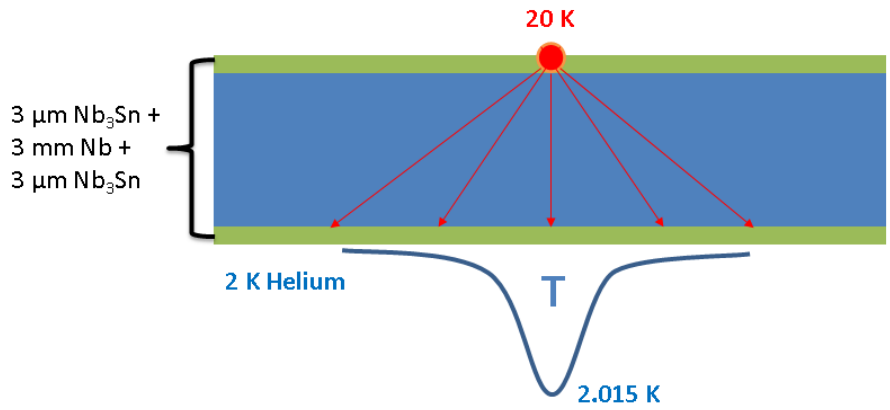

Figure 8.12: A schematic diagram showing the flow of heat through the Nb_3Sn cavity wall.

A thermal equilibrium[4] simulation code was developed to study heat transport in our cavity wall. This code includes many aspects that are unique to SRF cavities and not included in standard simulation software. This code includes, applied RF fields generating heat, temperature dependent BCS resistance (and residual resistance), temperature dependent conductivities, and Kapitza/thermal interface resistance at the helium interface. The model assumes a flat surface with RF fields and vacuum on the inside and liquid helium on the outside at a temperature T_b.

This code was developed based off of the same method used in the Cornell University SRF group's HEAT code [Pad83, VXP07], but extended to multilayer materials. We use cylindrical coordinates and assume azimuthal symmetry. This reduces the problem to two dimensions in r and z. We divide the problem into square mesh cells (of variable size). The method of successive

[4]Though dynamic simulation would be ideal, very small mesh-cells are required in the thin Nb_3Sn layer while the overall simulation is large. The small mesh cells require a small time step, Δt, to be used in order to prevent numerical divergence, while the large dimensions of the entire problem requires a (relatively) long simulation time to computer. This results in an exorbitant computation times when run on an ordinary compute ($\sim$ 10 years)–at least when using the forward difference scheme that we attempted.

over-relaxation [Had00] is used to solve the problem.

8.4.1 Model Details

We will give a short explanation of the technique [Pad83, VXP07, Had00]. The technique is explained in my greater detail in appendix A. The heat equation (in 1D) is given by,

$$\frac{\partial T}{\partial t} = \frac{k}{\rho c}\frac{\partial^2 T}{\partial x^2} \,, \tag{8.1}$$

where k is the thermal conductivity, ρ is the density, and c is the heat capacity. We can discretize the problem as,

$$\frac{T_{n,j} - T_{n-1,j}}{\Delta t} = \frac{k}{\rho c}\frac{T_{n-1,j+1} - 2T_{n-1,j} + T_{n-1,j-1}}{\Delta x^2} \,, \tag{8.2}$$

where Δt is the time step, Δx is the position step, and $T_{n,j}$ is the temperature of the j^{th} element at the n^{th} time step. We can solve for $T_{n,j}$ in terms of the $T_{n-1,j}$'s. In vector form we get,

$$\vec{T}_n = (A - 1)\vec{T}_{n-1} \,, \tag{8.3}$$

where A is a matrix containing the spatial relations of the $T_{n,j}$. At equilibrium[5],

$$\vec{T}_n - \vec{T}_{n-1} = A\vec{T}_{n-1} = \vec{b} = 0 \tag{8.4}$$

[5]We note that equation 8.4 does not hold at the boundaries or anywhere that heat is being added or removed from the system

There are various schemes for solving equations of this form. We use successive over relaxation.

For successive over relaxation we solve this equation iteratively (we will reuse the index n, but it now represents a computational step and is unrelated to time). We note that we can write A in terms of diagonal, D, lower triangular, L and upper triangular, U matrices ($A = D + L + U$). We introduce the over relaxation parameter ω. In this scheme we iterate this equation,

$$(D + \omega L)\vec{T}_n = \omega\vec{b} - [\omega U + (\omega - 1)D]\vec{T}_{n-1} \tag{8.5}$$

In terms of individual components,

$$T_{n,j} = (1 - \omega)T_{n-1,j} + \frac{\omega}{a_{jj}}\left(b_j - \sum_{i<j} a_{ji}T_{n-1,i} - \sum_{i>j} a_{ji}T_{n-1,i}\right) \tag{8.6}$$

There are various sufficient criteria under which this equation will converge to an equilibrium solution. Choosing the correct $0 < \omega < 2$ increases the speed of convergence.

We do not meet any of the known sufficient criteria for convergence. All the above math only holds if k is temperature independent, which it is not (nicely, we have lost all dependence on both c and ρ in this scheme and do not need to consider them at all). There are no known necessary criteria, however. Though we cannot guarantee convergence if it does converge then we know it is a solution. In practice we find convergence.

We have made our model more computationally efficient by simplifying the outer layer of Nb_3Sn. Since our layer of Nb_3Sn is small we do not expect to see

any significant lateral heat flow (this is not true on the inside where microns of heat flow can significantly change the BCS surface resistance). Instead, we use an effective interface resistance, κ_{eff} to that incorporates both the Kapitza conductance κ_{LHe} and the conductance of the Nb_3Sn layer, κ_{Nb3Sn},

$$\kappa_{\text{eff}} = \frac{\kappa_{\text{Nb3Sn}}\kappa_{\text{LHe}}}{\kappa_{\text{Nb3Sn}} + \kappa_{\text{LHe}}} \,. \tag{8.7}$$

We quickly summarize additional model details. We use the Kapitza/liquid helium thermal interface resistance from [VXP07, Lan07], and thermal conductivities from [KB96, CC64]. The thermal interface resistance between Nb_3Sn and niobium is not known for our material and is ignored. We adjust the critical temperature of Nb_3Sn based on the strength of the ambient magnetic field using equ. 2.12 and assuming a ($T = 0\,\text{K}$) superheating field of 425 mT. When the material reaches $T_c(H)$ we substitute in the normal conducting resistance and distribute the heating uniformly through the Nb_3Sn layer (the normal conducting penetration depth we calculate to be $\approx 6\,\mu\text{m}$.

8.4.2 Thermal Distribution of a Point Heat Source

In order to understand the temperature mapping of smell defects we conducted thermal simulations to find the temperature distribution of a 'point' heat source in a Nb_3Sn on Nb system. By 'point' we mean the heating is distributed into a 3 µm circle and at sufficiently low heating to avoid thermal runaway in Nb_3Sn. Figure 8.13 shows results (at outer wall) from a thermal simulation of a point heat source (on inner wall) at 2 K and 17 MV/m. The defect is generating 600 µWof heat. This creates a temperature rise on the outer wall of 1.0 mK which

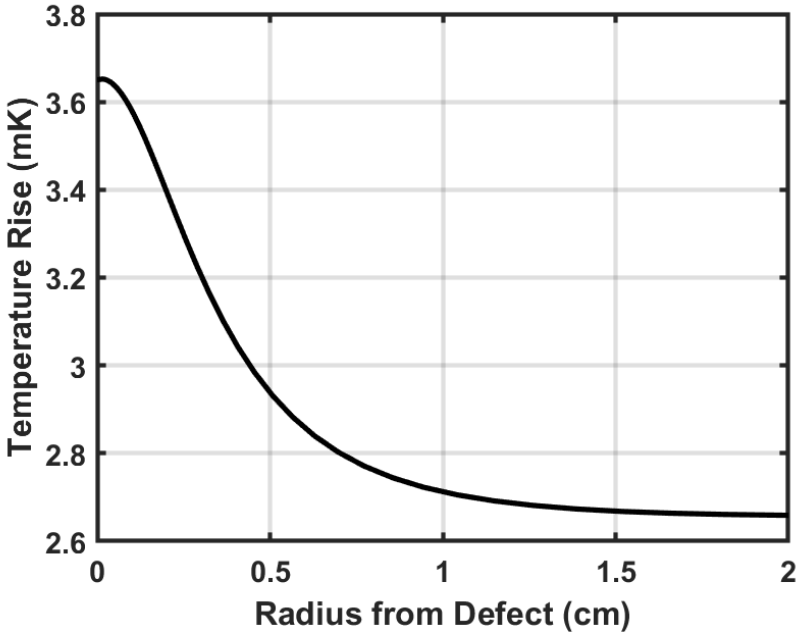

Figure 8.13: Calculated radial temperature distribution of point thermal defect in a Nb_3Sn cavity as measured from the outer wall. Calculation performed with a bath temperature of 2 K, 8 nΩ of residual surface resistance, and an accelerating gradient of 17 MV/m. This defect is generating 600 µW. The temperature rise from the defect is 1.0 mK. The plot does not go to zero since it includes the heating from the residual and BCS resistance. The plot does not include the impact of sensor sensitivity.

falls to only 50 µK, 1 cm away (thermometer spacing is roughly 1 cm).

8.4.3 Thermal Stability of Defects

In chapter 2 we briefly discussed the quench field of a normal conducting inclusion. We want to know how large of a normal conducting region would cause our cavity to quench–or how much heat a small defect must absorbed. We can use a simple 1D, single material, model to develop a conceptual idea of the problem before moving into more rigorous, multi-layer material simulations. We can

repeat the computation done in [PKH98][6] of spherical normal conducting defect (half-sphere), but with a temperature dependent thermal conductivity and we get,

$$r_{\text{crit}} = \frac{4\mu_0^2}{R_{\text{surf}} B^2} \int_{T_B}^{T_c} k(T) \mathrm{d}T \ , \tag{8.8}$$

where r_{crit} is the critical radius of maximum normal conducting region before thermal runaway and R_{surf} is the surface resistance of the normal conducting region. For niobium we find that $r_{\text{crit}} \approx 100\,\mu\text{m}$ and for Nb_3Sn we find that $r_{\text{crit}} \approx 0.5\,\mu\text{m}$ using this equation when $B = 75\,\text{mT}$, the $T_B = 2\,\text{K}$. We have to make a correction for Nb_3Sn since this is much less than the normal conducting penetration depth ($\approx 6\,\mu\text{m}$) we must integrate over the volume to find the losses,

$$r_{\text{crit}} = \sqrt{\frac{12\mu_0^2}{\rho_n B^2} \int_{T_B}^{T_c} k(T) \mathrm{d}T} \ , \tag{8.9}$$

where ρ_n is the normal conducting resistivity. This equation finds $r_{\text{crit}} \approx 2.3\,\mu\text{m}$, suggesting normal conducting defects larger than this could cause thermal runaway and quench.

The heat this defect produces is $370\,\mu\text{W}$. This suggests that the maximum power that can be put into an area smaller than a $r_{\text{crit}} \approx 2.3\,\mu\text{m}$ radius circle is $370\,\mu\text{W}$ without causing some form of thermal runaway at $B = 75\,\text{mT}$. Defects smaller than this (and creating less heating) could still drive a small region of material normal conducting around themselves.

This calculation is illustrative to show how much more susceptible Nb_3Sn

[6] Equ. 11.7 in text

can be to small defects due to its lower thermal conductivity. In reality we are not using bulk Nb_3Sn but $\approx 3\,\mu m$ of Nb_3Sn on a niobium substrate (similar to the critical radius size). The contact with the niobium substrate will further stabilize the Nb_3Sn region on top. In opposition to this, in our calculation we have not accounted for the increased losses caused by the nearby Nb_3Sn warming up. To fully calculate the stable region, we must use a simulation approach.

Figure 8.14 shows the results of thermal simulations. In these simulations, for a given normal conducting defect radius (and a Nb_3Sn film thickness), we increased the magnetic field until we found thermal runaway. A $3.0\,\mu m$ normal conducting region is found to have a $73\,mT$ quench field, roughly what we find in our Nb_3Sn cavities. This produces $\approx 600\,\mu W$ of dissipated power. The heating profile on the outer wall is shown in Fig. 8.13. This defect increases the temperature by $1\,mK$ on the outer wall, just below the quench field. This suggests the large jumps are either made up of multiple small jumps at different locations, or the heating is spread over a larger region.

An interesting consequence of the two layer system is that the quench field is roughly constant from $\approx 4 - 100\,\mu m$ (see Fig. 8.15). Defects larger than $100\,\mu m$ would be easy to find with microscopy and we do not find them. We expect defects to be closer to the grain size ($\approx 2\,\mu m$ in diameter). This size dependence could explain the narrow range of quench field we see in our cavities.

The thermal simulations show the Nb_3Sn is thermally unstable in the face of defects. Very small defects and relatively small amounts of (concentrated) heating can cause the material to quench. However, the simulations show how we can increase the stability of the Nb_3Sn region: decrease the layer thickness. If we decrease the Nb_3Sn layer to $1.5\,\mu m$ the quench field increases to $117\,mT \approx$

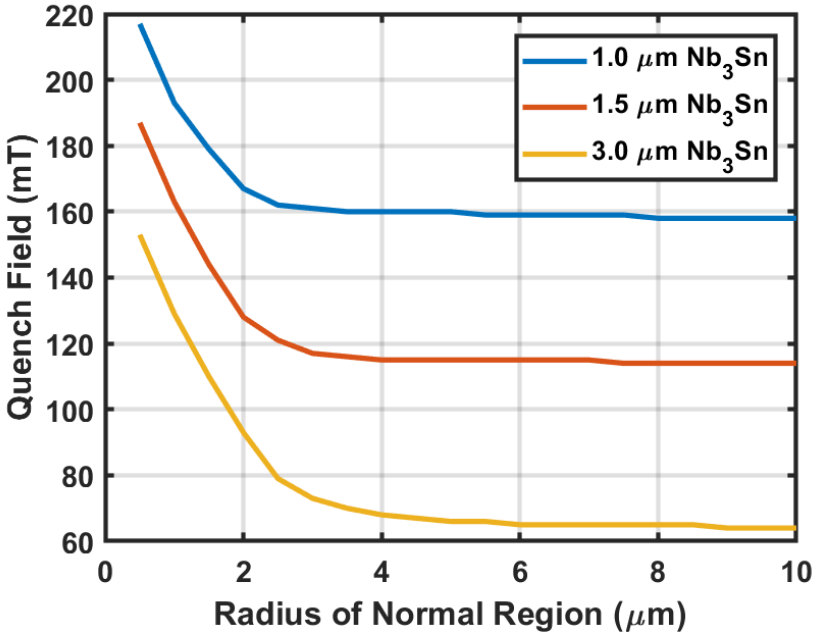

Figure 8.14: Thermal simulations of the quench field of normal conducting regions. The quench field versus radius of the normal conducting region is shown. Results are shown for 1 µm, 1.5 µm, and 3.0 µm thick Nb_3Sn layers. We see quench at 73 mT in our cavities which corresponds to a normal conducting region with a 3.0 µm radius. This produces ≈ 600 µW of heating. With a 1.5 µm Nb_3Sn layer thickness the quench field for a 3.0 µm normal conducting region increases to 117 mT ≈ 27 MV/m.

27 MV/m without even resolving the underlying defect. We could potentially use a 1 µm Nb_3Sn layer if we can achieve a consistent layer thickness (we want the Nb_3Sn layer to be thicker than several penetration depths everywhere).

8.5 Temperature Jump Models

We will now discuss some potential models for temperature jumps seen in our cavities.

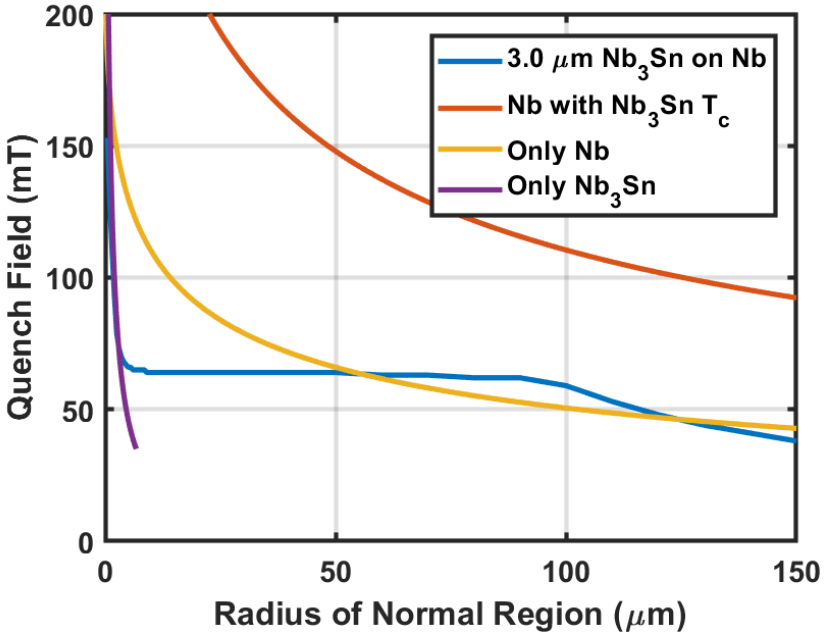

Figure 8.15: Thermal simulations of the quench field of normal conducting regions for 3.0 µm of Nb_3Sn on niobium, and calculated quench fields of thick Nb_3Sn, niobium only, and niobium with Nb_3Sn superconducting parameters only. At small radii ($r < 3$ µm) the quench field matches that of pure Nb_3Sn. At large radii the quench field is determined by the thermal stability of the niobium substrate. The thermal stability at large radii is slightly enhanced over that of niobium due to the increased T_c.

8.5.1 Vortex Nucleation and Josephson Junction Effects at Grain Boundaries

Those familiar with Josephson-junctions might find that these temperature jumps (and thus resistance/voltage jumps) are familiar. Voltage jump behavior is seen in microwave-induced/Shapiro[7] steps in Josephson-junctions and in the presence of magnetic flux [Tin12]. In the case of RF SQUIDs, magnetic vortices may enter the Josephson junction at a critical RF amplitude and experience hysteretic losses [Tin12]. The temperature jumps in Nb_3Sn cavities appear to

[7] Arrays of non-identical Josephson-junctions in RF fields have been seen to undergo Shapiro steps at the same time creating giant Shapiro steps [BB91]

be quantized (reported in [Hal17]) and there is a hysteresis curve as is seen in Josephson junctions. This suggests a candidate: T_c suppressed grain boundaries acting as weak links and inducing Josephson junction effects.

Weak link grain boundaries with Josephson junction effects and magnetic vortex nucleation have been seen in $YBa_2Cu_3O_7$ and iron-based superconductors [Gur14a, DEG+11]. Shapiro steps have even been demonstrated in Nb_3Sn showing the relevance of weak link grain boundaries [LF81]. The coherence length in Nb_3Sn is roughly the same as the grain boundary width making them particularly relevant. The relevance to Nb_3Sn SRF cavities was suggested by D. L. Hall shortly after temperature jumps were observed in Nb_3Sn cavities [HCL+17].

Model 1

A particularly relevant model is presented in [SG17]. This model looks at criteria specifically tailored to SRF cavities and particularly relevant here including long grain boundaries and short coherence lengths. This model was explored in relationship to our cavities in [Hal17, H+17a] and we will only discuss it briefly.

In their model once the surface magnetic field exceeds a critical field for the grain boundary a vortex may enter it. This vortex moves in the grain boundary and remains there during the RF cycle. When the RF field's sign switches an anti-vortex may nucleate into the boundary which annihilates with the first vortex, followed by another anti-vortex. At high fields, Cherenkov radiation from a moving vortex may evolve vortex-antivortex pairs. The vortex generates viscous losses as it travels the length of the grain.

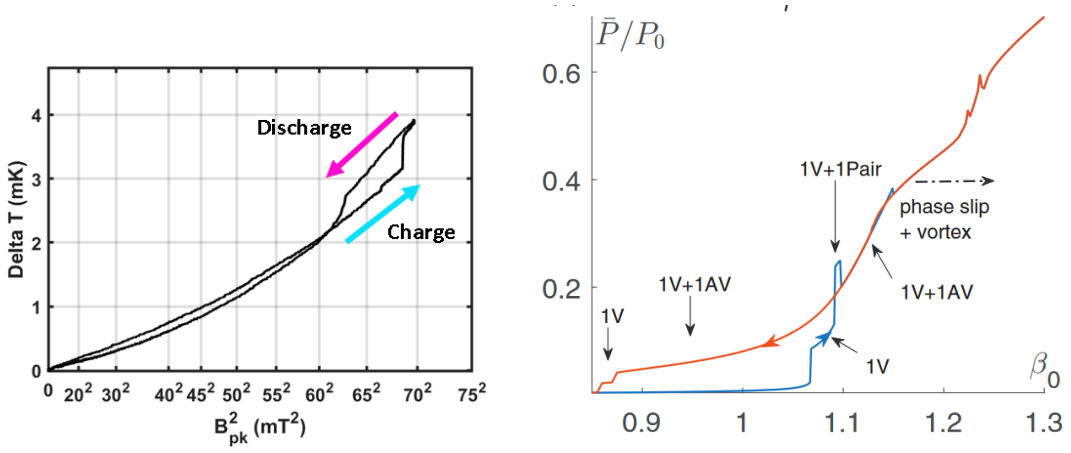

(a) (b)

Figure 8.16: a) Temperature jumps vs B^2 that we see in our Nb_3Sn cavities. b) Calculations from a grain-boundary model presented in [SG17]. Similar jump dynamics are seen in the model. The parameter β is the ratio of J_0/J_c, where J_0 is the amplitude of the RF driven current and J_c is the critical current for vortex entry. We are below the phase-slip region of this plot–in which vortices transition to a state that is spread across the entire grain boundary.

Figure 8.16 shows calculated loses from this model and our observed temperature jumps. We see that the theoretical model has similar temperature jumps and the observed hysteresis. The ideal grain boundaries shown in this equation do not permit large numbers of vortices (outside the 'phase-slip' regime which we are not in) and only two temperature jumps would be seen in this simplified model. However, simulations of more realistic grain boundaries permit multi vortices [SG17].

Using reasonable values for our grain boundaries D. L. Hall finds that the heating of one of these grain boundaries to be $\approx 400\,\mu W$[8] [Hal17]. This is in reasonable agreement with our thermal simulations for the size of the jumps we observe and the quench field we find. However, we note that a second vortex could not enter the grain boundary without causing quench. The multiple

[8]This estimate was based on an equation from A. Gurevich that we could not reproduce and does not appear in the paper. As such, this estimate should be met with skepticism.

jumps must come from multiple nearby grain boundaries. In this case quench likely initiates at a single grain boundary that is slightly worse than the others.

Model 2

Recently, members of the Center for Bright Beam have been working on models of flux entry and loss at grain boundaries [CPT+21]. This work includes calculating the critical temperature, T_c, of grain boundaries [KSA20], simulating vortex entry at grain boundaries using a time-dependent Ginsburg-Landau formulation of superconductivity [Pac20], and calculating the dissipation of magnetic vortices in a grain boundaries [CPT+21]. This model has been used to explain the Q-slope seen in early Nb_3Sn cavities made by Fermi National Accelerator Laboratory (FNAL) [CPT+21]. We will discuss this model here.

A. Pack *et. al.* have been conducting time-dependent Ginsburg-Landau simulations of magnetic vortex nucleation at grain boundaries in Nb_3Sn [Pac20]. The work finds that both bad chemical composition and steep grain boundary geometries can lead to vortex nucleation at a lower critical magnetic field. In addition, it is found that a set of magnetic vortices can become pinned in the Nb_3Sn grain boundary without entering the bulk or causing an avalanche of magnetic vortices. At a higher field (below the superheating field) vortices are then able to enter the bulk which would result in an avalanche of magnetic vortices and cavity quench (however, these simulations are DC/low frequency and dynamics might change in RF fields). Frames from simulations are shown in Fig. 8.17. Vortices pinned in the grain boundary was only found when grain boundaries had suppressed T_c. We do not see tin-rich or depleted grain boundaries in Nb_3Sn, but other phenomena such as strain can reduced T_c [KSA20, God06].

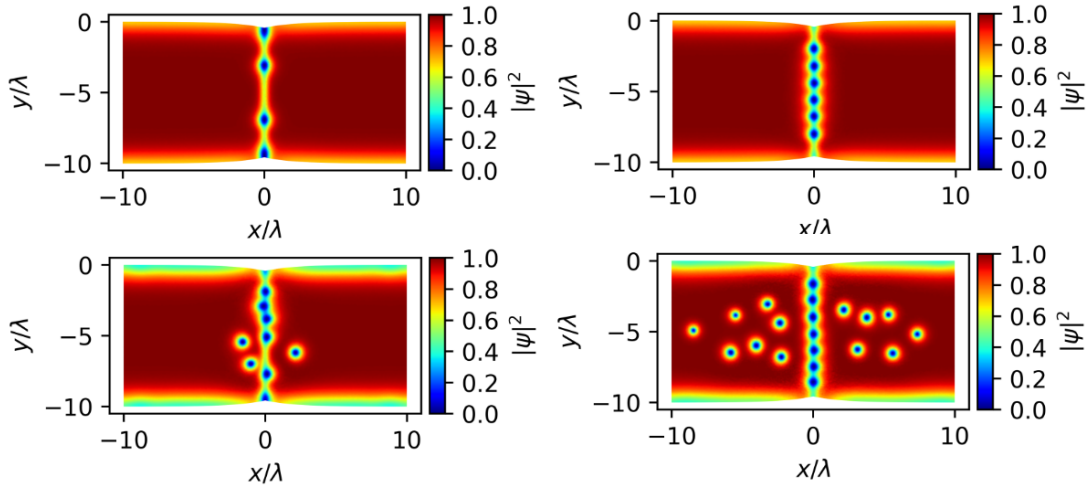

Figure 8.17: Frames from a time-dependent grain boundary simulation. We are viewing a cross-section. The simulations are infinite in the z axis, periodic in the x axis, and mirrored in the y-axis. The displayed value is the is Ψ, the superconducting order parameter. Vortices are seen as blue low semi-circular regions (low Ψ). Left to right, top to bottom, we see the progression of the system of the magnetic field is increased. We see vortices enter the grain boundary and become pinned, then eventually nucleation into the bulk. This figure was adapted from [CPT+21].

These simulations also look at how the grain boundary geometry at the surface impacts the flux entry field. They find steep grain boundary geometries decrease the field of first flux entry. Figure 8.18 shows a cartoon of how this works. We can imagine a magnetic vortex as a normal conducting core region with a vortex of supercurrent around it (even though it is not in the superconductor yet). It is a higher energy state for the normal conducting core to be in the superconductor, but a lower energy state for the supercurrent to be in the superconductor. By sitting in a steep grain boundary most of the supercurrent can be in the superconductor before the normal conductor core enters. This allows the vortex to gain the energy of the supercurrent entering the superconductor before it must pay the cost of the normal conducting core entering, reducing the effective barrier to entry. This makes the worst grain boundary geometry one

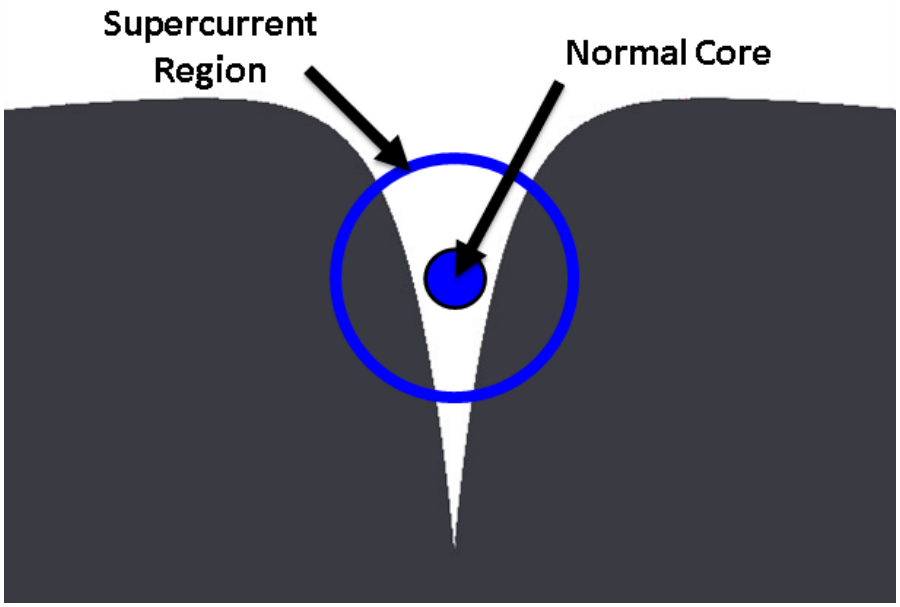

Figure 8.18: A toy schematic of a magnetic vortex sitting in a grain boundary. The normal conducting core can sit in the grain boundary and outside the superconductor while most of the supercurrent is in the superconductor.

that is roughly the width of the normal conducting core $\sim \xi$ and deeper than the width of the supercurrent $\sim \lambda$. In addition to this, we can imagine surface roughness locally enhancing the magnetic field (discussed in greater detail in the next chapter). A 'saddle' type geometry could see both decreased flux entry field and enhanced surface magnetic fields.

In [CPT+21] they look at the dissipation of magnetic vortices in a grain boundary. They calculate the drop in magnetic energy from a vortex nucleating into the grain boundary. During one RF cycle both vortices and antivortices will be nucleated into the grain boundary and two 'sets' of vortices and antivortices will annihilate each other during a single RF cycle. They assume that when vortex-anti-vortex pairs annihilate then the change in magnetic energy is lost as heat in the grain boundary. They additionally assume that many vortices enter the grain boundary as possible space by the penetration depth, λ. This gives

D/λ vortices in the grain boundary where D is the depth of the grain boundary (and the length of the boundary is $2D$). They arrive at an equation for the losses in the grain boundary [CPT+21][9],

$$P_{GB} = 4\frac{B\Phi_0}{\mu}\frac{fD^2}{\lambda}\ , \tag{8.10}$$

where Φ_0 is the magnetic flux quantum, and μ is the permeability of free space .

Using the above model, if we assume a grain boundary depth of 3 µm (a 6 µm long grain boundary is reasonable) and a surface magnetic field of 70 mT we get that $P_{GB} \approx 26\,\mu W$. This is much less than the heating we expect from the temperature jumps that we see in our cavities ($\approx 450\,\mu W$). This, in part, may be from their model not including every possible loss mechanism that can occur in the grain boundary. Their model looks only at the energy of magnetic vortices and not how these vortices may impact the supercurrents in Nb_3Sn (e.i., Josephson junction effects). The 'bad' grain boundaries that we see may be at bad region of the cavity where surface roughness causes severe surface magnetic field enhancement. We could estimate that this increases the losses to $\approx 50\,\mu W$. As we will see in the next chapter, this is not an absurd level of surface magnetic field enhancement (a factor of 2) in our Nb_3Sn cavities. Without additional dynamics this is far below the observed temperature jumps that we see and not enough to cause cavity quench at the fields we see, but the model gets the heating within a factor of 10 of what we see in measurement, which is quite good for a relatively simple model of the losses.

[9] We have inserted an extra factor of 4 to represent that 4 sets of vortices are eliminated per RF cycle where as their work only shows the losses of 1 set per cycle.

8.5.2 Localized Quench

Under the right set of parameters, we find an interesting phenomenon in our thermal simulations. The formation of the stable normal conducting region on the surface of the cavity. This normal conducting region is smaller than the critical defect size in niobium, but bigger than in bulk Nb_3Sn. Essentially, a local thermal runaway starts in the Nb_3Sn layers but is then stabilized by the higher conductivity of the niobium layer. At a higher field level these regions also become unstable and undergo thermal runaway.

Figure 8.19 shows a simulation where a small normal conducting region was formed. We see both a jump in temperature and a hysteresis loop. In this simulation there was a relatively small defect producing 200 µW in a 0.5 µm sphere (the thermal conductivity was additionally lower than that used in other simulation we have shown in this work, but within reasonable values for Nb_3Sn). At a critical field this grew into a larger normal conducting region of ≈ 4 µm. Upon lowering the fields the normal region persisted down to a lower field.

By tuning the values of conductivity and layer thickness a wide variety of normal sized regions can be found with different temperature jumps, though the stable regions are on the order of the Nb_3Sn layer thickness. We only know the value of the conductivity to, at best, a factor of two since we have no direct measurement of it in our cavity. In addition, we see variation in the Nb_3Sn layer thickness on the order of ≈ 500 nm (ignoring the 'thin regions' that are less than 1 µm).

This result is interesting since it allows temperature jumps to appear regardless of the underlying loss mechanism. Any sufficiently large and concentrated

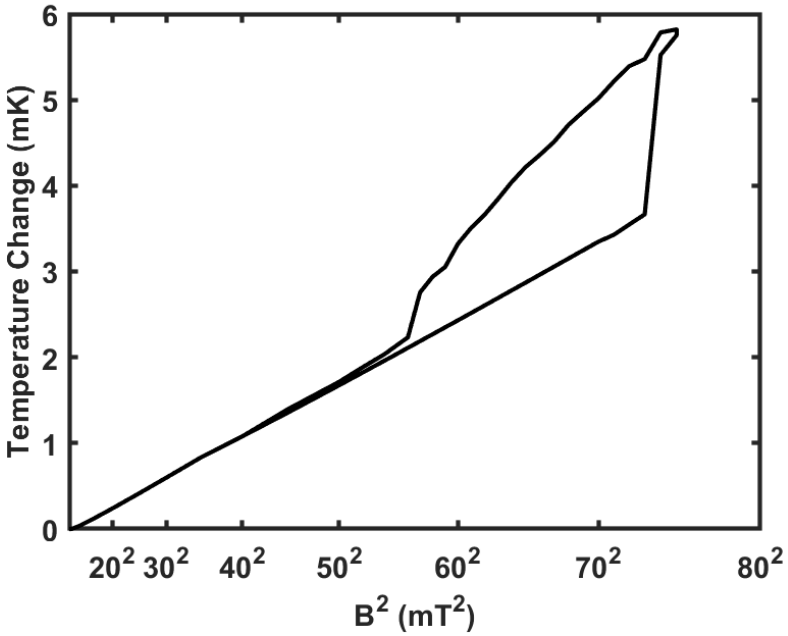

Figure 8.19: The simulated temperature versus the magnetic field with a small defect. The magnetic field is raised and lowered. At a critical field we see the formation of a stable normal conducting region. This region is self-sustaining once formed down to a lower field level. We see a hysteresis as the field is lowered. Thermal runaway was found 1 mT above the highest magnetic field shown here.

loss mechanism can trigger the formation of a small normal conducting region. Even electron impacts from multipacting type dynamics could trigger this even. This does, again, show the instability of 'thick' Nb_3Sn layers.

8.6 Summary

Here we have shown the first time-resolved thermometry of Nb_3Sn SRF cavities. These are only preliminary results, but interesting dynamics are already revealed. Temperature jumps, previously observed only at the cavity quench site, occur at many places across the cavity surface. Measurements of cavity

quench show new dynamics. The first cavity quench appears to be some form of multipacting induced quench. The quench site quickly transitions to a second, localized quench site. Previous measurements found the secondary electron yield of Nb_3Sn is only slightly higher than that of niobium[AJNK15]. The instability of the Nb_3Sn layer is likely contributing to multipacting causing quench. We are likely seeing some processing of the multipactor causing a slight increase in the accelerating gradient of the cavity, but then reaching the quench field of a localized defect.

A natural course of action might be to cut up the cavity and examine the quench region using microscopy. This has already been attempted [Hal17]. Figure 8.20 shows an SEM scan of the approximate quench site of a Nb_3Sn cavity. Unfortunately, there is no obvious candidate for quench in the image. The defects we are looking for are small and may be chemical in nature while the resolution of our temperature map is, at best, several mm. Finding the defect this way is a "needle in a hay-stack" sort of problem and we first need to know more about what we are looking for.

The dynamics of temperature jumps is more complicated than previously realized. Models of flux entry at grain boundaries are still tempting, but we see non-locality of some temperature jumps–identically timed jumps spread over several cm–that can't be explained by this theory. Perhaps there is an interplay between the multipacting type quench and the observed temperature jumps (e.g. electrons).

We examined models of temperature jumps based on flux entry at grain boundaries. We find that the model presented in [SG17] gives reasonable results for what we see in our cavities. The second model we look at has similar

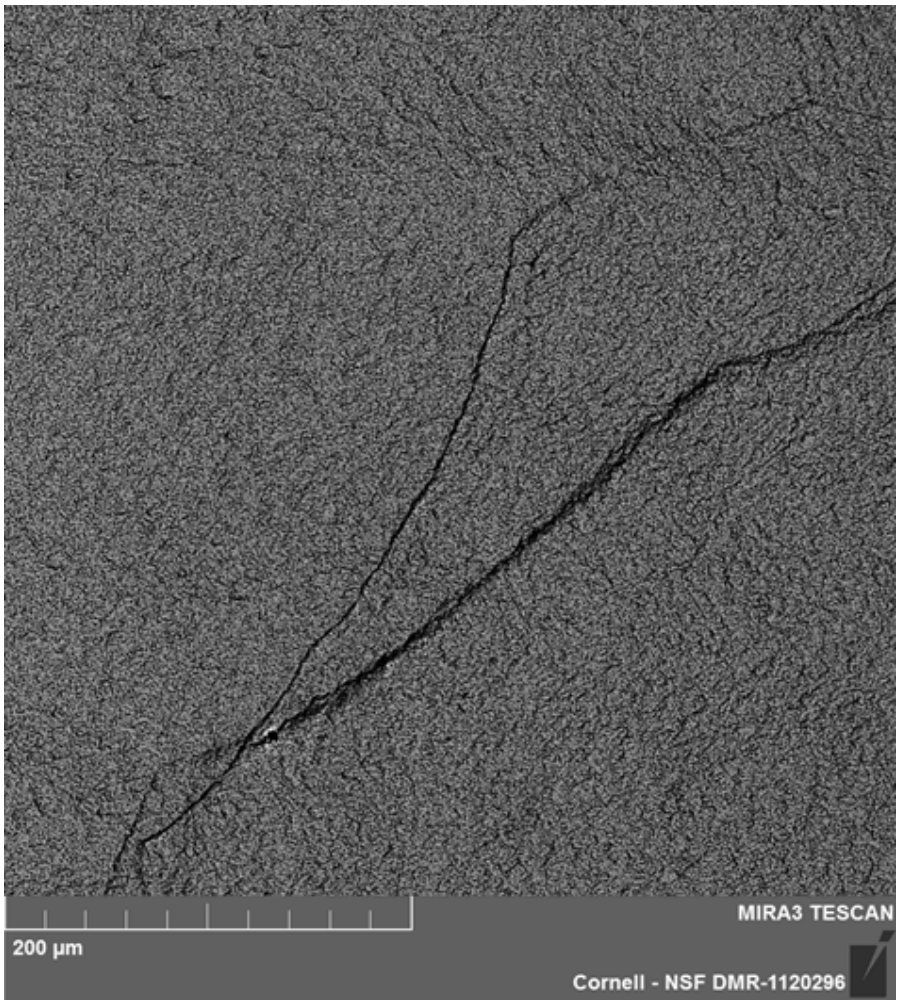

Figure 8.20: An SEM scan of the (second) quench site of a Nb_3Sn cavity as located using thermometry. The dark lines of grain boundaries of the niobium substrate. This figure was adapted from [Hal17].

results, but the losses are too small to account for what we in our cavities. This is likely from the neglect of Josephson effects in the grain boundaries. Their results on the nucleation of vortices at grain boundaries are still relevant and show dynamics that could replicate what we see (the sudden onset of pinned vortices in the grain boundary causing heating). Their results on the suppression of the field of first flux entry based on the grain boundary geometry is relevant in our Nb_3Sn cavities where we see relatively large surface roughness.

In studying the thermal stability of Nb_3Sn we find several important results. We see that thick Nb_3Sn layers are (relatively) thermally unstable. We find that our cavity quench field could be explained by a $\approx 3\,\mu m$ normal conducting region. This is on the order of the size of Nb_3Sn grains and grain boundaries. In addition, we find that in the multilayer material we can form small, stable normal conducting regions. These regions are formed by a smaller underlying defect creating heat in a small area. This both amplifies the losses caused by the underlying defect and can explain the temperature jumps we see in our cavities. Finally, we find the thermal instability could explain the observed small range of quench fields seen in our cavities.

We found that the film thickness and surface roughness both play an important role in cavity quench. By decreasing either of these we could potentially increase the quench field of our Nb_3Sn cavities.

CHAPTER 9

SURFACE ROUGHNESS

Nb_3Sn cavities produced at Cornell have rougher surfaces than conventional niobium cavities (as seen later, this is true of both BCP and EP niobium over the length scales that are relevant to the surface magnetic field enhancement). Previous simulations and calculations have shown that both bumps and pits in the surface of a cavity can cause local enhancement of the surface magnetic field [SP08]. If the magnetic field is sufficiently enhanced over a large enough area it could lower the quench field of the cavity[1]. In addition, we have seen that roughness and, particularly, grain boundary geometry can significantly decrease the field of first flux entry at grain boundaries.

Here we present both estimates of the impact of surface roughness on the surface magnetic field (field enhancement), and on first attempts to chemically polish the Nb_3Sn surface. We define the surface magnetic field enhancement as, γ, as $\gamma = H_{rough}/H_{smooth}$, where H_{rough} is the surface H-field along the rough surface and H_{smooth} is the surface H-field expected in the surface was smooth. We will detail the techniques used to estimate the degree of field enhancement in Nb_3Sn and compare it to other SRF cavity materials, introduce a useful measure of quantifying surface roughness, Amplitude Spectral Density (ASD), and we will show preliminary results from using standard SRF polishing techniques on Nb_3Sn sample: BPC, EP, and oxipolishing. Studies of chemical polishing of Nb_3Sn has also been presented in [Pud20, PKE+18, PKE+17a, PKE+17b, Hil80]. Here we find that some of these techniques are successful in reducing surface

[1]The increased surface area and changes in local magnetic field could also impact the quality factor of the cavity, but we find this effect negligible in our cavities. This was also found negligible in [XKR12].

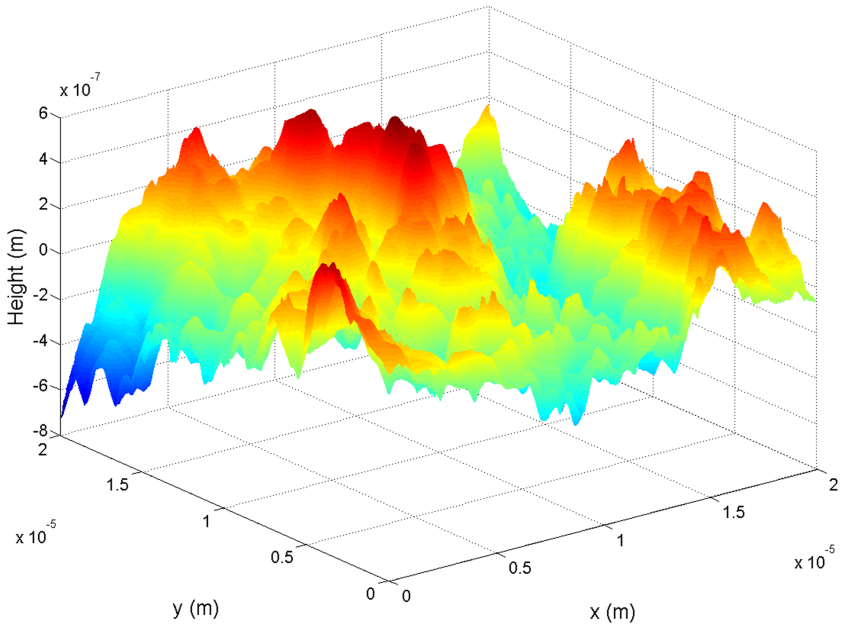

Figure 9.1: A surface plot of an AFM scan of a Nb_3Sn surface.

roughness but need further optimization before use on cavities.

9.1 Estimating Surface Magnetic Field Enhancement

9.1.1 Method

Atomic Force Microscope (AFM) [BQG86] scans of Nb_3Sn (and niobium) samples are taken to get height map data (see Fig. 9.1). An Asylum MFP-3D AFM was used with a scanning density of 1024 points on a 20 µm line. Line-scan segments are taken across multiple scan locations (from 3 scan locations) and the local magnetic field is calculated. The calculation of the surface magnetic is done using the 2D finite element code SUPERLANS2 (SLANS2) [MY95]. We further detail the calculation/simulation process here.

The method of calculation used was based on the work of V. Shemelin and

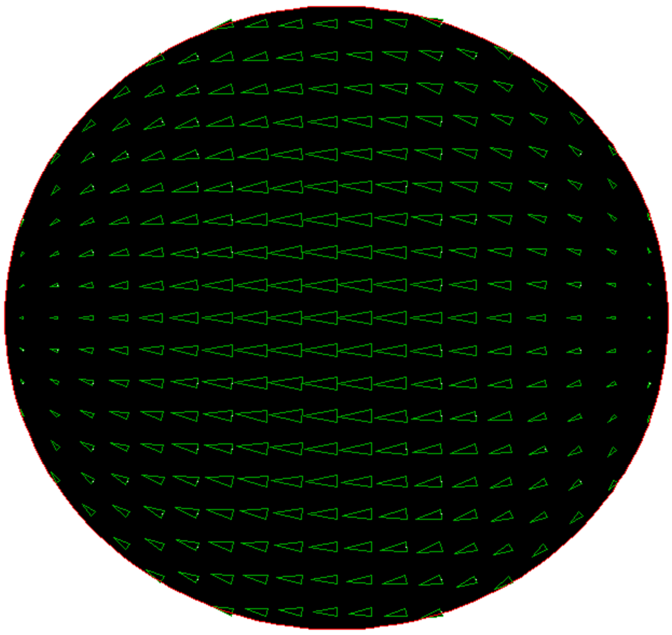

Figure 9.2: Vector field plot of the surface H-field at the flat end if a cylindrical pillbox cavity operated in the TE-111 mode.

H. Padamsee [SP08]. In their paper the surface magnetic fields of pits and bumps were calculated using SLANS2. This was done by creating a model with an elliptical bump or rounded pit in the center of the flat end of an otherwise cylindrical cavity then solving for the magnetic fields in the TE-111 mode. The TE-111 mode in a cylindrical cavity has an approximately constant, uniform surface magnetic field in the middle of the circular ends (see Fig. 9.2), making this location ideal for calculating the magnetic field enhancement in a uniform field. We wish to know the enhancement in a uniform magnetic field because the feature sizes are on the order of microns over which the surface field would be approximately uniform if the surface was smooth. The use of a cylindrical cavity simply gives us appropriate boundary conditions for solving the electromagnetic problem.

Using a full 3D EM simulator proves difficult due to the intricate geometry and high degree of accuracy needed. The required mesh densities make the sim-

ulations prohibitively intensive to run on readily available computers. Instead a 2D EM eigenmode solver is used (azimuthally symmetric)–SLANS2. Line-scan segments were taken through the 3D height data to create segments such as the one shown in figure 9.3a. This 2D data is given to SLANS2, which solves for the electromagnetic field assuming this height map data is rotated 360° to create the 3D geometry.

The magnetic fields are not truly constant inside the model cavity. In this mode, the magnetic field decreases when moving transversely towards the center of the cavity and when moving radially away from the center. When setting up the models it was important to ensure the rough geometry remained where the field is approximately constant. Shemelin and Padamsee [SP08] adjusted the size of the ellipsoidal bumps while keeping the geometric ratios (height to width) constant. When the bump penetrated more than $1/80^{th}$ of the way into the cavity (end to end), the H-field enhancement factor dropped by 0.01, as such, our rough patch geometry was scaled [2] so that it did not penetrate this far into the cavity. Radially, it was noticed that for a smooth cavity the H-field dropped by 5% when moving out $1/10^{th}$ of the way from the center of the cavity, as such, the geometry was scaled so that it did not exceed this. In addition, the rough patch could not significantly change the electromagnetic fields elsewhere in the cavity. For all geometries tested with the above conditions, the frequency of the mode only changed by 0.1% and the electromagnetic fields were unchanged far from the rough patch.

The height map data could not be directly input into the SLANS2 geometry. Doing so would command SLANS2 to linearly interpolate the points, creating a

[2]The surface H-field enhancement factor in a uniform H-field is independent of the scale of the feature and only depends on the relative geometry [Kub14]

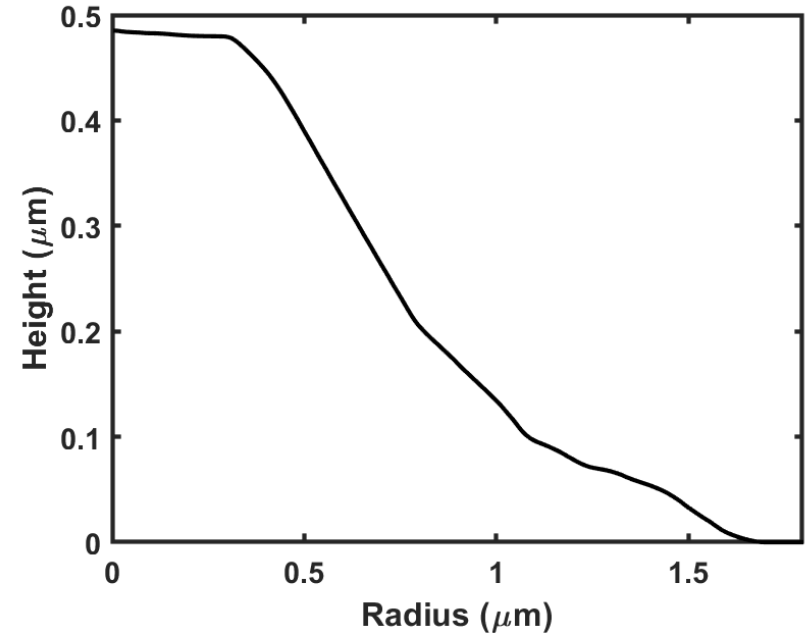

(a)

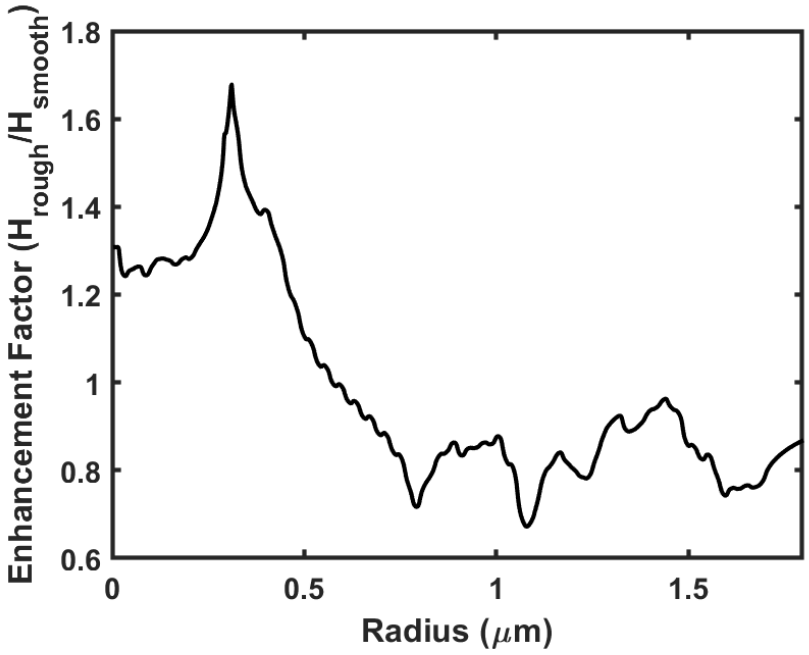

(b)

Figure 9.3: a) An AFM height map used for simulating surface H-field. b) The field enhancement found for the height map shown above.

geometry with sharp spikes. Instead, smooth curves are needed. The only curve available in SLANS2 is an elliptical arc. To input the geometry an algorithm was written to interpolate the height map data using ellipses. This algorithm was written so that the interpolated line appeared to be a reasonable estimate of geometry (no wild oscillations between data points), but the algorithm did not minimize the curvature. This could bias the results since the H-field enhancement is dependent on the curvature of the geometry.

The mesh density was optimized by increasing the mesh density until the improvement was not considered worth the detriment of smaller simulation geometry. Unfortunately, SLANS2 has a maximum number of mesh cells/points that can be used. Increasing the mesh density limits the maximum length of line-scan segment that can be simulated, potentially reducing the accuracy. Densities of 1, 2, 4 and 6 mesh cells per data point were tested. In general, the field enhancement increased everywhere with increasing mesh density. Going from 4 to 6 increased the field enhancement by approximately 0.01. Increasing to 6 mesh cells would reduce the maximum length of sample that could be simulated, and it was decided that 4 mesh cells was optimal.

To choose the line-scan segments studied, a procedure was established to pick segments: A cross section was taken through an AFM map; a flat spot near the average height of the sample was chosen as the starting point; another flat point was chosen that was 1.5 to 3 µm away (the furthest point was chosen if available). This was done to try to keep the samples as randomized as possible within the restraints of the computation. The $\approx$ 3 µm upper limit was chosen because longer segments could not be computed in SLANS2. 10 line-scan segments were chosen this way for each sample from 3 different scans. For the

'baseline' Nb_3Sn sample the average length of a segment was 2.24 µm.

9.1.2 Impact of Surface Roughness

The magnetic field enhancement was computed by taking the ratio of surface magnetic fields at the same radial component, r (e.i., $\gamma(r) = H_{rough}(r, h(r))/H_{smooth}(r, 0)$, where h(r) is the height at r of the rough surface). This ratio was taken along the surface H-field line through r = 0, where the surface field best estimates surface fields inside real accelerator cavities. The result is shown in Fig. 9.3b for one rough patch.

The H-field enhancement factor of all mesh cells in the rough patch of all 30 line-scan segments is histogrammed in figure 9.4. This histogram is weighted for the arc length of the mesh cell. The mean of the distribution is ($0.958 \pm 0.011(stat)$). 10% of the points are over 1.2, 5% of the points are above 1.29 and 1% of the points are above 1.45. We will use the 1% value as a measure of the severity of magnetic field enhancement seen on a surface when comparing surfaces. This local magnetic field enhancement could enhance heating from defects and lower the effective activation field of defects.

In addition to magnetic field enhancement we can also use our data to measure the impact on Q. To calculate the enhancement of the quality factor $\sum H^2\, ds$ (where ds is the arc length) was computed over the rough region (or equivalent region on the smooth geometry) for the rough and smooth geometries and the ratio of the two was taken. This assumes that no location surpasses the critical field and becomes normal-conducting[3]. Figure 9.5 shows an (un-

[3]As discussed by Knobloch *et al.* for Niobium cavities [KGPL99], if fields are high enough

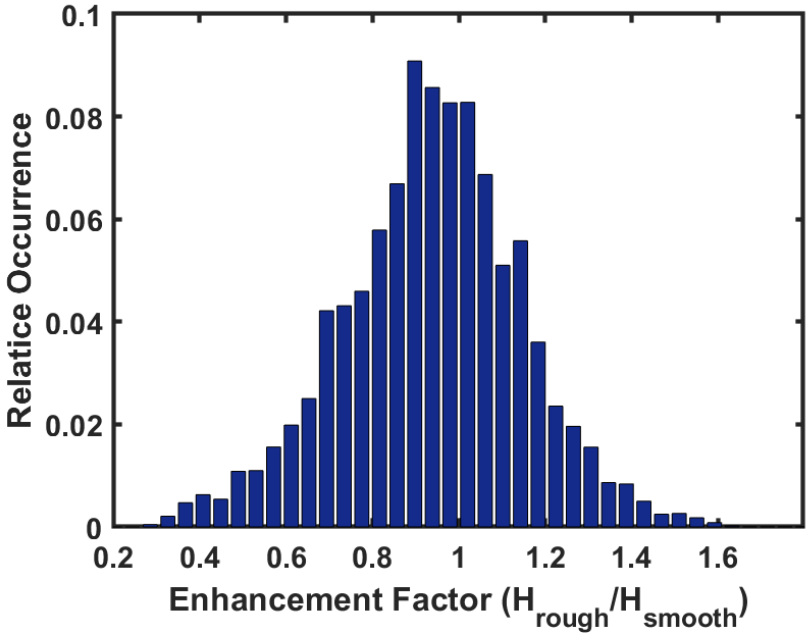

Figure 9.4: Histogram of relative area with a certain surface magnetic field enhancement factor of Nb_3Sn.

weighted) histogram of the Q-factor enhancements for all 30 line-scan segments. The weighted (by length) mean of the distribution is $(1.038 \pm 0.010(stat))$. This is an overall negligible effect on the quality factor (as we expected [XKR12]).

9.2 Characterization of Surface Roughness

To continue our discussion of surface roughness we need a good way to compare the roughness across samples. Surface roughness is often quoted in terms of R_a, the arithmetic mean deviation of the surface heigh in the scan. This simple method has two draw backs: it is dependent on the size of the scan area, and it gives no information on the length scale of the roughness. The magnetic

that some enhanced regions start to go normal-conducting then the quality factor will begin to drop, making roughness effects important.

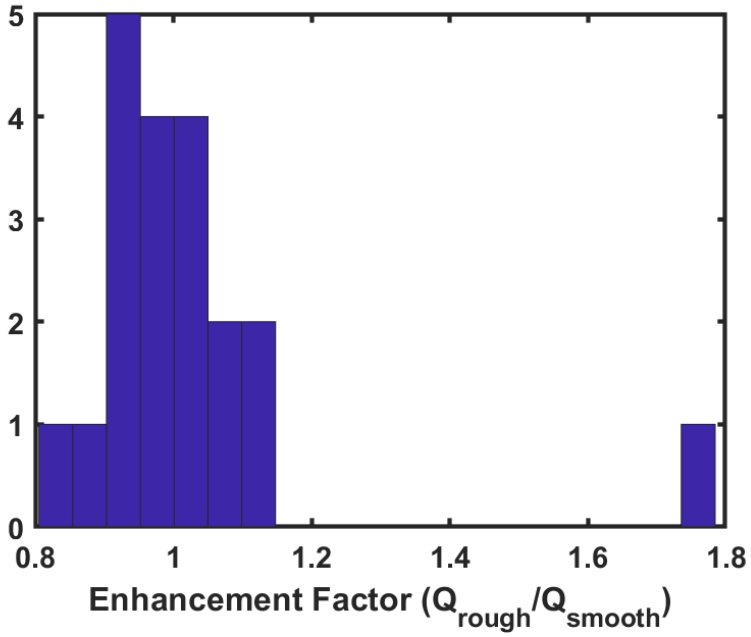

Figure 9.5: Histogram of quality factor enhancement of the samples simulated. The weighted (by length) mean of the distribution is $(1.038 \pm 0.010(stat))$.

field enhancement of a bump (roughness) depends on its height, thickness and width [Kub14] making any single number characterization of the roughness inappropriate. This is because a large amplitude bump that rises slowly will contribute far less to the surface magnetic field enhancement than a smaller amplitude bump that rises sharply. In addition to this, chemical etches may preferentially favor certain spatial-frequency (one over length units) bands when reducing roughness. To better characterize the surface roughness, we have adopted an "Amplitude Spectral Density" (ASD) approach based off Power Spectral Density (PSD) characterizations of surface topography. This characterization has been used heavily in optics and microelectronics and was applied to niobium surfaces by C. Xu *et. al.* [XTRK11] on which we base our approach.

In this approach, we take the Fast Fourier Transform (FFT) of each line of our AFM scan and take the average of the absolute value for each spatial fre-

quency, f_λ. 'Spatial frequency' is given by, $f_\lambda = 1/\lambda$, where λ is the wavelength of the component in the sinewave decomposition of the heightmap. Though the process is defined using spatial frequency we will display our plots using the wavelength. If we had an infinite scan size and sampling rate, we would receive an amplitude density. Instead, we receive discrete frequencies and amplitudes. We assume that the spectrum is continuous between points and rescale the values to be a density (in frequency) by multiplying by the square root of the scan size. The ASD is related to the arithmetic mean deviation roughness by $R_a = \sqrt{\int \text{ASD}^2 df_\lambda} = \sqrt{\int \text{PSD} df_\lambda}$. The advantage of ASD here is that height is more readily relatable to the magnetic field enhancement ($\gamma \approx$ height/width), making it easier to locate on which length scale the roughness matters the most. In particular, where ASD/λ is maximal is roughly the worse contribution to the magnetic field enhancement.

There are still several corrections that need to be applied to get the true ASD. Any roughness components with wavelengths larger than the scan size will be spread out over all the frequencies in the FFT, increasing the measured roughness and possibly skewing the plot. To correct for this and remove the low frequency components, the heightmaps are deskewed [XTRK11]. In this process a 3^{rd} order polynomial is fit to, then subtracted from each line in the AFM scan (see Fig. 9.6a). After this process, it is assumed that the largest wavelength component is compromised, and it is ignored. The second issue is that frequency components exist in that height map that are in between FFT frequencies. Again, these components will be spread over the FFT frequencies, skewing the data. To correct for this we apply a Tukey window function (see Fig. 9.6b) [XTRK11]. This smoothly reduces the heightmap at the edges to remove the mismatch at the ends caused by frequency components that do not perfectly divide the scan

size.

One correction that we do no apply is anti-aliasing. We have ignored this because the AFM we utilize already applies anti-aliasing and because high frequency components have a very small amplitudes and are unlikely to skew the data.

Finally, the ASD from scans of multiple samples were averaged and the standard deviation was calculated based on the three (or more) scans.

As an example, we can use this technique to compare niobium and Nb_3Sn surface roughness. Figure 9.7 shows the ASD before and after coating of a sample that was BCP'd before coating and one that was EP'd before coating. At short length scales the roughness is determined primarily by the coating process rather than by the substrate roughness. On longer scales substrate roughness and coating process determine roughness.

Earlier we stated that ASD/λ is related to the surface magnetic field enhancement (as a rough estimate). Figure 9.8 shows a plot of this value for a Nb_3Sn sample. The most severe range for magnetic field enhancement occurs in the 1-5 μm range. This is on the order of the Nb_3Sn grain size–a result of the roughness developing during material growth (discussed in chapter 10). Since this is the most important range for magnetic field enhancement we will show ASD only up to 10 μm in subsequent plots.

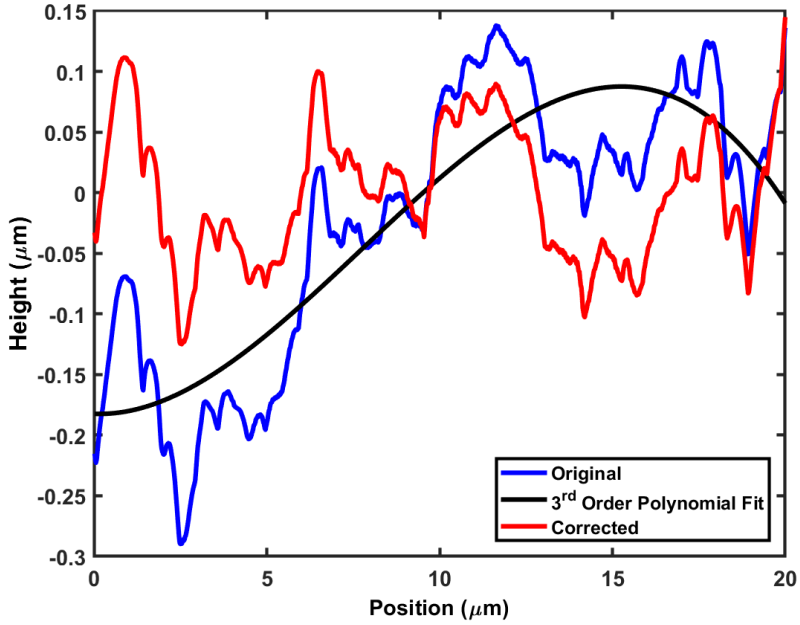

(a)

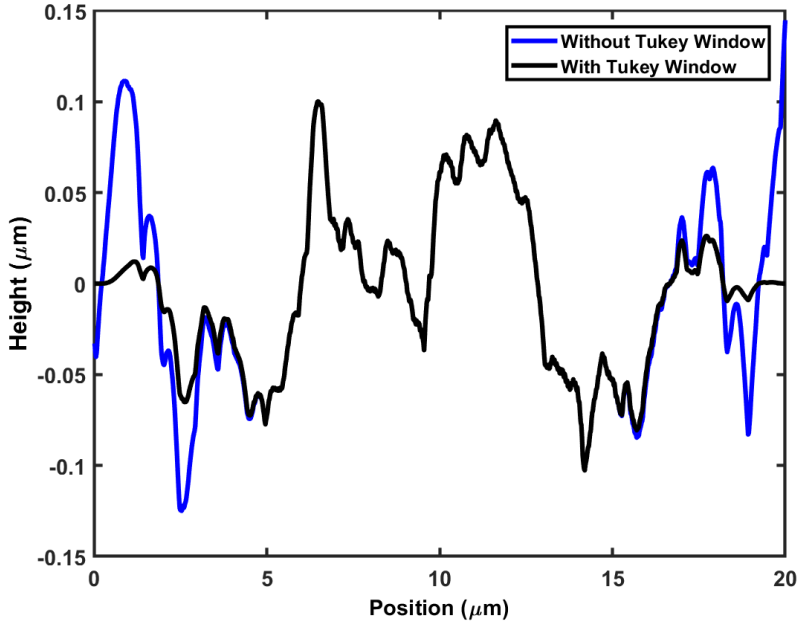

(b)

Figure 9.6: Corrections to heigh map data for ASD processing: a) The polynomial correction applied to a height profile. The polynomial is fit to the height map, then subtracted from the height map. b) The Tukey window function applied to a height profile (already polynomial corrected). Note that the profile falls to zero at the edges after the Tukey window function is applied.

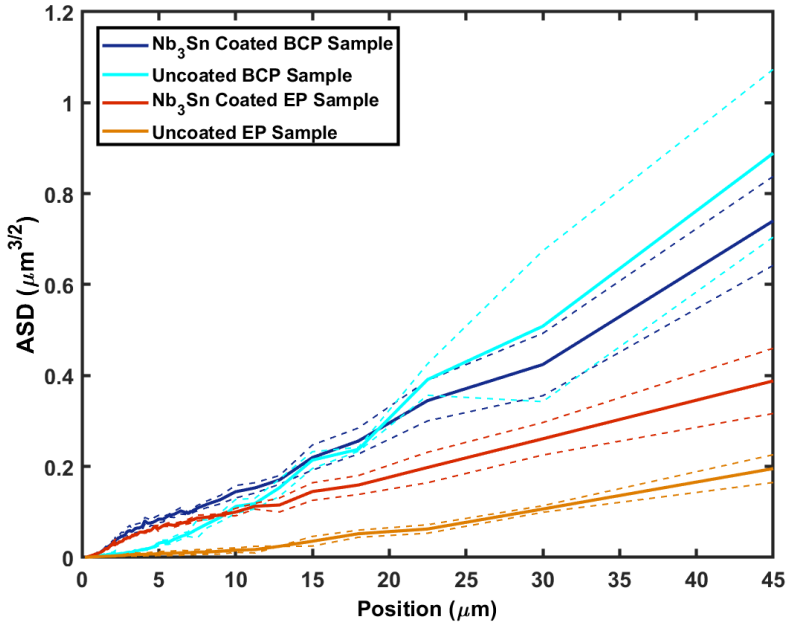

Figure 9.7: ASD of samples before and after coating for different pre-treatments. We see a significant difference between Nb_3Sn and niobium below 10 µm showing where the growth process has increased the surface roughness. Above 10 µm we see that the substrate roughness contributes most of the surface roughness. One standard deviation error bars are shown by dotted lines.

9.3 Chemical Treatments

Chemical polishing are commonly applied to niobium SRF cavities to create smoother surfaces. We discussed common techniques in section 4.2: Buffered Chemical Polish (BCP), Electropolishing (EP), and oxipolishing. Since we already have the facilities and chemicals to attempt these techniques, we can apply them to Nb_3Sn as a first attempt. Here we show the results. We start by describing our technique for each sample and showing the effect on the surface roughness. We will then look at the chemical composition after the treatment[4]. Additional work on chemical post-treatments have been reported by U. Pudasaini [Pud20].

[4]Some of this work was done by H. Hu and is reported in [HLP19].

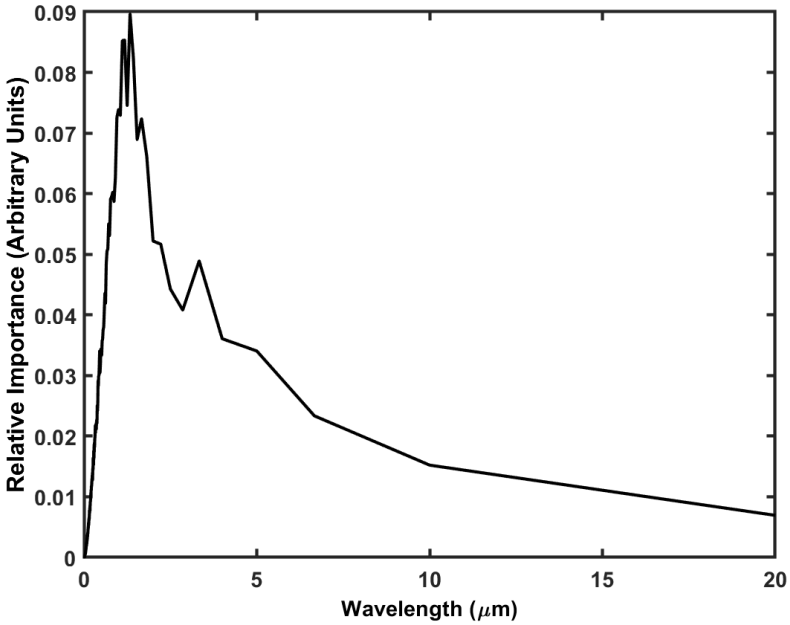

Figure 9.8: ASD/λ of a Nb_3Sn sample. This acts as a rough estimate of the magnetic field enhancement. This suggests that the 1-5 µm wavelength range is the most relevant for surface magnetic field enhancement.

9.3.1 Roughness Reduction

Buffered Chemical Polish

The first BCP test was done with a standard 1:1:2 solution for 30 s at room temperature (typical etch rate of 1 µm/min). The treatment significantly reduced the roughness, however, after the etching there appeared to be spots where bare niobium was showing suggesting most of the Nb_3Sn layer was destroyed. The destruction of the surface layer was confirmed through Energy Dispersive x-ray Spectroscopy (EDS) measurements showing little tin signal on the surface. The typical etch rate of this solution is considered to be 1 µm/min for niobium, however, this number is an average etch rate during long BCP treatment. It has been found that the etch rate is much faster at the start of the process and slows

down over time [Zha14]. This fast initial etch rate (possibly) combined with the different material gives us too fast an etch rate to be controllable.

To slow the etching rate and make the reaction more controllable, a 1:1:8 BCP mixture was created and used to etch samples. Samples received 15 s, 30 s, 75 s, and 150 s of etching. The samples were weighed before and after etching, suggesting that the removal rate was ≈ 800 nm/min. Figure 9.9 shows the change in ASD for the 75 s (≈ 1 µm removal), and 150 s (≈ 2 µm removal) treated samples (the 15 s and 30 s are not shown). All the treatments showed an negligible reduction in surface roughness–even with almost the entire removal of the Nb_3Sn layer.

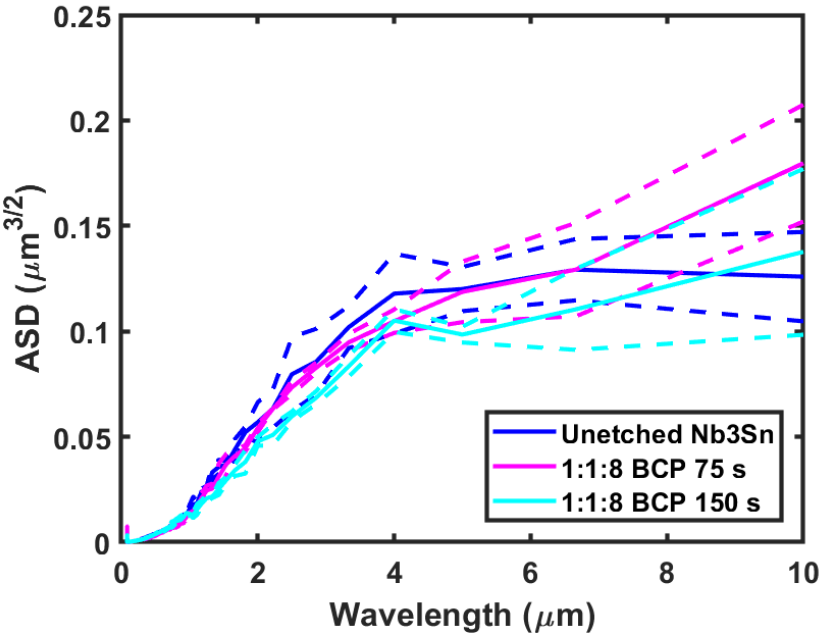

Figure 9.9: ASD plots for comparing untreated and BCP treated Nb_3Sn samples. One standard deviation error bars are shown by dotted lines.

Electropolishing

A standard niobium EP solution (1:9 of HF (48%) to H_2SO_4(96%)) was used for electropolishing. During EP a voltage is applied across the sample and a cathode and current is produced. The characteristic of the resultant current is key to the success of the process. Oscillations must be seen in the current or polishing will not take place [Zha14]. To find the correct area for polishing (instead of just etching) an I-V curve was produced. Figure 9.10 shows the mapped out curve which has the expected functional form [Zha14]. Current oscillation were seen from $\approx$ 1.3 V to 2.2 V. A voltage of 1.4 V as chosen for electropolishing of samples. Using the oxidation and reduction reactions at the anode and cathode and the density of Nb_3Sn an etch rate of 13.5 nm/min per mA/cm^3 was determined [HLP19].

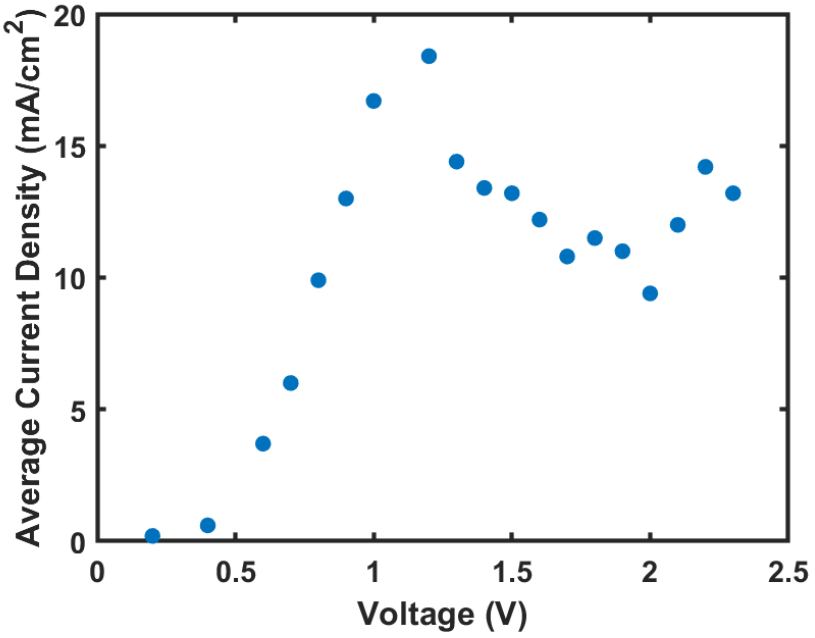

Figure 9.10: I-V Curve for room temperature electropolishing. Current oscillations were found from $\approx$ 1.2 V to 2 V–showing the 'polishing regime.' The plotted current is the average current at the voltage.

One Nb_3Sn sample was electropolished at room temperature using the above setup with an estimated 1.4 µm of material removed[5]. The ASD of this sample is shown in Fig. 9.11. A statistically significant reduction in the surface roughness is seen from ≈ 2 µm to 6 µm wavelength range–which is of particular important to Nb_3Sn surface magnetic field enhancement. The surface roughness is reduced by roughly a factor of 2. In theory, the maximum achievable surface roughness reduction of electropolishing with this much removal is a factor of 4 [Wag54].

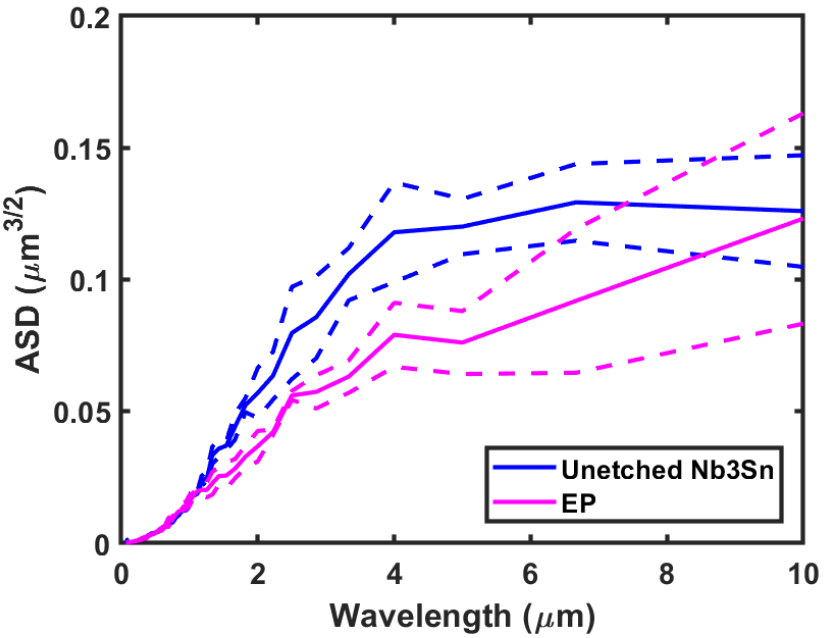

Figure 9.11: ASD comparing surface roughness of an unpolished and an electropolished Nb_3Sn sample. One standard deviation error bars are shown by dotted lines.

Oxipolishing

The most successful of the techniques we have tried has been oxipolishing. Samples received 6, 15, and 24 passes of oxipolishing (30 V) which is estimate to

[5]Additional EP Nb_3Sn samples were reported in [PFH+17], but were not in the polishing regime of the I-V curve (no oscillations) and did not show surface roughness reduction.

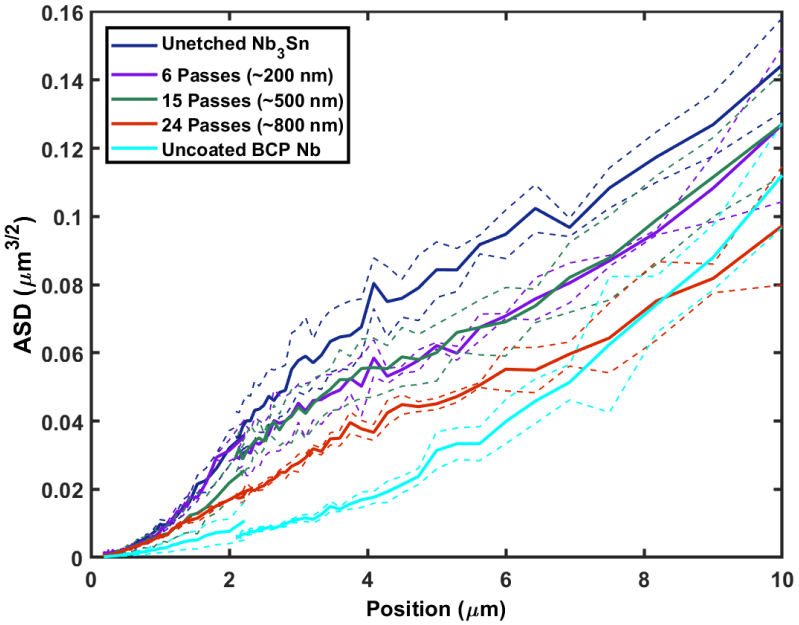

Figure 9.12: ADS of Nb_3Sn samples that received different amounts of oxipolish. Approximate amount of removal listed. BCP niobium is also shown for comparison. One standard deviation error bars are shown by dotted lines.

remove 200 nm, 500 nm, and 800 nm of material respectively. Figure 9.12 shows the ASD for this treatment. The 24 pass oxipolish managed to half the surface roughness over a wide range of wavelengths with only 800 nm of material removal.

We posit that this surface roughness reduction should halve the magnetic field enhancement and can calculate it again as we did in section 9.1. A normalized histogram of the oxipolished Nb_3Sn (24 passes) surface field enhancement results is shown in Fig. 9.13 along with the unetched Nb_3Sn results. For the oxipolish Nb_3Sn, 10% of the points are over 1.08, 5% of the points are above 1.15 and 1% of the points are above 1.21. This is less than half the magnetic field enhancements found for unetched Nb_3Sn where 10% of the points are over 1.2, 5% of the points are above 1.29 and 1% of the points are above 1.45.

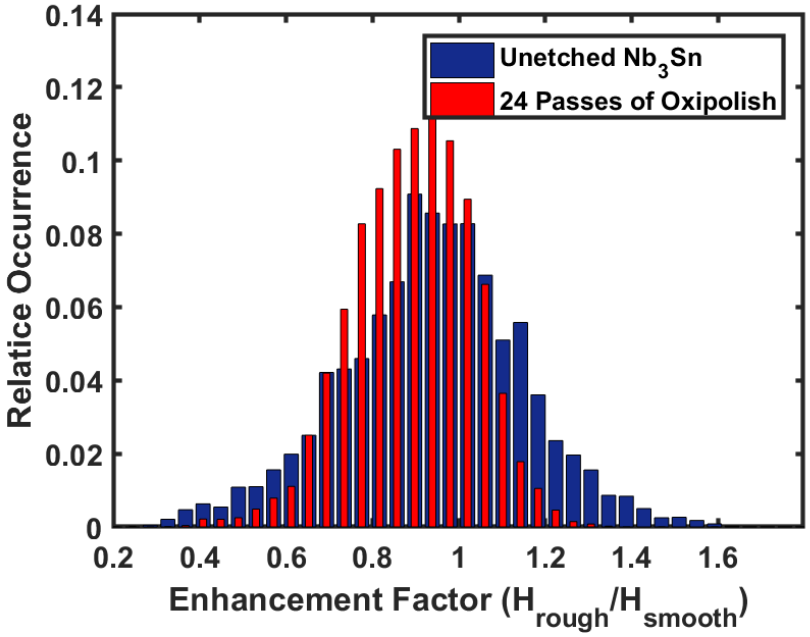

Figure 9.13: Histogram of relative area with a certain surface magnetic field enhancement factor of unetched and oxipolished Nb_3Sn.

The oxipolish histogram has a center of 0.914 ± 0.007(stat) while the histogram of the unetched sample has a center of 0.958 ± 0.011(stat). Having an average less than 1 is not unexpected as sharp peaks with a large surface magnetic field can depress the magnetic field over a large area, lowering the mean value of the enhancement factor. It is interesting that the oxipolished histograms center is less than the unetched samples' center. This could be due to unaccounted for systematic errors in our analysis but could also be caused by etching changing the shape of the surface. If we shift the oxipolish histogram to have the same center as the unetched histogram, then 1% of the points are above 1.25.

9.4 Microscopy and Chemical Composition

Scanning Electron Microscopy (SEM) and Energy Dispersive x-ray Spectroscopy (EDS) was used to further examine the samples. This reveals additional details of the resultant surface including topological and chemical composition. We will show only SEM backscatter scans. In this scan mode darker regions suggest flat, horizontal (with respect to the 'vertical' electron beam) surfaces while light regions suggest slopes–often seen at the edges of material grains. The bottom of 'sharp' pit will appear dark while the top of a sharp spike will appear light. In addition to this, changes in brightness can imply changes in material composition or the charging of an insulated material–the latter we do not expect to see here. EDS analysis has both a lateral and depth spread to the measurement. In the data shown we are using a 15 keV electron beam for which we expect a penetration depth of $\approx 1\,\mu m$ in Nb_3Sn. If the material changes during the penetration depth, then the chemical composition found will be a combination of the two layers. SEM is a qualitative technique while EDS will give us quantitative chemical information.

SEM scans of the 1:1:8 BCP samples are shown in Fig. 9.14. After the 150 s BCP treatments the surface looks like a moonscape of craters. We suspect that the 150 s BCP treatment has removed most of the Nb_3Sn revealing the structure of the Nb-Nb_3Sn interface. Only small chunks of Nb_3Sn remains. EDS analysis finds that the tin to niobium ratio has dropped significantly, supporting the hypothesis that the layer was mostly removed. The sample that received the 75 s BCP appears to show a mix of 'crater' like topology and regular Nb_3Sn grain structure. EDS analysis of this sample reveals the surface to still be stoichiometric–suggesting at least $\approx 1\,\mu m$ of Nb_3Sn remains. The 150 s

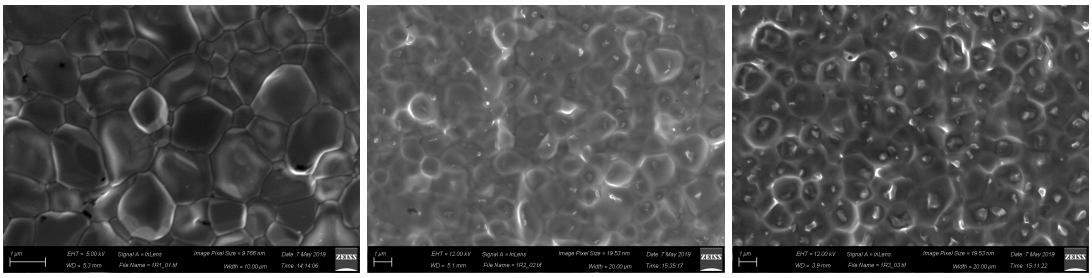

(a) (b) (c)

Figure 9.14: SEM (backscatter) scans of Nb_3Sn samples showing changes from BCP treatments. a) 10×7.5 µm scan of unetched Nb_3Sn. b) 20×15 µm scan of a sample after received 75 s of BCP. c) 20×15 µm scan of a sample after received 150 s of BCP. A 1:1:8 BCP solution was used.

BCP treatment confirms that our 1:1:8 BCP treatment does not achieve roughness reduction with almost the entire layer removed and needs modification to be useful on Nb_3Sn.

Figure 9.15 shows SEM scans of the EP sample. Of particularly interest is that on the 100 µm scan large 'white' region are visible. These spots of numerous across the surface. These appear to be regions of much thicker and roughness Nb_3Sn, suggesting that these regions were not etched/polished. This may suggest that small hydrogen bubbles formed on the Nb_3Sn surface in these locations and suppressed etching. This is seen in EP of niobium cavities but on a larger scale. EDS analysis reveals the light sections to be 23.5 at. % tin while the dark areas are 4 at. % tin. This suggests that the dark areas are only $\approx$ 200 nm and we significantly underestimated our etching rate–or the coating on this Nb_3Sn sample was particularly thin.

Figure 9.15 shows SEM scans of the oxipolished sample. Though we find a stoichiometric film, we find some residue on the surface. It is reported in HF and oxipolishing attempts on Nb_3Sn in [Pud20, P$^+$19] that extended HF rinses is associated with the production of residue on the surface. In addition, Hf rinses

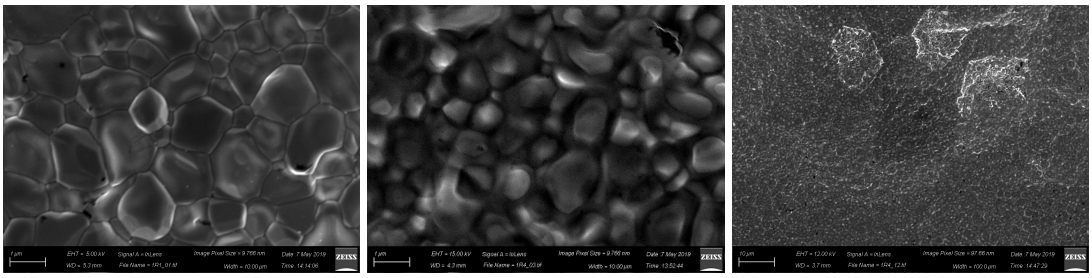

(a) (b) (c)

Figure 9.15: SEM (backscatter) scans of a Nb_3Sn sample showing changes from EP treatment. a) 10×7.5 µm scan of unetched Nb_3Sn. b) 10×7.5 µm scan of the EP sample. c) 100×75 µm of the EP sample. Note the large white portions on the scan where the material appears to be thicker. EDS analysis reveals these sections to be 23.5 at. % tin while the dark areas are 4 at. % tin.

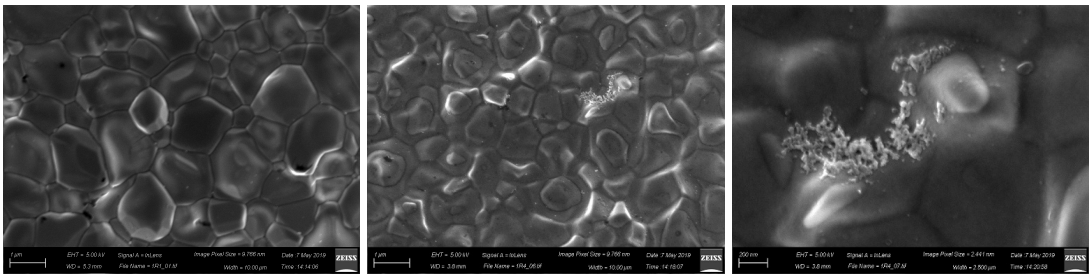

(a) (b) (c)

Figure 9.16: SEM (backscatter) scans of a Nb_3Sn sample showing changes from the oxipolishing treatment. a) 10×7.5 µm scan of unetched Nb_3Sn. b) 10×7.5 µm scan of the sample that received 24 passes of oxipolish. c) 2.5×1.875 µm scan of the sample that received 24 passes of oxipolish. Note the visible residue.

have been reported to degrade performance [Pos14].

9.5 Summary

We have seen that our Nb_3Sn surface is significantly rougher than that typically used in niobium SRF cavities. This can significantly increase the local magnetic field and potentially limit the accelerating gradient in the cavity (directly, or by making other defects worse/activate at lower accelerating gradients). Reduc-

ing the surface roughness is potentially a relatively easy route to increasing the accelerating gradients in Nb_3Sn cavities.

One way to approach reducing the surface roughness of Nb_3Sn cavities is chemical polishing. We presented preliminary investigations of standard chemical polishing used on niobium cavities. The best results were found for oxipolishing with excellent polishing results (halving roughness with 1 µm of material removal), but visible (under SEM) residue on the surface. Appropriately optimized EP is also a good candidate. Using a simple EP setup, we did see surface roughness reduction, but only by a factor of two after removing almost the entire surface layer. We have not seen good results from a BCP technique, and this would likely require significant investigation.

One potential problem of chemical techniques that we have not investigated is their impact on surface chemistry. We have seen in our work in section 7.6.4 (and elsewhere in the SRF world [PRG+20, Man20]) that the first several nanometers of material can have a significant impact on the final SRF performance. Unfortunately, the EDS techniques we use are insensitive to the near surface. In elemental materials maintaining the chemical composition of the surface is relatively simple (this might sound trivial but oxides, adsorb layers, and interstitials can be changed). In compound materials it is much harder to maintain proper surface chemistry: you may end up with several nanometers of off-stoichiometry Nb_3Sn or even a layer of elemental niobium or tin. As we noted, surface residue and degraded RF performance after an HF rinse has been seen [Pud20, P+19, Pos14]. Perfecting chemical techniques to maintain surface chemistry is worthwhile but will likely require expertise in chemistry that is beyond that of the author.

We will instead continue by pursuing a second route to smoother Nb_3Sn: optimizing material growth to create a surface that is smoother. Though we did not bring attention to it, Fig. 9.7 shows the roughness of samples before and after coating with Nb_3Sn and reveals that roughness–in the relevant length scales/λ–does not come from the substrate but from the growth of the Nb_3Sn. We will investigate growing smoother Nb_3Sn (among other things) in the next chapter.

CHAPTER 10

Nb_3Sn MATERIAL GROWTH

We have identified several potential limits to the performance of Nb_3Sn SRF accelerator cavities, but the question remains: what do we do to correct them? We looked at chemical polishing in the last chapter to control surface roughness, but another promising area is to modify the material growth process to grow smoother films to start with. We can apply this to all deleterious defects/features in our cavities and see if we can prevent them from forming. To this end, we have been studying the growth of Nb_3Sn with the Centre for Bright Beams (CBB) [SCP+21, S+21b, S+19b, S+19a, KSA20, LAH+17, H+17b]. The understanding of material growth allows us to determine how defects likely grow and how to modify the growth process to suppress them. Additional work investigating Nb_3Sn material growth has been reported in [P+19, SPR+20, Pud20]. We will start by looking at sample studies done to investigate the growth process. We will supplement this with theoretical and calculated results and make hypotheses of how some of our defects form. Finally, we will put together how to suppress two issues we have identified: roughness and tin-depleted regions.

It must be understood that the work presented below is a amalgam of work done by multiple researchers and credit should not be given to the author in isolation[1]. This work was is also based on previous work from the Cornell University SRF group [Hal17, Pos14]. In addition, we will need to refer to calculations or research that has not been published by those who conducted the work.

[1]We would like to acknowledge all those who contributed to this work as CBB collaborators or undergraduate researchers: T. Arias, Z. Baraissov, P. Cueva, J. Ding, D. L. Hall, H. Hu, M. Kelley, D. Liarte, M. Liepe, J. T. Maniscalco, D. Muller, J. Sethna, N. Sitaraman, Cornell University; R. Farber, S. Sibener, C. Thompson, S. Wilson, University of Chicago; R. Hennig, University of Florida; S. Posen, Fermi National Accelerator Laboratory.

We cannot publish their work so we will have to suffice referring to this unpublished work.

10.1 Material Growth Studies

We will start by looking at a sample-based material growth study. The principle of this experiment is simple: grow Nb_3Sn on samples, but stop the growth process at certain points in the process, turn off the furnace, and examine the samples with microscopy[2]. This investigation was started by D. L. Hall [Hal17]. We have expanded on this work with more samples and TEM + EDS microscopy on sample cross-sections[3]. These cross-sections illuminate the growth dynamics.

The study was started with a particular interested on how anodization of the sample before coating prevents the formation of 'thin regions' in Nb_3Sn coatings. These regions are comparatively large ($\approx$ 10 µm compared to $\approx$ 2 µm) Nb_3Sn grains that are only $\approx$ 300 nm thick [Hal17]. The interaction of the oxide layer with the system provides important information and we will continue to look at both anodized ($\approx$ 100 nm Nb_3O_5) and samples with only their native oxide ($\approx$ 3 nm).

We will look at 10 (2 samples at 5 temperatures) of these samples in here. Figure 10.1 shows a toy model of the growth process temperature curve and shows the temperature of the samples that we will look at. We will look at samples just after the 500 C nucleation step, at 3 temperatures during the ramp

[2]This is not a perfect representation of the growth stage for several reasons: continued dynamics during cooldown (potentially even phase changes), solidification of liquids, and changes in oxide layer. We expect these changes to be small and we can still gain a lot of qualitative information.

[3]The microscopy of cross-sections presented here was conducted by P. Cueva under the supervision of D. Muller at Cornell University.

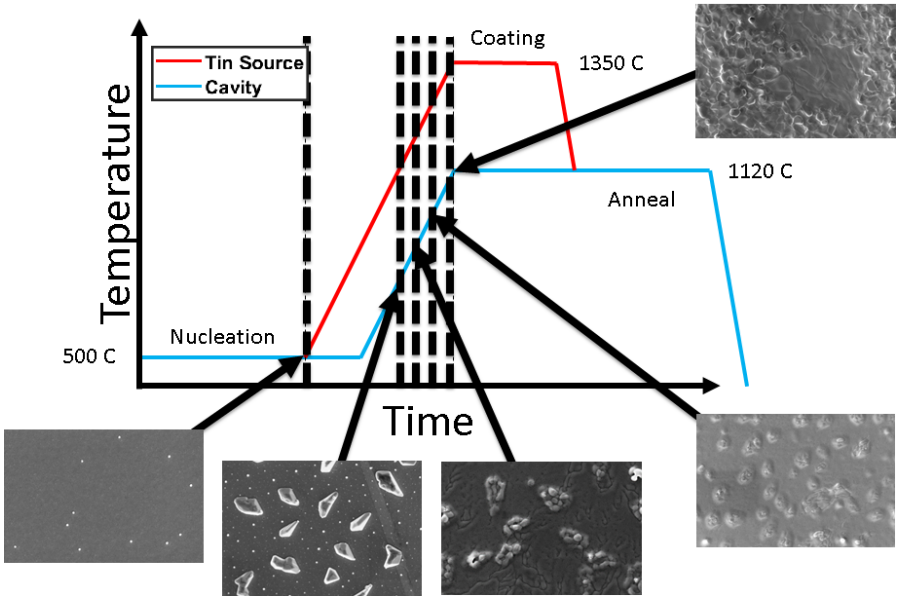

Figure 10.1: Schematic of the Nb_3Sn tin diffusion growth process with sample 'stop' temperatures marked. The plot begins with the 500 C nucleation step. We will look samples that are stopped after nucleation, 800 C, 875 C, 950 C, and 1120 C.

to coating temperatures, then one at the start of the 'full temperature' coating process. At each of these temperatures we will look at an anodized and a native oxide sample.

Before we look at the samples we would like to make several notes about the process of acquiring TEM and TEM-EDS cross-sections scans to make the results easier to interpret. The cross-sections are created by using a Focused Ion Beam (FIB) to cut out a section of the sample ('lift out'). After processing the cross-section is $\approx$ 50 nm thick. To protect the sample during this procedure a layer of platinum is sputtered on top. This platinum layer is still visible in some of the TEM cross-sections (in particularly in Fig. 10.4e). We have oriented all cross-section images so that the niobium substrate is at the bottom and the 'cavity vacuum' is at the top. EDS scans are shown overlayed on the TEM image. The EDS maps are calibrated to Sn/(Nb + Sn) to allow the stoichiometry

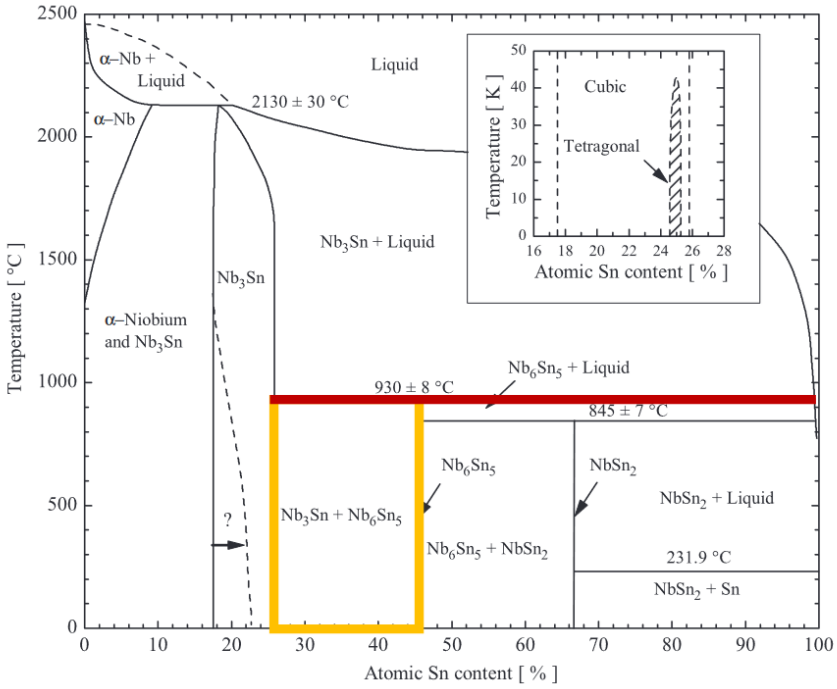

Figure 10.2: The phase diagram of the binary Nb-Sn systems. The A15 structure is favorable from 18 to 25 at. %. The inset shows a low-temperature phase diagram depicting a change in crystal structure. The Nb_3Sn + Nb_6Sn_5 region and the 930 C transition to Nb_3Sn + Sn liquid are highlighted for reference. This image was adapted from [God06] which in turn was adapted from [CC64].

to be observed. TEM-EDS has a limited resolution that is roughly the sample thickness–making the stoichiometry of thin layers of material difficult to ascertain. Selected-Area Electron Diffraction (SAED) can be used to look at the crystal structure of materials in the TEM cross-section, allowing us to find A15/Nb_3Sn areas below the resolution of EDS and investigate crystal structure and grain orientation elsewhere.

Figure 10.3 shows SEM scans of all 10 samples. We will note several important aspects here before going into more detail below. After the nucleation step we see many small clumps on the surface. These are tin nucleation sites on the surface. We see that there appears to be much more of these tin sites on the surface of the anodized sample. At the 800 C state large tin rich structures

are seen on the surface. By the 875 C step these crystal have broken down into sub crystals. These tin rich structures have gone through a phase transition to Nb_3Sn (and tin). This is indicated as a transition at 930 C in the phase diagram (see Fig. 10.2), but the temperature may be slightly lower. In addition, the phase diagram in Fig. 10.2 represents Nb-Sn phases in bulk material and we may find different behavior in thin films. At the 950 C we also see grains on most of the surface that appear to be Nb_3Sn grains. Finally, at the top of the growth curve we see a familiar Nb_3Sn structure (but with smaller grain sizes). We will now look at cross-sections to gain more insight into the growth mechanism.

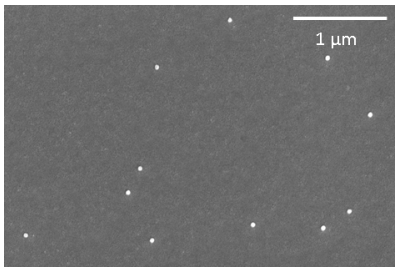

(a) Native: 500 C.

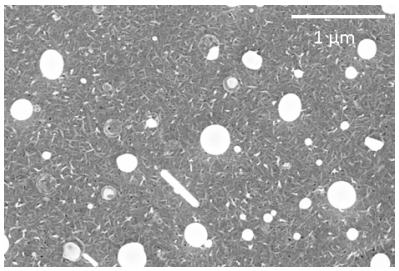

(b) Anodized: 500 C.

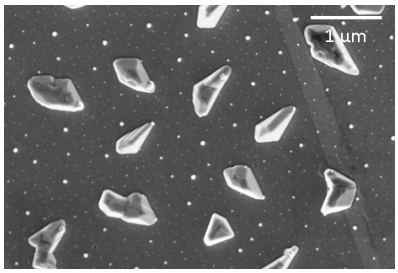

(c) Native: 800 C.

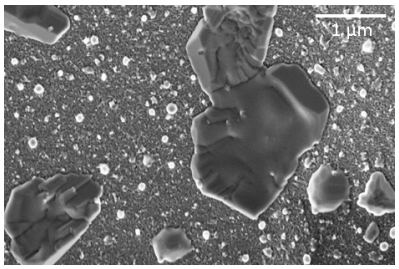

(d) Anodized: 800 C.

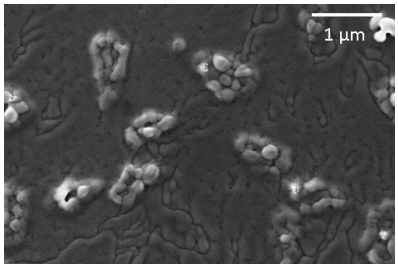

(e) Native: 875 C.

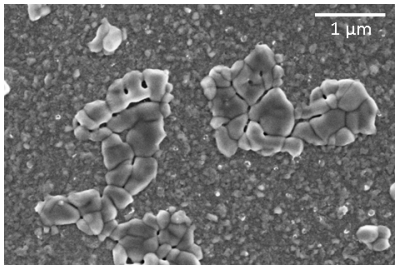

(f) Anodized: 875 C.

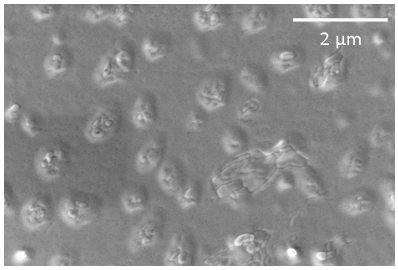

(g) Native: 950 C.

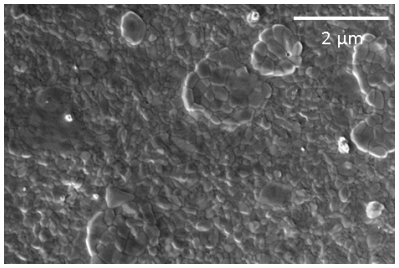

(h) Anodized: 950 C.

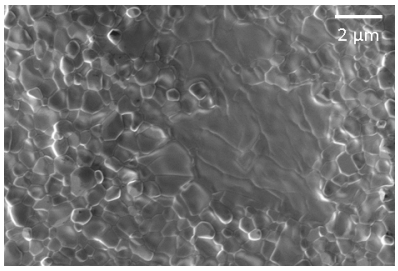

(i) Native: 1120 C.

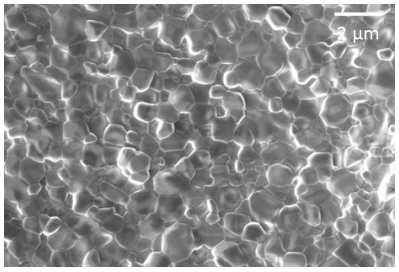

(j) Anodized: 1120 C.

Figure 10.3: SEM scans of the layer growth samples. The left side had only the native oxide before the Nb_3Sn growth process while the right side was anodized to have a ≈ 100 nm oxide.

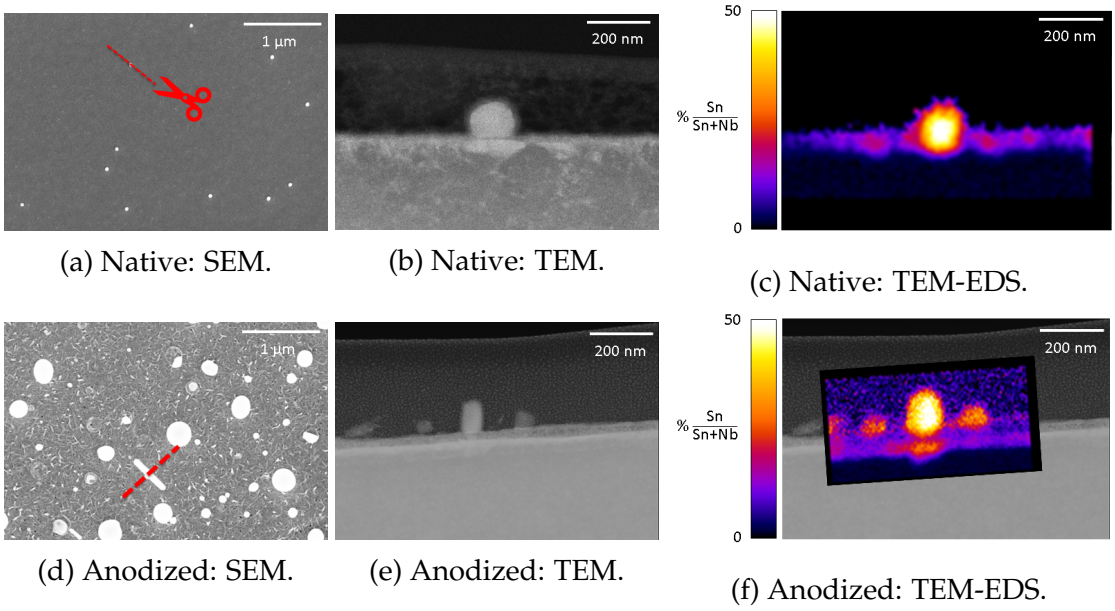

(a) Native: SEM. (b) Native: TEM. (c) Native: TEM-EDS.

(d) Anodized: SEM. (e) Anodized: TEM. (f) Anodized: TEM-EDS.

Figure 10.4: Microscopy of the post-nucleation samples. a) and d) highlight the 'kind' of area the cross-section was taken through but are not the actual location and are only for reference. b) e) show TEM cross-sections. c) and f) show TEM-EDS maps. Images b, c, e, and f courtesy of P. Cueva and D. A. Muller, Cornell University and Center for Bright Beams (CBB).

Figure 10.4 shows TEM cross-sections and TEM-EDS scans of post-nucleation samples. On both the samples we see a tin-rich substance on the surface (SAED reveals this to be an amorphic crystal structure). These are not 100% tin but have niobium components–possibly a mix $NbSn_2$, Nb_6Sn_5, and tin–showing movement of niobium up into the nucleation sites. We see the presence of another structure on the surface of the native oxide sample. SAED shows this to have an A15 structure, indicating the presence of Nb_3Sn. There are two different grain orientation on the surface with a grain boundary directly beneath the nucleation site. In the pre-anodized sample the dynamics are much the same but we can see a $\approx$ 30 nm oxide layer still on the surface. Nb_3Sn is growing both above and below the oxide layer (the niobium is likely both diffusing upward from the bulk and being absorbed from the oxide layer as the oxide breaks down).

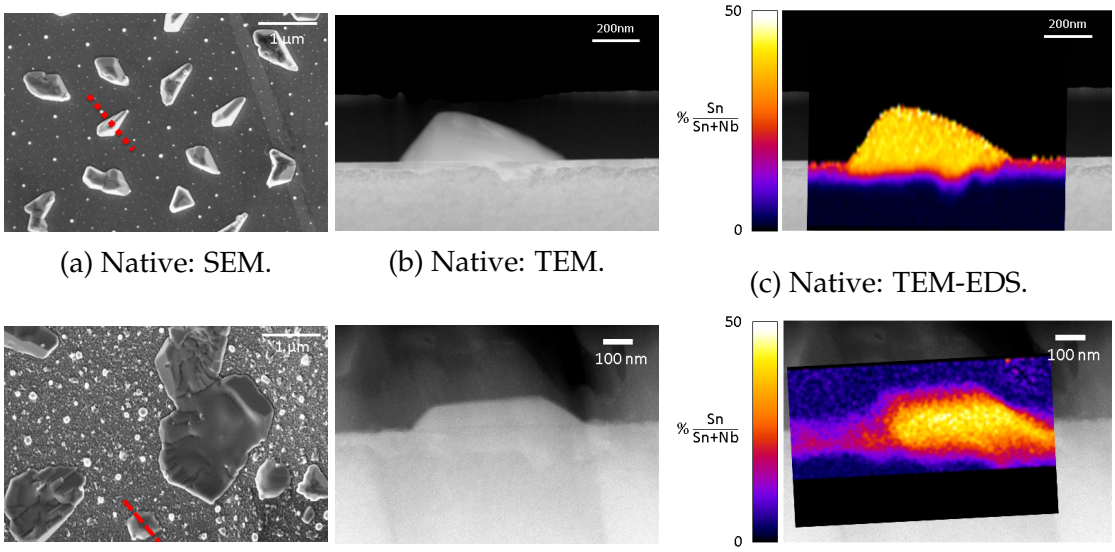

(a) Native: SEM. (b) Native: TEM. (c) Native: TEM-EDS.

(d) Anodized: SEM. (e) Anodized: TEM. (f) Anodized: TEM-EDS.

Figure 10.5: Microscopy of the 800 C samples. a) and d) highlight the 'kind' of area the cross-section was taken through but are not the actual location and are only for reference. b) e) show TEM cross-sections. c) and f) show TEM-EDS maps. Images b, c, e, and f courtesy of P. Cueva and D. A. Muller, Cornell University and Center for Bright Beams (CBB).

Figure 10.5 shows TEM cross-sections and TEM-EDS scans of 800 C samples. On both the samples we see we see a large tin rich structure, likely a mix of Nb_3Sn + Nb_6Sn_5 (see Fig. 10.2). This structure is amorphous. Again, we see significant movement of niobium into the tin nucleation sites and Nb_3Sn on the surface. On the native oxide sample, we see relatively flat Nb_3Sn. It is two grains with a grain boundary beneath the tin rich structure. The area between tin rich structures is characterized by these (relatively) large epitaxial/single crystal Nb_3Sn. By contrast the pre-anodized sample has larger tin rich structures and many smaller and rougher Nb_3Sn grains on the surface.

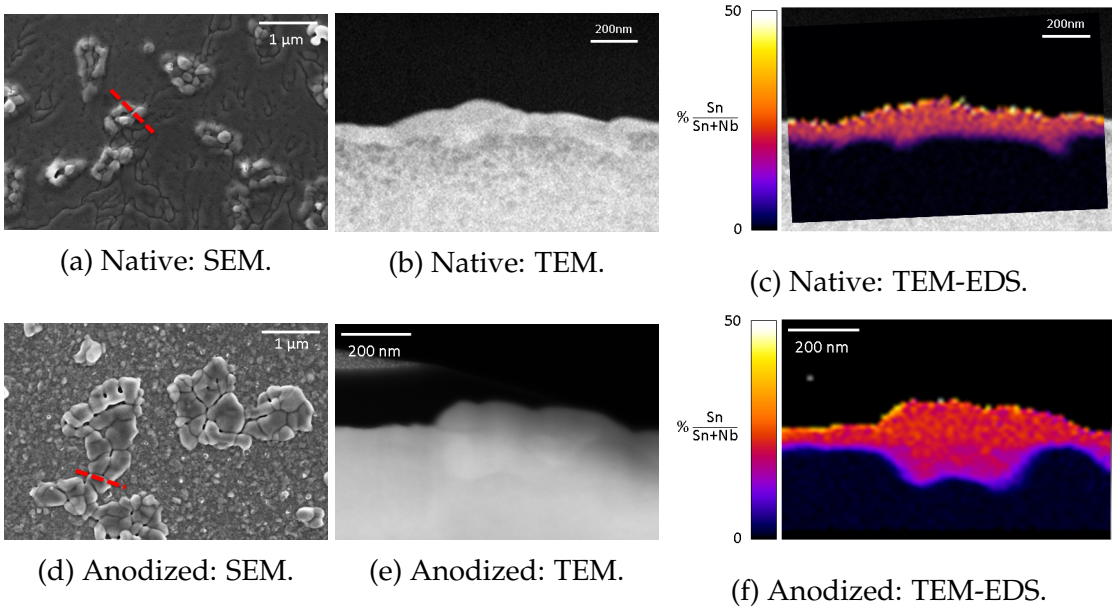

(a) Native: SEM. (b) Native: TEM. (c) Native: TEM-EDS.

(d) Anodized: SEM. (e) Anodized: TEM. (f) Anodized: TEM-EDS.

Figure 10.6: Microscopy of 875 C samples. a) and d) highlight the 'kind' of area the cross-section was taken through but are not the actual location and are only for reference. b) e) show TEM cross-sections. c) and f) show TEM-EDS maps. Images b, c, e, and f courtesy of P. Cueva and D. A. Muller, Cornell University and Center for Bright Beams (CBB).

Figure 10.6 shows TEM cross-sections and TEM-EDS scans of 875 C samples. As noted above, we see the large tin-rich nucleation sites transition into Nb_3Sn by this temperature. The Nb_3Sn layer is thick enough that TEM-EDS has sufficient resolution to see the tin to niobium ratio in the middle of the regions. We can see that the Nb_3Sn is stoichiometric in the middle. It is tempting to interpret the TEM-EDS scans as showing tin depletion near the niobium substrate, but the resolution is not enough to say this conclusively. In between the tin nucleation sites we see similar behavior to the 800 C samples: large Nb_3Sn grains on the sample with only the native oxide, and multi-grain Nb_3Sn on the sample that was pre-anodized.

At temperatures beyond this Nb_3Sn grain continue to grow, and we get our familiar structure. As the coating process continues, we get a thicker film with

larger grains. As Nb_3Sn grains grow the depth of their grain boundaries (relative to the peak height of the grain) increases and surface becomes rougher. As previous mentioned, we form large, thin grains on the samples with only a native oxide layer but do not see them on the samples that were anodized. Cross-sections of thin regions (see Fig. 10.7 below) shows little growth through these large grain areas and large amounts of growth around grain boundaries. Thick film Nb_3Sn growth has been shown to be dominated by tin diffusion through grain boundaries [Hil80]. The observed growth supports this.

We summarize some key growth takeaways from this experiment:

- More tin nucleation sites are present on pre-anodized sample and more tin is present on the surface.
- Early growth is dominated by niobium diffusing up and tin diffusing down (and niobium absorbed from the decomposing oxide layer).
- Later growth is dominated by tin diffusion through grain boundaries[4].
- Nb_3Sn forms early in the growth process–during the 500 C nucleation step.
  - Large, possibly epitaxial Nb_3Sn grains form between tin nucleation sites on the samples that have only their native oxide.
  - Many small Nb_3Sn grains form between tin nucleation sites on the pre-anodized samples (as we will discuss below, this disrupts the formation of thin film regions).

In addition to these, Density Functional Theory (DFT) calculation by N. Sitarman *et. al.* examine the formation energies of Nb-Sn com-

[4]This is further supported by unpublished calculations by N. Sitaraman of the diffusion speed of tin and niobium through Nb_3Sn.

pounds [SCP+21]. A key takeaway from this calculation is that in a niobium-rich environment (such as ours here) at high temperatures it is energetically favorable to grow tin depleted Nb_3Sn by taking tin from stoichiometric regions. The only things preventing the formation of tin depletion are excess tin and the slow diffusion rate of tin and niobium through bulk Nb_3Sn (kinetically limited). This has two important implications: we will form tin depleted regions if we entirely run out of tin, and any Nb_3Sn that exists far ($\sim$ 10 nm) from a grain boundary (including the niobium substrate boundary and vacuum boundary) will remain at its current stoichiometry unless the sample is annealed for a very long time ($\approx$ days).

10.2 Defect Formation

We will now discuss qualitative models of how several types of defects form.

10.2.1 Formation of Thin Regions

We will start with thin grain regions since these were a large motivating factor in beginning this study. Figure 10.7 shows a TEM cross-section of the edge of a thin film region and an SEM of a thin region is shown in Fig. 10.3i. We have seen that after nucleation we have Nb_3Sn on the surface. With only the native oxide layer on the surface we form large single grain crystals. We suspect that these are result of epitaxial growth on the niobium. Measurements by J. Lee *et. al.* find thin regions (on a single niobium grain) all have the same grain orientation [LPM+18]. This suggests that they are the result of epitaxial growth on the

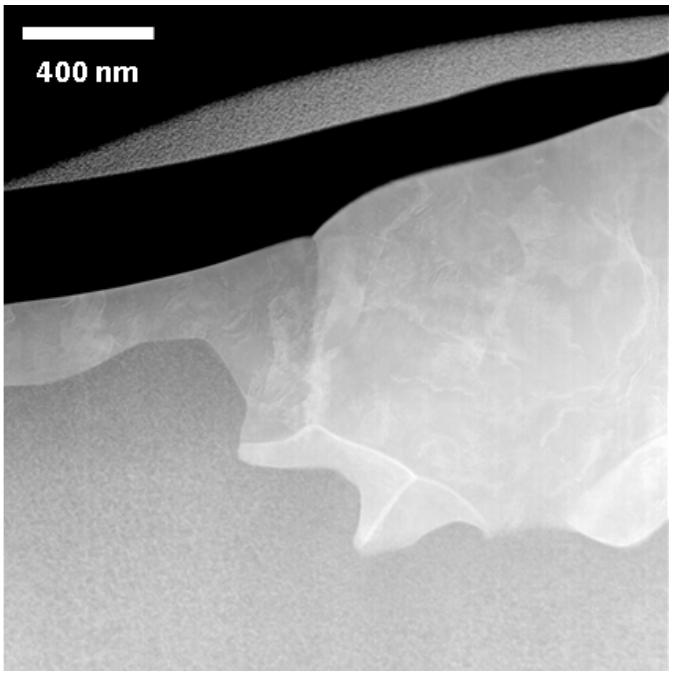

Figure 10.7: TEM cross-section of the boundary between a thin grain region and an 'ordinary' multi-grain region.

niobium substrate and supports our hypothesis that our Nb_3Sn growth on 'native oxide' samples is epitaxial. The multigrain Nb_3Sn formed at tin nucleation sites will grow and disrupt many of these single grain regions, but with limited nucleation site some of these large single grain regions will survive. These regions remain thin because the diffusion of tin and niobium through bulk Nb_3Sn is much slower compared to the diffusion of tin through grain boundaries. Not having grain boundaries, they grow relatively slowly and remain thin. In short, there are three factors at play that contribute to the formation of thin regions: epitaxial Nb_3Sn growth, relatively rare nucleation sites, and the slow diffusion of tin and niobium through Nb_3Sn

Anodizing the film before coating introduces several factors that reduce the chance of forming a thin region. The growth of Nb_3Sn on the oxide layer disrupts the epitaxial growth (especially considering that the oxide is amorphous),

creating many small grains. The oxide may also act as a temporary barrier, preventing growth on the niobium surface before large amounts of tin are present. In addition, we get many more tin nucleation sites when using an anodized substrate which help disrupt any epitaxial regions from becoming large. We can also create samples without thin regions by increase the tin flux on the sample [Hal17]. This supports that increased tin nucleation sites can also disrupt the formation of thin regions, but anodization has multiple components that reduces the likelihood of forming thin regions.

10.2.2 Sub-surface Tin-Depletion

Figure 10.8a shows a type of defect that we have seen in Nb_3Sn samples: a tin depleted region in a Nb_3Sn grain. Though the one we show here is deep enough that we do not expect it to affect performance there may be those close enough to the surface that they impact performance. In addition, if chemical polishing was applied to such a sample, it might reveal these tin depleted regions and reduce the performance.

We present a model of how this kind of defect forms[5]. We expect tin depleted regions to form at any point when we run out of free tin during the growth process. Figure 10.8b presents a toy plot of the amount of free tin available in the system during growth. We suspect that in the 'regular' growth process we run out of excess tin during the temperature ramp from ramp from 500 C to 1120 C and/or during the early coating process (when growth is faster and using more tin–whereas growth is further diffusion limited later in the coating process). During this period, we grow tin depleted Nb_3Sn at the Nb-Nb_3Sn

[5]This model was suggested by N. Sitaraman and is presented in [SCP+21]

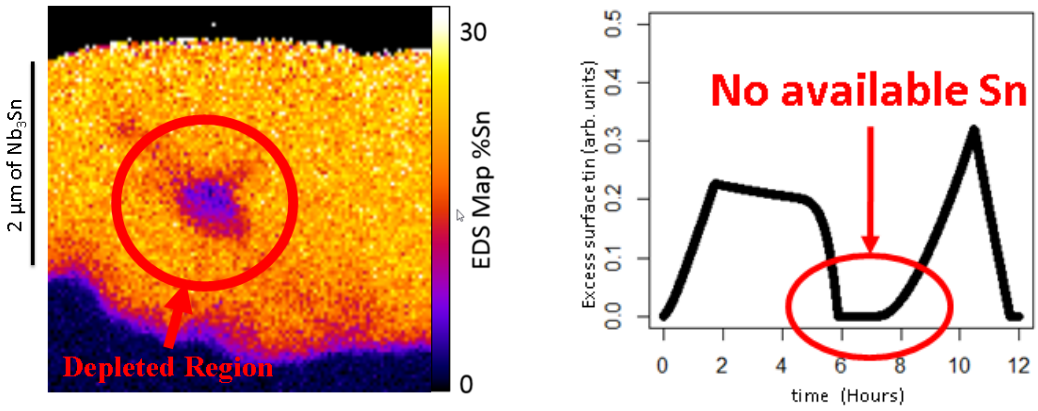

(a) (b)

Figure 10.8: a) EM-EDS of a Nb_3Sn sample. A pocket of tin depleted Nb_3Sn is seen in the middle of a Nb_3Sn grain [H⁺17b]. b) A toy model plot of the tin availability in our growth furnace during the growth process. Tin depleted regions may form at any point where we run out of tin (in this example, during the ramp from 500 C to 1120 C). a) Images provided courtesy of P. Cueva and D. A. Muller, Cornell University and Center for Bright Beams (CBB). b) This plot provided curtesy of N. Sitaraman.

boundary. Eventually the tin supply catches up and excess tin is available again, but a considerably thick layer of tin depleted Nb_3Sn has formed. Tin will begin to 'fill in' this area, but the center of the region is now far from the nearest grain boundary and filling in the middle is diffusion/kinetically limited. Though the edges of the tin-depleted region can 'fill in' with tin, the center is never 'filled in' during our coating process.

To prevent these tin depleted regions it is best to find a process where we never run out of free tin. This may include a shorter nucleation time, more $SnCl_2$, and ramping up the tin heater earlier to increase the flux of tin. Unfortunately studying these tin depleted regions is almost impossible as they require FIB lift outs to look at that are time consuming and statistically limited (due to the time-consuming nature of the measurement we cannot do many). Another option might be to chemically etch away the first 1 µm of the Nb_3Sn layer to

expose these pockets and then looking for the regions using SEM maps. This requires a chemical etching/polishing technique that we are confident won't itself change the surface chemistry.

10.2.3 Near Surface Tin-Depletion

Our investigation of the "double gap" observed in R vs T plots (in section 7.6) suggests the presence of tin depleted regions on/near the surface of our cavity. We expect these to form in the same way as sub-surface tin depleted regions discussed above, but that we run out of tin at a different time. We suspect these come from running out of excess tin early in the process when the first 100 nm are forming: during nucleation or early part of the ramp from 500 C to 1120 C. The solution to this is similar: a shorter nucleation time or increased $SnCl_2$. Increasing the temperature of the $SnCl_2$ source may also allow more tin to settle on the surface of the cavity. Using a lower cavity temperature during nucleation may also be beneficial. Calculations by N. Sitaraman find that the different oxide structure that exist at lower temperature could increase the amount of tin deposited on the surface.

10.2.4 Surface Roughness

These growth studies give us certain ways to limit the roughness of our Nb_3Sn layer. The easiest way is to grow a thinner Nb_3Sn layer. We see that the longer the cavity is coated for the larger Nb_3Sn grains become and the rougher the surface becomes. The dependence on the surface roughness on film thickness

has been shown in [P+19, SPR+20, Pud20]. Simply growing 1 µm instead of 3 µm of Nb_3Sn will significantly reduce the surface roughness. We will revisit this assertion in the conclusion.

We can also reduce the surface roughness by improving the uniformity of the nucleation. We see in our growth studies that niobium moves up into the tin nucleation sites. These sites eventually become Nb_3Sn that has 'risen' above the surface. These early tin sites remain in the Nb_3Sn structures all the way through the process, contributing to roughness. This is best seen in Fig. 10.3h. Very large tin nucleation sites may create additional roughness. Increasing tin flux earlier in the process may improve uniformity and decrease roughness, but it could similarly create large tin droplets on the surface if not done carefully.

10.3 Summary

Through layer growth studies we have learned a great deal about how Nb_3Sn forms. This has given us paths to suppress several types of defects that have been implicated in Nb_3Sn performance limitations: thin film regions, tin depleted regions, and surface roughness. This knowledge also forms a base to help mitigate any future defects that are discovered in Nb_3Sn SRF cavities.

An interesting area of further development is looking at how $SnCl_2$ interacts with the oxide layer. It has been shown that $SnCl_2$ reacts with the niobium oxide on the surface and that different characteristics of the oxide film may play a role [S+19a]. The oxide has many parameters that can be changed. There are several crystal structure that exists in the 100 - 500 C range and there may be an optimal oxide form. In addition to this, the oxide can have many chemical

groups in and on the surface that may change the reaction rate (for instance, OH^- groups). Careful design of this surface oxide may prove extremely useful to getting good Nb_3Sn films.

Another promising area of research is that of tin electroplating on niobium which is being pursued by Z. Sun [S+19c, S+19b]. In this process a layer of tin is electroplated onto a niobium substrate that is then heated to create Nb_3Sn. This could potentially create a perfect 'nucleation' process with a flat and uniform 'nucleation' of tin. Avoiding the formation of tin depletion is simply a matter of reducing the time the sample is heated for. This could create very good Nb_3Sn if perfected.

CHAPTER 11

CONCLUSION

We have set out to determine the cause of pre-mature cavity quench in niobium-3 tin (Nb_3Sn) SRF accelerator cavities. We have created new diagnostic equipment, gathered a large amount of experimental information, commented on and developed models for cavity quench, and investigated how to grow better Nb_3Sn that might improve the quench field. In this chapter we will summarize the key results from these chapters. We will then pull together these results and suggest a route to improved Nb_3Sn cavities. Using these results, we have developed a new coating technique. We will present preliminary results from this new coating process that has managed to suppress the second gap phenomenon we see in our cavities. Finally, we will comment on future development and the outlook of Nb_3Sn SRF cavities.

11.1 Experimental Equipment Development

We have developed two fantastic new tools for investigating SRF cavity performance: a dynamic temperature mapping system and the Cornell High Pulsed Power Sample Host Cavity (CHPPSHC).

The dynamic temperature mapping system is a first of its kind system that is capable of taking temperature maps of SRF cavities at 50 ksps while achieving extremely low noise (as low as 15 µK). This system can reveal new dynamics and will be key to studying the quench mechanism of Nb_3Sn cavities. More broadly it will increase the understanding of dynamic losses in SRF cavities and help identify issues with niobium, Nb_3Sn, and any other new materials. This

system is fully functional and has been used to make measurements of Nb_3Sn cavities.

The CHPPSHC is an exciting tool for testing the ultimate quench field of new SRF materials. This system accepts a small sample of a material and is used to find the quench field of the material in RF fields. The system is optimized so that RF fields rise quickly, and the ultimate quench field can be reached. The system can reach the superheating field of current SRF materials in mere microseconds. This will allow us to test the true field limit of Nb_3Sn and quickly test the quench fields of new material Nb_3Sn formulations. Beyond Nb_3Sn this cavity can be used to test new materials without have to make an entire cavity. The CHPPSHC has been fabricated and commissioning will begin before the end of the year.

11.2 Experimental Results

11.2.1 RF Cavity Tests and Analysis

We have conducted RF testing on various RF cavities and have learned much about the quench field. We tested the temperature dependence of the quench field and manufactured a new high frequency ($> 1.3\,\text{GHz}$) cavities to test the frequency dependence of the quench field (among other things). We summarize three key results that give us information about the quench mechanism, limiting possible defects,

- There is a small range of typical quench fields: $14\,\text{MV/m}$ to $18\,\text{MV/m}$

(59 mT to 76 mT).

- The quench mechanism is temperature independent from 1.8 K to 4.2 K.
- The quench mechanism is not strongly frequency dependent.

In addition to this, our cavities show a multi-gap behavior in the BCS surface resistance. This implies that superconductivity is somehow being suppressed. We investigated models including tin depleted regions and normal conducting surface layers. Both models fit the data well. Though both models are possible, we have yet to find a normal conducting layer on the surface of our Nb_3Sn cavities while we have seen lightly tin depleted grains and thin surface layers of tin depleted Nb_3Sn in TEM-EDS cross-sections. The simulations show that the tin depleted regions make up $\approx 0.1\%$ of the surface so it is likely that we simply have not seen more severely tin depleted regions using microscopy. Measurements shown below further supports the hypothesis that this multi-gap behavior is caused by tin depleted regions. These regions increase the resistance of our Nb_3Sn cavities.

11.2.2 Temperature Mapping

We have shown the first time-resolved thermometry of Nb_3Sn SRF cavities and took videos of cavity quench. We imaged the first quench of a Nb_3Sn cavity and saw dynamics that look like a multipacting induced quench. After several quenches there was a transition to a second quench site. This second site was a single localized quench site, as has been seen in older quench maps of Nb_3Sn cavities.

Temperature jumps, previously observed only at the cavity quench site, were seen at many locations on the cavity. We examined models of temperature jumps based on magnetic flux entry at grain boundaries. We find that the model presented in [SG17] gives reasonable results for what we see in our cavities. Though the model presented in [CPT+21] does not provide enough heating (in its current form) to account for the temperature jumps we see, it gives qualitative agreement with the dynamics we see. Still, the model is within an order of magnitude of what we expect which still makes it a promising candidate. The model also replicates temperature and frequency independence that we see, making it an excellent candidate. In addition, this model implicates grain boundary geometry and surface roughness as contributing factors to cavity quench. These explanations both imply that a thinner, less rough Nb_3Sn layer would reduce the impact of grain boundaries on cavity performance and potentially increase the quench field.

Using a thermal simulation we examine heating, temperature jumps, and thermal stability in our Nb_3Sn cavities. We see that thick Nb_3Sn layers are (relatively) thermally unstable. We find that our cavity quench field could be explained by a $\approx 3\,\mu m$ normal conducting region. In addition, we find that in the multilayer material we can form small, stable normal conducting regions. These regions are formed by a smaller underlying defect creating heat in a small area. This both amplifies the losses caused by the underlying defect and can explain the temperature jumps we see in our cavities. The thermal instability also explains our small range of quench fields. For a normal conducting region in the range of 4 to $100\,\mu m$ in radius we find roughly the same quench field of 60 to 68 mT. Only once defects become smaller than ~ grain size will quench field start increasing (assuming the defect is not lossier than a normal conducting

region of the same size–which might not be true). We would only expect very bad coatings to have defects worse than a 100 µm region of normal conducting material–in which case we would likely see something using microscopy–explaining the small spread of achieved quench fields. This also explains the apparent temperature independence: increasing the bath temperature only decreases the 'maximum defect size.' Assuming we are well below this, we would not see a temperature dependence below 4.2 K. This implies that simply reducing the Nb_3Sn film thickness could substantially increase the achievable quench field. Reducing the Nb_3Sn thickness to 1.5 µm could potentially increase the quench field to ≈ 27 MV/m without addressing the underlying defect.

11.2.3 Surface Roughness

We have shown that our Nb_3Sn surface is significantly rougher than that typically used in niobium SRF cavities. This can significantly increase the local magnetic field and potentially limit the accelerating gradient in the cavity (directly, or by making other defects worse/activate at lower accelerating gradients) and lower the barrier to magnetic vortex entry at grain boundaries. Reducing the surface roughness is potentially a relatively easy route to increasing the accelerating gradients in Nb_3Sn cavities.

We examined standard chemical treatments used to polish niobium cavities. We found good preliminary results from electropolishing and oxipolishing. Oxipolishing managed to halve the surface roughness with only 1 µm of material removal. Still more studies are needed to see if these treatments have deleterious effects on the surface chemistry (the first several nm) and we continued by

focusing on growing smoother Nb_3Sn.

11.3 Material Growth

We showed results from a material growth study and discussed theoretical calculations of Nb_3Sn growth. This research was conducted with the Center for Bright Beams (CBB) collaboration. Our key takeaways from these sample studies are,

- More tin nucleation sites are present on pre-anodized sample and more tin is on the surface.
- Early growth is dominated by niobium diffusing up and tin diffusing down (and niobium absorbed from the decomposing oxide layer).
- Later growth is dominated by tin diffusion through grain boundaries.
- Nb_3Sn forms early in the growth process.
- Large, possibly epitaxial Nb_3Sn grains form between tin nucleation sites on the samples that have only their native oxide.
- Many small Nb_3Sn grains form between tin nucleation sites on the pre-anodized samples.
- Niobium and tin diffusion through bulk Nb_3Sn is slow.
- It is energetically favorable to form tin depleted Nb_3Sn in the absence of free tin.
- Changing the stoichiometry of Nb_3Sn far from grain boundaries ($>\sim$ 10 nm) is a slow process ($\sim$ 1 hour) at our coating temperatures due to slow diffusion of niobium and tin through Nb_3Sn.

From this understanding we suggest methods to suppress the formation of performance impacting defects:

- Tin depleted regions: Ensure we never run out of tin during the growth process. This can accomplished through the use of anodization, increased $SnCl_2$, a shorter nucleation step, and increasing the temperature of our tin source heater earlier in the process.
- Surface roughness: More uniform nucleation and growing thinner films. We can easily reduce our film thickness from 3 µm to 1 µm by shortening the coating time. By increasing our tin flux, we might create a more uniform nucleation layer. Luckily, this requires the same modifications as for preventing tin depleted regions.

In addition to this, we have provided an explanation of how anodization prevents the formation of thin film regions and improves nucleation.

11.4 How to Increase the Accelerating Gradient of Nb_3Sn Accelerator Cavities

In the above section we have summarized potential mechanisms contributing to the cavity quench, but what is the quench mechanism? We see a multipacting-type quench and a localized quench in our temperature. We expect equator multipacting to have a frequency dependence, but do not see an increase in the quench field in high frequency cavities. A possible way to reconcile this is that we have hit two quench mechanisms that lie at almost the same field at 1.3 GHz:

the beginning of the multipacting band, and a second quench mechanism that is frequency independent. Since we have not done temperature mapping on high frequency Nb_3Sn cavities we don't know what type of quench occurs there, but we may not see the multipacting quench. A recent Nb_3Sn cavity from CBB collaborator S. Posen achieved increased accelerating gradients (we will discuss this in more detail below) [PLS+21]. In testing this cavity, they experienced multipacting that had to be processed to get to higher accelerating gradients. This supports that we are seeing two close together (in onset field) quench mechanisms. The transition between quench sites was from processing of a multipactor that slightly increased the accelerating gradient to the point that another defect caused quench.

Even without detailed knowledge of the quench mechanism we can say that the thermal instability of the Nb_3Sn layer heavily contributes to the premature cavity quench. The poor thermal conductivity creates a feedback effect near defects: the heating raises the temperature, which increases the local surface resistance, which increases the hearing. This makes defects 'worse' than they would otherwise be. In this scenario it is much easier to cause the cavity to quench. In this thermally unstable regime, it is easy for small heat sources/defects to cause thermal runaway. The energy could come from flux entry and heating at grain boundaries (localized quench), from electron impacts (multipacting quench), or other source.

Unlike in niobium, in Nb_3Sn our thermal simulations find almost no difference in the quench field of a normal conducting defect in going from 2 K to 4.2 K (unless the defects are much larger than we expect). In addition, for a wide range of defect sizes we get the same quench field–potentially explaining

the small range of observed quench fields. Still, these defect does not perfectly match our measurement frequency dependence. Based on the frequency scaling of the normal conducting resistance, our thermal simulations suggest that if the quench field of normal conducting region at 1.3 GHz is $\approx$ 18 MV/m it would drop to 15 MV/m at 2.6 GHz and to 13.5 MV/m at 3.9 GHz. To make this thermal model work we would still need a frequency independent underlying defect (such as vortex entry at grain boundaries). Still these thermal simulations suggest that decreasing the thickness of our Nb_3Sn layer is an easy change that can improve the thermal stability of Nb_3Sn to defects and multipacting.

We have also seen that surface roughness can play a role in cavity quench in multiple ways. Local magnetic field enhancement can decrease the 'activation' filed of a defect and increase the losses of a defect. We have seen that a poor grain boundary geometry can lower the first field of vortex entry. This makes reducing surface roughness reduction a great target for improving quench field.

We have detailed two goals: decrease the film thickness and reduce the surface roughness. Though it may not be related to the quench mechanism, we can also attempt to improve the stoichiometry of our Nb_3Sn and remove the 'multi-gap' behavior. Using our knowledge from layer growth studies we can design a new coating procedure to accomplish this. We propose these changes to the coating process:

- Anodize the cavity. We need this to both improve nucleation and prevent thin grain regions that would be detrimental when combined with a thinner coating.
- Maximize the temperature of secondary/tin heat source at the start of the process (this also raises the temperature of the $SnCl_2$ but by how much is

not known). This will help avoid running out of tin during the growth process.

- Skip the pause at the nucleation step and continue directly to the coating temperature (as fast as the furnace can be safely ramped). Again, we do this to add tin to the surface as quickly as possibly to prevent tin depleted sites, and hopefully, create more uniform nucleation.
- Reduce the coating time to achieve a thinner film. We suggest a 45 min coating time as a first try. This should create a 1.5 µm Nb_3Sn layer in our growth furnace.

11.4.1 Suppression of Multi-Gap Superconductivity in a Nb_3Sn Cavity

We have used the above method to create a new Nb_3Sn cavity. The coating temperature profile is shown in Fig. 11.1. Upon removing the cavity from the coating furnace, we could see that it was 'shinier'–implying a decrease in surface roughness. A picture of the cavity is shown in Fig. 11.2. Analysis of a sample coated using the same coating profile found a strong decrease in the surface roughness. Figure 11.3 shows the ASD of this sample compared to our standard coating. The roughness is significantly decreased in the 2 to 6 µm range, slightly more than halving at the 4 µm wavelength.

RF testing results are shown in Fig. 11.4. An exciting result is that we have seen the disappearance of the multi-gap behavior. Figure 11.4a shows the BCS resistance acquired from fitting a single-gap BCS model. We usually find the BCS resistance (when using a single-gap fitting algorithm) to be $\approx 8\,n\Omega$ at 4.2 K.

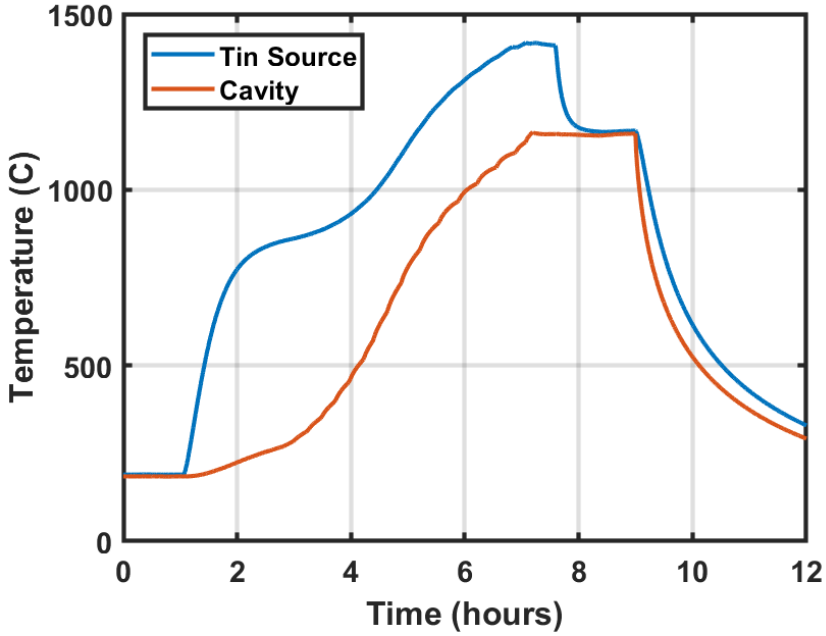

Figure 11.1: The coating temperature profile of the new coating. The secondary heater is turned on and allowed to warm up for 2 hours, then the cavity temperature is ramped up to 1120 C. When the tin source reaches 1350 C we hold the tin source at there for 45 min then turn off the secondary heater. We wait 1 hour for the cavity to anneal at 1120 C then turn of the main heater.

We find that the BCS resistance at 4.2 K is a mere 3.5 nΩ in this cavity. The energy gap was similarly improved, found to be $2.28 \cdot k_b T_c$ compared to be $\approx 2.12 \cdot k_b T_c$. This is a fantastic performance improvement that implies that 1.3 GHz Nb_3Sn TESLA elliptical cavities could (theoretically) be made with a Q of $7.8 \cdot 10^{10}$ at 4.2 K. A cavity of this performance would be ≈ 5 times more efficient than the best performing niobium cavities.

We did see an increase in residual resistance in this cavity. Optical inspection reveals small (≈ 0.5 mm across) 'white spots' on the interior cavity surface (bottom half cell only). We suspect that these are either large thin/patchy regions of Nb_3Sn, or a large drop of tin (during nucleation) that created a large, rough, and complicated Nb_3Sn surface. Unfortunately, we cannot investigate these objects

Figure 11.2: Left: The new Nb_3Sn cavity. Right: A standard coating Nb_3Sn cavity. Note that the new cavity it is shinier suggesting a smoother surface.

without destroying the cavity. These types of regions are both associated with increased residual resistance. For a next coating run we will likely pause at a nucleation temperature of 400 C for several hours in hopes that we can improve nucleation and avoid these defects.

Unfortunately the cavity quenched at 14 MV/m. Temperature mapping (and radiation production) revealed this to be a multipacting quench. Prior to testing this cavity, the vertical test insert suffered a helium leak into the ultra-high

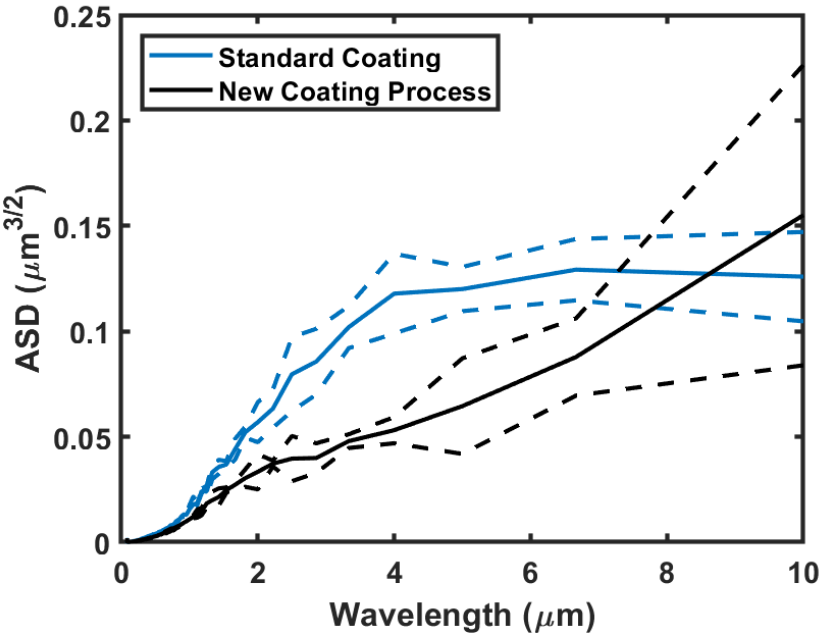

Figure 11.3: ASD of a sample coated with the same process as the new cavity coating. There is a statistically significant reduction in the surface roughness in the 2 to 6 µm wavelength range.

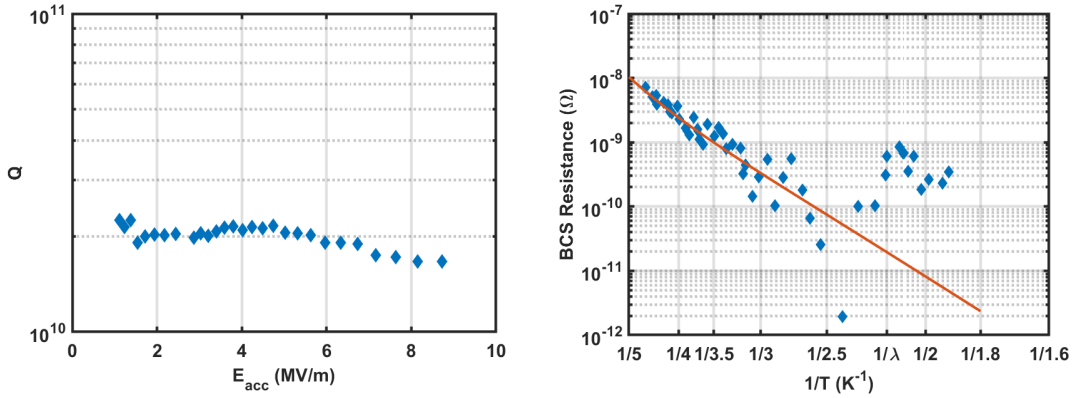

(a) (b)

Figure 11.4: RF testing results from the new cavity. a) Q vs E at 4.2 K. The cavity quenched from a field emitter at 14 MV/m. b) The fit BCS-resistance of the new cavity coating versus temperature ($1/T$). There is no longer any apparent 'multi-gap' behavior. The BCS resistance at 4.2 K is 3.35 nΩ (at 3 MV/m). Note: this plot includes data at temperatures above 4.2 K.

vacuum region. This caused electrical discharges/arcing that created debris. The insert was disassembled and cleaned but there is still an increased chance of debris/dust being present in the system and causing a field emitter. This is likely not the ultimate quench of this cavity. The cavity has been cleaned and is awaiting a retest wherein, hopefully, it will reach a higher accelerating gradient.

Recently[1] Center for Bright Beams (CBB) collaborator S. Posen coated a cavity at Fermi National Accelerator Laboratory (FNAL) that achieved a 24 MV/m accelerating gradient [PLS+21]. This cavity coating included some similarities to ours: increased tin heater temperature early in the process, a thinner Nb_3Sn layer ($\approx$ 1 µm), and a smooth, shiny surface (R_a = 63 nm vs R_a = 94 nm for our improved cavity[2]). Though the coating profiles are not identical this suggests our cavity might see similar improvement. Our work here also offers a potential explanation as to why this cavity has improved performance compared to historic coatings.

11.5 Future Outlook

This is an exciting time for the development of Nb_3Sn SRF accelerator cavities. Nb_3Sn achieves high quality factors at 4.2 K operation and usable accelerating gradients. We have reached the point where Nb_3Sn is already appropriate for some accelerator projects. We might see the first Nb_3Sn accelerator projects started in the next decade. We are already seeing the early development of cryocooled Nb_3Sn cavities [SHL+20, DPG+20, CCPR20] and Nb_3Sn SRF electron

[1] This was done before we created our cavity or our suggested growth process changes.
[2] R_a is used in the referenced text.

guns[3]. The development of small scale Nb_3Sn based accelerators represents not just an improvement to current technology, but the development of a whole new branch of accelerators that advance other fields and industries. We may see these Nb_3Sn based accelerators employed in road construction, medicine, water treatment, security (cargo scanning), and small scale research [HW15, HS09].

We have seen considerable advancement of Nb_3Sn cavities in the past decade. A decade ago the usable gradient ($Q > 10^{10}$) was less than 5 MV/m and we have seen it increase to 21 MV/m. In addition, the material science understands of Nb_3Sn growth and grain boundary dynamics has advanced substantially. Historical development was best characterized as 'guess and check' based on a hunch. In a system with so many variables one has to get very lucky to hit the correct set of parameters. We are now developing models that can lead us to these parameters and better coating methods. On top of this, alternative coating method development [G$^+$21, Val21, KHS21, S$^+$21a, G$^+$19, RSI$^+$16, BBR$^+$16] is underway at many institutions. These offer new tools to adjust the Nb_3Sn coating. Tin electroplating (and thermal annealing) [S$^+$19c, S$^+$19b] is a particularly exciting area of development that could make high performance Nb_3Sn cavities. In the next decade we may see Nb_3Sn cavities that surpass their niobium brethren in accelerating gradients and already they already surpass niobium in efficiency.

[3]Personal communications.

APPENDIX A

THERMAL MODEL DETAILS

In chapter 8 we introduced a thermal code for solving the equilibrium state of a Nb_3Sn SRF surface. There we gave only a brief introduction to the functioning of the code. Here we give specific details of the code and the equations that are solved. We will start by detailing the equations in a bulk, single material, then move on to boundary conditions, and multiple layers.

We restrict ourselves purely to the case of rotational symmetry. We use cylindrical coordinates (r, z, θ) and can ignore θ. Furthermore, we restrict our geometry to a disk of radius R, chosen to be large enough that the defect has no significant impact on the temperature at the edge of the disk (2 cm for all results shown in this work). Our disk is a total thickness z_T while the Nb_3Sn and niobium layers are z_{T1} and z_{T2} respectively (see Fig. A.1).

A.1 Equations in a Single Material

A.1.1 Bulk Equations

We start by deriving the equations in a single material. We subdivide our problem into a grid in r and z (r_i and z_j) where each mesh element is at the temperature $T_{i,j}$ (see Fig. A.2). Each mesh element represents an annular ring (see Fig. A.3a) of volume $V_{i,j}$. Figure A.3b shows the relevant volume, and side areas of the annular ring and are given by,

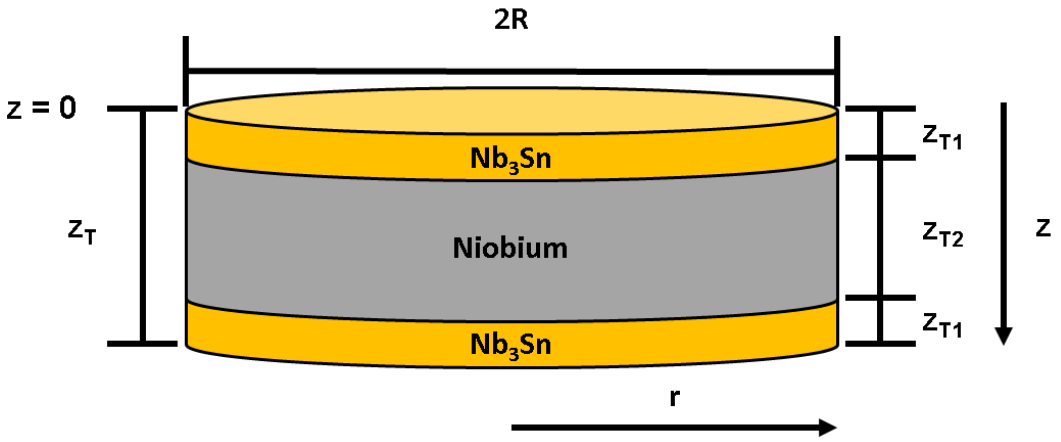

Figure A.1: A diagram of the simulation showing length scales. We simulate a disk of radius R that is z_T thick. We define $z = 0$ as the RF surface with z increasing as we move towards the helium interface.

$$
\begin{aligned}
A1_{i,j} &= 2\pi r_{i+1}\left(z_{j+1} - z_j\right) \\
A2_{i,j} &= 2\pi r_i\left(z_{j+1} - z_j\right) \\
A3_i &= \pi\left(r_{i+1}^2 - r_i^2\right) \\
A4_i &= A3_i = \pi\left(r_{i+1}^2 - r_i^2\right) \\
V_{i,j} &= \pi\left(r_{i+1}^2 - r_i^2\right)\cdot\left(z_{j+1} - z_j\right) \ .
\end{aligned}
\tag{A.1}
$$

We can look at the heat flow, ΔQ, into and out of the i, j^{th} element during a short period of time, Δt. Heat will move from the 4 adjacent elements and heat will be deposited in the material from RF losses. The heat flow from the $i+1, j^{\text{th}}$ element into the i, j^{th} element is given by,

$$
\frac{\Delta Q}{\Delta t} = A1_{i,j}\cdot kr_{i,j}\cdot\frac{\mathrm{d}T}{\mathrm{d}r} = A1_{i,j}\cdot kr_{i,j}\cdot\frac{(T_{i+1,j} - T_{i,j})}{\Delta r}\ , \tag{A.2}
$$

$kr_{i,j}$ is an effective thermal conductivity between these two elements. Δr is the 'distance' between these two elements when finding the gradient of the temper-

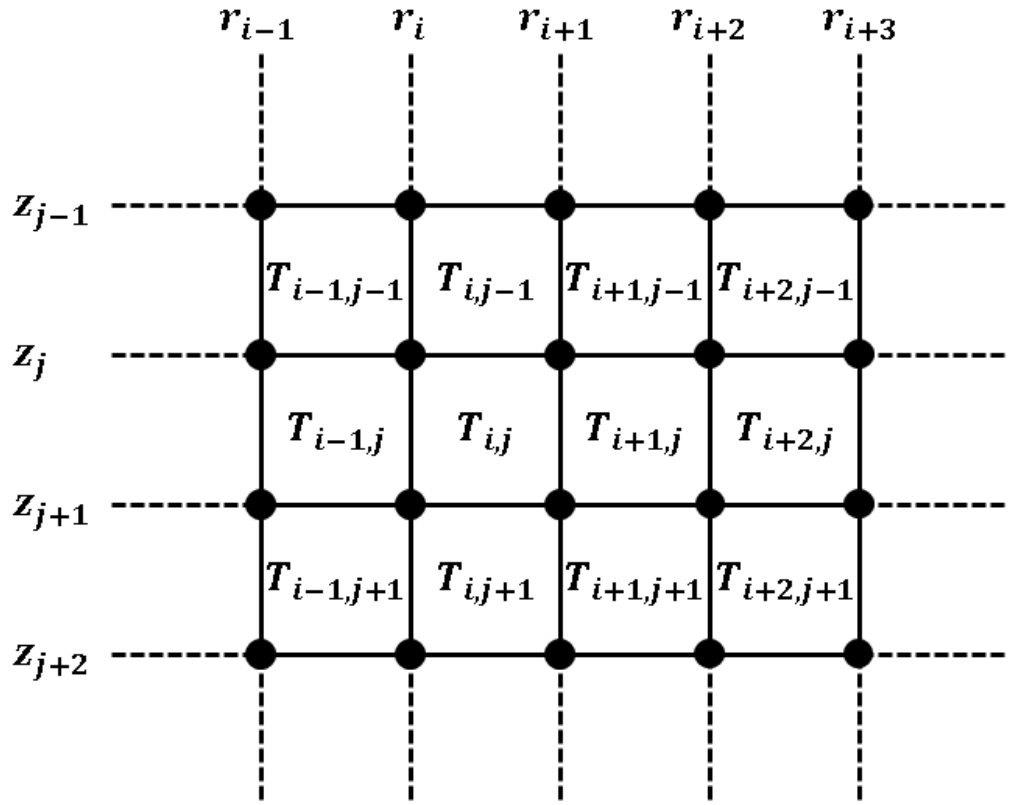

Figure A.2: A diagram showing how we discretize the r-z plane into elements. The temperature of the i, j^{th} element is $T_{i,j}$ and the upper left corner of the element is (r_i, z_j).

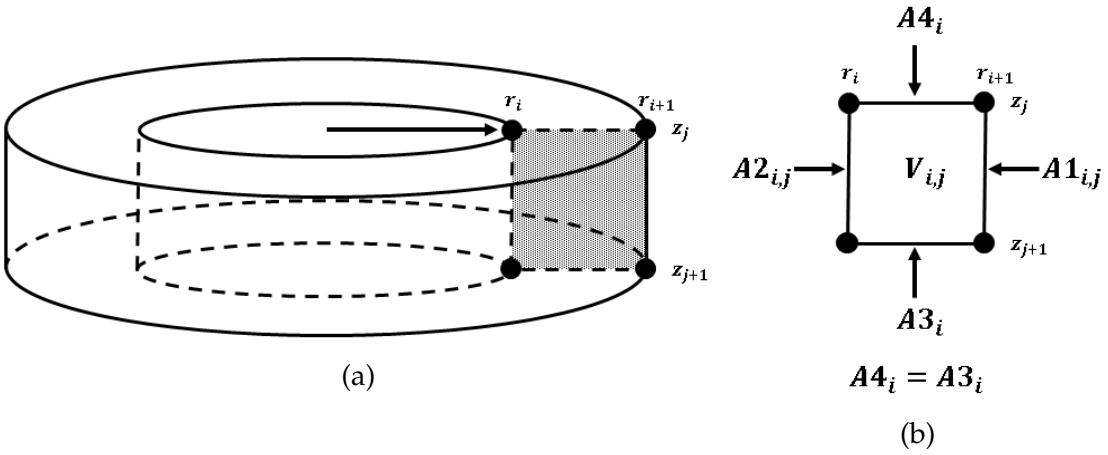

Figure A.3: a) A diagram of a single mesh element showing the full annular ring geometry. b) The same mesh element with area elements of the sides labeled. The areas are defined in equation A.1. Though $A3$ and $A4$ are identical we maintain the separate labels to make equations easier to read. Note: $A3$ and $A4$ are independent of the z coordinate.

ature change. Here we will use the distance between the midpoint of the two elements,

$$\Delta r = (r_{i+1} + r_{i+2})/2 - (r_i + r_{i+1})/2 = (r_{i+2} - r_i)/2 \,, \tag{A.3}$$

which reduces to half the distance between the surfaces adjacent to $A1_{i,j}$. For simplicity we define,

$$C1_{i,j} = \frac{2 \cdot A1_{i,j}}{(r_{i+2} - r_i)} \,, \tag{A.4}$$

with which equation A.2 reduces to,

$$\frac{\Delta Q}{\Delta t} = C1_{i,j} \cdot kr_{i,j} \cdot \left(T_{i+1,j} - T_{i,j}\right) \,. \tag{A.5}$$

We can similarly apply this to the other 3 adjacent elements and arrive at[1],

$$\begin{aligned} \frac{\Delta Q}{\Delta t} = {} & C1_{i,j} \cdot kr_{i,j} \cdot \left(T_{i+1,j} - T_{i,j}\right) + C2_{i,j} \cdot kr_{i-1,j} \cdot \left(T_{i-1,j} - T_{i,j}\right) + ... \\ & C3_i \cdot kz_{i,j-1} \cdot \left(T_{i,j-1} - T_{i,j}\right) + C4_i \cdot kz_{i,j} \cdot \left(T_{i,j+1} - T_{i,j}\right) + QRF_{i,j} \,, \end{aligned} \tag{A.6}$$

where,

[1]We note that this is a discretized form of the heat equation in cylindrical coordinates. We rewrite the left-hand side as,

$$\frac{\Delta Q}{\Delta t} = \frac{V_{i,j}}{V_{i,j}} \frac{c\rho}{c\rho} \cdot \frac{\Delta Q}{\Delta t} = V_{i,j} \cdot c\rho \cdot \frac{T_{i,j}(t + \Delta t) - T_{i,j}(t)}{\Delta t} \,,$$

where c is the heat capacity and ρ is the density. We have simply used a conceptual derivation here to arrive at our discretized form instead of starting with the heat equation.

$$
\begin{aligned}
C2_{i,j} &= \frac{2 \cdot A2_{i,j}}{(r_{i+1} - r_{i-1})} \\
C3_i &= \frac{2 \cdot A3_i}{(z_{i+2} - z_i)} \\
C4_i &= \frac{2 \cdot A4_i}{(z_{i+1} - z_{i-1})} \ ,
\end{aligned}
\tag{A.7}
$$

$kz_{i,j}$ is the effective thermal conductivity between the i, j^{th} and the $i, j+1^{\text{th}}$ elements, and $QRF_{i,j}$ is the energy absorbed from the RF fields in the i, j^{th} element during a time period Δt.

If the difference in temperature between adjacent elements is small the form of the effective thermal conductivity is not of particular importance. We use the approximation,

$$
\begin{aligned}
kr_{i,j} &= k\left(\frac{T_{i+1,j} + T_{i,j}}{2}\right) \\
kz_{i,j} &= k\left(\frac{T_{i,j+1} + T_{i,j}}{2}\right) \ .
\end{aligned}
\tag{A.8}
$$

After solving the problem we must then confirm that the temperature/conductivity change is sufficiently small and reduce the mesh size if it is not.

We note that in the equilibrium state the net change in energy of the mesh element is zero and that $\Delta Q = 0$. Using this we reorganize the equation A.6 as,

$$
\begin{aligned}
QRF_{i,j} = &\left(C1_{i,j} \cdot kr_{i,j} + C2_{i,j} \cdot kr_{i-1,j} + C3_i \cdot kz_{i,j-1} + C4_i \cdot kz_{i,j}\right) T_{i,j} + ... \\
&- C1_{i,j} \cdot kr_{i,j} \cdot T_{i+1,j} - C2_{i,j} \cdot kr_{i-1,j} \cdot T_{i-1,j} - C3_i \cdot kz_{i,j-1} \cdot T_{i,j-1} + ... \\
&- C4_i \cdot kz_{i,j} \cdot T_{i,j+1} \ ,
\end{aligned}
\tag{A.9}
$$

where we have moved $QRF_{i,j}$ to the left-hand side and reorganized the right-hand side so that the first term contains all diagonal terms (in a matrix representation). We now have an equation of the form,

$$\begin{aligned} \vec{b} &= A \cdot \vec{T} \\ b_k &= \sum_l A_{k,l} T_l \ , \end{aligned} \tag{A.10}$$

where A is a matrix relation and T and b are column vectors consisting of all mesh elements in the system (say, if we have an $N \times M$ mesh then T and b are $N \cdot M$ element vectors and A is an $N \cdot M \times N \cdot M$ matrix). Equation A.10 can be solved sequentially by the method of successive over-relation using the equation [Had00],

$$(D + \omega L)\vec{T}_n = \omega\vec{b} - [\omega U + (\omega - 1)D]\vec{T}_{n-1} \ , \tag{A.11}$$

where D, L, and U are the diagonal, upper triangular, and lower triangular components of A, and ω is the 'over relaxation parameter' which we will discuss in more detail below. We iterate this equation–where $\vec{T}_{n+1}$ is the next step in the iteration–and (hopefully) the sequence converges to the equilibrium state. We write out the equation in terms of the components and solve for T_n,

$$T_{n,k} = (1 - \omega)T_{n-1,k} + \frac{\omega}{a_{kk}}\left(b_k - \sum_{l<k} a_{kl}T_{n-1,l} - \sum_{l>k} a_{kl}T_{n-1,l}\right) . \tag{A.12}$$

For the bulk equation this becomes,

$$T'_{i,j} = (1-\omega)T_{i,j} + \omega \cdot ...$$
$$\frac{QRF_{i,j} + C1_{i,j} \cdot kr_{i,j} \cdot T_{i+1,j} + C2_{i,j} \cdot kr_{i-1,j} \cdot T_{i-1,j} + C3_i \cdot kz_{i,j-1} \cdot T_{i,j-1} + C4_i \cdot kz_{i,j} \cdot T_{i,j+1}}{C1_{i,j} \cdot kr_{i,j} + C2_{i,j} \cdot kr_{i-1,j} + C3_i \cdot kz_{i,j-1} + C4_i \cdot kz_{i,j}} \tag{A.13}$$

where we have dropped the n indices and represent the next step as T' in order to allow the equation to fit on the page.

A.1.2 Boundary Conditions

The above equation holds in the bulk of the material but must be modified at the boundaries. No heat flows across the r = 0 boundary due to the azimuthal symmetry requirement. We choose that no heat flows across the $r = R$ boundary at the edge of the simulation. If R is chosen to be sufficiently large this will not impact the results. At the RF surface ($z = 0$) the heat flow is zero, with the exception of the RF heating which is already included in equation A.17. At the helium interface ($z = z_T$) heat moves into the helium bath and we have the additional heat flow,

$$\frac{\Delta Q}{\Delta t} = A3_i \cdot \kappa_i \cdot \left(T_{i,j} - T_B\right) , \tag{A.14}$$

where T_B is the helium bath temperature, and κ is the thermal interface conductance. We will discuss the helium thermal interface resistance in more detail below.

In a single material we have 9 cases consider for our numerical problem

(edges, corners, and bulk). Below we show the modified version of the second term of equation A.17 required for each case

- Case 1: $r_i = 0$ and $z_j = 0$.

$$\omega \cdot \frac{QRF_{i,j} + C1_{i,j} \cdot kr_{i,j} \cdot T_{i+1,j} + C3_i \cdot kz_{i,j-1} \cdot T_{i,j-1}}{C1_{i,j} \cdot kr_{i,j} + C3_i \cdot kz_{i,j-1}}$$

- Case 2: $r_i \neq 0$, $r_{i+1} \neq R$, and $z_j = 0$.

$$\omega \cdot \frac{QRF_{i,j} + C1_{i,j} \cdot kr_{i,j} \cdot T_{i+1,j} + C2_{i,j} \cdot kr_{i-1,j} \cdot T_{i-1,j} + C3_i \cdot kz_{i,j-1} \cdot T_{i,j-1}}{C1_{i,j} \cdot kr_{i,j} + C2_{i,j} \cdot kr_{i-1,j} + C3_i \cdot kz_{i,j-1}}$$

- Case 3: $r_{i+1} = R$ and $z_j = 0$.

$$\omega \cdot \frac{QRF_{i,j} + C2_{i,j} \cdot kr_{i-1,j} \cdot T_{i-1,j} + C3_i \cdot kz_{i,j-1} \cdot T_{i,j-1}}{C2_{i,j} \cdot kr_{i-1,j} + C3_i \cdot kz_{i,j-1}}$$

- Case 4: $r_i = 0$, $z_j \neq 0$, and $z_{j+1} \neq z_T$.

$$\omega \cdot \frac{QRF_{i,j} + C1_{i,j} \cdot kr_{i,j} \cdot T_{i+1,j} + C3_i \cdot kz_{i,j-1} \cdot T_{i,j-1} + C4_i \cdot kz_{i,j} \cdot T_{i,j+1}}{C1_{i,j} \cdot kr_{i,j} + C3_i \cdot kz_{i,j-1} + C4_i \cdot kz_{i,j}}$$

- Case 5: $r_i \neq 0$, $r_{i+1} \neq R$, $z_j \neq 0$, and $z_{j+1} \neq z_T$. Bulk material. Equation A.17 needs no modification.

- Case 6: $r_{i+1} = R$, $z_j \neq 0$, and $z_{j+1} \neq z_T$.

$$\omega \cdot \frac{QRF_{i,j} + C2_{i,j} \cdot kr_{i-1,j} \cdot T_{i-1,j} + C3_i \cdot kz_{i,j-1} \cdot T_{i,j-1} + C4_i \cdot kz_{i,j} \cdot T_{i,j+1}}{C2_{i,j} \cdot kr_{i-1,j} + C3_i \cdot kz_{i,j-1} + C4_i \cdot kz_{i,j}}$$

- Case 7: $r_i = 0$ and $z_{j+1} = z_T$.

$$\omega \cdot \frac{A3_i \cdot \kappa_i \cdot T_B + C1_{i,j} \cdot kr_{i,j} \cdot T_{i+1,j} + C4_i \cdot kz_{i,j} \cdot T_{i,j+1}}{A3_i \cdot \kappa_i + C1_{i,j} \cdot kr_{i,j} + C4_i \cdot kz_{i,j}}$$

- Case 8: $r_i \neq 0$, $r_{i+1} \neq R$, and $z_{j+1} = z_T$.

$$\omega \cdot \frac{A3_i \cdot \kappa_i \cdot T_B + C1_{i,j} \cdot kr_{i,j} \cdot T_{i+1,j} + C2_{i,j} \cdot kr_{i-1,j} \cdot T_{i-1,j} + C4_i \cdot kz_{i,j} \cdot T_{i,j+1}}{A3_i \cdot \kappa_i + C1_{i,j} \cdot kr_{i,j} + C2_{i,j} \cdot kr_{i-1,j} + C4_i \cdot kz_{i,j}}$$

- Case 9: $r_{i+1} = R$ and $z_{j+1} = z_T$.

$$\omega \cdot \frac{A3_i \cdot \kappa_i \cdot T_B + C2_{i,j} \cdot kr_{i-1,j} \cdot T_{i-1,j} + C4_i \cdot kz_{i,j} \cdot T_{i,j+1}}{A3_i \cdot \kappa_i + C2_{i,j} \cdot kr_{i-1,j} + C4_i \cdot kz_{i,j}}$$

Thermal Interface Resistance

When T_B is less than the superfluid transition of liquid helium ($\approx$ 2.17 K) the interface thermal resistance is dominated by the Kapitza resistance [Lan07]. In this regime thermal transport is dominated by phonon coupling between the superfluid helium and the cavity wall and the electronic transport does not contribute. The thermal interface conductance depends strongly on material parameters and even different material preparations can change the thermal interface conductance [Mit73]. There have been no detailed studies of the thermal interface conductance between Nb_3Sn and superfluid helium. For our thermal model we use the Kapitza resistance of annealed niobium from [Mit73]. Since thermal breakdown in our multilayer system is dominated by the instability of the Nb_3Sn we expect that the results for thermal breakdown should not be significantly different. The difference in interface conductance could cause significant changes in the simulated outer wall temperatures. We additionally note that above $\sim$ 10 000 W/m^2 of heat flow we may enter a film boiling regime [Lan07] which has a significantly lower conductance than the Kapitza regime, however, heat flow remains significantly below this threshold in our system.

When T_B is above the superfluid transition (but still liquid) the heat transport is dominated by electronic transport and is far less dependent on the wall material [Lan07]. As discussed in section 5.5.2 there are several regimes of heat transport: normal conduction, nucleate boiling, and film boiling (see Fig. A.4) [Lan07]. At low accelerating gradients we are in the normal conduction region but see that we that we transition to nucleate boiling before quench (as evinced by temperature 'slips' seen in section 5.5.2). We restrict ourselves to looking only at the nucleate film boiling regime. In this regime we approximate the heat conductance as (based on [Lan07]).

$$\kappa_i \approx 50\,\mathrm{kW/m^2K^2}\,(T_{i,J} - T_B)\ , \tag{A.15}$$

though the exactly coefficient and polynomial dependence is not known for Nb_3Sn.

A.2 Equations in a Multi-layer Material

Now that we have the equations for a single layer material extending it to multiple layers is relatively simple. For the out layer of Nb_3Sn at the helium interface we will make an approximation and treat the outer layer as a modification to our helium bath thermal interface. At the RF layer we add a layer with a different thermal conductivity. The equations stay relatively the same except for computing the thermal conductivities. Two different equations are used for the two different layers, but the niobium-Nb_3Sn interface requires special care. Similar to the helium interface, there is thermal interface conductance at the interface between the metals. Unfortunately, this interface resistance is unknown.

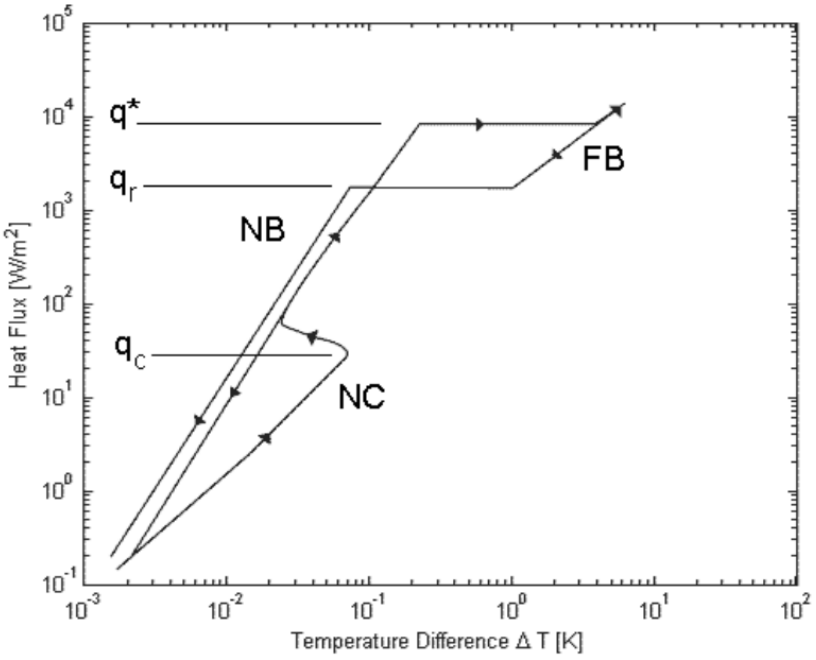

Figure A.4: Schematic of regions of different steady-state heat flow behaviors versus the heat flow plot. The x-axis shows the elevated temperature of the wall compared to the helium bath. This figure was adapted from [Lan07].

Instead, we use the simple average of the thermal conductivities on either side of the interface.

At the helium interface layer, we the approximation that heat flow across the Nb_3Sn is one-dimensional. By the time the heat has diffused through $\sim 3\,\text{mm}$ of niobium there is insignificant variation on lengths of $\sim 1\,\mu\text{m}$ and we expect insignificantly lateral heat diffusion while diffusing through the outer Nb_3Sn layer. We can then treat the material as an additional thermal interface resistance and use an effective thermal interface resistance,

$$\kappa_{\text{eff}} = \frac{\kappa_{\text{Nb3Sn}}\kappa_{\text{LHe}}}{\kappa_{\text{Nb3Sn}} + \kappa_{\text{LHe}}}\,, \tag{A.16}$$

where κ_{Nb3Sn} is the contribution from the Nb_3Sn layer. κ_{Nb3Sn} and κ_{LHe} depend on

the temperature of the outer wall, T_{wall}. We solve the equations,

$$\begin{aligned} P &= \kappa_{\text{LHe}}(T_{\text{wall}})\,(T_{\text{wall}} - T_B) \\ P &= \int_{T_{i,j}}^{T_{\text{wall}}} \frac{k(T)}{z(T)} \mathrm{d}T = \kappa_{\text{Nb3Sn}}(T_{\text{wall}}, T_B)\left(T_{i,j} - T_{\text{wall}}\right) , \end{aligned} \tag{A.17}$$

self-consistently to find the thermal interface conductance's and T_{wall}.

Meshing

We use variable sized meshing allowing us the use high density meshing in the Nb_3Sn layer and near the simulated defect and a low mesh density far from the defect where there is less temperature variation. In z-direction we use 25 – 100 nm mesh elements in the Nb_3Sn layer and mesh elements that gradually grow from 100 nm in the niobium layer. In the r-direction we use a similar linear mesh density near the defect that grow as r increases. For small defects ($r_{\text{defect}} <$ 5 µm) we use 25 nm mesh elements out to 10 µm and for large defects we use 500 nm mesh elements out to 200 µm.

Defects and Normal Conducting Regions

We may define a small region in the simulation to be a defect and apply addition RF loses in this area. To define a defect we define a radius for which all Nb_3Sn mesh elements within it (defined by the distance from $(r, z) = (0, 0)$ to the center of the mesh element) has additional specified heating. When looking at normal conducting regions (defect or from overheating) we distribute the heating within the penetration depth ($\approx$ 6 µm) of the material up to the niobium

layer. We use the penetration depth to determine the energy deposited in the mesh element given its size and distance from the surface.

Implementation

We make one additional note about our specific implementation of the over relaxation algorithm. When we iterate equation A.17 we only use a single temperature vector. By this we mean that we do not compute $\vec{T}_{n+1}$ purely from the $\vec{T}_n$ but also from the $T_{n+1,i,j}$ that have already been computed. We start our iteration at $(r, z) = (0, 0)$, iterate over all r_i, and then increment z_j. This gives us the algorithm,

$$T'_{i,j} = (1-\omega)T_{i,j} + \omega \cdot ... \\ \frac{QRF_{i,j} + C1_{i,j} \cdot kr_{i,j} \cdot T_{i+1,j} + C2_{i,j} \cdot kr'_{i-1,j} \cdot T'_{i-1,j} + C3_i \cdot kz'_{i,j-1} \cdot T'_{i,j-1} + C4_i \cdot kz_{i,j} \cdot T_{i,j+1}}{C1_{i,j} \cdot kr_{i,j} + C2_{i,j} \cdot kr'_{i-1,j} + C3_i \cdot kz'_{i,j-1} + C4_i \cdot kz_{i,j}} \tag{A.18}$$

where $T'_{i-1,j}$, $T'_{i,j-1}$, $kr'_{i-1,j}$, and $kz'_{i,j-1}$ have already been computed for the current iteration. We note that if this algorithm has converged then the solution will still be an equilibrium solution of our problem (since at equilibrium the $T'_{i,j} = T_{i,j}$). However, we find that this algorithm approaches convergence faster than equation A.17.

A.3 Convergence and Over Relaxation

If the algorithm converges to an equilibrium, it will take an infinite number of iterations to find the exact equilibrium solution, we thus define a cutoff criterion for terminating iterations. We calculate all power entering the simulation through RF losses, P_C, and exiting through the helium bath, P_E, after each iteration. We consider the algorithm to have converged and stop iterating when $|P_C - P_E| < 0.01 \cdot P_C$. We explored additional termination criteria (namely, the sum of all temperature changes during an iteration) and forced simulations to continue for millions of additional iterations and found this to be a good convergence/termination criterion.

The over relaxation parameter, ω, may vary between $0 < \omega < 2$. Changing ω changes the speed of the convergence. For our problem we have typically used a value of 1.8 and found relatively fast convergence, though the optimal value of ω may vary depending on the exact problem being solved.

A.4 Equilibria and Sequential Simulations

We make an important note about this simulation code: it only finds an equilibrium, not a specific equilibrium. At any time, our system may have multiple equilibria. In particular, the 'thermal runaway' state–where the entire surface is normal conducting, and the temperatures are high–is an equilibrium state of our numerical problem unless B_{surface} is low. Simply because the system has converged to the thermal runaway state does not mean that a lower temperature equilibrium does not exist for the system. In fact, we find that when $\omega = 1.95$

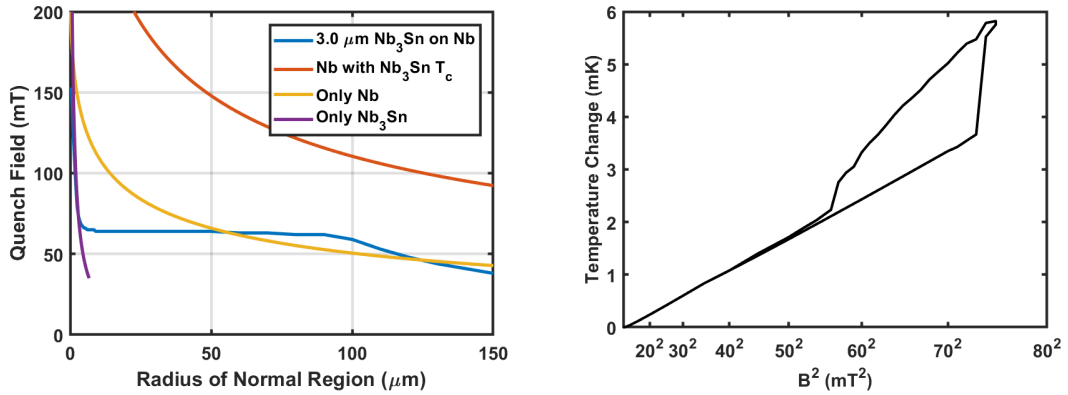

(a) (b)

Figure A.5: Figures 8.15 and 8.19 from chapter 8. We reproduce them here for easy reference we are discussing the process and potential errors involved therein in producing these results. a) Thermal simulations of the quench field of normal conducting regions for 3.0 µm of Nb_3Sn on niobium, and calculated quench fields of thick Nb_3Sn, niobium only, and niobium with Nb_3Sn superconducting parameters only. At small radii ($r < 3$ µm) the quench field matches that of pure Nb_3Sn. b) The simulated temperature versus the magnetic field with a small defect. The magnetic field is raised and lowered. At a critical field we see the formation of a stable normal conducting region. This region is self-sustaining once formed down to a lower field level. We see a hysteresis as the field is lowered.

many of our configurations approach the thermal runaway state despite finding a low temperature equilibrium when $\omega = 1.8$ or less. In some ways this algorithm cannot tell us the critical fields of a defect as we cannot guarantee that there is not a lower temperature equilibrium when we find thermal runaway. Thus, when interpreting these results, we must use physical intuition or other information. For example, in Fig. A.5a we show the critical/quench field versus the radius of a normal conducting defect. We gain some trust in these calculations by comparing it to the quench fields calculated for single layer Nb_3Sn and niobium analytically which match for small and large defects. These sorts of interpretations are always needed.

In Fig. A.5b we show the evolution of a system as the magnetic

field/accelerating gradient is raised and lowered, but we are using simulation that only finds equilibrium states and is not time resolved. For these simulations we have repeated the simulation as the field is charged using the previous result at the previous magnetic field as the starting condition of the system at the new magnetic. In this way we hope to follow the evolution of heating and stay at the 'same' equilibrium. However, as noted above we cannot guarantee what equilibrium we will converge to. Though we see a hysteresis loop in this process, all we can say with certainty is that there are two equilibrium states between 57 and 73 mT. The two equilibrium states might persist above and below these values and real-world system might not jump between these states at the field we have found.

BIBLIOGRAPHY

[A+00] B. Aune et al. The Superconducting TESLA Cavities. *Phys. Rev. ST Accel. Beams*, 3:92001, 2000.

[A+12] G. Aad et al. Observation of a New Particle in the Search for the Standard Model Higgs Boson with the ATLAS Detector at the LHC. *Physics Letters B*, 716(1):1–29, 2012.

[AAC+99] C. Z. Antoine, A. Aspart, J. P. Charrier, H. Safa, and B. Visentin. Alternative Approaches for Surface Treatment of Nb Superconducting Cavities. In *Proc. 9th Int. Conf. RF Superconductivity (SRF'99)*, pages 109–117. JACoW Publishing, Nov. 1999.

[ABHT83] L. Allen, M. Beasley, R. Hammond, and J. Turneaure. RF Surface Resistance of High-Tc Superconducting A15 Thin Films. *IEEE Transactions on Magnetics*, 19(3):1003–1006, may 1983.

[AJNK15] S. Aull, T. Junginger, H. Neupert, and J. Knobloch. Secondary Electron Y.eld of SRF Materials. In *Proc. 17th Int. Conf. RF Superconductivity (SRF'15)*, pages 686–690. JACoW Publishing, Sep. 2015.

[AKS05] P. Avrakhov, A. Kanareykin, and N. Solyak. Traveling Wave Accelerating Structure for A Superconducting Accelerator. pages 4296 – 4298, 06 2005.

[AMC86] G. Arnolds-Mayer and E. Chiaveri. On a 500 MHz Single Cell Cavity with Nb3Sn Surface. In *Proceedings of The Third Workshop on RF Superconductivity*, Chicago, 1986.

[Ban20] N. Banerjee. *Towards More Efficient Accelerating RF Systems: Superconducting Energy Recovery LINACs and Thermometry of High Q Cavities*. Phd, Cornell University, 2020.

[BB91] S. P. Benz and C. J. Burroughs. Coherent Emission from Two-Dimensional Josephson Junction Arrays. *Applied Physics Letters*, 58(19):2162–2164, 1991.

[BBR+16] E. Barzi, M. Bestetti, F. Reginato, D. Turrioni, and S. Franz. Synthesis of Superconducting Nb3Sn Coatings on Nb Substrates. *Superconductor Science and Technology*, 29(1):15009, 2016.

[BBZ+07] D. Baars, T. R. Bieler, A. Zamiri, F. Pourboghrat, and C. Compton. Crystal Orientation Effects During Fabrication of Single or Multi-Crystal NB SRF Cavities. In *Proc. 13th Int. Conf. RF Superconductivity (SRF'07)*. JACoW Publishing, Oct. 2007.

[BCS57] J. Bardeen, L. N. Cooper, and J. R. Schrieffer. Theory of Superconductivity. *Phys. Rev.*, 108:1175–1204, Dec 1957.

[Beh13] T. Behnke. The International Linear Collider Technical Design Report - Volume 4: Detectors. 6 2013.

[BEW05] D. H. Bilderback, P. Elleaume, and E. Weckert. Review of Third and Next Generation Synchrotron Light Sources. 38(9):S773–S797, apr 2005.

[BGM+19] D. Bafia, A. Grassellino, O. S. Melnychuk, A. S. Romanenko, Z-H. Sung, and J. Zasadzinski. Gradients of 50 MV/m in TESLA Shaped Cavities via Modified Low Temperature Bake. In *Proc. 19th Int. Conf. RF Superconductivity (SRF'19)*, pages 586–591. JACoW Publishing, Jun.-Jul. 2019. https://doi.org/10.18429/JACoW-SRF2019-TUP061.

[BKM+97] P. Boccard, P. Kneisel, G. Müller, J. Pouryamout, and H. Piel. Results from some Temperature Mapping Experiments on Nb3Sn RF Cavities. In *Proceedings of the Eighth Workshop on RF Superconductivity*, Padova, 1997.

[BPG+15] C. Becker, S. Posen, N. Groll, R. Cook, C. M. Schlepütz, D. L. Hall, M. Liepe, M. Pellin, J. Zasadzinski, and T. Proslier. Analysis of Nb3Sn Surface Layers for Superconducting Radio Frequency Cavity Applications. *Applied Physics Letters*, 106(8):082602, feb 2015.

[BQG86] G. Binnig, C. F. Quate, and Ch. Gerber. Atomic Force Microscope. *Phys. Rev. Lett.*, 56:930–933, Mar 1986.

[BS17] Y. Bang and G. R. Stewart. Superconducting Properties of the s-Wave State: Fe-Based Superconductors. *Journal of Physics: Condensed Matter*, 29(12):123003, feb 2017.

[BWB+99] W. Belzig, F. K. Wilhelm, C. Bruder, G. Schön, and A. D. Zaikin. Quasiclassical Green's Function Approach to Mesoscopic Superconductivity. *Superlattices and Microstructures*, 25(5):1251–1288, 1999.

[Cam85] I. E. Campisi. High Field RF Superconductivity: To Pulse or Not to Pulse? *IEEE Transactions on Magnetics*, 21(2):134–141, mar 1985.

[CBC+07] A. Canabal, J. D. Bowyer, P. Chacon, N. A. Gillespie, M. A. Madrid, and T. Tajima. Development of a Temperature Mapping System for 1.3-GHz 9-Cell SRF Cavities. In *Proc. 22nd Particle Accelerator Conf. (PAC'07)*, pages 2406–2408. JACoW Publishing, Jun. 2007.

[CC64] G. D. Cody and R. W. Cohen. Thermal Conductivity of Nb3Sn. *Rev. Mod. Phys.*, 36(1):121–123, jan 1964.

[CCPR20] G. Ciovati, G. Cheng, U. Pudasaini, and R. A. Rimmer. Multi-Metallic Conduction Cooled Superconducting Radio-Frequency Cavity with High Thermal Stability. *Superconductor Science and Technology*, 33(7):07LT01, may 2020.

[CHPS09] Z. A. Conway, D. L. Hartill, H. Padamsee, and E. N. Smith. Defect Location in Superconducting Cavities Cooled with HE-II Using Oscillating Superleak Transducers. In *Proc. 14th Int. Conf. RF Superconductivity (SRF'09)*, pages 113–116. JACoW Publishing, Sep. 2009.

[Cio04] G. Ciovati. Effect of Low-Temperature Baking on the Fadio-Frequency Properties of Niobium Superconducting Cavities for Particle Accelerators. *Journal of Applied Physics*, 96(3):1591–1600, 2004.

[Cio14] G. Ciovati. AC/RF Superconductivity. *arXiv:1501.07398 [cond-mat, physics:physics]*, 2014. arXiv: 1501.07398.

[CKML03] G. Ciovati, P. Kneisel, G. Myneni, and W. A. Lanford. Effect of Low Temperature Baking on Niobium Cavities. In *Proc. 11th Workshop RF Superconductivity (SRF'03)*, pages 562–571. JACoW Publishing, Sep. 2003.

[CMG+17] M. Checchin, M. Martinello, A. Grassellino, A. Romanenko, and J. F. Zasadzinski. Electron Mean Free Path Dependence of the Vortex Surface Impedance. 30(3):034003, jan 2017.

[CMS+10] G. Ciovati, G. Myneni, F. Stevie, P. Maheshwari, and D. Griffis. High Field Q Slope and the Baking Effect: Review of Recent Ex-

perimental Results and New Data on Nb Heat Treatments. *Phys. Rev. ST Accel. Beams*, 13:022002, Feb 2010.

[CP87] S. A. Campbell and L. M. Peter. Determination of the Density of Lead Dioxide Films by in situ Laser Interferometry. *Electrochimica Acta*, 32(2):357–360, 1987.

[CPT+21] J. Carlson, A. Pack, M. K. Transtrum, J. Lee, D. N. Seidman, D. B. Liarte, N. S. Sitaraman, A. Senanian, M. M. Kelley, J. P. Sethna, T. Arias, and S. Posen. Analysis of Magnetic Vortex Dissipation in Sn-Segregated Boundaries in Nb3Sn Superconducting RF Cavities. *Phys. Rev. B*, 103:024516, Jan 2021.

[CRZ+06] G. Carta, G. Rossetto, P. Zanella, L. Crociani, V. Palmieri, and F. Todescato. Attempts to deposit Nb3Sn by MO-CVD. In *Proceedings of the international workshop on thin films and new ideas for pushing the limits of RF superconductivity*, Padua, 2006.

[CS08a] G. Catelani and J. P. Sethna. Temperature Dependence of the Superheating Field for Superconductors in the High-κ London Limit. *Phys. Rev. B*, 78:224509, Dec 2008.

[CS08b] G. Catelani and J. P. Sethna. Temperature Dependence of the Superheating Field for Superconductors in the high-kappa London limit. *Physical Review B*, 78(22):224509, dec 2008.

[DEG+11] J. H. Durrell, C-B. Eom, A. Gurevich, E. E. Hellstrom, C. Tarantini, A. Yamamoto, and D. C. Larbalestier. The Behavior of Grain Boundaries in the Fe-Based Superconductors. 74(12):124511, nov 2011.

[DGH65] P. G. De Gennes and J. P. Hurault. Proximity Effects Under Magnetic Fields. *Physics Letters*, 17(3):181–182, July 1965.

[DH75] D. Dew-Hughes. Superconducting A-15 Compounds: A Review. *Cryogenics*, 15(8):435–454, August 1975.

[DHL17] J. Ding, D. L. Hall, and M. Liepe. Simulations of RF Field-induced Thermal Feedback in Niobium and Nb3Sn Cavities. In *Proc. 18th Int. Conf. RF Superconductivity (SRF'17)*, pages 920–924. JACoW Publishing, Jul. 2017. https://doi.org/10.18429/JACoW-SRF2017-THPB079.

[Die78] H. Diepers. Method for the Anodic Polishing of Surfaces of Intermetallic Niobium Compounds and Niobium Alloys. *US Patent 4,072,588*, pages 1–5, 1978.

[DJD+81] H. Devantay, J. L. Jorda, M. Decroux, J. Muller, and R. Flükiger. The Physical and Structural Properties of Superconducting A15-Type Nb-Sn Alloys. *Journal of Materials Science*, 16(8):2145–2153, aug 1981.

[DKR+06] S. M. Deambrosis, G. Keppel, V. Ramazzo, C. Roncolato, R. G. Sharma, and V. Palmieri. A15 Superconductors: An Alternative to Niobium for RF Cavities. *Physica C: Superconductivity*, 441(1–2):108–113, 2006.

[DNG78] R. C. Dynes, V. Narayanamurti, and J. P. Garno. Direct Measurement of Quasiparticle-Lifetime Broadening in a Strong-Coupled Superconductor. *Phys. Rev. Lett.*, 41:1509–1512, Nov 1978.

[DPG+20] R. C. Dhuley, S. Posen, M. I. Geelhoed, O. Prokofiev, and J. C. T. Thangaraj. First Demonstration of a Cryocooler Conduction Cooled Superconducting Radiofrequency Cavity Operating at Practical CW Accelerating Gradients. *Superconductor Science and Technology*, 33(6):06LT01, apr 2020.

[DR84] B. David and H. Rogalla. Determination of Optimum Preparation Parameters for Thin High-Tc Nb3Ge Films. In A. F. Clark and R. P. Reed, editors, *Advances in Cryogenic Engineering Materials : Volume 30*, pages 631–638. Springer US, Boston, MA, 1984.

[DRR+09] S. M. Deambrosis, V. Ramazzo, A. A. Rossi, V. Rupp, R.G. Sharma, S. Stark, F. Stivanello, and V. Palmieri. A15 Superconductors by Thermal Diffusion in 6 GHz Cavities. In *Proceedings of SRF 2009*, Berlin, 2009.

[DSMS71] H. Diepers, O. Schmidt, H. Martens, and F. S. Sun. A New Method of Electropolishing Niobium. *Physics Letters A*, 37(2):139–140, 1971.

[EBC+13] R. G. E., B. Bullock, B. Clasby, B. Elmore, F. Furuta, Mingqi Ge, D. Gonnella, D. L. Hall, A Ganshyn, Y. He, V. Ho, G. Hoffstaetter, J. Julian Kaufman, M. Liepe, T. O'Connell, S. Posen, P. Quigley, J. Sears, E. Smith, V. Shemelin, and V. Veshcherevich. High Q Cav-

ities for the Cornell ERL Main Linac. In *Proceedings of SRF 2013*, Paris, sep 2013.

[Edw95] D. A. Edwards (ed.). TESLA Test Facility (TTF) Linac Conceptual Design Report. Technical Report Ch. 4, 1995.

[EKR+15] G. V. Eremeev, M. J. Kelley, C. E. Reece, U. Pudasaini, and J. Tuggle. Progress with Multi-Cell Nb3Sn Cavity Development Linked with S.ple Materials Charaterization. In *Proceedings of SRF 2015*, Whistler, 2015.

[Ere09] G. V. Eremeev. Review of RF Properties of NbN and MgB2 Thin Coating on Nb S.ples and Cavities. In *Proc. 14th Int. Conf. RF Superconductivity (SRF'09)*, pages 159–163. JACoW Publishing, Sep. 2009.

[fmi] MATLAB fminsearch Function. `https://www.mathworks.com/help/matlab/ref/fminsearch.html`. Accessed: 2021-10-11.

[G+19] M. Ge et al. CVD Coated Copper Substrate SRF Cavity Research at Cornell University. In *Proc. 19th Int. Conf. RF Superconductivity (SRF'19)*, pages 381–386. JACoW Publishing, Jun.-Jul. 2019. https://doi.org/10.18429/JACoW-SRF2019-TUFUB8.

[G+21] G. Gaitan et al. Development of a System for Coating SRF Cavities Using Remote Plasma CVD. In *Proc. 20th Int. Conf. RF Superconductivity (SRF'21)*, Lansingm MI, USA, Jun 2021.

[Gal14] J. N. Galayda. The Linac Coherent Light Source-II Project. In *Proc. 5th Int. Particle Accelerator Conf. (IPAC'14)*, pages 935–937. JACoW Publishing, Jun. 2014. https://doi.org/10.18429/JACoW-IPAC2014-TUOCA01.

[GC13] A. Gurevich and G. Ciovati. Effect of Vortex Gotspots on the Radio-Frequency Surface Resistance of Superconductors. *Phys. Rev. B*, 87(5):54502, feb 2013.

[Gen03] R. L. Geng. Multipacting Simulations for Superconducting Cavities and RF Coupler Waveguides. In *Proc. 20th Particle Accelerator Conf. (PAC'03)*. JACoW Publishing, May 2003.

[GGB+04] V. Guritanu, W. Goldacker, F. Bouquet, Y. Wang, R. Lortz, G. Goll, and A. Junod. Specific Heat of Nb3Sn: The Case for a Second Energy Gap. *Phys. Rev. B*, 70(18):184526, nov 2004.

[GH80] M. Grundner and J. Halbritter. XPS and AES Studies on Oxide Growth and Oxide Coatings on Niobium. *Journal of Applied Physics*, 51(1):397–405, January 1980.

[GK17] A. Gurevich and Takayuki Kubo. Surface Impedance and Optimum Surface Resistance of a Superconductor with an Imperfect Surface. *Phys. Rev. B*, 96:184515, Nov 2017.

[God06] A Godeke. A Review of the Properties of Nb3Sn and their Variation with A15 Composition, Morphology and Strain State. *Superconductor Science and Technology*, 19(8):R68—-R80, aug 2006.

[Gon16] D. Gonella. *The Fundamental Science of Nitrogen-Doping of Niobium Superconducting Cavities*. PhD thesis, Cornell University, 2016.

[GPL20] S. Ginnett, R. D. Porter, and M. Liepe. Two-Gap Superconductivity in Nb3Sn SRF Cavities. Technical report, Cornell University, 2020.

[Gra75] K. E. Gray. ISS Depth Profile Analysis of Anodized Niobium. *Applied Physics Letters*, 27(8):462, 1975.

[GRB+18] A. Grassellino, A. Romanenko, D. Bice, O. Melnychuk, A. C. Crawford, S. Chandrasekaran, Z. Sung, D. A. Sergatskov, M. Checchin, S. Posen, M. Martinello, and G. Wu. Accelerating Fields Up to 49 MV/m in TESLA-Shape Superconducting RF Niobium Cavities via 75 C Vacuum Bake, 2018.

[GRS+13a] A Grassellino, A Romanenko, D Sergatskov, O Melnychuk, Y Trenikhina, A Crawford, A Rowe, M Wong, T Khabiboulline, and F Barkov. Nitrogen and Argon Doping of Niobium for Superconducting Radio Frequency Cavities: a Pathway to Highly Efficient Accelerating Structures. *Superconductor Science and Technology*, 26(10):102001, aug 2013.

[GRS+13b] A. Grassellino, A. Romanenko, D. Sergatskov, O. Melnychuk, Y. Trenikhina, A. Crawford, A. Rowe, M. Wong, T. Khabiboulline, and F. Barkov. Nitrogen and Argon Doping of Niobium for Superconducting Radio Frequency Cavities: a Pathway to Highly

Efficient Accelerating Structures. *Superconductor Science and Technology*, 26(10):102001, 2013.

[GRT+17] A Grassellino, A Romanenko, Y Trenikhina, M Checchin, M Martinello, O S Melnychuk, S Chandrasekaran, D A Sergatskov, S Posen, A C Crawford, S Aderhold, and D Bice. Unprecedented Quality Factors at Accelerating Gradients Up to 45 MVm-in Niobium Superconducting Resonators via Low Temperature Nitrogen Infusion. *Superconductor Science and Technology*, 30(9):094004, aug 2017.

[Gur14a] A. Gurevich. Challenges and Opportunities for Applications of Unconventional Superconductors. *Annual Review of Condensed Matter Physics*, 5(1):35–56, 2014.

[Gur14b] A. Gurevich. Reduction of dissipative nonlinear conductivity of superconductors by static and microwave magnetic fields. *Phys. Rev. Lett.*, 113:087001, Aug 2014.

[H+17a] D. L. Hall et al. Cavity Quench Studies in Nb3Sn Using Temperature Mapping and Surface Analysis of Cavity Cut-outs. In *Proc. 18th Int. Conf. RF Superconductivity (SRF'17)*, pages 840–843. JACoW Publishing, Jul. 2017. https://doi.org/10.18429/JACoW-SRF2017-THPB041.

[H+17b] D. L. Hall et al. Surface Analysis of Features Seen on Nb3Sn S.ple Coupons Grown by Vapour Diffusion. In *Proc. 8th Int. Particle Accelerator Conf. (IPAC'17)*, pages 1130–1133. JACoW Publishing, May 2017. https://doi.org/10.18429/JACoW-IPAC2017-MOPVA119.

[Had00] A. Hadjidimos. Successive Overrelaxation (SOR) and Related Methods. *Journal of Computational and Applied Mathematics*, 123(1):177–199, 2000. Numerical Analysis 2000. Vol. III: Linear Algebra.

[Hak88] M. Hakimi. TMS Symposium on Niobium and Niobium Alloys in Superconducting Applications Bronze-processed Nb3Sn for R.F. Applications. *Journal of the Less Common Metals*, 139(1):159–165, 1988.

[Hal70a] J. Halbritter. Change of Eigenstate in a Superconducting RF

Cavity Due to a Nonlinear Response. *Journal of Applied Physics*, 41(11):4581–4588, 1970.

[Hal70b] J. Halbritter. Comparison Between Measured and Calculated RF Losses in the Superconducting State. *Zeitschrift für Physik*, 238(5):466–476, 1970.

[Hal17] D. Hall. *New Insights into the Limitations on the Efficiency and Achievable Gradients in Nb3Sn SRF Cavities*. PhD thesis, Cornell University, 2017.

[Ham75] R. Hammond. Electron Beam Evaporation Synthesis of A15 Superconducting Compounds: Accomplishments and Prospects. *IEEE Transactions on Magnetics*, 11(2):201–207, mar 1975.

[HCL+17] D. L. Hall, P.l Cueva, D. Liarte, J. Maniscalco, D. A. Muller, R. D. Porter, and J. P. Sethna. Quench Studies in Single-Cell Nb3Sn Cavities Coated using Vapour Diffusion. In *Proceedings of IPAC 2017*, Copenhagen, may 2017.

[Hei01] M. A. Hein. *Microwave Properties of Superconductors*, pages 21–53. Springer Netherlands, Dordrecht, 2001.

[Hel05] R. Hellborg, editor. *Electrostatic Accelerators: Fundamentals and Applications*. Particle Acceleration and Detection. Springer-Verlag, Berlin Heidelberg, 2005.

[HF19] W. Han and F. Fang. Fundamental Aspects and Recent Developments in Electropolishing. *International Journal of Machine Tools and Manufacture*, 139:1–23, 2019.

[HGM+84] H. Heinrichs, T. Grundey, N. Minatti, G. Muller, M. Peiniger, H. Piel, G. Unterborsch, and H. P. Vogel. Activities on RF-Superconductivity at Wuppertal. In *Proceedings of the Second Workshop on RF Superconductivity*, Geneva, 1984.

[HHO74] J. Hasse, W. D. Hermann, and R. Orlich. On the Microwave Absorption of Superconducting Nb3Sn. *Zeitschrift für Physik*, 271(3):265–268, 1974.

[Hil80] B Hillenbrand. The Preparation of Superconducting Nb3Sn Sur-

faces for RF applications. In *Proceedings of the First Workshop on RF Superconductivity*, Karlsruhe, 1980.

[HLLS17] D. L. Hall, M. Liepe, D. Liarte, and J. P. Sethna. Impact of Trapped Magnetic Flux and Thermal Gradients on the Performance of Nb3Sn Cavities. In *Proceedings of IPAC 2017*, Copenhagen, may 2017.

[HLM16] D. L. Hall, M. Liepe, and J. T. Maniscalco. RF Measurements on High Performance Nb3Sn Cavities. In *Proc. 7th Int. Particle Accelerator Conf. (IPAC'16)*, pages 2320–2322. JACoW Publishing, May 2016. https://doi.org/10.18429/JACoW-IPAC2016-WEPMR024.

[HLP19] H. Hu, M. Liepe, and R. D. Porter. Reducing Surface Roughness of Nb3Sn Through Chemical Polishing Treatments. In *Proc. 19th Int. Conf. RF Superconductivity (SRF'19)*, pages 48–50. JACoW Publishing, Jun.-Jul. 2019. https://doi.org/10.18429/JACoW-SRF2019-MOP013.

[HMP+75] B. Hillenbrand, H. Martens, H. Pfister, K. Schnitzke, and G. Ziegler. Superconducting Nb3Sn Cavities. *IEEE Transactions on Magnetics*, 11(2):420–422, mar 1975.

[HMS92] E. Haebel, A. Mosnier, and J. Sekutowicz. Cavity Shape Optimization for a Superconducting Linear Collider. In *Proceedings of the Fifteenth Conference on High energy accelerators*, volume 2, pages 957–959, Hamburg, 1992.

[HP97] T. Hays and H. Padamsee. Measuring the RF Critical Field of Pb, Nb, and Nb3Sn. In *Proceedings of the Eighth Workshop on RF Superconductivity*, pages 789–794, Padova, 1997.

[HPL18] S. Halls, R. D. Porter, and M. Liepe. Temperature Mapping Improvements of Superconducting Radio-Frequency Cavities. Technical report, Cornell University, 2018.

[HS09] W. Henning and C. Shank. Accelerators for America's Future. 2009.

[HW15] S. Henderson and T. Waite. Workshop on Energy and Environmental Applications of Accelerators. 6 2015.

[Jac35] P. A. Jacquet. Electrolytic Method for Obtaining Bright Copper Surfaces. *Nature*, 135(3426):1076–1076, June 1935.

[JCC+91] J. F. Julião, J. W. R. Chagas, H. L. Cesar, N. L. Dias, F. Decker, and U. U. Gomes. Anodic Niobium Pentoxide Films: Growth and Thickness Determination by in situ Optoelectrochemical Measurements. *Electrochimica Acta*, 36(8):1297–1300, 1991.

[JZS+14] Y. J. Jo, J. Zhou, Z. H. Sung, P. J. Lee, and D. C. Larbalestier. Specific Heat of Nb3Sn: The case for a Single Gap. *APL Materials*, 2(10):106101, 2014.

[KAK+18] J. M. Koszegi, K. Alomari, J. Knobloch, O. Kugeler, and B. Schmitz. A Combined Temperature and Magnetic Field Mapping System for SRF Cavities. In *Proc. 9th Int. Particle Accelerator Conf. (IPAC'18)*, pages 1228–1231. JACoW Publishing, Apr.-May 2018. https://doi.org/10.18429/JACoW-IPAC2018-TUZGBE5.

[KB96] F. Koechlin and B. Bonin. Parametrization of the Niobium Thermal Conductivity in the Superconducting State. *Superconductor Science and Technology*, 9(6):453, 1996.

[KB03] V. G. Kogan and S. L. Bud'ko. Anisotropy Parameters of Superconducting MgB2. *Physica C: Superconductivity*, 385(1):131–142, March 2003.

[KGPL99] J. Knobloch, R. L. Geng, H. Padamsee, and M. Liepe. High-Field Q Slope in Superconducting Cavities due to Magnetic Field Enhancement at Grain Boundaries. In *Proc. 9th Int. Conf. RF Superconductivity (SRF'99)*, pages 77–91. JACoW Publishing, Nov. 1999.

[KHS21] M. Liepe K. Howard and Z. Sun. Thermal Annealing of Sputtered Nb3Sn and V3Si Thin Films for Superconducting RF Cavities. In *Proc. 20th Int. Conf. RF Superconductivity (SRF'21)*, Lansing, MI, USA, Jun 2021.

[KL95] P. Kneisel and B. Lewis. Advanced Surface Cleaning Methods: Three Years of Experience with High Pressure Ultrapure Water Rinsing of Superconducting Cavaties. Technical report, Continuous Electron Beam Accelerator Facility, Newport News, VA (United States), 1995.

[KMR87] P. Kneisel, G. Muller, and C. Reece. Investigation of the Surface Resistance of Superconducting Niobium Using Thermometry in Superfluid Helium. *IEEE Transactions on Magnetics*, 23(2):1417–1421, 1987.

[Kno97] J. Knobloch. *Advanced Thermometry Studies of Superconducting Radio-Frequency Cavities*. Phd, Cornell University, 1997.

[Kri12] M. Krishnan. Niobium Coatings for SRF Cavities Produced by High Power Impulse Magnetron Sputtering. In *Proceedings of the fifth international workshop on thin films and new ideas for pushing the limits of RF superconductivity*, Newport News, 2012.

[Kro03] V. F. Kroupa. *Phase Lock Loops and Frequency Synthesis: Kroupa/Phase Lock Loops*. J. Wiley & Sons, Ltd, Chichester, UK, April 2003.

[KSA20] M. M. Kelley, N. S. Sitaraman, and T. A. Arias. Ab initio theory of the impact of grain boundaries and substitutional defects on superconducting Nb3Sn. 34(1):015015, dec 2020.

[KTO05] N. Koizumi, T. Takeuchi, and K. Okuno. Development of Advanced Nb3Al Superconductors for a Fusion DEMO Plant. *Nuclear Fusion*, 45(6):431, 2005.

[Kub14] T. Kubo. Two-Dimensional Models of the Magnetic-Field Enhancement at Pit and Bumps. In *Proc. 5th Int. Particle Accelerator Conf. (IPAC'14)*, pages 2525–2527. JACoW Publishing, Jun. 2014. https://doi.org/10.18429/JACoW-IPAC2014-WEPRI024.

[KWS70] M. L. Kinter, I. Weissman, and W. W. Stein. Chemical Polish for Niobium Microwave Structures. *Journal of Applied Physics*, 41(2):828–829, February 1970.

[L+17] D. Liarte et al. SRF Theory Developments from the Center for Bright Beams. In *Proc. 18th Int. Conf. RF Superconductivity (SRF'17)*, pages 835–839. JACoW Publishing, Jul. 2017. https://doi.org/10.18429/JACoW-SRF2017-THPB040.

[LAH+17] D. B. Liarte, T. Arias, D. L. Hall, M. Liepe, J. P. Sethna, N. Sitaraman, A. Pack, and M. K. Transtrum. SRF Theory Developments from the Center for Bright Beams. 2017.

[Lan07] J. Lantz. *Heat Transfer Correlations Between a Heated Surface and Liquid and Superfluid Helium*. Phd, Linkopings Universitet, 2007.

[LD00] M. S. Li and D. Domínguez. AC Resistivity of d-Wave Ceramic Superconductors. *Phys. Rev. B*, 62:14554–14558, Dec 2000.

[LDGL09] M. Li, Z. Du, C. Guo, and C. Li. Thermodynamic Optimization of the Cu–Sn and Cu–Nb–Sn Systems. *Journal of Alloys and Compounds*, 477(1):104–117, 2009.

[Lee11] S. Y. Lee. *Accelerator Physics*. WORLD SCIENTIFIC, 3rd edition, 2011.

[LF81] T. W. Lee and Charles M. Falco. Josephson Effects in Ultrashort Mean-Free-Path Superconductors. *Applied Physics Letters*, 38(7):567–569, April 1981.

[LHK+18] D. B. Liarte, D. L. Hall, P. N. Koufalis, A. Miyazaki, A. Senanian, M. Liepe, and J. P. Sethna. Vortex Dynamics and Losses Due to Pinning: Dissipation from Trapped Magnetic Flux in Resonant Superconducting Radio-Frequency Cavities. *Phys. Rev. Applied*, 10:054057, Nov 2018.

[LPM+18] J. Lee, S. Posen, Z. Mao, Y. Trenikhina, K. He, D. L. Hall, M. Liepe, and D. N. Seidman. Atomic-Scale Analyses of Nb3Sn on Nb Prepared by Vapor Diffusion for Superconducting Radiofrequency Cavity Applications: a Correlative Study. 32(2):024001, dec 2018.

[LPT+17] D. B. Liarte, S. Posen, M. K. Transtrum, G. Catelani, M. Liepe, and J. P Sethna. Theoretical Estimates of Maximum Fields in Superconducting Resonant Radio Frequency Cavities: Stability Theory, Disorder, and Laminates. *Superconductor Science and Technology*, 30(3):033002, jan 2017.

[M+15] M. Martinello et al. Trapped Flux Surface Resistance Analysis for Different Surface Treatments. In *Proc. 17th Int. Conf. RF Superconductivity (SRF'15)*, pages 115–119. JACoW Publishing, Sep. 2015.

[Man20] J. Maniscalco. *Studies of the Field-Dependent Surface Resistance of Nitrogen-Doped Niobium for Superconducting Accelerators*. PhD thesis, Cornell University, 2020.

[MGH+16] J. Maniscalco, D. Gonnella, D. L. Hall, P. Koufalis, and M. Liepe. Pulsed Field Limits in SRF Cavities. In *Proceedings of IPAC 2016*, Busan, may 2016.

[MGL17] J. T. Maniscalco, D. Gonnella, and M. Liepe. The Importance of the Electron Mean Free Path for Superconducting Radio-Frequency Cavities. *Journal of Applied Physics*, 121(4):43910, 2017.

[Mit73] K. Mittag. Kapitza Conductance and Thermal Conductivity of Copper, Niobium and Aluminium in the Range from 1.3 to 2.1 K. *Cryogenics*, 13(2):94–99, 1973.

[Mit10] S. Mitsunobu. Status of KEK Studies on MgB2. In *Proceedings of the fourth international workshop on thin films and new ideas for pushing the limits of RF superconductivity*, Padua, 2010.

[MK85] G. Mueller and P. Kneisel. Development of Sensitive Thermometers for Calibrated Surface Temperature Measurements of Niobium Cavities Immersed in Superfluid Helium. Technical report, Cornell University, 1985.

[MKM96] G Müller, P Kneisel, and D Mansen. Nb3Sn Layers on High-Purity Nb Cavities with Very High Quality Factors and Accelerating Gradients. In *Proceedings of the Fifth European Particle Accelerator Conference*, Sitges, 1996.

[ML18] J. T. Maniscalco and M. Liepe. A Computational Method for More Accurate Measurements of the Surface Resistance in SRF Cavities. In *Proc. 9th Int. Particle Accelerator Conf. (IPAC'18)*, pages 2458–2460. JACoW Publishing, Apr.-May 2018. https://doi.org/10.18429/JACoW-IPAC2018-WEPMF042.

[MM65] B. W. Maxfield and W. L. McLean. Superconducting Penetration Depth of Niobium. *Phys. Rev.*, 139:A1515–A1522, Aug 1965.

[MM78] H. Martens and R. Martens. Method for the Manufacture of a Superconductive Nb3Sn Layer on a Niobium Surface for High frequency Applications. *US Patent 4,105,512*, 1978.

[MO87] S. A Mucklejohn and N. W. O'Brien. The Vapour Pressure of Tin(II) Chloride and the Standard Molar Gibbs Free Energy Change for Formation of SnCl2(g) from Sn(g) and Cl2(g). *The Journal of Chemical Thermodynamics*, 19(10):1079–1085, 1987.

[MRYJbA11] M. Moarrefi-Romeileh, H. Yavari, A. A. Joata-bayrami, and M. R. Abolhassani. Temperature Dependence of Transmittance and Effective Surface Resistance of MgB2 Film. *Physica B: Condensed Matter*, 406(21):4135–4138, 2011.

[MY95] D. G. Myakishev and V. P. Yakovlev. The New Possibilities of SuperLANS Code for Evaluation of Axisymmetric Cavities. In *Proc. 16th Particle Accelerator Conf. (PAC'95)*. JACoW Publishing, May 1995.

[MZRB79] D. F. Moore, R. B. Zubeck, J. M. Rowell, and M. R. Beasley. Energy Gaps of the A15 Superconductors Nb3Sn, V3Si, and Nb3Ge Measured by Tunneling. *Phys. Rev. B*, 20(7):2721–2738, oct 1979.

[NM75] V. Novotny and P. P. M. Meincke. Single Superconducting Energy Gap in Pure Niobium. *Journal of Low Temperature Physics*, 18(1):147–157, January 1975.

[Oka90] H. Okamoto. Nb-Sn (Niobium-Tin). *Binary Alloy Phase Diagrams, II Ed., Ed. T.B. Massalski*, 1990.

[Oka03] H. Okamoto. Nb-Sn (Niobium-Tin). *Journal of Phase Equilibria*, 24(4):380, jul 2003.

[ONSA04] S. Ono, T. Nagasaka, H. Shimazaki, and H. Asoh. Fabrication of Porous Niobia by Anodizing of Niobium. *Proc. Electrochem. Soc*, 19(2006):123, 2004.

[P+19] S. Posen et al. Nb3Sn at Fermilab: Exploring Performance. In *Proc. 19th Int. Conf. RF Superconductivity (SRF'19)*, pages 818–822. JACoW Publishing, Jun.-Jul. 2019. https://doi.org/10.18429/JACoW-SRF2019-THFUB1.

[P+21] R. D. Porter et al. Dynamics of RF Dissipation Probed via High-speed Temperature Mapping. In *Proc. 20th Int. Conf. RF Superconductivity (SRF'21)*, Lansingm MI, USA, Jun 2021.

[Pac20] A. Pack. Superconductivity at its Limit: Simulating Superconductor Dynamics Near the Superconducting Superheating Field in Eilenberger and Ginzburg-Landau Theory. *Theses and Dissertations*, April 2020.

[Pad83] H. Padamsee. Calculations for Breakdown Induced by "Large Defects" in Superconducting Niobium Cavities. *IEEE Transactions on Magnetics*, 19(3):1322–1325, 1983.

[Pad17] H. Padamsee. 50 Years of Success for SRF Accelerators-A Review. 30(5):053003, apr 2017.

[Pei83] M. Peiniger. *Herstellung Und Test Eines S-Band Resonators Mit Nb3Sn Oberflache*. PhD thesis, Universitat GeS.thochschule Wuppertal, 1983.

[PFH+17] R. Porter, F. Furuta, D. Hall, M. Liepe, and J. Maniscalco. Effectiveness of Chemical Treatments for Reducing the Surface Roughness of Nb3Sn. In *8th Int. Particle Accelerator Conf.(IPAC'17), Copenhagen, Denmark, 14â 19 May, 2017*, pages 1145–1148. JACOW, Geneva, Switzerland, 2017.

[PGH+12] S. Posen, D. Gonnella, G. H. Hoffstaetter, M. Liepe, and J. Oh. Residual Resistance Studies at Cornell. In *Proc. 3rd Int. Particle Accelerator Conf. (IPAC'12)*, pages 2393–2395. JACoW Publishing, May 2012.

[PGH+20] T. Proslier, N. Groll, D. L. Hall, S. Posen, A. Glatz, R. Cook, and M. Liepe. Tunneling Spectroscopy Studies of Nb3Sn for SRF Cavities. In *Proc. Virtual International Workshop on Nb3Sn SRF Science, Technology, and Applications (Nb3SnSRF'20)*, Nov. 2020.

[PH17] S. Posen and D. L. Hall. Nb3Sn Superconducting Radiofrequency Cavities: Fabrication, Results, Properties, and Prospects. *Superconductor Science and Technology*, 30(3):33004, 2017.

[PHL+19] R. D. Porter, H. Hu, M. Liepe, N. A. Stilin, Z. Sun, and M. J. Tao. Progress in Nb3Sn SRF Cavities at Cornell University. In *Proc. North American Particle Accelerator Conf. (NAPAC'19)*. JACoW Publishing, Sep. 2019.

[PHLM16] R. D. Porter, D. L. Hall, M. Liepe, and J. T. Maniscalco. Surface Roughness Effect on the Performance of Nb3Sn Cavities. In *Proc. 28th Linear Accelerator Conf. (LINAC'16)*, pages 129–132. JACoW Publishing, Sep. 2016. https://doi.org/10.18429/JACoW-LINAC2016-MOPRC027.

[PKE+17a] U. Pudasaini, M. J. Kelley, G. V. Eremeev, C. E. Reece, and H. Tian. Electrochemical Finishing Treatment of Nb3Sn Diffusion-coated Niobium. In *Proc. 18th Int. Conf. RF Superconductivity (SRF'17)*, pages 900–905. JACoW Publishing, Jul. 2017. https://doi.org/10.18429/JACoW-SRF2017-THPB070.

[PKE+17b] U. Pudasaini, M. J. Kelley, G. V. Eremeev, C. E. Reece, and J. Tuggle. Post-Processing of Nb3Sn Coated Nb. In *Proc. 8th Int. Particle Accelerator Conf. (IPAC'17)*, pages 1190–1193. JACoW Publishing, May 2017. https://doi.org/10.18429/JACoW-IPAC2017-MOPVA144.

[PKE+18] U. Pudasaini, M. J. Kelley, G. V. Eremeev, C. E. Reece, and J. Tuggle. Studies of Electropolishing and Oxypolishing Treated Diffusion Coated Nb3Sn Surfaces. In *Proc. 9th Int. Particle Accelerator Conf. (IPAC'18)*, pages 3954–3957. JACoW Publishing, Apr.-May 2018. https://doi.org/10.18429/JACoW-IPAC2018-THPAL131.

[PKH98] H. Padamsee, J. Knobloch, and T. Hays. *RF Superconductivity for Accelerators*. Wiley Series in Beam Physics and Accelerator Technology. Wiley, 1st edition, 1998.

[PL11] S. Posen and M. Liepe. Stoichiometric Nb3Sn in First S.ples coated at Cornell. In *Proceedings of SRF 2011*, Chicago, Illinois, jul 2011.

[PL13] S. Posen and M. Liepe. RF Test Results of the First Nb3Sn Cavities Coated at Cornell. In *Proceedings of SRF 2013*, Paris, sep 2013.

[PL14] S. Posen and M. Liepe. Advances in Development of Nb3Sn Superconducting Radio-Frequency Cavities. *Physical Review Special Topics - Accelerators and Beams*, 17(11):112001, nov 2014.

[PLM19] R. D. Porter, M. Liepe, and J. T. Maniscalco. High Frequency Nb3Sn Cavities. In *Proc. 19th Int. Conf. RF Superconductivity (SRF'19)*, pages 44–47. JACoW Publishing, Jun.-Jul. 2019. https://doi.org/10.18429/JACoW-SRF2019-MOP011.

[PLP14] S. Posen, M. Liepe, and Th. Proslier. Nb3Sn Materials Studies. In *Proc. 27th Linear Accelerator Conf. (LINAC'14)*, pages 92–94. JACoW Publishing, Aug.-Sep. 2014.

[PLS+21] S. Posen, J. Lee, D. N. Seidman, A. Romanenko, B. Tennis, O. S.

Melnychuk, and D. A. Sergatskov. Advances in Nb3Sn Superconducting Radiofrequency Cavities Towards First Practical Accelerator Applications. 34(2):025007, jan 2021.

[PLX11] S. Posen, M. Liepe, and Y. Xie. Cornell SRF New Materials Program. In *Proceedings of IPAC 2011*, San Sebastian, sep 2011.

[PMRT15] S. Posen, M. Merio, A. Romanenko, and Y. Trenikhina. Fermilab Nb3Sn R&D Program. In *Proceedings of SRF 2015*, Whistler, dec 2015.

[PMS08] H. Padamsee, DESY Maschinenphysik, and Valery Shemelin. Magnetic Field Enhancement at Pits and Bumps on the Surface of Superconducting Cavities. *TTC-Reports (2008),*, 01 2008.

[Por20] R. D. Porter. Dynamics of RF Dissipation - High-Speed Temperature Mapping. Presented at the TESLA Technology Collaboration (TTC) Meeting in Hamburg, Germany, 2020.

[Pos14] S. Posen. *Understanding and Overcoming Limitation Mechanisms in Nb3Sn Superconducting RF Cavities*. PhD thesis, Cornell University, 2014.

[Pou74] M. Pourbaix. *Atlas of electrochemical equilibria in aqueous solutions / by Marcel Pourbaix ; translated from the French by J. A. Franklin (except sections I, III 5, and III 6, which were originally written in English).* National Association of Corrosion Engineers, Houston, Tex, 2d english ed. edition, 1974.

[PRG+20] S. Posen, A. Romanenko, A. Grassellino, O. S. Melnychuk, and D. A. Sergatskov. Ultralow Surface Resistance via Vacuum Heat Treatment of Superconducting Radio-Frequency Cavities. *Phys. Rev. Applied*, 13:014024, Jan 2020.

[PSFW64] J. M. Pierce, H. A. Schwettman, W. M. Fairbank, and P. B. Wilson. RF Losses in Superconducting Lead and Niobium. In *Proc. 9th Int. Conf. on Low Temp Phys.*, pages 396–399, Aug. 1964. https://doi-org.proxy.library.cornell.edu/10.1007/978-1-4899-6443-4.

[Pud20] U. Pudasaini. Growth And Properties Of Vapor Diffused Nb3Sn Coating For Superconducting Radiofrequency Accelerator Cavity Applications. *Dissertations, Theses, and Masters Projects*, January 2020.

[PVL15] S. Posen, N. Valles, and M. Liepe. Radio Frequency Magnetic Field Limits of Nb and Nb3Sn. *Phys. Rev. Lett.*, 115(4):47001, jul 2015.

[RDPM19] M. Liepe R. D. Porter and J. T. Maniscalco. High Frequency Nb3Sn Cavities. In *Proc. 20th Int. Conf. RF Superconductivity (SRF'19)*, Dresden, Germany, Jun 2019.

[RDS+09] A.A. Rossi, S. M. Deambrosis, S. Stark, V. Ramazzo, V. Rupp, R. G. Sharma, F. Stivanello, and V. Palmieri. Nb3Sn films by Multilayer Sputtering. In *Proceedings of SRF 2009*, Berlin, 2009.

[RECS13] A. Romanenko, C. J. Edwardson, P. G. Coleman, and P. J. Simpson. The Effect of Vacancies on the Microwave Surface Resistance of Niobium Revealed by Positron Annihilation Spectroscopy. *Applied Physics Letters*, 102(23):232601, 2013.

[Rom09] O. Romanenko. *Surface Characterization of Nb Cavity Sections - Understanding the High Field Q-Slope*. PhD thesis, Cornell University, 2009.

[Ros19] M. C. Ross. LCLS-II: Status, Issues and Plans. In *Proc. 19th Int. Conf. RF Superconductivity (SRF'19)*, pages 1–8. JACoW Publishing, Jun.-Jul. 2019. https://doi.org/10.18429/JACoW-SRF2019-MOFAA1.

[RSI+16] G. Rosaz, A. Sublet, K. IlY.na, S. Calatroni, M. Taborelli, S. Aull, A. Myasaki, W. Venturini-Delsolaro, K. Schirm, M. Karppinen, N. Schwerg, M. Therasse, F. Leaux, A. Fontenla, and J. B. Descarrega. Production and R&D Thin Films Activities at CERN for SRF Applications. In *Proceedings of TESLA Technology Workshop*, Paris, 2016.

[Rv15] S. Rudtsch and C. von Rohden. Calibration and Self-Validation of Thermistors for High-Precision Temperature Measurements. *Measurement*, 76:1–6, 2015.

[S+95] Q. S. Shu et al. An Advanced Rotating T-R Mapping & its Diagnoses of TESLA 9-Cell Superconducting Cavity. In *Proc. 16th Particle Accelerator Conf. (PAC'95)*. JACoW Publishing, May 1995.

[S+19a] N. Sitaraman et al. Ab Initio Calculations on the Growth and Superconducting Properties of Nb3Sn. In *Proc. 19th Int. Conf. RF Su-*

perconductivity (SRF'19), pages 39–43. JACoW Publishing, Jun.-Jul. 2019. https://doi.org/10.18429/JACoW-SRF2019-MOP010.

[S+19b] Z. Sun et al. Electroplating of Sn Film on Nb Substrate for Generating Nb3Sn Thin Films and Post Laser Annealing. In *Proc. 19th Int. Conf. RF Superconductivity (SRF'19)*, pages 51–54. JACoW Publishing, Jun.-Jul. 2019. https://doi.org/10.18429/JACoW-SRF2019-MOP014.

[S+19c] Z. Sun et al. Fast Sn-Ion Transport on Nb Surface for Generating NbxSn Thin Films and XPS Depth Profiling. In *Proc. North American Particle Accelerator Conf. (NAPAC'19)*. JACoW Publishing, Sep. 2019.

[S+21a] Md. N. Sayeed et al. Cylindrical Magnetron Development for Nb3Sn Deposition via Magnetron Sputtering. In *Proc. 20th Int. Conf. RF Superconductivity (SRF'21)*, Lansingm MI, USA, Jun 2021.

[S+21b] N. Sitaraman et al. New Recipes to Optimize the Niobium Oxide Surface from First-Principles Calculations. In *Proc. 20th Int. Conf. RF Superconductivity (SRF'21)*. JACoW Publishing, Jul. 2021.

[S+21c] Z. Sun et al. Toward Stoichiometric and Low-Surface Roughness Nb3Sn Thin Films via Direct Electrochemical Deposition. In *Proc. 20th Int. Conf. RF Superconductivity (SRF'21)*, Lansingm MI, USA, Jun 2021.

[Sab13] S. Sabharwal. Electron Beam Irradiation Applications. In *Proc. North American Particle Accelerator Conf. (NAPAC'13)*, pages 745–748. JACoW Publishing, Sep.-Oct. 2013.

[Saf01] H. Safa. High Field Behavior of SCRF Cavities. In *Proc. 10th Workshop RF Superconductivity (SRF'01)*. JACoW Publishing, Sep. 2001.

[Sai03] K. Saito. Development of Electropolishing Technology for Superconducting Cavities. In *Proceedings of the 2003 Particle Accelerator Conference*, volume 1, pages 462–466 Vol.1, 2003.

[SB20] V. D. Shemelin and S. A. Belomestnykh. *Multipactor Near the Cavity Equator*, pages 67–90. Springer International Publishing, Cham, 2020.

[SCP+21] N. S. Sitaraman, J. Carlson, A. R. Pack, R. D. Porter, M. U. Liepe, M. K. Transtrum, and T. A. Arias. Ab Initio Study of Antisite Defects in Nb3Sn: Phase Diagram and Impact on Superconductivity. *Physical Review B*, 103(11):115106, March 2021. arXiv: 1912.07576.

[SDR92] N. J. Simon, E. S. Drexler, and R. P. Reed. Properties of Copper and Copper Alloys at Cryogenic Temperatures. Final Report. 2 1992.

[Set21] J. P. Sethna. *Statistical Mechanics: Entropy, Order Parameters, and Complexity: Second Edition*. Oxford University Press, 2 edition, January 2021.

[SG17] A. Sheikhzada and A. Gurevich. Dynamic Transition of Vortices into Phase Slips and Generation of Vortex-Antivortex Pairs in Thin Film Josephson Junctions Under DC and AC Currents. *Phys. Rev. B*, 95(21):214507, jun 2017.

[SH68] J. S. Steinhart and S. R. Hart. Calibration Curves for Thermistors. *Deep Sea Research and Oceanographic Abstracts*, 15(4):497–503, 1968.

[SHL+20] N. Stilin, A. Holic, M. Liepe, R. D. Porter, and J. Sears. Stable CW Operation of Nb3Sn SRF Cavity at 10 MV/m using Conduction Cooling. *arXiv:2002.11755 [physics]*, February 2020. arXiv: 2002.11755.

[SKR03] W.J. Schneider, P. Kneisel, and C.H. Rode. Gradient Optimization for SC CW Accelerators. In *Proceedings of the 2003 Particle Accelerator Conference*, volume 5, pages 2863–2868 vol.5, 2003.

[Sla50] J. C. Slater. *Microwave Electronics*. The Bell Telephone Laboratories series. Van Nostrand, New York, NY, USA, 1950.

[SP08] V. Shemelin and H. Padamsee. Magnetic Field Enhancement at Pits and Bumps on the Surface of Superconducting Cavities. Technical report, Cornell University, 2008.

[SPR+20] M. N. Sayeed, U. Pudasaini, C. E. Reece, G. V. Eremeev, and H. E. Elsayed-Ali. Effect of Layer Thickness on Structural, Morphological and Superconducting Properties of Nb3Sn Films Fabricated by Multilayer Sequential Sputtering. 756:012014, jun 2020.

[Ste15] G. R. Stewart. Superconductivity in the A15 Structure. *Physica C: Superconductivity and its Applications*, 514:28–35, July 2015.

[Sti78] J. B. Stimmell. *Microwave superconductivity of Nb3Sn*. PhD thesis, Cornell University, 1978.

[SW62] E. Saur and J. Wurm. Preparation und Supraleitungseigenschaften von Niobdrahtproben mit Nb3Sn-Uberzug. *Die Naturwissenschaften*, 49(6):127–128, 1962.

[SW14] Andrew Sessler and Edmund Wilson. *Engines of Discovery*. World Scientific, revised and expanded edition, 2014.

[Tin12] M. Tinkham. *Introduction to Superconductivity*. Dover Books on Physics Series. Dover Publications, Incorporated, 2nd edition, 2012.

[TPL19] M. Tao, R. D. Porter, and M. Liepe. Continuous Temperature Measurement of SRF Cavities: Recording Quench Events with an Improved Temperature Mapping System. Technical report, Cornell University, 2019.

[TRK+06] H. Tian, C. E. Reece, M. J. Kelley, S. Wang, L. Plucinski, K. E. Smith, and M. M. Nowell. Surface Studies of Niobium Chemically Polished Under Conditions for Superconducting Radio Frequency (SRF) Cavity Production. *Applied Surface Science*, 253(3):1236–1242, 2006.

[TSGS02] C. Toffolon, C. Servant, J. C. Gachon, and B. Sundman. Reassessment of the Nb-Sn System. *Journal of Phase Equilibria*, 23(2):134–139, mar 2002.

[Tsu02] T. Tsuyoshi. Possibility of MgB2 Application to Superconducting Cavities. In *Proceedings of EPAC 2002*, Paris, 2002.

[TWX+16] Teng Tan, M. A. Wolak, X. X. Xi, T. Tajima, and L. Civale. Magnesium Diboride Coated Bulk Niobium: A New Approach to Higher Acceleration Gradient. *Scientific Reports*, 6(1):35879, December 2016.

[Val13] N. Valles. *Pushing the Frontiers of Superconducting Radio Frequency Science: From the Temperature Dependence of the Superheating Field of*

Niobium to Higher-Order Mode Damping in Very High Quality Factor Accelerating Structures. PhD thesis, Cornell University, 2013.

[Val21] R. Valizadeh. Synthesis of Nb and Alternative Superconducting Film to Nb for SRF Cavity as Single Layer. In *Proc. 20th Int. Conf. RF Superconductivity (SRF'21)*, Lansingm MI, USA, Jun 2021.

[Vel87] V. F. Veley. *Modern Microwave Technology*. Fundamentals of the Physics of Solids. Prentice-Hall, 1987.

[VF16] A-M. Valente-Feliciano. Superconducting RF Materials Other than Bulk Niobium: A Review. *Superconductor Science and Technology*, 29(11):113002, sep 2016.

[VL11a] N. Valles and M. Liepe. The Superheating Field of Niobium: Theory and Experiment. In *Proceedings of SRF 2011*, pages 293 – 301, Chicago, Illinois, jul 2011.

[VL11b] N. R. A. Valles and M. Liepe. Designing Multiple Cavity Classes for the Main Linac of Cornell's ERL. In *Proc. 24th Particle Accelerator Conf. (PAC'11)*, pages 937–939. JACoW Publishing, Mar.-Apr. 2011.

[VLF+14] N. Valles, M. Liepe, F. Furuta, M. Gi, D. Gonnella, Y. He, K. Ho, G. Hoffstaetter, D. S. Klein, T. O'Connell, S. Posen, P. Quigley, J. Sears, G. Q. Stedman, M. Tigner, and V. Veshcherevich. The Main Linac Cavity for Cornell's Energy Recovery Linac: Cavity Design through Horizontal Cryomodule Prototype Test. *Nuclear Instruments and Methods in Physics Research Section A: Accelerators, Spectrometers, Detectors and Associated Equipment*, 734:23–31, jan 2014.

[VXP07] J. Vines, Y. Xie, and H. Padamsee. Systematic Trends for the Medium Field Q-slope. In *Proc. 13th Int. Conf. RF Superconductivity (SRF'07)*. JACoW Publishing, Oct. 2007.

[Wag54] C. Wagner. Contribution to the Theory of Electropolishing. 101(5):225, 1954.

[Wei84] W. Weingarten. Electron Loading. In *Proc. 2nd Int. Conf. RF Superconductivity (SRF'84)*. JACoW Publishing, Jul. 1984.

[XHL09] Y. Xie, J. H. Hinnefeld, and M. Liepe. Design of a TE-Type Cavity for Testing Superconducting Material S.ples. In *Proc. 14th Int. Conf. RF Superconductivity (SRF'09)*, pages 281–285. JACoW Publishing, Sep. 2009.

[XKR12] C. Xu, M. J. Kelley, and C. E. Reece. Analyzing Surface Roughness Dependence of Linear RF Losses. In *Proc. 26th Linear Accelerator Conf. (LINAC'12)*, pages 210–212. JACoW Publishing, Sep. 2012.

[XRK13] B. P. Xiao, C. E. Reece, and M. J. Kelley. Superconducting Surface Impedance Under Fadiofrequency Field. *Physica C: Superconductivity*, 490(Supplement C):26–31, 2013.

[XTRK11] C. Xu, H. Tian, C. E. Reece, and M. J. Kelley. Enhanced Characterization of Niobium Surface Topography. *Phys. Rev. ST Accel. Beams*, 14:123501, Dec 2011.

[Zha14] L. Zhao. *Surface Polishing of Niobium for Superconducting Radio Frequency (SRF) Cavity Applications*. PhD thesis, The College of William and Mary, 2014.